



UNIVERSITY *of the*
WESTERN CAPE

***EFFECT OF ZINC OXIDE NANORIDGE HEIGHT ON SOLAR
CELL PERFORMANCE***

BY

MAGDELINE MOHLAO SEABI



**A thesis submitted in partial fulfilment of the requirement for the
degree of Magister Scientiae in the Department of Physics and
Astronomy, University of the Western Cape (UWC)**

Supervisor: Dr T.F.G. Muller (UWC)

Co-supervisor: Prof S. Bolokang (CSIR)

October 2021

DEDICATION

This thesis is dedicated to my Parents; Matsobane Seabi and Maite Seabi, my siblings; Mahloromela Seabi, Phološo (Billy) Seabi and Emmanuel Seabi, my uncles; Wesley Ramaselele, Phetole Rakgabale and Collen Ramaselele, my aunts; Sharron Ramaselele and Mapula Rakgabale, my spiritual leader; His Grace the Right Rev. Bishop Dr B.E Lekganyane and my late grandparents; my grandmother Mahadia Ramaselele, my grandfathers; Phineas Seabi and Mampshe Rakgabale, and my granduncle; Dalton Ramaselele.



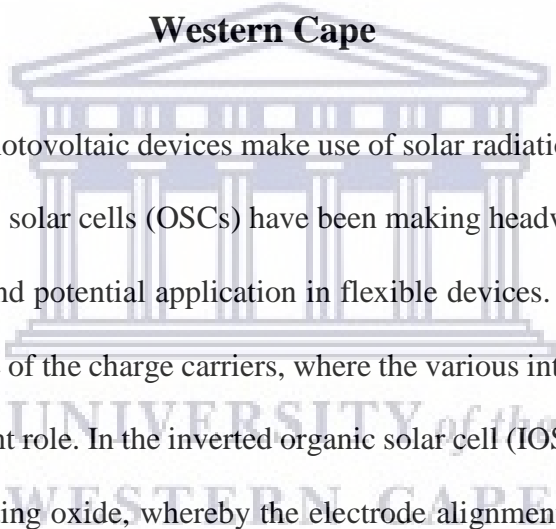
ABSTRACT

Effect of zinc oxide nanoridge height on solar cell performance

By

M.M. Seabi

**MSc. Mini-Thesis, Department of Physics and Astronomy, University of the
Western Cape**



Environmentally friendly photovoltaic devices make use of solar radiation as the energy source to generate electricity. Organic solar cells (OSCs) have been making headway in the last decade due to their cost-effectiveness and potential application in flexible devices. One of the disadvantages of OSCs is the short lifetime of the charge carriers, where the various interfaces that are present in the material play a significant role. In the inverted organic solar cell (IOSC), electrons are injected into the transparent conducting oxide, whereby the electrode alignment is reversed compared to the conventional structure. Nanosized zinc oxide (ZnO) thin-films with nanoridges/ripples embedded on the surface of the thin-film can be used as an electron transport/hole-blocking layers in inverted organic solar cells to enhance light-capturing by the active layer of the solar cell.

This study reports on a simple approach to improving the morphological and optical properties of ZnO nanoridges by means of incorporating hydrothermally synthesised wurtzite ZnO nanoparticle seeds under a controlled synthesis period and temperature. The seeded ZnO nanoridge thin-films

were used as electron transport layers (ETL) to enhance the electron transportation to the indium tin oxide (ITO) electrode, and for hole blocking purposes where the polymer-blend active layer consisting of [6,6]-phenyl-C61-butyric acid methyl ester (PCBM) as electron acceptor and poly(3-hexylthiophene) (P3HT) as electron donors are concerned, and to supply stability in the interface of the polymer-ETL layers. Ultimately, the effect of the ZnO nanoparticle size on the heights of the film's ripples, its subsequent effect on light-capturing by the active layer, and the photovoltaic performance of the solar cell using hydrothermal synthesis to synthesise ZnO nanoparticles were investigated.

At the initial stage, ZnO nanoparticles were investigated and subsequently utilised as seeds to induce ripple growth in spin-coated ZnO thin-films. The ZnO nanoparticles under period and temperature control showed good agreement of crystallographic properties under x-ray diffraction (XRD) and high-resolution transmission microscopy (HRTEM). ZnO nanoparticles produced at a longer synthesis period and higher temperature showed improvement in the optical properties. The seeded ZnO nanoridges showed uniform coverage at the surface of the ITO under scanning electron microscopy measurements. The step-height of the ripples showed a decrease with an increase in the synthesis period and temperature. The decreasing step-height promoted the increased transparency of the thin-films as the ultraviolet-visible (UV-Vis) transmission spectroscopy revealed improved optical properties compared to the unseeded ZnO nanoridges thin-film.

The electrical properties of the IOSCs demonstrated that seeding ZnO nanoridges ETLs with hydrothermally synthesised ZnO nanoparticles at higher temperature and a longer period of 180°C and 6 hours, respectively, improves the charge absorption in the active layer, charge mobility, and stability in the polymer-ETL interfaces. The obtained power conversion efficiency values were found to range from 0.4-2.3%, corresponding to a direct decrease in the height of the nanoridge thin-films and a direct decrease in the width size distribution of the nanoridges with increasing synthesis temperature and period control.



KEYWORDS: Electron Transporting Layer; Hydrothermal Synthesis; Inverted Organic Solar Cell; Metal Oxide; Nanoparticles; Nanoridges; Sol-Gel Synthesis; Nanocrystalline; Ramp-Annealing; Spin Coating; Thin-film, ZnO.




DECLARATION

I declare that “*Effect of zinc oxide nanoridge height on solar cell performance*” is my own work, that it has not been submitted for any degree or examination in any other university, and that all the sources I have used or quoted have been indicated and acknowledged by complete references.

Full name: Magdeline Mohlao Seabi

Date: October 2021

Signed: 



UNIVERSITY *of the*
WESTERN CAPE

ACKNOWLEDGEMENTS

I would firstly like to thank God of Mount Zion. Had it not been Him, as He was always on my side, I would've left my research project and soaked in depression and mental instability. However, I managed to bounce back on track and finish my project by His will.

Secondly, I would like to thank my spiritual leader, His Grace the Right Rev. Bishop Dr B.E. Lekganyane, for his continuous words and actions of encouragement to us young people to major in the field of science and technology. His continued dignified leadership and humility do not go unnoticed. As science students from his religious institution, we draw inspiration from his volunteering programs and apply it in our careers and everyday lives. The educational skills we acquire in our respective institutions, then use them to better our communities. I would also like to thank him for the gracious spiritual leadership and guidance he has established in my life from a very young age until I was able to get to my masters level; the spiritual leadership that has built me into the responsible young woman I am today. Coming from a community where education is overlooked, I would've turned out badly, but due to his guidance, I managed to succeed to my master's level, which is a huge achievement.

My supervisor, Dr Theophillus F.G Muller, has constantly motivated me to become a better science student, and for that, I will forever be grateful. Coming to a foreign land, not knowing much, he has made a smooth transition for me and a comfortable environment to showcase my capabilities

and encouraged me to become a better version of myself in terms of intellectual improvement. Working with him has taught me that daily consistent hard work put in studies yields better results and that kindness and humility go a very long way. His kindness and patience were witnessed when I went into mental instability. He, however, has shown support and never gave up on me even when it was challenging to work with me. I would also like to thank my co-supervisor, Prof Bolokang for his constant academic support, especially during a very confusing time of the global Covid-19 pandemic. I would also like to thank Prof Arendse and Dr Cummings. I appreciate their humility and support in helping me with my sample characterisation and words of encouragement have contributed to accumulating most of my results in a concise period and driving me towards finishing my write-up. I want to thank Prof Modibane for introducing me to MSc Nanoscience Postgraduate and Learning Platform and supporting me throughout the journey; this platform has opened many other bright opportunities.

It goes without saying that putting up the writing-up part of the work is straining; however, with the help of my writing coach Zainonesa Abrahams-October, I could write up my thesis to a suitable scientific standard. For that, I'll forever appreciate her patience, care and some of the working principles she shared with me.

I appreciate my family, mom, father, siblings and uncles and aunts, I love and draw inspiration from. I want to thank them for the continuous encouragement, support and inspiring words to improve academically and socially. My mom, in particular, is someone I draw so much academic inspiration from because she went from being a diploma holder to 2 honours degrees holder and

planning to do her masters and PhD. Despite the challenges she faces in life, such as losing her mom to mental illness and having to take care of her siblings and her mentally ill grandmother and aunt, she is still a goal-driven individual with big dreams and hopes for her academic life, her business journey and the academic life of her children and siblings. That, for me, is enough to keep me going and know that the “sky doesn’t have to be the limit” –Mokone Mmola. My father’s support in tough times is highly appreciated. His words and actions of encouragement have groomed me to face my fears and know that anything is possible, especially when you believe in yourself. My family is my rock. Their support, kind efforts, and better change they bring about in my life never go unnoticed. I’m grateful for their constant motivation to keep pushing and not give up on my master’s degree despite the mental trauma and loneliness in a foreign land I have suffered.

I want to thank my friends in the science field Mokone Mmola and Tebatso Maake, for their patience, understanding, academic and social support, and willingness to read and edit my work to a better scientific standard. Their friendship and professional support have pushed me to work hard and smart to reach my goals. I appreciate their continuous presence in my life as I draw inspiration from them.

My close friends, Brian Ramogayana, Colia Mahlase, and Katisho Mogashoa, have been my social support system. I appreciate their emotional support. Their jokes about the ups and downs I have come across during my master’s degree term have cheered me up. The sisterhood relationship with

Colia has kept me pushing as she is a woman of hard work, dedication and a goal-driven mindset. That has inspired me also to work hard and keep moving until I reach my goals.

I humbly appreciate my co-postgraduate students at G45. Coming to a foreign land was never smooth sailing. However, some of these co-postgraduate students have become my friends, such as Amy James and Khudzai Sithole. Their academic support will forever be appreciated.

Norman Bowers, Siyabonga Mduli, Bello Muhammad, Natasha Peterson, Siphesihle Magubane, Stephen Klue and Siphelo Ngqoloda are highly appreciated for the experimental general science research assistance I've received from them.

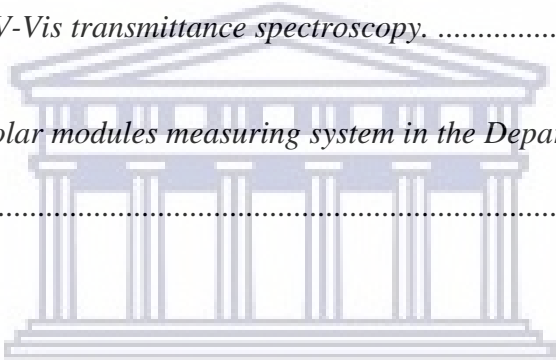
Lastly, I would like to acknowledge the University of the Western Cape, The department of Physics and Astronomy, for allowing me to showcase and improve my academic skills, I have accumulated previously in the University of Limpopo; the Nanoscience postgraduate teaching and training platform, South Africa platform for their funding, Council for Scientific and Industrial Research for AFM measurements, Ithemba Labs for their assistance in XRD characterisation, University of the Western Cape scanning microscope unit for HRTEM and HRSEM characterisation, Chemical Science Department for UV-Vis and FTIR characterisation.

LIST OF FIGURES

<i>Figure 1.1: Representation of several radiation attenuating effects occur when radiation crosses the atmosphere: the radiation either diffuse, reflects, and scatter [1.13].</i>	4
<i>Figure 1.2: Shape of the solar spectrum in terms of irradiance ($W/m^2 \cdot nm$) and the absorption of various wavelengths (nm) for AM 1.5 conditions [1.14].</i>	5
<i>Figure 1.3: Global Horizontal Irradiance [1.17].</i>	6
<i>Figure 1.4: A traditional photovoltaic device and the working principle behind it [1.21].</i>	11
<i>Figure 1.5: The energy band diagram of a p-n junction [1.2].</i>	13
<i>Figure 1.6: (a) p-i-n diode, (b) the energy band diagram of p-i-n diode [1.24].</i>	14
<i>Figure 1.7: Plot of the I-V characteristics for a traditional solar cell [1.29].</i>	18
<i>Figure 1.8: Working principle of a Cz-Si solar cell: upon photon absorption and charge carrier production [1.31].</i>	20
<i>Figure 1.9: General design of a) an organic solar cell [1.42].</i>	26
<i>Figure 1.10: Energy level diagram of a charge-carriers diffusion system in organic solar cells; IP_D is the ionisation potentials, $h\nu$ is the photon energy, and electron affinity is represented by χ_D and χ_A. The photo-induced electron propagation is the initial step for generating free charge carriers and is demonstrated by the arrow between LUMO levels [1.42].</i>	27

<i>Figure 1.11: Solar cell power conversion efficiencies-NREL-2018 chart [1.47].</i>	31
<i>Figure 1.12: General design of (a) conventional organic solar cell (COSC) (b) inverted organic solar cell (IOSC) [1.42].</i>	34
<i>Figure 1.13: (a) Hexagonal Wurtzite structure [1.51], (b) powder form of ZnO material [1.52].</i>	36
<i>Figure 1.14: representation of ZnO crystal structures: (a) cubic rocksalt B1, (b) cubic zinc blende B3, and (c) hexagonal wurtzite B4. The shaded grey and black spheres represent Zn and O atoms, respectively [1.53].</i>	37
<i>Figure 1.15: Schematic representation of a wurtzite ZnO structure containing lattice parameters in the basal plane and c in the basal direction; and 109.070° in an ideal crystal are the bond angles [1.53].</i>	38
<i>Figure 1.16: AFM images of different ZnO film surfaces on indium-tin oxide used as hole-blocking layers in IOSCs. (a) ZnO film was spin-coated using bare zinc acetate solution, (b)–(f) ZnO films were spin-coated by utilising ZnO NPs and zinc typical acetate solutions. From (b) to (f), the mass of ZnO NPs in addition to the zinc acetate solution was increased. Amount of ZnO NPs added to 21ml of zinc acetate solution was 0.25, 1, 3, 5 and 10mg for (b)–(f), respectively [1.1].</i>	43
<i>Figure 1.17: Photovoltaic performances of IOSCs consisting of ZnO thin-films with various surface structures in Figure 1.16(a)–(f). Each device's PCE, FF, and short-circuit current are summarised [1.1].</i>	44

<i>Figure 2. 1: General hydrothermal synthesis of NPs calibrated at X°C temperature for Y period.</i>	64
<i>Figure 2.2: Schematic diagram of the general process steps involved in Sol-gel- Dip-coating techniques of nanomaterials synthesis.</i>	69
<i>Figure 2.3: Sol-gel method- Spin-coating of unseeded ZnO NRs and seeded ZnO NPs-ZnO NRs calibrated at 140°C and 180°C for 6 hrs and calibrated at 200°C for 3 hrs and 6 hrs.</i>	70
<i>Figure 2. 4: The flow chart diagram illustrating the steps involved in fabricating IOSCs.</i>	72
<i>Figure 2. 5: (a) The band gap diagram of IOSCs made of 2 electrodes (indium-tin-oxide and silver (Ag)), ETL (ZnO), a hole-transport layer, (MoO₃), and an active layer (P3HT: PCBM) (b) Schematic diagram of the IOSC-based P3HT: PCBM layer with ZnO nanoridge layer as ETL.</i>	73
<i>Figure 2. 6: (a) FTIR instrument [2.15] and (b) Working principle behind FTIR.</i>	74
<i>Figure 2. 7: (a) XRD instrument [2.27]. (b) Schematic diagram of working principle of XRD. .</i>	79
<i>Figure 2. 8: (a) HRTEM instrument [2.29] and (b) schematic is depicting the working principle behind HRTEM.</i>	81
<i>Figure 2. 9: (a) HR-SEM instrument [2.36] and (b) Working principle behind HR-SEM.</i>	85
<i>Figure 2. 10: EDS elemental distribution and quantification data [2.38].</i>	86

<i>Figure 2.11: Elemental distribution map of NaCl [2.40].</i>	87
<i>Figure 2.12: Schematic diagram of a stylus profilometry setup [2.42].</i>	89
<i>Figure 2.13: Schematic diagram of an Interferometric profilometer [2.42].</i>	90
<i>Figure 2.14: (a) Spectrophotometer [2.49] and (b) Working principle behind UV-vis absorption spectroscopy.</i>	94
<i>Figure 2.15: (a) Experimental measurement setup for transmission spectroscopy [2.50] and (b) working principle behind UV-Vis transmittance spectroscopy.</i>	95
<i>Figure 2.16: (a) and (b): Solar modules measuring system in the Department of Physics (UWC).</i>	99
	
<i>Figure 3.1: Hydrothermal synthesis of ZnO NPs calibrated at 200°C for 3 hrs and 6 hrs and calibrated at 140°C and 180°C for 6 hrs.</i>	113
<i>Figure 3.2: FTIR spectra of ZnO NPs calibrated at 3 hrs and 6 hrs at 200°C, respectively.</i>	117
<i>Figure 3.3: FTIR spectra of ZnO calibrated at 140°C and 180°C for 6 hrs, respectively.</i>	120
<i>Figure 3.4: XRD pattern of ZnO NPs synthesised for 3 hrs and 6 hrs at 200°C, respectively.</i>	125
<i>Figure 3.5: Intensity versus 2θ around (101) peaks of ZnO NPs synthesised for 3 and 6 hrs at 200°C, respectively.</i>	126

<i>Figure 3. 6: W-H models of ZnO NPs prepared for 3 hrs and 6 hrs at 200°C, respectively.....</i>	127
<i>Figure 3. 7: XRD pattern of ZnO NPs synthesised at 140°C and 180°C for 6 hrs, respectively.</i>	129
<i>Figure 3. 8: Intensity versus 2θ around (101) peaks of ZnO NPs synthesised at 140°C and 180°C for 6 hrs, respectively.....</i>	130
<i>Figure 3. 9: W-H models of ZnO NPs prepared at 140°C and 180°C for 6 hrs.</i>	131
<i>Figure 3. 10: The bright-field HR-TEM images of ZnO NPs prepared for (a) 3 hrs and (b) 6 hrs at 200°C.....</i>	135
<i>Figure 3. 11: Particle size distribution of ZnO NPs prepared for (a) 3 hrs and (b) 6 hrs at 200°C.</i>	136
<i>Figure 3. 12: (a) The HR-TEM lattice images of ZnO NPs prepared for (a) 3 hrs and (b) 6 hrs at 200°C.....</i>	137
<i>Figure 3. 13: SAED pattern of ZnO NPs prepared for (a) 3 hrs and (b) 6 hrs at 200°C.</i>	138
<i>Figure 3. 14: The bright-field HR-TEM image of ZnO prepared for 6 hrs at (a) 140°C and (b) 180°C.....</i>	140
<i>Figure 3. 15: The particle size distribution of ZnO prepared for 6 hrs at (a) 140°C and (b) 180°C.</i>	141

<i>Figure 3. 16: The HR-TEM lattice image of ZnO prepared for 6 hrs at (a) 140°C and (b) 180°C.</i>	142
<i>Figure 3. 17: The HR-TEM image SAED pattern of ZnO prepared for 6 hrs at (a) 140°C and (b) 180°C.</i>	143
<i>Figure 3.18: UV-Vis optical absorption spectra of ZnO NPs synthesised at 200°C for 3 hrs and 6 hrs.</i>	145
<i>Figure 3. 19: UV-Vis optical absorption spectra of ZnO NPs synthesized at 140°C and 180°C for 6 hrs.</i>	147
<i>Figure 4. 1: Sol-gel-spin-coating synthesis of ZnO nanoridges and seeded ZnO NPs-ZnO NRs with ZnO NPs hydrothermally synthesised at 200°C for 3 hrs and 6 hrs and at 140°C and 180°C for 6 hrs.</i>	162
<i>Figure 4. 2: The height profile of ZnO nanoridges synthesised from a zinc acetate solution and ZnO NPs seeds produced at 140°C for 6 hrs.</i>	164
<i>Figure 4. 3 (a): HR-SEM-EDS spectrum analysis, (b): HR-SEM-EDS elemental composition of Zn and O for seedless ZnO NRs and ZnO NPs-seeded ZnO NRs with ZnO NPs that were hydrothermally synthesised at 140 °C and 180°C for 6 hrs, and 3 hrs and 6 hrs at 200°C, respectively.</i>	168

<i>Figure 4.4: SEM images of unseeded ZnO and seeded ZnO NPs-ZnO nanoridges calibrated for 3 hrs and 6 hrs at 200°C.</i>	170
<i>Figure 4. 5: Width size distribution of unseeded ZnO and seeded ZnO NPs-ZnO nanoridges calibrated for 3 hrs and 6 hrs at 200°C.</i>	171
<i>Figure 4. 6: SEM images of unseeded ZnO and seeded ZnO NPs-ZnO nanoridges calibrated at 140°C and 180°C for 6 hrs.</i>	174
<i>Figure 4. 7: Width size distribution of unseeded ZnO and seeded ZnO NPs-ZnO nanoridges calibrated at 140°C and 180°C for 6 hrs.</i>	174
<i>Figure 4. 8: Absorbance spectra of unseeded ZnO NRs and seeded ZnO NPs-ZnO NRs for 3 hrs and 6 hrs, at 200°C.</i>	178
<i>Figure 4. 9: Optical transmittance of unseeded ZnO NRs and seeded ZnO NPs-ZnO NRs for 3 hrs and 6 hrs, at 200°C.</i>	179
<i>Figure 4. 10: Tauc plots with direct band gap values of unseeded ZnO NRs and seeded ZnO NPs-ZnO NRs for 3 hrs and 6 hrs, at 200°C.</i>	180
<i>Figure 4. 11: Absorbance spectra of unseeded ZnO and seeded ZnO NPs-ZnO NRs with ZnO NPs hydrothermally fabricated at 140°C and 180°C for 6 hrs.</i>	183

Figure 4. 12: Optical transmittance of ZnO nanoridge structured thin-films deposited with the combination of bare zinc acetate solution and ZnO nanoparticles synthesised at 140°C and 180°C for 6 hrs..... 184

Figure 4. 13: Tauc plots with direct band gap values of ZnO NPs-ZnO nanoridges calibrated at 140°C and 180° for 6 hrs. 185

Figure 5. 1: (a) The band gap diagram of IOSCs made of two electrodes (indium-tin-oxide and silver (Ag)), ETL (ZnO), a hole-transport layer, (MoO₃), and an active layer (P3HT: PCBM) (b) Schematic diagram of the IOSC-based P3HT: PCBM layer with ZnO nanoridge layer as ETL. 196

Figure 5. 2: The flow chart diagram illustrating the steps involved in fabricating IOSCs. 197

Figure 5. 3: (a) Dark JV-curve measurements and (b) JV-curves of IOSC containing unseeded ZnO NRs ETL and seeded ZnO NPs-ZnO NRs ETLs of ZnO NPs synthesised for 3 hrs and 6 hrs at 200°C..... 199

Figure 5. 4: (a) Dark JV-curve measurements and (b) JV-curves of IOSC containing unseeded ZnO NRs ETL and seeded ZnO NPs-ZnO NRs ETLs of ZnO NPs synthesised at 140°C and 180°C for 6 hrs. 203

LIST OF TABLES

<i>Table 1.1: Examples of the semiconductors used in PV devices with corresponding band gaps [1.19].</i>	9
<i>Table 1.2: Best laboratory solar cells efficiencies of various solar cells [1.40].</i>	30
<i>Table 2. 1: Analytical characterisation techniques.</i>	61
<i>Table 3. 1: FTIR of ZnO NPs at various synthesis time intervals.</i>	118
<i>Table 3. 2: FTIR of ZnO NPs at various temperature values.</i>	121
<i>Table 3. 3: Calculated crystallite size and microstrain for ZnO NPs prepared at 200°C 3 hrs and 6 hrs at 200°C, respectively.</i>	128
<i>Table 3. 4: Calculated crystallite size and microstrain for ZnO NPs prepared at 140°C and 180°C for 6 hrs</i>	132
<i>Table 3. 5: Bulk ZnO JCPDS card 00-036-1451 [3.14].</i>	133
<i>Table 3. 6: The estimated band gap values of the absorption peaks observed in Figure 3.18..</i>	146
<i>Table 3. 7: The estimated band gap values of the absorption peaks observed in Figure 3.19..</i>	148

<i>Table 4. 1: Average nanoridges height (nm) of seedless ZnO NRs and ZnO NPs-seeded ZnO NRs of NPs hydrothermally synthesised for 3 hrs and 6 hrs at 200°C.</i>	165
<i>Table 4. 2: Average nanoridges height (nm) of seedless ZnO NRs and ZnO NPs seeded-ZnO NRs of NPs hydrothermally synthesised for 6 hrs at 140°C and 180°C.</i>	166
<i>Table 4. 3: Average NPs sizes with error for ZnO NPs (period calibration), step-height (nm), and average nanoridges width sizes of unseeded ZnO and seeded ZnO NPs-ZnO nanoridges calibrated for 3 hrs and 6 hrs at 200°C.</i>	172
<i>Table 4. 4: Average NPs sizes with error for ZnO NPs (temperature calibration), the Step-height, and the average nanoridges width size distribution of ZnO NPs-ZnO nanoridges calibrated at 140°C and 180°C for 6 hrs.</i>	175
<i>Table 4. 5: Band gap values (eV) and width distribution of the nanoridges (nm) and height values of the films (nm) of unseeded ZnO nanoridges ZnO NPs-ZnO NRs with ZnO NPs that were synthesised at 200°C for 3 hrs and 6 hrs.</i>	181
<i>Table 4. 6: Band gap values (eV) and average width distribution of the nanoridges (nm) and height values of the films (nm) of ZnO NPs-ZnO nanoridges calibrated at 140°C and 180°C for 6 hrs.</i>	186
<i>Table 5. 1: Power conversion efficiency (PCE), fill factor (FF), open-circuit voltage (V_{oc}), and short-circuit J_{sc} of IOSC containing unseeded ZnO NRs ETL and seeded ZnO NPs-ZnO NRs ETLs of ZnO NPs synthesised for 3 hrs and 6 hrs at 200°C.</i>	201

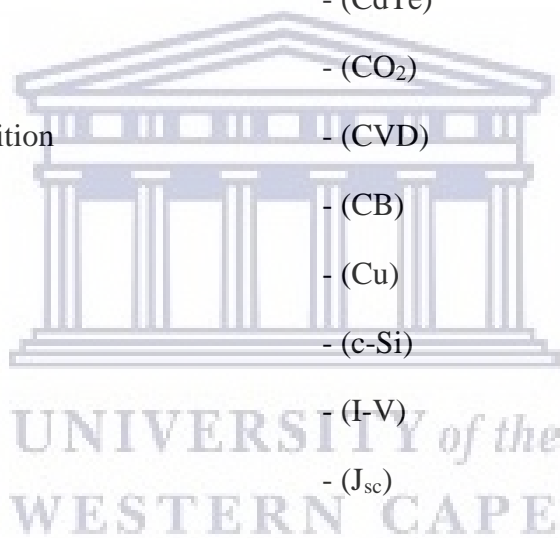
Table 5. 2: Power conversion efficiency (PCE), fill factor (FF), open-circuit voltage (V_{oc}), and short-circuit J_{sc}) of IOSC containing unseeded ZnO NRs ETL and seeded ZnO NPs-ZnO NRs ETLs of ZnO NPs synthesised at 140°C and 180°C for 6 hrs, respectively. 204



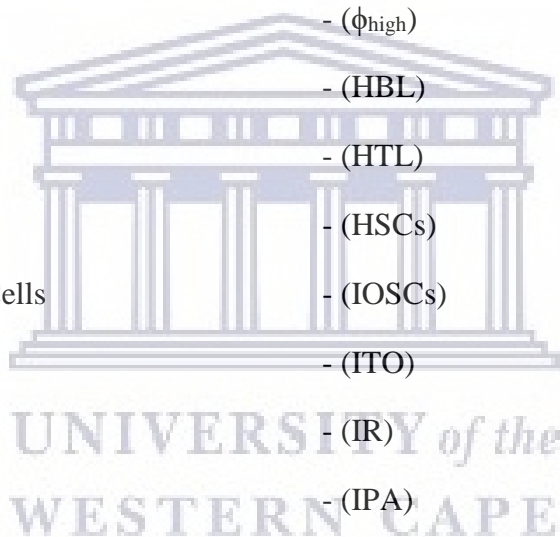
UNIVERSITY *of the*
WESTERN CAPE

LIST OF ABBREVIATIONS, ACRONYMS AND SYMBOLS

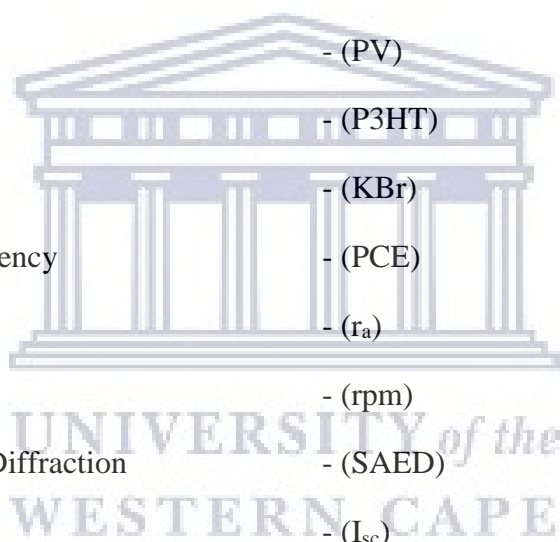
Air Mass	- (AM)
Angle	- (θ)
Astronomical Unit	- (AU)
Bulk-Heterojunction	- (BHJ)
Cadmium Telluride	- (CdTe)
Carbon Dioxide	- (CO ₂)
Chemical Vapour Deposition	- (CVD)
Conduction Band	- (CB)
Copper	- (Cu)
Crystalline Silicon	- (c-Si)
Current-Voltage	- (I-V)
Current Density	- (J _{sc})
Efficiency	- (η)
Electron Transport Layer	- (ETL)
Electron-Volt	- (eV)
Energy Gap	- (E _g)
Energy Dispersive Spectroscopy	- (EDS)
Ethanolamine	- (MEA)
Fermi-Level	- (E _f)



Field-Emission Gun	- (FEG)
Fill-Factor	- (FF)
Fourier Transform Infrared	- (FTIR)
Gold	- (Au)
Highest Occupied Molecular Orbital	- (HOMO)
High-Resolution Scanning Electron Microscopy	- (HR-SEM)
High-Resolution Transmission Electron Microscopy	- (HR-TEM)
High-Work Function	- (ϕ_{high})
Hole-Blocking Layer	- (HBL)
Hole-Transport Layer	- (HTL)
Hybrid Solar Cells	- (HSCs)
Inverted Organic Solar Cells	- (IOSCs)
Indium-Tin Oxide	- (ITO)
Infrared	- (IR)
Iso-Propanol	- (IPA)
Kelvin	- K
Lifetime	- (τ_f)
Low-Work Function	- (ϕ_{low})
Lowest Unoccupied Molecular Orbital	- (LUMO)
Molybdenum Oxide	- (MoO_x)
Molybdenum Trioxide	- (MoO_3)
Multi-Crystal Silicon	- (mc-Si)



Nanometre	- (nm)
Nanoparticles	- (NPs)
Nanoridge/ripples	- (NRs)
Open-Circuit Voltage	- (V_{oc})
Organic Solar Cells	- (OSCs)
Oxygen	- (O_2)
Phenyl-C61-Butyric Acid Methyl Ester	- (PCBM)
Photon Energy	- (E_{ph})
Photovoltaic	- (PV)
Poly 3-Hexylthiophene	- (P3HT)
Potassium Bromide	- (KBr)
Power Conversion Efficiency	- (PCE)
Ramp-Annealing	- (r_a)
Revolutions Per Minute	- (rpm)
Selected-Area Electron Diffraction	- (SAED)
Short Circuit Current	- (I_{sc})
Shunt Resistance	- (R_{sh})
Silver	- (Ag)
Single-Crystal Silicon	- (Cz-Si)
Titanium Dioxide	- (TiO_2)
Transmission Electron Microscopy	- (TEM)
Ultraviolet	- (UV)



Ultraviolet-Visible	- (UV-Vis)
Valence Band	- (VB)
Wavelength	- (λ)
X-ray Diffraction	- (XRD)
Zinc Acetate Dihydrate	- (ZAD)
Zinc Oxide	- (ZnO)
2-Dimension	- (2-D)
3-Dimension	- (3-D)



UNIVERSITY *of the*
WESTERN CAPE

TABLE OF CONTENTS

DEDICATION	i
ABSTRACT	ii
KEYWORDS	v
DECLARATION	vi
ACKNOWLEDGEMENTS	vii
LIST OF FIGURES	xi
LIST OF TABLES	xix
LIST OF ABBREVIATIONS, ACRONYMS AND SYMBOLS	xxii
Chapter 1: Introduction	1
1.1 Background	2
1.2 Solar energy harvesting	2
1.2.1 Solar irradiation.....	2

1.4.3.1 Dye-sensitised solar cell (DSSC)	23
1.4.3.2 Hybrid solar cells	23
1.4.3.2.1 Perovskite solar cells	24
1.4.3.3 Organic solar cells	24
1.4.3.3.1 Polymer solar cells.....	27
1.4.3.3.2 Conventional organic solar cells (COSC) and inverted organic solar cells (IOSCs)	29
1.4.3.4 The nanomaterial-based electron transport layer in inverted organic solar cells	34
1.4.4 ZnO Properties	35
1.4.4.1 A brief overview of ZnO characteristics	35
1.4.4.2 Crystal structure.....	36
1.4.4.2.1 Lattice parameters.....	38
1.4.4.3 Electronic band structure	39
1.4.5 Nano-zinc oxide as ETL in the photovoltaic device	40
1.5 Problem statement	44

1.6 Aim.....	45
1.7 Objectives.....	45
1.8 Layout of the thesis	46
References	48
Chapter 2: Synthesis and Characterisation Techniques	59
Introduction	60
2.1 Synthesis techniques	62
2.1.1 Hydrothermal synthesis	62
2.1.1.2 Background.....	62
2.1.1.2 Experimental setup	64
2.1.2 Sol-Gel Method	65
2.1.2.1 Background.....	65
2.1.2.2 Dip-coating	68
2.1.2.3 Spin-coating	69
2.1.2.4 Experimental setup	70

2.1.3 Inverted organic solar cells synthesis.....	71
2.2 Characterisation techniques.....	73
2.2.1 Fourier Transform Infra-Red Spectroscopy.....	73
2.2.1.1 Background.....	73
2.2.1.2 Experimental setup	75
2.2.2 X-ray Diffraction Technique (XRD)	75
2.2.2.1 Background.....	75
2.2.2.2 Experimental setup	79
2.2.3 High-Resolution Transmission Electron Microscopy.....	80
2.2.3.1 Background.....	80
2.2.3.2 Experimental setup	83
2.2.4 High-Resolution Scanning Electron Microscopy	83
2.2.4.1 Background.....	83
2.2.4.2 Energy Dispersive X-ray Spectroscopy (EDS)	85
2.2.4.3 Experimental setup	87

2.2.5 Thickness Profilometry	88
2.2.5.1 Background.....	88
2.2.5.2 Experimental setup	90
2.2.6 Optical Spectroscopy	91
2.2.6.1 Background.....	91
2.2.6.2 Absorbance Spectroscopy and Transmittance Spectroscopy	93
2.2.6.3 Experimental setup	96
2.2.7 Current-Voltage characterization.....	96
2.2.7.1 Background.....	96
2.2.7.2 Experimental setup	98
References	100
Chapter 3: ZnO particles Synthesis and Characterization.....	110
Introduction.....	111
3.1 Synthesis of ZnO Nanoparticles by Hydrothermal Method	112
3.2 ZnO Nanoparticles Characterization	114

3.3 Results and discussion.....	115
3.3.1 Chemical analysis of ZnO Nanoparticles	115
3.3.1.1 FTIR analysis of ZnO Nanoparticles under period calibration	116
3.3.1.2 FTIR analysis of ZnO Nanoparticles under temperature calibration	119
3.3.2 Structural analysis of ZnO Nanoparticles	122
3.3.2.1 XRD analysis of ZnO Nanoparticles produced under period variation	124
3.3.2.1.1 Structural analysis.....	124
3.3.2.1.2 Williamson-Hall analysis.....	125
3.3.2.2 XRD analysis of ZnO Nanoparticles produced under temperature variation	128
3.3.2.2.1 Structural analysis.....	128
3.3.2.2.2 Williamson-Hall analysis.....	129
3.3.3 Structural & Morphological analysis of ZnO Nanoparticles	132
3.3.3.1 HR-TEM analysis of ZnO Nanoparticles produced under period variation	135
3.3.3.1.1 Bright-field transmission electron microscopy (BF-TEM)	135

3.3.3.1.2 Particle size distribution	136
3.3.3.1.3 HR-TEM lattice images	137
3.3.3.1.4 The scattered area electron diffraction (SAED)	138
3.3.3.2 HR-TEM analysis of ZnO NPs produced under temperature variation	139
3.3.3.2.1 Bright-field transmission electron microscopy (BF-TEM)	139
3.3.3.2.2 Particle size distribution	140
3.3.3.2.3 HR-TEM lattice images	141
3.3.3.2.4 The scattered area electron diffraction (SAED)	142
3.3.4 Optical properties of ZnO Nanoparticles	143
3.3.4.1 UV-Vis absorption analysis of ZnO Nanoparticles synthesised hydrothermally under period variation	145
3.3.4.2 UV-Vis absorption analysis of ZnO Nanoparticles synthesised hydrothermally under temperature variation	147
3.4 Conclusion.....	149
References	153

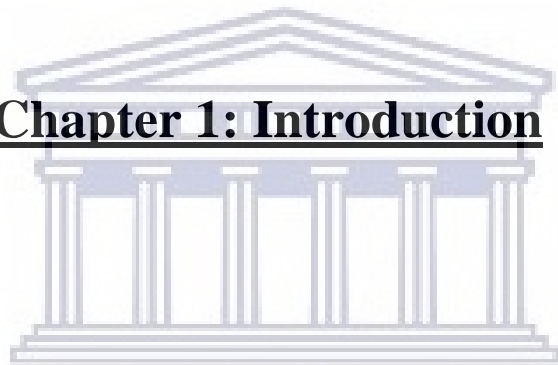
Chapter 4: Synthesis and Characterisation of ZnO nanoridges and ZnO NPs-seeded ZnO nanoridges	160
Introduction	161
4.1 Synthesis of ZnO NPs-seeded ZnO Nanoridges by sol-gel (spin-coating) technique	161
4.2 ZnO NPs-ZnO Nanoridges Characterization	162
4.3 Results and discussion.....	163
4.3.1 Topographic analysis of ZnO NPs-seeded ZnO nanoridges	163
4.3.1.1 Analysis of ZnO NRs and ZnO NPs-ZnO nanoridges thin-film thickness under period calibration.....	164
4.3.1.2 Analysis of ZnO NRs and ZnO NPs-ZnO nanoridges thin-film thickness under temperature calibration	165
4.3.2 Morphological and chemical composition analysis of ZnO NPs-seeded ZnO nanoridges	167
4.3.2.1 HR-SEM-EDS analysis	167
4.3.2.2 HR-SEM analysis of ZnO NPs-seeded ZnO nanoridges produced under period calibration	169
4.3.2.2.1 Bright-Field HR-scanning electron microscopy (BF-HR-SEM) .	169

4.3.2.2.2	Width size distribution	170
4.3.2.3	HR-SEM analysis of ZnO NPs-ZnO nanoridges produced under temperature calibration	172
4.3.2.3.1	Bright-Field HR-scanning electron microscopy (BF-HR-SEM) .	172
4.3.2.3.2	Width size distribution	174
4.3.3	Optical properties of ZnO NPs-ZnO nanoridges	175
4.3.3.1	UV-Vis transmittance spectroscopy of ZnO nanoridges produced under period variation.....	177
4.3.3.2	UV-Vis transmittance spectroscopy of ZnO nanoridges produced under temperature variation.....	180
4.4	Conclusion	187
References	188
Chapter 5: Synthesis and Characterisation of Inverted Organic Solar Cells	192
Introduction	193
5.1 Experimental setup	194
5.1.1	Fabrication of IOSC layers	194

5.2 Inverted Organic Solar Cells I-V Testing set-up.....	197
5.3 IOSCs' J-V Curves results and discussion.....	198
5.3.1 Analysis of J-V curves of IOSC fabricated with ZnO NPs-seeded ZnO nanoridges ETLs (ZnO NPs under synthesis period control)	198
5.3.2 Analysis of J-V curves of IOSC fabricated with ZnO NPs-seeded ZnO nanoridges ETLs (ZnO NPs under synthesis temperature control)	201
5.4 Conclusion	205
References	209
Summary and Future Work	212
6.1 Summary	213
6.2 Future Work	215
APPENDIX	216



Chapter 1: Introduction



UNIVERSITY *of the*
WESTERN CAPE

Chapter 1: Introduction

1.1 Background

For the last two decades, many reports and articles have been published about the manufacturing and development of solar cells (PV devices). Immense effort has been placed into this field due to the world's continuous energy demand. At present, PV devices are still expensive to design, manufacture and maintain and show smaller efficiencies compared to their competitive energy sources [1.1, 1.2, 1.3].

1.2 Solar energy harvesting

The Sun is one of the constituents of the solar system [1.4] and radiates enormous amounts of energy. It consists of mainly hydrogen [1.5]. The Sun's existence dates around 4-5 billion years ago, according to the current model. It radiates electromagnetic energy in different wavelengths. The energy is produced during nuclear fusion reaction whereby high pressured hydrogen undergoes reaction turning to helium [1.5, 1.6, 1.7]. It radiates adequate energy, which can address the global energy crisis [1.7]. Moreover, the sun is expected to continue existing for the next 4-5 billion years; this makes it the best candidate for clean, renewable, and sustainable energy sources [1.3].

1.2.1 Solar irradiation

As it is emphasised, the primary source of energy to the Earth is the electromagnetic radiation. It is measured and described as solar irradiance [1.8]. Irradiance is an essential component in the performance of photovoltaics models [1.8]. This component is measured as instantaneous power

over an area; directly or simulated by a stochastic model. Irradiance is measured in W/m^2 . The solar spectral irradiance is the measure of the solar radiation at a wavelength of light [1.9]. Figure 1.2 represents an approximation of the solar spectral irradiance at various wavelengths, which is also a blackbody spectrum at 5800 K [1.9].

The solar spectrum is made up of several electromagnetic waves, radiating 7% of ultraviolet radiation (UV), 46% of infrared radiation (IR), and 47% of visible light (Vis) [1.3]. 90% of the solar irradiance on the outer surface of the Earth's atmosphere [1.10] is about $\sim 1370 \text{ W/m}^2$ and is deemed to be the solar constant obtained when the Sun and the Earth are spaced at 1 AU, with the mean distance between the Earth and the Sun of 149 597 890 km [1.11]. This solar constant covers the solar spectrum from the IR through the visible to the UV frequency range [1.5]. During solar radiation, the sun rays are directed to the Earth's surface through direct and diffuse paths. Direct sun rays can hit the Earth's surface directly without scattering. Diffuse radiation usually occurs when light is reflected, absorbed, or scattered due to the absorption of dust, air, and water molecules in the atmosphere [1.5]. Therefore when light is directed to the Earth, it hits the surface of the Earth at different angles [1.12]. Figure 1.1 represents the different paths and angles as the sun rays hit the surface of the Earth's ground.

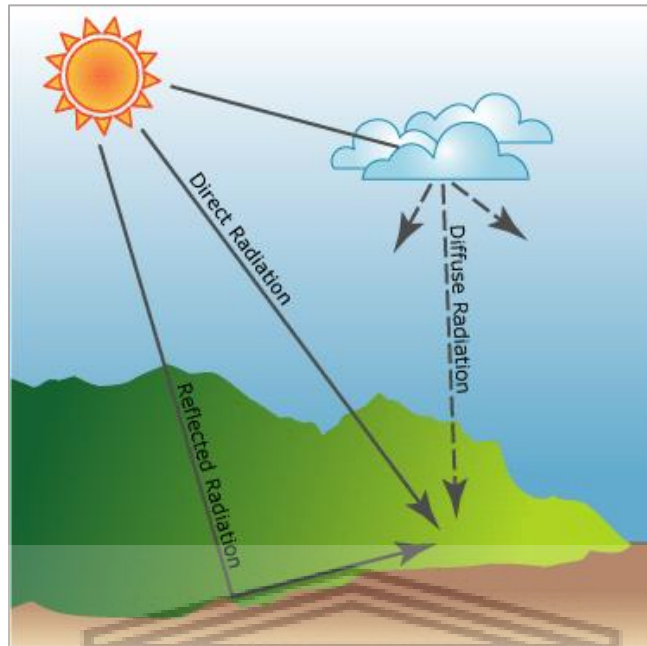


Figure 1.1: Representation of several radiation attenuating effects occur when radiation crosses the atmosphere: the radiation either diffuse, reflects, and scatter [1.13].

The path length which the solar radiation has to pass through the atmosphere before reaching the surface of the Earth is called the air mass. AM 1.0 is obtained when the Sun radiates outside the atmosphere and hits the Earth directly overhead at 0° (zenith angle). It is calculated using equation (1.1) [1.5]. The standard conditions of AM 1.5 are chosen as the average global representative of the solar radiation atmospheric path length at a zenith angle of 48.2° above sea level [1.5].

$$AM = \frac{1}{\cos\theta_z}. \quad (1.1)$$

On cold, cloudy days, direct radiation is estimated to be 0% and diffuse radiation as 100% [1.6].

Furthermore, as the sun rays are directed to the surface of the Earth, the properties of the irradiation

alter due to absorption of the ultraviolet radiation by the ozone layer and absorption of some of the IR by water and CO₂. Therefore a large amount of radiation hitting the Earth's surface, represented in Figure 1.2, contributes to visible light and IR rays from the spectrum. Figure 1.2 illustrates the shape of the solar spectrum and the absorption of various wavelengths at AM 1.5 condition. The air mass conditions correspond to the sun's solar spectrum at sea level at zenith (AM 1) and 48.2° zenith (AM 1.5) [1.8].

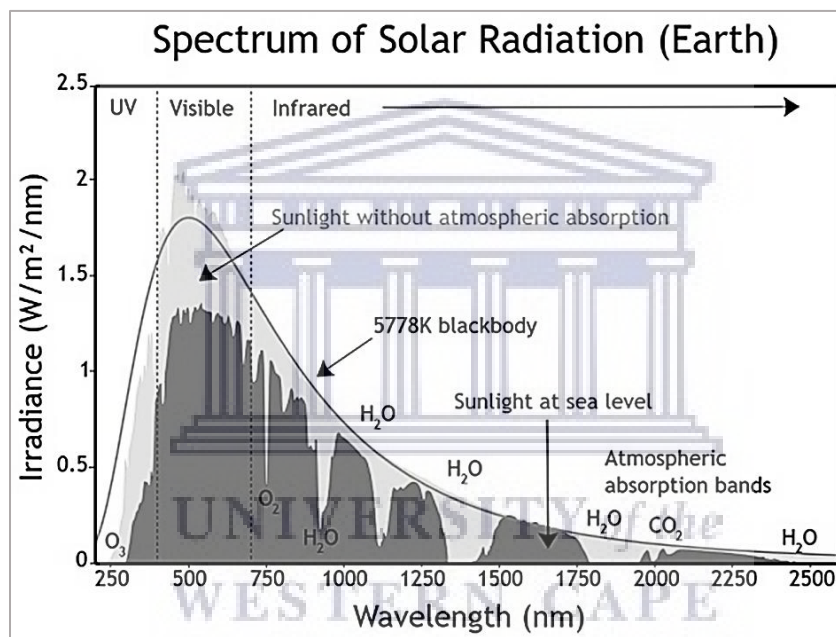


Figure 1.2: Shape of the solar spectrum in terms of irradiance ($W/m^2 \cdot nm$) and the absorption of various wavelengths (nm) for AM 1.5 conditions [1.14].

Figure 1.3 represents the global mean solar irradiance map. It can be deduced from the map that a vast amount of solar energy is radiated around countries that are situated closer to the equator. In accounts of the average annual global solar radiation, Central Europe accounts for an estimated 1000 kWhm⁻², the central part of Asia and Canada accounts for 1700 kWhm⁻², and an outstanding estimation of 2200 kWhm⁻² is distributed around African countries such as Kenya, the Democratic Republic of Congo, Gabon, and Somalia [1.15]. 30 TW is the predicted amount of power to sustain the economic growth by 2050 [1.7]. Therefore by implementing appropriate solar energy harnessing technologies with supporting infrastructure for solar technology, accessibility to electricity can be accelerated, and environmental pollution due to CO₂ can be mitigated [1.7, 1.16].

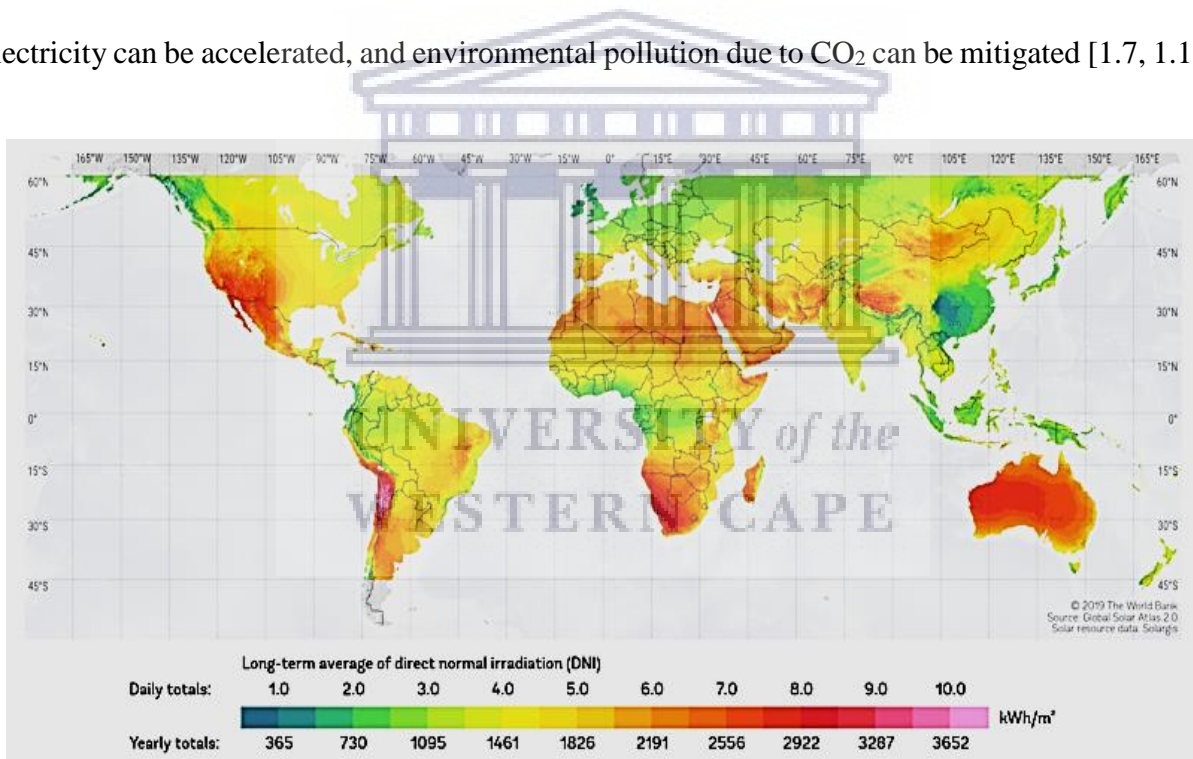


Figure 1.3: Global Horizontal Irradiance [1.17].

1.3 The photovoltaic effect

1.3.1 History

The photovoltaic (PV) effect is a process whereby electricity is directly generated from the excitation of electrons by a beam of photons directed to a semiconducting material in a circuit [1.18]. The photovoltaic concept was first introduced in 1839 by Edmond Becquerel [1.18]. In this study, Edmond Becquerel [1.18] observed the photovoltaic effect after shining a beam of light onto silver-coated platinum in a polar solvent and producing an electric current [1.18].

1.3.2 The physics of photovoltaic device/solar cell devices.

Attainment of effective photon energy conversion to photovoltaic electricity rest upon the following four critical aspects and need to be considered [1.2].

- Appointment of suitable photon absorption material.
- Generation of electron-hole pairs (charge carriers) by breaking the electrostatic bonds between atoms.
- Dissociation of oppositely charged free carriers within suitable material before their rapid recombination.
- Carrier mobility through the junctions and the electrical contacts to the external load for the electric current generation.

The challenge faced in PV technology is improving the concepts mentioned above to attain effective performing PV devices. Suppose any of the above-highlighted concepts become

hampered. In that case, the PV device will less likely convert solar energy to electricity efficiently. Therefore, electric current can be efficiently attained by exploring new materials with suitable properties to absorb photons and generate charge carriers and designing PV devices that prompt dissociation of charge carriers and provide free charge mobility through the external load [1.2].

1.3.2.1 Materials used to make solar cell

Existing materials can be categorised into three main classes: electrical conductors, insulators, and semiconductors. These materials are classified based on electrical conductivity (ϕ) or the energy band gap (E_g) of the material [1.2]. Semiconductors are suitable materials for the absorption of photons and the generation of charge carriers. Semiconductors have various properties that fit the PV technology and have been studied for the past 70 years [1.2]. Examples of the semiconductors used in PV devices are displayed in Table 1.1 [1.19]. Favourable semiconductors for the field of PV technology have high optical absorption coefficient, direct band gap, greater mechanical strength, low density of charge recombination centres, and are highly stable [1.2]. Moreover, these semiconductors are expected to offer improved wherewithal to produce electronic devices that effectively dissociate and create charge carriers [1.2].

Table 1.1: Examples of the semiconductors used in PV devices with corresponding band gaps [1.19].

Semiconductor structure	Band gaps at 25°C (eV)
Si	1.12
PbS	0.37
GaAs	1.43
CdTe	1.50
CdSe	1.75
ZnSe	2.70
CdS	2.42

1.3.2.2 Design and architecture of the solar cell

A solar cell is typically a junction diode slightly different from a conventional p-n junction diode as solar cells are considered large-area p-n junctions. Moreover, the p-n junction diode cannot produce electricity from solar radiation while solar cells convert solar light to electricity [1.2]. Solar cell construction is executed by depositing a thick p-type semiconductor layer on a proportionally thin n-type semiconductor layer. A grid of Ohmic electrodes and a rectifying Schottky contact are grown on top of the p- and n-type semiconductor, respectively. The Ohmic electrode takes up a grid design while the Schottky contact takes up a transparent thin-film design to minimise the effect of shading, preventing obstruction of light to reach the space-charge region. These contacts also play a role in providing current flow through the external circuit. A thin glass

encapsulates the entire assembly to prevent the PV module from experiencing mechanical shock [1.6, 1.2].

1.3.2.2.1 Working principle of the solar cell

After establishing suitable materials owing to suitable structural, optical and mechanical properties, the materials are then engineered together to make up a solar cell. The following process describes the design and fabrication of a solar energy conversion device capable of generating and dissociating carrier charges before recombination. A very strong built-in potential (electric field) is required for carrier charge dissociation. Therefore to achieve charge generation and carrier charge mobility, one or more interfaces/layers are produced, and suitable semiconductors and two electrodes are combined to form a PV device. Therefore, a typical PV device consists of several interfaces made of conductive materials, semiconductors, and insulators. Interfaces play a significant role in solar cells' operations and performances. Therefore, interfacial morphology and the injection, extraction, and mobility of charge carriers are further examined in the following section. Figure 1.4 illustrates a typical photovoltaic device and the working principle behind it [1.2, 1.20].

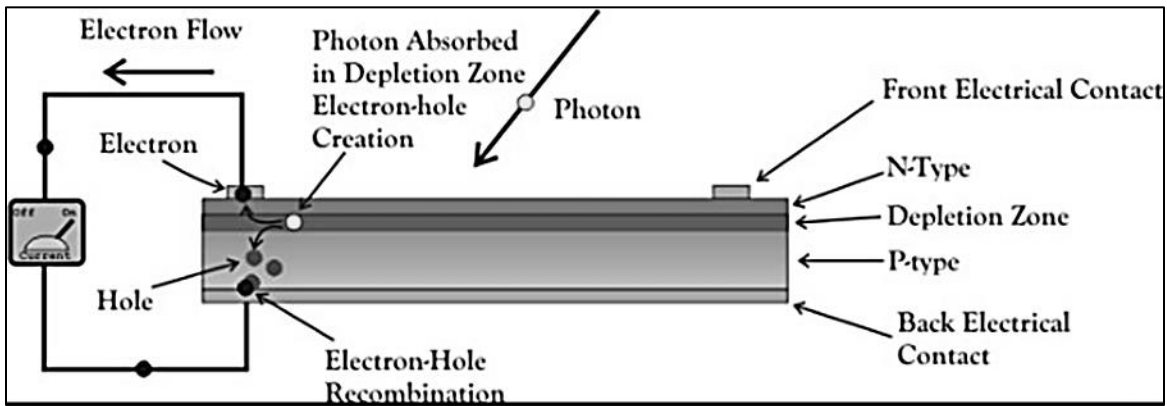


Figure 1.4: A traditional photovoltaic device and the working principle behind it [1.21].

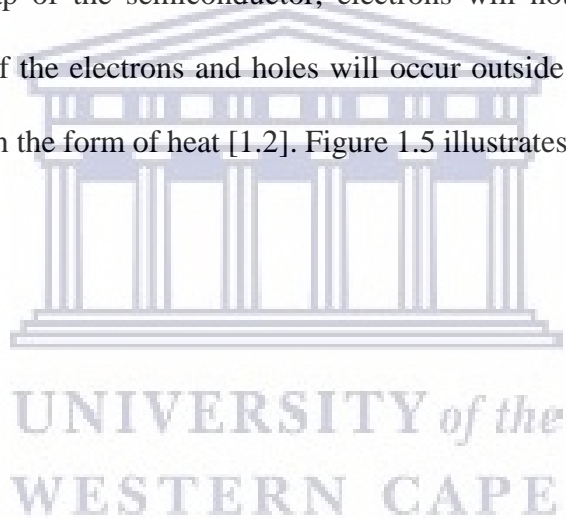
Most modern PV devices operate on the principle of a traditional p-n junction, p-i-n junction Schottky junction, and Ohmic junction devices.

1.3.2.2.1.1 p-n junction

The semiconductors in p-n junction devices consist of the p-type and n-type electrical conduction in two adjacent regions. When the two semiconductors are brought into contact, they form a p-n junction [1.2]. The p-type side consists of a material with an excess of holes, and the n-type side of the semiconductor crystal lattice consists of a material with an excess of electrons. As the semiconductors are brought into contact, some of the excess electrons diffuse across the junction and combine with holes to form electron-hole pairs/ negative ions. Therefore, as the electrons diffuse, they leave behind positive ions at the n-type side. This process occurs until there are no more excess electrons to diffuse to the p-side, leading to the formation of the depletion region. The depletion region is the area with the built-in electric field (V_{bi}) [1.22]. It is described by the slope of the built-in electric field produced in the energy band diagram shown in Figure 1.5. The built-

in potential restricts further electron diffusion unless a forward-bias is placed on the junction to assist electron transfer from the n-side to the p-side.

The electron-hole pair lifetime is monitored by recombination lifetime τ_R before electrons could recombine with the corresponding holes in the n-type side due to the short-lived life. When an external load is connected, electrons propagate from the n-type semiconductor region and propagate across the external circuit generating an electric current, losing potential, and recombining with the holes in the p-type semiconductor region. Should the energy of the photons be less than the energy gap of the semiconductor, electrons will not reach the p-n junction. Therefore, recombination of the electrons and holes will occur outside the space-charge region, leading to a loss of energy in the form of heat [1.2]. Figure 1.5 illustrates the energy band diagram of a p-n junction.



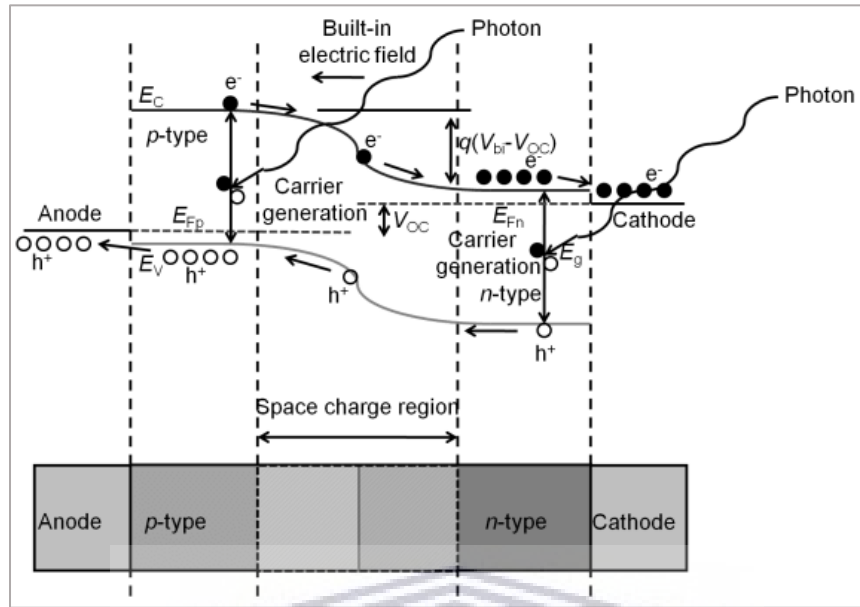


Figure 1.5: The energy band diagram of a p-n junction [1.2].

1.3.2.2.1.2 p-i-n junction

Doping the concentration of impurities into an either region of the two semiconductors to create the p-n junction is one factor that affects the depletion region's health. Low doping or high doping concentration creates no significant improvement in creating current flow through the external load because the space charge region either widens or becomes thin. Therefore to achieve improvement in PV activity, optimisation of doping concentration is required to create a space charge region of an order of about $2 \mu\text{m}$ [1.2], which is the thickness comparable to a typical thin-film solar cell [1.2]. However, reaching high performance in PV activity is challenging for many material scientists, physicists, and chemists [1.2]. Therefore, advanced planning and designing of the space charge region thickness are required. One way of optimising the width of the space

charge region is by applying a p-i-n junction during the device's construction. In the p-i-n junction, an intrinsic semiconductor is layered between the p-type semiconductor and the n-type semiconductor. The intrinsic semiconducting layer act as a Fermi-level alignment layer between the p-type semiconductor and the n-type semiconductor, inducing optimisation of the width of the space charge region. Figure 1.6 illustrates the energy band diagram of a p-i-n junction or diode where W is the width, E_c is the conduction band (CB) energy, and E_v is the valence band (VB) energy, F_i , E_{Fn} , and E_{Fp} are the Fermi energy levels [1.2, 1.23]. F_n is the Quasi-Fermi energy of electrons, E_v is the valence band energy of a semiconductor, F_p is the Quasi-Fermi energy of holes, and F_i is the intrinsic energy [1.23].

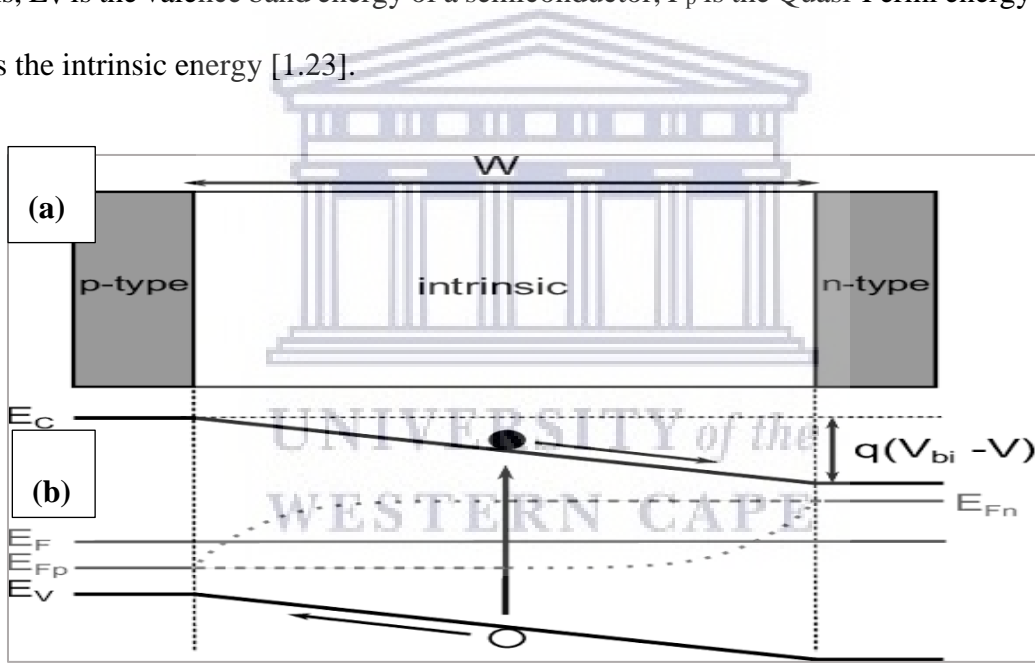


Figure 1.6: (a) p-i-n diode, (b) the energy band diagram of p-i-n diode [1.24].

1.3.2.2.1.3 Metal/semiconductor contacts (Schottky junction and Ohmic junction)

Schottky junctions are metal-semiconducting electrical contacts. Schottky contacts are fabricated through metal deposition on a clean n-type semiconductor layer, and Ohmic contacts are formed by metal deposition on a p-type semiconductor layer. A potential height barrier to charge transfer is established between the metal and the semiconductor due to the difference in the work functions of the metal (σ_m) and the electron affinity of the semiconductor (σ_s) when brought into contact. When there is no diffusion of electrons from the n-type semiconductor to the metal and no defects at the metal-semiconductor interface, then the potential barrier σ_b is given by $\sigma_b = \sigma_m - \sigma_s$ [1.2]. The Schottky junction is formed when the potential barrier height of the metal-semiconductor contact is large due to the alignment of a metal's work function and the electron affinity of the semiconductor [1.25]. This process may occur given that $\sigma_m > \sigma_s$ for a metal-n-type semiconductor junction [1.25]. Under this condition, the electrons will leave positive ions that will generate a depletion region. In the Ohmic junction, there is no potential barrier generated due to the electron affinity of the semiconductor being larger than the work function of the metal [1.26]. Therefore, as $\sigma_m < \sigma_s$, then electrons will diffuse from the metal to the semiconductor because of the semiconductor's low energy that promotes the upward shift of the Fermi level in the semiconductor until equilibrium is achieved. Therefore, this process causes the current conduction in both directions of the metal-semiconductor junction [1.26].

The role of Schottky junctions and Ohmic junctions is to effectively extract and transport photo-created charge carriers through the external circuit to create current flow. Schottky and Ohmic

contacts typically take up a grid design or become transparent to trap incoming light effectively and efficiently [1.2].

1.3.2.3 I-V characteristics of a solar cell

Fundamental electrical characteristics of the solar cell are carried out by attaining I-V curves, also referred to as electric J_{sc} as a function of external voltage (bias). A typical I-V curve plot is represented in Figure 1.7 [1.27].

Efficiency (η) is the parameter used to monitor the performance of the solar cell; it is the ratio of the device's generated power ($P=VI$) to the incident power (P_{in}) of the light illuminated on the solar cell, described in equation 1.2. Here V_m and I_m is the maximum voltage and maximum current of the cell obtained at the maximum power point, respectively and P_{in} is the power due to the incident light [1.27].


$$\eta = \frac{V_m I_m}{P_{in}} \quad (1.2)$$

Usually, the incident power for AM 1 and AM 1.5 conditions are 92.5 mW/cm^2 and 100 mW/cm^2 , respectively [1.28].

The fill factor (FF), a measure of the squareness of the impinged I-V curve, is used to determine the maximum power illuminated for all types of solar cells. FF is directly related to charge dissociation efficiency. The fill factor is represented as the ratio of the P_m square to the power of V_{oc} and I_{sc} , where V_{oc} is the open-circuit voltage, and I_{sc} is the short circuit current [1.2]. The open-

circuit voltage is the maximum voltage obtained when no current is produced by the solar cell [1.27]. The short circuit current is defined as the current produced by zero voltage across the solar cell [1.27]. The highlighted square represents the cell's maximum power, which is the area of the square [1.2]. Equations (1.3) and (1.4) are yields of these relationships [1.2, 1.27, 1.29]

$$FF = \frac{V_m I_m}{V_{oc} I_{sc}}, \quad (1.3)$$

$$\eta = \frac{V_m I_m}{P_{in}}. \quad (1.4)$$


UNIVERSITY of the
WESTERN CAPE

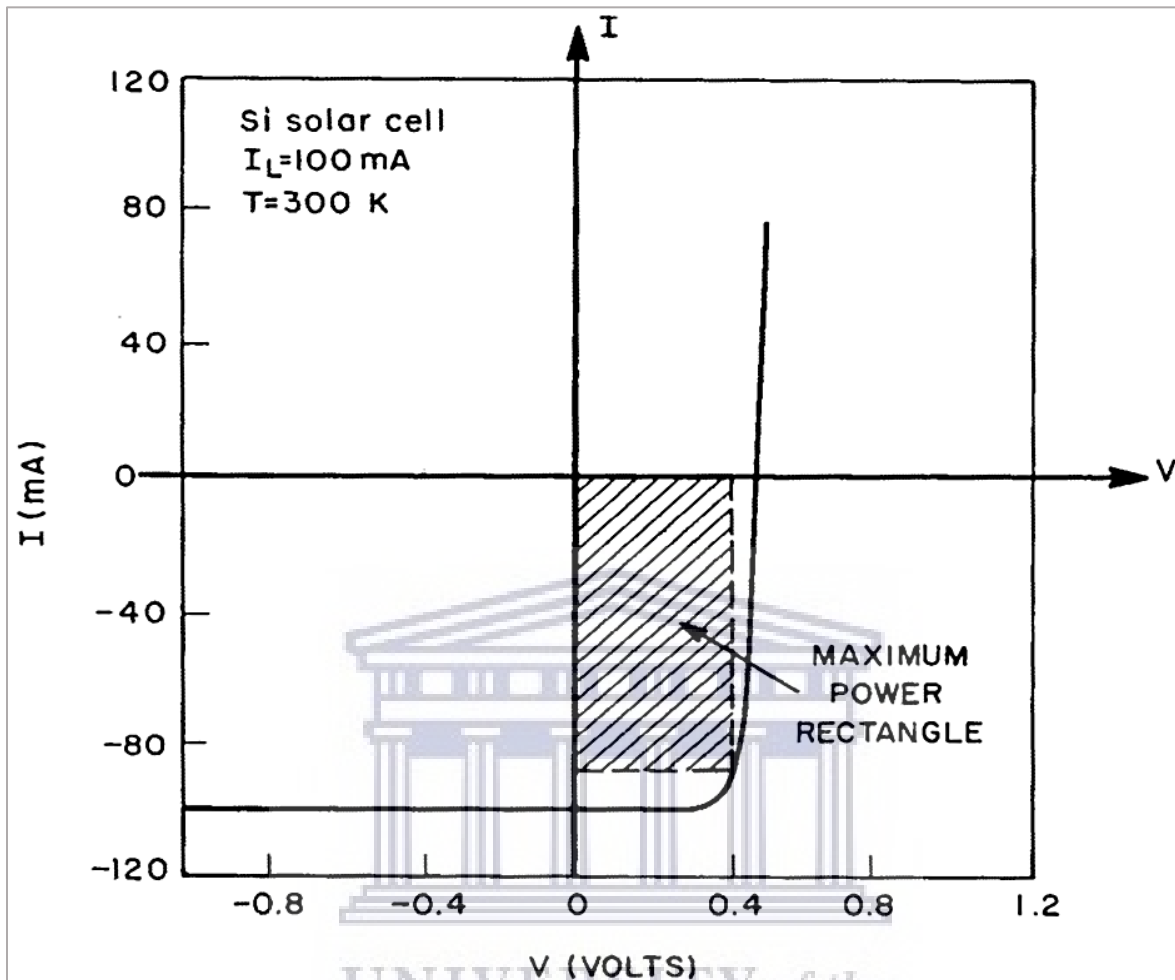


Figure 1.7: Plot of the I-V characteristics for a traditional solar cell [1.29].

1.4 The generations of solar cells

Currently, solar cells are used in abundance and operate without any form of pollution, making them the ideal devices within the renewable and sustainable energy field [1.30]. Solar cells can be classified in terms of three generations of development stages.

1.4.1 The first generation of solar cells: Silicon-based solar cells

The first generation was based on crystalline semiconductors, the Schottky barrier inventions. Schottky barrier devices were produced by pressing a semi-transparent metal layer onto a semiconductor, causing a photovoltaic effect to occur due to asymmetric electronic junction occurrence, which allowed proper access of the incident light causing electronic vibration within the semiconductor. Silicon solar cells were fabricated after discovering silicon's semi-conductive property in the 1950s [1.18]. Bulk n-type and p-type silicon wafers' production stream advanced to a more desirable state. The production led to a p-type Si production whereby an n-type silicon wafer was run in boron trichloride gas. Therefore the production of p-n junction structures was introduced and gave photovoltaic technology a better chance of performing in the market sector. The first silicon solar cell was produced in 1954 by Chapin Fuller and Pearson, and it provided an efficiency of 6% [1.18]. In Fuller and Pearson's study, single-crystal silicon (Cz-Si) wafer was fabricated for light absorption and a p-n junction for carrier charge separation. The working principle of a typical Cz-Si solar cell; upon photon absorption throughout the Cz-Si wafer and charge-carrier separation leading to diffusion of photo-created charge carriers is illustrated in Figure 1.8 [1.31].

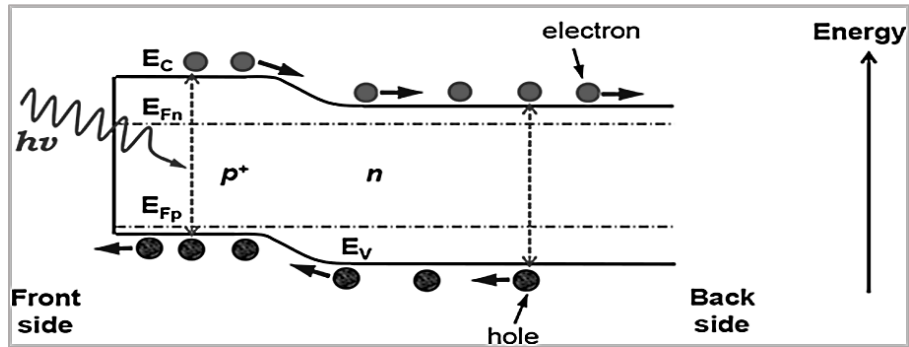


Figure 1.8: Working principle of a Cz-Si solar cell: upon photon absorption and charge carrier production [1.31].

From 1954 [1.32], there has been a steady improvement in the performance of bulk crystal grown Cz-Si solar devices [1.31, 1.32]. Texturization, passivation, shallow junctions, anti-reflective coating, and metallisation are the factors that were further modified to fabricate effective working solar devices in the 1970s-1980s [1.31]. These early designs of Cz-Si obtained an efficiency of 19% at SUNTECH Company and 23% efficiency laboratory-scale solar cells. Furthermore, Cz-Si reached 20.7% commercial efficiencies at the SANYO Electric Co. LTD. [1.31]. Cost-effective multi-crystalline silicon solar cells (Mc-Si) emerged in the 1980s, substituting the Cz-Si solar cells. However, not long after Mc-Si solar cells' introduction, the devices came to be at the same track in terms of costs and efficiencies with the Cz-Si solar cells. Therefore, for many years Mc-Si solar cells have experienced the inability to reach higher efficiencies than that of Cz-Si solar cells [1.31].

With intensive and detailed studies over the last two decades, silicon solar cells reached considerable PCEs, close to the Shockley-Queisser thermodynamics limit. The Shockley-Queisser thermodynamics limitation is a theoretical study performed by Shockley and Queisser using

thermodynamic arguments to determine the maximal efficiencies that solar cells can reach theoretically. Generally, in theory, solar cells cannot exceed ~33% efficiencies [1.31]. Silicon-based solar cells' efficiencies allowed them to be established in the market for the last 25 years. However, their complexity and high-cost rate of production are drawbacks that hinder them from competing in the commercial electricity sector successfully [1.33].

1.4.2 The second generation of solar cells: Thin- film solar cells

The second generation of solar cells was produced from inorganic thin-film assemblies. Thin-film-based solar cells have sparked interest since 1970 due to their large-scale production ability and cost-effectiveness compared to the first generation [1.31]. Thin-film-silicon-based (TF-Si) solar cells have been fabricated by utilising TF-Si as absorbers and depositing them through plasma-enhanced vapour deposition [1.31]. The advanced photovoltaic study led to the commercialisation of multi-junction-germanium-based solar cells as one of the TF-Si solar cells [1.31]. Further continuous research on TF-Si solar cells led to the discovery of chalcogenides and was suited for photovoltaic field application due to their favourable electrical and optical properties. Chalcogenides are polycrystalline semiconductors with band gaps ranging from 1-3 eV [1.31]. Two chalcogenides that spark an interest due to their chemical properties are CdTe and copper indium gallium selenide (CIGS). They have direct band gaps and greater absorption coefficients [1.34]. These properties enable them to act as the best candidates for thin-film absorbers. Further studies led to the first production of CdTe solar cells that reached a power conversion efficiency (PCE) of 22.1% [1.34]. Moreover, advanced studies on CdTe solar cells led to the production of

highly advanced thin-film solar cells, whereby superstrate configuration borosilicate glass: Cd₂SnO₄ZnSO₄: CdS: CdTe: metal solar cell was produced. This study was done by the General Electrical Research Group in 2012 [1.31] and has demonstrated 18.3% efficiencies of a laboratory solar cell [1.31]. Due to CIGS's 1.3 eV wide optical band gap, CIGS solar cells reached a PCE of 20%. [1.32]. Although the second generation of solar cells shows good qualities in combating the global energy crisis, some economic aspects still need to be addressed [1.34]. Aspects such as the need for film quality improvement, reduction in the complexity of manufacturing processes, and increase in components recycling as some of the material(s) in use may be toxic. Moreover, high-cost materials may denote the second generation of solar cells as unfavourable for large-area terrestrial applications [1.34].

1.4.3 The third generation of solar cells

The third generation of solar cells is the current generation that recent attention is drawn onto in the 2014-2024 decade and beyond [1.35]. The third generation is expected to reach an efficiency higher than 33% [1.7]. Third-generation solar cells are anticipated to harness solar energy and convert it to electricity efficiently and at a lower cost rate of production because of their ability to operate without noise or air pollution and less complexity in fabrication [1.7]. Moreover, United Nations countries pledged in the 2015 national assembly to move away from fossil fuels used for electricity production. In agreement, 200 countries found it fitting to resolve the global energy crisis and mitigate climate change due to CO₂ emissions by investing in renewable energy resources [1.35]. The third generation of solar cells includes dye-sensitised, organic solar cells and perovskite solar cells.

1.4.3.1 Dye-sensitised solar cell (DSSC)

The first dye-sensitised solar cell (DSSC) was developed in 1972 by depositing chlorophyll onto a zinc oxide (ZnO) layer. This experiment opened room for new studies to develop and advance. Progress was achieved in this field until an efficiency of 7% was obtained in 1991 [1.36]. Usually, the mesoporous metal oxides are mainly used in DSSC and in most cases, titanium oxide is used in place of zinc oxide. After a series of experiments by using different dyes and electrolytes, an efficiency of 13% was reached. In DSSC, an excited electron proceeds from photon absorption by the organic semiconductor dye. The electron then diffuses through the metal oxide interface at a faster rate, leaving a hole. The hole and the electron are transferred to the electrode, therefore generating electricity. The carrier charges revive on the surface of the semiconductor, and this process is repeated [1.36].

1.4.3.2 Hybrid solar cells

Hybrid solar cells were developed to rectify the problems associated with the absorption of photons in conventional organic solar cells. They were developed by merging organic solar cells materials with inorganic solar cells components [1.36]. OPVs are easier to fabricate at a cheaper rate. However, organic solar cells suffer from instability and rapid deterioration [1.36], while inorganic solar cells are costly to fabricate and have not reached the Shockley-Queisser limit [1.31]. Recently perovskite-based solar cells are receiving significant attention as the promising candidate in the hybrid solar cell field.

1.4.3.2.1 Perovskite solar cells

An alternative to the expensive Si-based solar cells is the third generation of excitonic photovoltaic devices made of hybrid (organic-inorganic) materials. Perovskites are among the hybrid materials and have reached the top position in less than ~5 years due to substantial/reasonable improvement of the PCE at low processing costs [1.37]. Perovskite is a naturally occurring mineral of calcium titanate (CaTiO_3) [1.38]. Materials of the same form ABX_3 of the crystal structure are called perovskite materials, and this form is generic. The A cation occupies the cubo-octahedral site shared with twelve anions, and the B cation is shared with six anions at the octahedral site [1.39] and holds the same crystal structure as that of the perovskite mineral [1.37]. A and B are cations in the ABX_3 general crystal structure, and X is the anionic oxides, i.e. O^{2-} or halogens (F^-). Usually, A is greater than B. Recently, perovskites have emerged as solar cells of interest after DSSCs. A standard model of a perovskite-based solar cell consists of a glass-coated front electrode, a hole-transport layer, a perovskite layer as the active layer, an electron transport layer, and a back metal electrode. The first perovskite PV device was reported in 2006, yielding an efficiency of 10%. From that discovery, more studies emerged, and to date, perovskite was reported to yield 25.5% efficiency [1.40]. Perovskite solar cells make use of very toxic material such as lead, suffer intensive instability, and therefore, they will be challenging to commercialise [1.40].

1.4.3.3 Organic solar cells

Currently, scientists have based their interest in designing and fabricating lightweight, flexible, and highly efficient solar cells. As the field advances, newer photovoltaic devices are made up of

a series of different p-n junctions with varying band gaps. Organic solar cells (OSCs/OPVs) meet the desired properties of the PV field because they are usually transparent and thin-layered for adequate light absorption of several wavelengths of the solar spectrum in the active layer. A typical conventional organic solar cell consists of transparent glass coated substrate with transparent conductive material, usually an oxide layer (TCO). Indium-tin oxide (ITO) is mostly preferred in numerous studies [1.1, 1.16, 1.33] due to its transparency and conductive properties. A hole-transporting layer (HTL) is often the first layer to be deposited onto the substrate. Usually, the HTLs deposited on the coated substrate comprise conjugated polymers such as Poly [2-methoxy-5-(2-ethylhexyloxy)-1,4-phenylenevinylene]. Deposition of a thin metal oxide layer such as tungsten oxide (WO_2) or molybdenum oxide (MoO_x) is usually applied on top of the conjugated polymer. For sufficient charge carrier production, an active layer is introduced on top of the HTL, followed by the deposition of the electron transport layer (ETL) on top of the active layer. ETLs are often zinc oxide (ZnO) or titanium dioxide (TiO_2) in most studies [1.1, 1.41]. Top electrodes are usually thermally evaporated onto the ETL for collecting generated electrons in the active layer [1.42]. The schematic diagram of a standard design and chemical operation of an organic solar cell is shown in Figure 1.9 a).

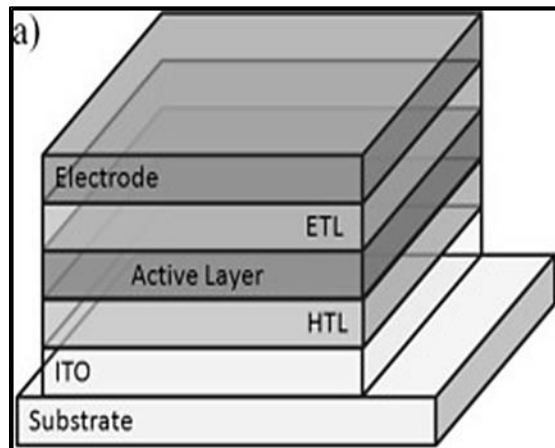


Figure 1.9: General design of a) an organic solar cell [1.42].

In OPVs, the mobility of charge carriers at the interfaces operates on the HOMO-LUMO principle, illustrated in Figure 1.10, whereby the mobility of charge carriers is maintained by the offset energy levels between the interfaces of the layers that make up the cell. Upon photon absorption by the organic semiconductor, electrons in the highest occupied molecular orbital (HOMO) level of the active layer diffuses into its lowest unoccupied molecular orbital (LUMO) level, leaving a hole. The resultant hole in the HOMO level and the electron in its LUMO level are attracted to each other due to Coulombic attraction. An electron-hole pair is then formed, and its bound state of an electron and the resultant hole is called an exciton [1.20]. However, organic materials have low dielectric constant and instability. Therefore dissociating the exciton at room temperature becomes difficult due to the Coulombic force. Application of a material with a suitable dielectric constant leads to the binding energy exceeding the thermal energy and causes dissociation. Moreover, for stability, an acceptor material is introduced to facilitate the transfer of free carrier

charges to the electrodes [1.42, 1.20]. The electrons then dissociate into the ETL's LUMO level [1.20].

OPVs form part of third-generation solar cells. A family of OPVs includes polymer solar cells, conventional organic solar cells, and inverted organic solar cells [1.36].

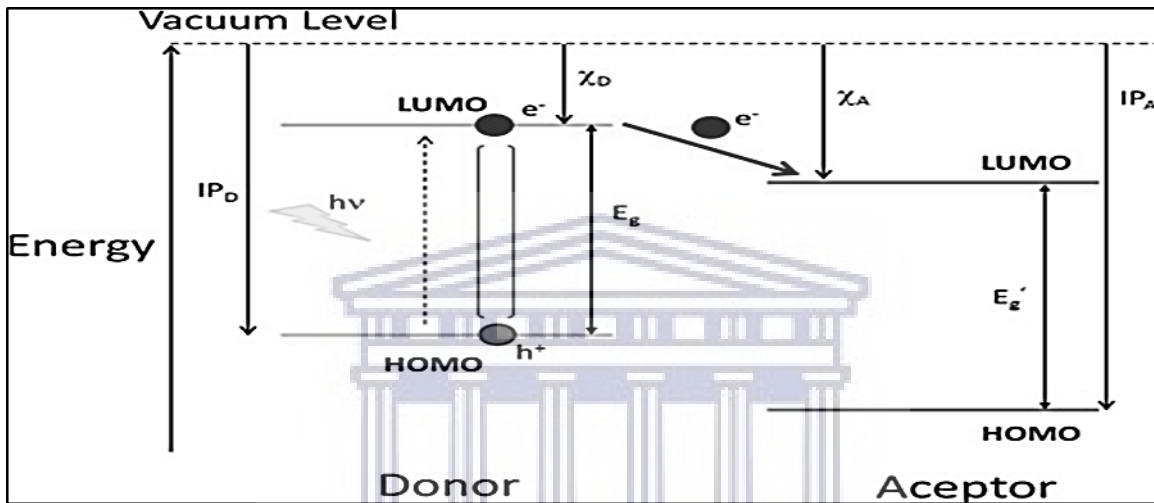


Figure 1.10: Energy level diagram of a charge-carriers diffusion system in organic solar cells; IP_D is the ionisation potentials, $h\nu$ is the photon energy, and electron affinity is represented by χ_D and χ_A . The photo-induced electron propagation is the initial step for generating free charge carriers and is demonstrated by the arrow between LUMO levels [1.42].

1.4.3.3.1 Polymer solar cells

Polymer solar cells have been fabricated for the last decade [1.27]. The first polymer solar cell was fabricated by pressing a single semiconducting material between two electrodes with different work functions suitable for electric current flow through the load [1.36]. However, although the

structure may be simple and cost-effective, its shortfalls include low absorption density and insufficient carrier charge properties [1.36]. Therefore, the resultant efficiency was less than 1% [1.36]. Among the group of polymer solar cells, the bulk hetero-junction solar cells and inverted solar cells are most favourable due to their operational mechanism [1.36]. From the literature studies reported and different experiments using a variety of materials, BHJ solar cells were developed. The first BHJ polymer solar cells were produced in 1993 by Saricifta et al., [1.33]. G. Yu et al., [1.43] reported on the insight of the bulk hetero-junction concept. It was discovered that by mixing (poly (2-methoxy-5-(2'-ethyl-hexyloxy)-1, 4-phenylenevinylene)) (MEH-PPV) as the donor material and fullerene 60 as an acceptor material, an absorber layer is achieved [1.33, 1.36]. Based on this absorber layer, the solar cell reached a PCE of 14% by 2014 [1.33, 1.36]. The absorber layer in BHJ solar cell consists of the donor-acceptor blend. These absorber layers are usually organic semiconductors. Often, the donor materials are conjugated polymers, oligomers, or conjugated pigments, and acceptor materials are fullerene derivatives [1.42]. For polymer organic solar cells to absorb a certain range of the solar spectrum, solar cell devices were further designed as multi-layered solar cell structures, also referred to as tandem structures. This allowed the different layers with distinctive band gaps in the tandem structure to absorb light at different parts of the solar spectrum. However, this study was challenging because of low efficiencies and high costs of production [1.36].

1.4.3.3.2 Conventional organic solar cells (COSC) and inverted organic solar cells (IOSCs)

COSC devices are a prime interest in solar energy harvesting as they make use of organic active layers. Organic active layers essentially provide various characteristics that set COSC devices apart from other types of solar cells in terms of harvesting solar energy. These characteristics include lightweight, flexibility, and simplified fabrication methods at low cost [1.44]. Most effective operational COSC devices take up the soluble fullerene derivative PCBM and P3HT conducting polymer as electron acceptors and electron donors, respectively. PCE of P3HT: PCBM blend-based OPV devices have reached 18.2% in the year 2021 from 12.6% in the year 2020 [1.40, 1.45, 1.46]. The efficiency of organic solar cells proves to have improved from the year 2000 to date. Figure 1.11 is the solar cell power conversion efficiencies-NREL-2018 chart. It illustrates the different highest obtained solar cell power conversion efficiencies by different types of solar cells produced as time/period changes from NREL solar cell efficiency tables [1.47]. Comparing organic solar cells to other solar cells designs shown in Table 1.2 and Figure 1.11, organic solar cells have to optimise the interfaces of the layers. Their latest reported efficiency sits at number six over nine different solar cells with 18.2% [1.46].

Moreover, organic solar cells are illustrated as one of the best candidates for future solutions to the energy crisis. Careful optimisation of the layers of the OPVs may lead to high performing solar cells that may surpass their competitors that including the monocrystalline gallium arsenide solar cells with PCE of 29.1%, monocrystalline silicon solar cells with PCE of 26.1%, perovskite solar cells that sit with a PCE of 25.5%, etc. as shown in Table 1.2. Working organic solar cells can be

attained by implementing post-growth processes of OPV layers. Thermal annealing is among the post-growth processes that may provide a working device and improve the COSC PCE by improving the crystalline structure of the thin-films making up the COSC. Post-growth processes in OPVs enhances the absorption coefficient by developing the interfacial contacts between the electrodes. The most critical issues faced by OPV are the stability of the device's layers, charge mobility, and the low charge-collecting area of the active layer [1.44, 1.48].

Table 1.2: Best laboratory solar cells efficiencies of various solar cells [1.40].

Solar Cell Type	Highest Efficiency (Last updated 19/02/2021)
Monocrystalline silicon (mono-Si)	26.1%
Polycrystalline silicon (multi-Si)	23.3%
Amorphous silicon (a-Si)	14.0%
Monocrystalline gallium arsenide (GaAs)	29.1%
Cadmium telluride (CdTe)	22.1%
Copper indium gallium selenide (CIGS)	23.4%
Dye-sensitised (DSSC)	13.0%
Organic (OSC)	18.2%
Perovskite (PSC)	25.5%

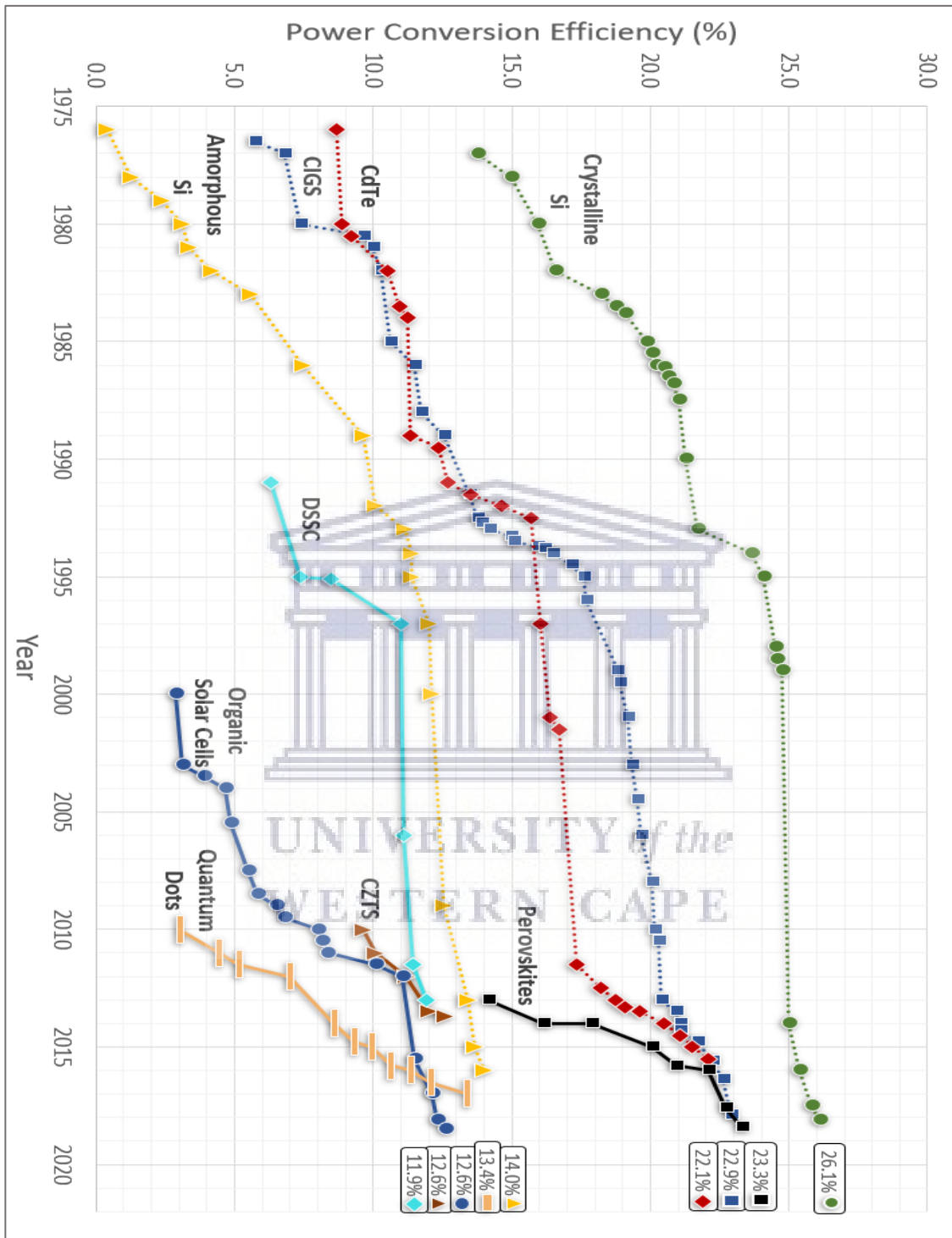


Figure 1.11: Solar cell power conversion efficiencies-NREL-2018 chart [1.47].

To combat these issues, an inverted OPV is used to change charge collection at the electrodes. In IOSCs, high-work function metal is used as the anode and low-work function metal as the cathode. Electron-transport layer (ETL) and hole-transport layers (HTL) play a significant role in transporting extracted charges in the active layer to the respective electrodes. It is challenging to select a material for ETL and HTL synthesis [1.44]. Qualities of HTL and ETL include high transparency, excellent electrical properties, and high chemical stability [1.48].

At the top electrode (hole-collecting electrode), the materials usually used as the anode are Ag or Au. Both Ag and Au are high-work function metals. Ag is predominately used; as it provides a slow oxidation shift [1.48]. Its work function range from 4.3 eV to 5.0 eV [1.48]. The work function favours efficient hole extraction. Ag does not absorb in the visible region of the electromagnetic spectrum.

Furthermore, this work function range better matches with the HOMO levels of the frequently incorporated active layer. Ag is favoured over Au and Al, as Au is expensive, and Al demonstrates a work function that is less well-matched to the HOMO levels of the commonly used active layer. To achieve an effective working IOSC, HTL is incorporated between the active layer and the top electrode. The most commonly used HTL in IOSC include a polymer such as PEDOT: PSS and metal oxides such as V_2O_5 , WO_3 , and MoO_3 [1.48].

Metal oxides are suitable for HTL application because they have a high work function that greatly influences efficient hole transport and extraction at the HTL/Ag interface. Metal oxides are also suited as HTL as their electronic levels best match with the HOMO levels of the active layer. V_2O_5

can be used as a HTL in IOSCs. It shows positive enhancement with a low concentration of the precursor of 1:150 if spin-coated. However, due to its highly toxic character in nature under ambient conditions, V_2O_5 suffers from instability [1.48]. WO_3 has a high work-function of 4.80 eV, enhancing the hole-transport and extraction at the Ag/ WO_3 interface. Optimum thickness in IOSC should range from ~ 5 to ~10 nm [1.48].

A decrease in the thickness value of WO_3 can provide low surface coverage on top of the adjacent film. Higher thickness values may lead to increased series resistance, therefore lowering the PCE of the device. MoO_3 is preferred over the stated metal oxides due to its excellent intrinsic electrical and optical properties. It has the HOMO levels that best match the electronic levels of P3HT:PCBM and shows compatibility with the work function of the top electrode at Ag/ MoO_3 [1.48]. It offers excellent blocking abilities of oxygen and metal ions into the active layer. MoO_3 has good electron blocking capability, and its required optimal thickness of ~10 nm results in efficient working IOSC [1.48]. Furthermore, it can be synthesised through the solution synthetic method and the CVD synthesis process [1.48]. Finally, MoO_3 is compatible with the standard roll-to-roll production process under ambient conditions. Figure 1.12 shows the general models of COSCs and IOSCs in (a) and (b) respectively.

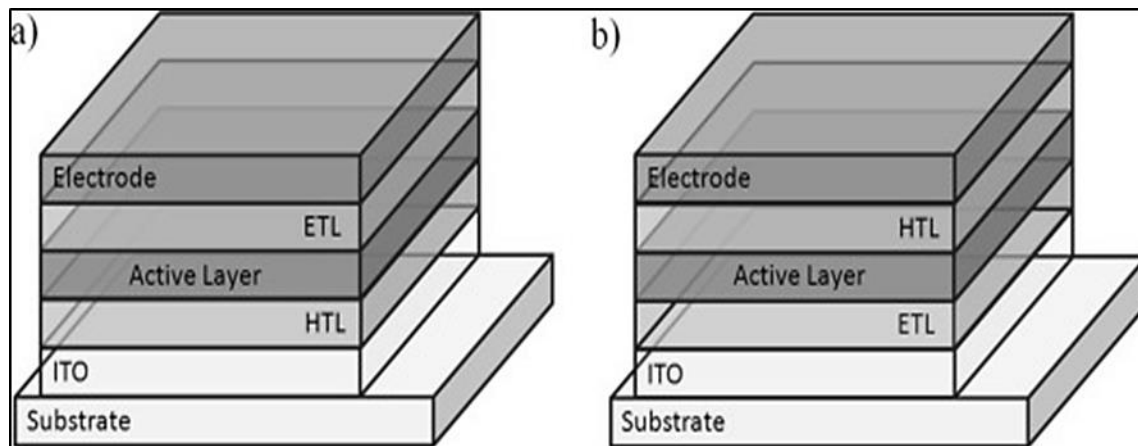


Figure 1.12: General design of (a) conventional organic solar cell (COSC) (b) inverted organic solar cell (IOSC) [1.42].

1.4.3.4 The nanomaterial-based electron transport layer in inverted organic solar cells

The bottom electrode where electrons are collected requires good stability for effective electron collection and low work function to match electronic levels with the electron acceptor layer. The electrode should also have the ability to generate built-in potential at low resistance [1.48]. A suitable electron transport layer incorporated in IOSC should bring IOSC to high performance by efficiently transporting electrons to the electrode and providing excellent hole-blocking abilities [1.48]. ETLs incorporated should further be highly transparent in the visible region of the electromagnetic spectrum and well matching electronic levels with the LUMO level of the polymer layer. There is a limited choice of materials to use for ETL because most materials' electronic levels do not match well with the LUMO of the active layer, or they suffer instability at the ETL/ITO interface. Therefore ZnO and TiO_x are the widely used ETLs in polymer-based IOSC.

TiO_x is a porous crystalline metal oxide. It is predominately used as a standard in dye-sensitised solar cells. TiO₂ is not a suitable ETL material for BHJ IOSCs as it is challenging to have it deposited homogeneously onto ITO at the simplified, cost-effective deposition processes. TiO₂ is, however, not as good as ZnO thin-films as ETLs because it is required that TiO₂ is heavily optimised to reach the transparency and charge mobility at an order of ZnO [1.48].

1.4.4 ZnO properties

In this section, the structural properties that include lattice parameters and electronic band structural properties of ZnO are outlined.

1.4.4.1 A brief overview of ZnO characteristics

Zinc Oxide (ZnO) is a versatile, cost-effective group II-IV, an n-type semiconductor material with a wide band gap of 3.37 eV and an exciton binding energy of 60 meV [1.49]. ZnO has been reported to be a unique position occupant among the wide band gap energy semiconductors (GaN, ZnS, etc.) due to its fascinating structural and optical properties, which can be easily tuned [1.49, 1.50]. Figure 1.13 (a) and (b) show one of ZnO crystal structures (hexagonal wurtzite structure) and the powdered form of ZnO, respectively.

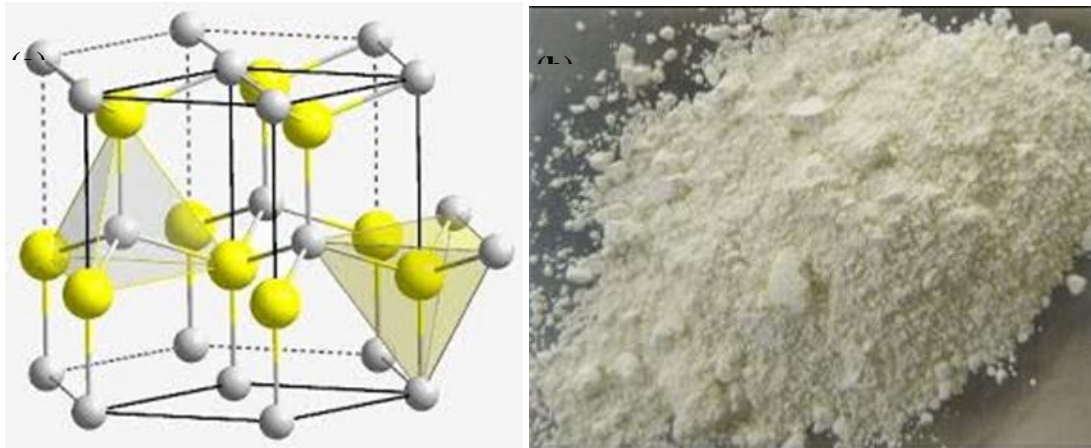


Figure 1.13: (a) Hexagonal Wurtzite structure [1.51], (b) powder form of ZnO material [1.52].

1.4.4.2 Crystal structure

Most of the group –II-VI binary compound semiconductors crystallise as either cubic zinc blende or hexagonal wurtzite structure. However, there is the third crystal structure called the rocksalt structure. ZnO crystallises mainly in two crystal structures: the hexagonal wurtzite and the rocksalt structures [1.53]. Figure 1.14 illustrates the three ZnO crystal structures. The hexagonal wurtzite structure is mainly utilised in the thin-film industry as a highly transparent conducting oxide. The rocksalt structure dominates the geology industry as a spinal phase, used to facilitate an understanding of the Earth's lower mantle. The hexagonal wurtzite structure of ZnO is the most thermodynamically stable crystal structure among the three. It is known to illustrate the piezoelectric properties.

ZnO wurtzite structure is non-centrosymmetric, containing polar surfaces. The structure is composed of two interpenetrating hexagonal close-packed sublattices of cations; Zn and anions;

O, positioned at a length of cation-anion bond in the c-direction. The theoretical lattice parameters of ZnO are $a = 3.2500 \text{ \AA}$ and $c = 5.2060 \text{ \AA}$ [1.53]. Due to the two different elements present in ZnO, its ideal c/a ratio for the hexagonal close packing unit is 1.60 [1.53]. In an ideal wurtzite structure, α and β make up a bond angle of 109.070° , as illustrated in Figure 1.15 [1.53]. In a real ZnO crystal structure, the hexagonal wurtzite deviates from the ideal crystal arrangement by alteration of the c/a ratio. The deviation may be due to the point defects that may include zinc antisites, oxygen vacancies, and lattice dislocations that may lead to the change in the lattice parameters that may affect the arrangements of the cations and anions within the crystal [1.53].

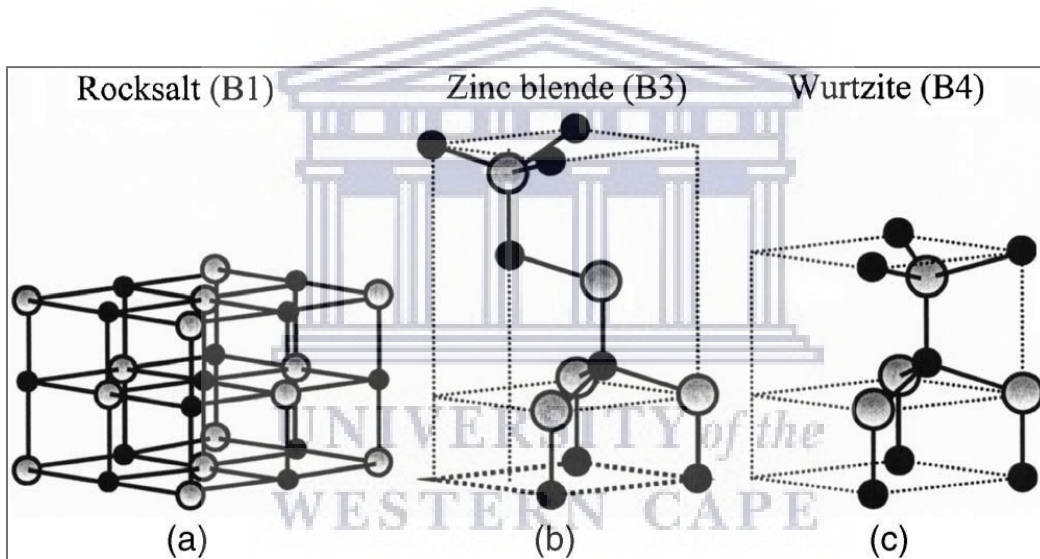


Figure 1.14: representation of ZnO crystal structures: (a) cubic rocksalt B1, (b) cubic zinc blende B3, and (c) hexagonal wurtzite B4. The shaded grey and black spheres represent Zn and O atoms, respectively [1.53].

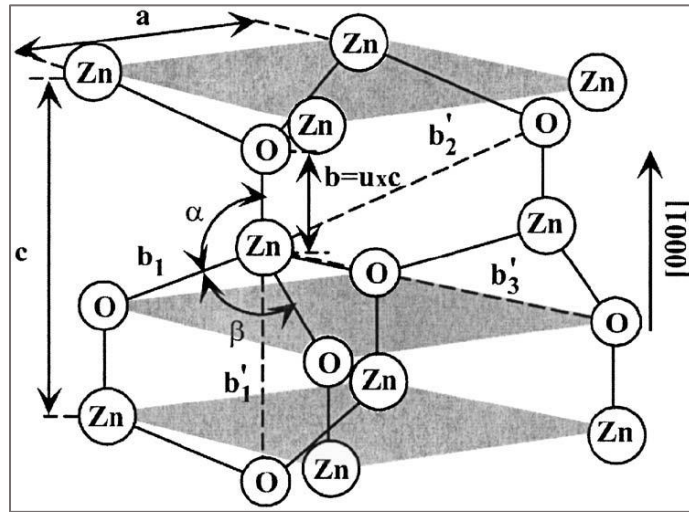


Figure 1.15: Schematic representation of a wurtzite ZnO structure containing lattice parameters in the basal plane and c in the basal direction; and 109.070° in an ideal crystal are the bond angles [1.53].

1.4.4.2.1 Lattice parameters

Lattice parameters are essential in the development of semiconductor devices. In a unit cell, a set of atoms is arranged in a particular way, located upon the lattice points. The points are repeating periodically in 3-D and may be thought to form tiny boxes called unit cells. These unit cells fill the space lattice. The lattices fall into seven different groups, called the crystal systems. Crystal systems are differentiated by the length between points in the unit cell and angles between the sides of the unit cell. The distance between two points on the corners of the unit cell is called the lattice parameters. Each lattice parameter is denoted by a , b , and c , while the angles are denoted by Greek letters α , β , and γ [1.54]. Four factors affect the size of the lattice parameters of the semiconductors [1.53].

1. The concentration of free-electrons. The change in the concentration affects the potential of the bottom of the potential that is usually occupied by electrons.
2. The concentration of foreign elements, crystal defects, and the difference in the ionic radii among these crystal defects and the foreign elements as matrix ions are substituted.
3. The external strains may be attributed to the substrates.
4. The temperature of the crystal system

Moreover, periodically altering lattice parameters are due to a vast amount of imperfections and defects. These defects and faults are responsible for changing the mechanical, optical, thermal, and electrical properties of ZnO lattice parameters. Accurate measurements of the lattice parameters of any crystalline material are done by high-resolution x-ray diffraction (HRXRD) [1.53].

1.4.4.3 Electronic band structure

The electronic band structure is an essential property for any semiconductor. Vital semiconductor properties such as the band gap value and the electron-hole relationship/ composition ratio may be derived from the electronic band structure. ZnO is considered the most suitable semiconductor due to its high transparency in the UV-vis region of the electromagnetic spectrum, high exciton binding energy of 60 meV, and more excellent stability at room temperature. Therefore it is essential to study the electronic band structure of ZnO as the study may give an understanding of the electrical potential ZnO holds. The electronic band structure consists of six valence bands corresponding to

the oxygen's 2p ranging between -6 eV to 0 eV and two conduction bands at ~3 eV. The conduction bands are strongly localised on zinc and correspond to the unoccupied Zn's 3s orbitals [1.53].

ZnO has been a potential material for a wide range of applications such as gas sensors [1.55], photocatalysis [1.56], and solar cells [1.16]. Furthermore, the hexagonal wurtzite structured ZnO is chemically stable at room temperature, harmless, and easy to synthesise, thus leading to bulk production of ZnO-based optical devices such as organic solar cells [1.57]. ZnO is one of the most easily synthesised semiconductors. Therefore, it is one of the potential materials to manipulate the absorption of light to generate electrical output from organic solar cells [1.16]. ZnO nanoridges thin-films as a potential ETL candidate to influence light absorption have been synthesised by carefully selecting the appropriate heating method for the spin-coated ZnO thin-films [1.1].

1.4.5 Nano-zinc oxide as ETL in the photovoltaic device

ZnO is one of the widely used ETLs in IOSCs. It is characterised by low work function, high optical transparency, non-toxicity, and Fermi-energy and conduction band that matches the LUMO of the acceptor material of P3HT:PCBM and can be attained at any desired low-cost solution processes [1.58]. ZnO has proven to exist in different nanostructures as ETL in IOSC: compact layer [1.48], nanoridges [1.1], and nanorods [1.59]. Crystalline optimisation of ZnO by annealing at low temperature has improved IOSC performance [1.48]. The ZnO layer's morphology, thickness, and level of roughness play a significant role in the IOSC PCE. However, it has been reported that selective synthesis methods result in the desired morphology, thickness, and subsequently, the desired level of roughness required with minimal optimisation is attained. The

widely used forms of synthesis include hydrothermal synthesis [1.59], laser deposition [1.57], molecular beam epitaxy (MBE) [1.57], sol-gel method (spin-coating) [1.49]. Among the ZnO synthetic techniques, the sol-gel method (spin-coating) comes across as a favourable method. It leads to better surface contact between the active layer and the ETL, thus more likely to increase photon collection in the active layer [1.60].

As surface roughness, thickness, and morphology of ZnO thin-film play a role in the performance of IOSC, it has been reported that roughness and step-height optimisation of ZnO thin-films can be achieved through slow-annealing Zinc acetate solution to 275°C [1.1] at a specific rate. Ramp-annealing has proven to improve J_{sc} and also increase FF. An increase in J_{sc} has shown enhanced light absorption in the active layer and efficient transportation of electrons to the ITO. Roughness and optimised step-height allow light to be scattered in random directions and reflected from the top electrode by increasing the path length inside the polymer layer [1.48]. This process increases electron extraction and hole blocking at the P3HT: PCBM/ZnO/ITO interfaces.

D.C. Lim et al., [1.1] reported on the spontaneous formation of nanoridges on the surface of ZnO thin-films as a hole-blocking layer in inverted organic solar cells. This study combined commercial ZnO nanoparticles with zinc acetate solution and deposited them onto the ITO substrate to form nanoridge structures. It has been demonstrated how the formation of homogeneous nanoridges' height can be controlled by adding an adjusted amount of ZnO nanoparticles into zinc acetate solution for best IOSC performance, provided the solution is deposited as ETL. It serves the purpose of hole-blocking and electron transportation. The method that was used to fabricate ZnO

nanoridges thin-film was Sol-gel (spin coating). The height and homogeneity of the ripple structures were analysed using atomic force microscopy, and optical measurements were made by UV-Vis transmittance spectroscopy. Hall effects measured carrier mobility J_{sc} -V characteristics of IOSC devices were measured under AM 1.5 [1.1] (standard terrestrial solar spectrum [1.31]).

In the analysis, adding ZnO nanoparticles to the zinc acetate solution proved to assist in homogeneous ripples size formation and enhance IOSC devices' performance. The effect of the addition of ZnO nanoparticles to the zinc acetate solution on the height and homogeneous appearance of nanoridges is detailed in Figure 1.16. It was found that the mean height of the structure in Figure 1.16 (a) is inhomogeneous and is a composition of ~ 100 nm and ~ 20 nm mean height of the nanoridges. As the weight Of ZnO NPs was increasingly added into zinc acetate solutions respectively, homogeneous nanoridges demonstrated in Figure 1.16 (b)-(f) were formed. The height of the ripples decreased with an increase in the amount of ZnO NPs from ~ 70 nm to <30 nm, and the structure of the ripples became more homogeneous [1.1].

The fabricated ZnO thin-films demonstrated in Figure 1.16 were further used for IOSC devices as the ETL and PEC measurements were taken. The photovoltaic performances of IOSCs consisting of ZnO thin-films with various surface structures are in Figure 1.16 (a-f). PCE, FF, and short-circuit current of each device are demonstrated in Figure 1.17. The IOSC device fabricated based on the thin-film in Figure 1.16 (a) reached an efficiency of 2.78%, higher than previously reported device efficiencies at $<1.8\%$. These results suggest that the formation of nanoridges plays a vital role in increasing PCEs in IOSCs. A decrease in the PCEs of the devices fabricated from 21ml

zinc acetate solution with added ZnO nanoparticle was demonstrated as the mass of the ZnO nanoparticle was increased. However, the remarkable value of the PCE achieved in this study was 3.2%, corresponding to the ZnO nanoridges with an average height of ~ 70 nm [1.1].

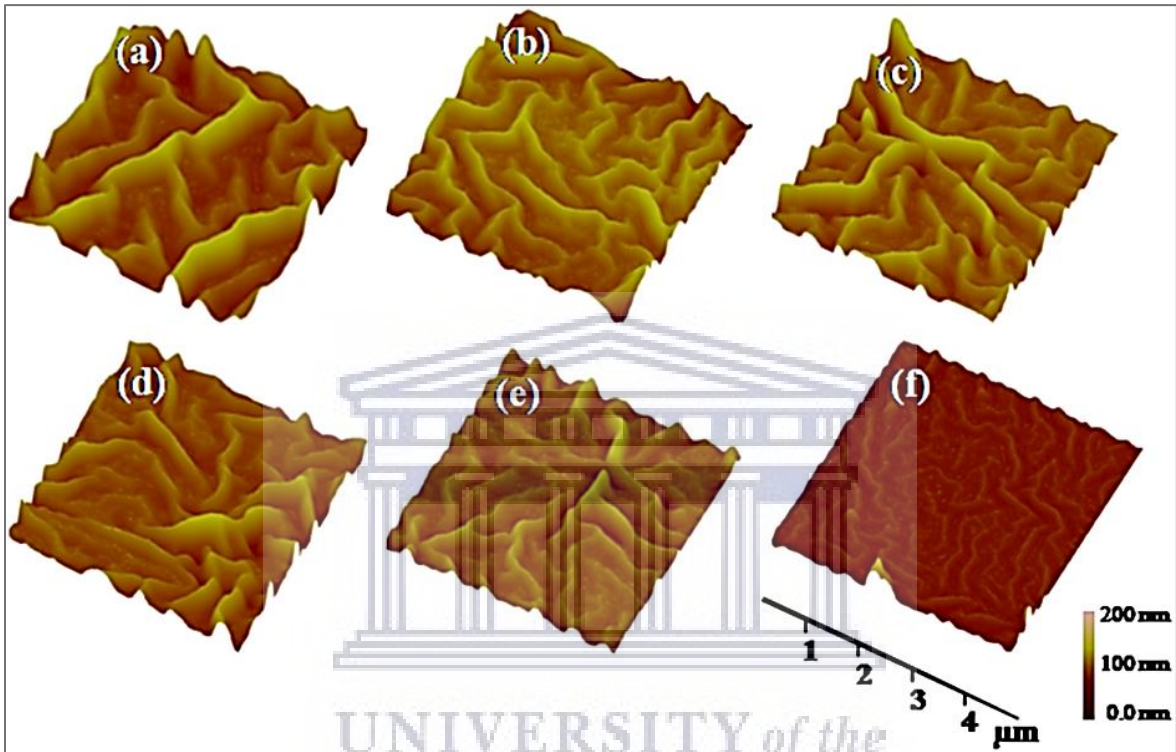


Figure 1.16: AFM images of different ZnO film surfaces on indium-tin oxide used as hole-blocking layers in IOSCs. (a) ZnO film was spin-coated using bare zinc acetate solution, (b)–(f) ZnO films were spin-coated by utilising ZnO NPs and zinc typical acetate solutions. From (b) to (f), the mass of ZnO NPs in addition to the zinc acetate solution was increased. Amount of ZnO NPs added to 21ml of zinc acetate solution was 0.25, 1, 3, 5 and 10mg for (b)–(f), respectively [1.1].

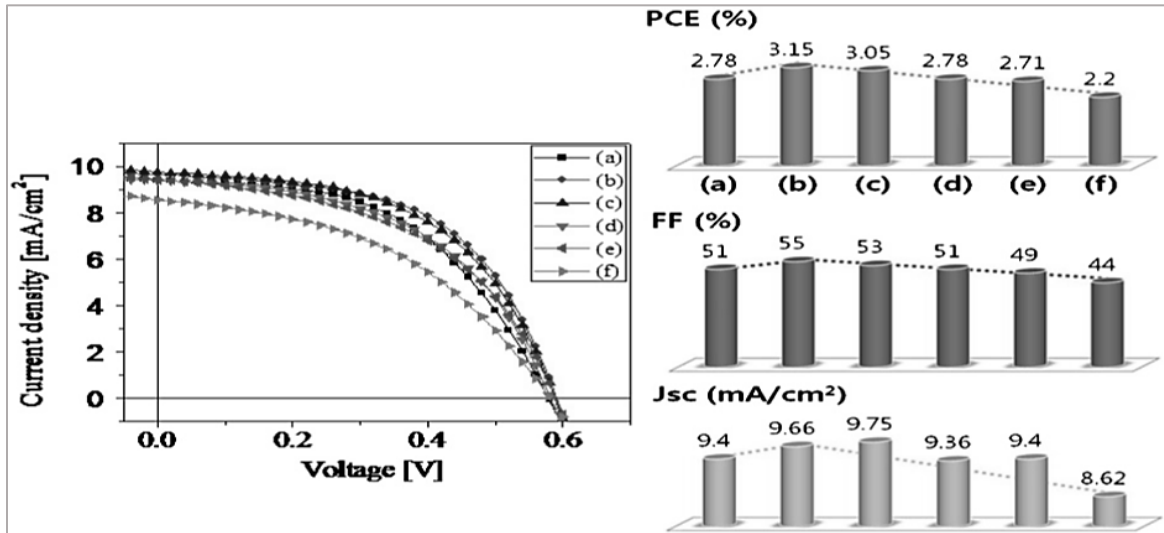


Figure 1.17: Photovoltaic performances of IOSCs consisting of ZnO thin-films with various surface structures in Figure 1.16(a)–(f). Each device's PCE, FF, and short-circuit current are summarised [1.1].

1.5 Problem statement

The research question under consideration is whether ZnO nanoparticles can be synthesised to incorporate in homogenous ZnO thin-film manufacture. Consequently, what effect does the height and width of the ETL ZnO nanoridges have on the performance of the IOSCs?

We postulate that the height of the ripples on the ZnO surface can be controlled by utilising ZnO nanoparticles as a constituent for thin-film growth. In the present study, the effect of the ZnO nanoparticle size on the heights of the ripples of the film, and its subsequent effect on light-capturing by the active layer, and the photovoltaic performance of the solar cell using hydrothermal synthesis to synthesise ZnO nanoparticles is investigated, and the results of the study presented.

1.6 Aim

This project aims to solve a portion of the world's energy crisis by studying, gaining knowledge and insight on improving the performance of PV devices and by further fabricating and testing the PV devices. An article in 2017 was published on the spontaneous synthesis of ZnO nanoridges-based organic solar cells by D.C. Lim et al., [1.1]. The authors have studied the effect of ZnO NPs on the performance of organic solar cells. J.Y. Kim et al., [1.61], O. Wiranwetchayan et al., [1.62], and A. Ranjitha et al., [1.63] worked on various metal oxides nanocrystalline thin-films as buffer layers in organic solar cells. Their work studied metal oxides as ETLs and HTLs for organic solar cells performance testing and selecting the buffer layer that results in better organic solar cell performance. The fundamental goal of this study is to explore a series of factors that affect the height of the nanoridges for IOSCs performance.

In particular, we aim to investigate the effect of ZnO NPs size synthesised through the hydrothermal method on the heights of nanoridges of ZnO thin-film on light-capturing by the active layer and the photovoltaic performance of the solar cell.

1.7 Objectives

- To synthesise ZnO nanoparticles using hydrothermal synthesis at time frames of 3 hrs and 6 hrs and a temperatures range of 140°C and 180°C.
- To synthesise ZnO thin-film through sol-gel synthesis from subsequent ZnO nanoparticles powder with the smallest nanoparticles size.

- Analyse the structural properties of ZnO nanoparticles using a transmission electron microscope (TEM), scanning electron microscope (SEM), and x-ray diffraction (XRD) technique.
- Investigate the optical properties of ZnO NPs using ultra-violet spectroscopy absorption (UV-Vis spec).
- Analyse the structural properties of ZnO thin-films using a scanning electron microscope (SEM).
- Investigate the optical properties of ZnO thin-films using ultra-violet spectroscopy (UV-Vis spec), transmission spectroscopy.
- To measure FF, J_{sc} , V_{oc} , and PCE by J-V characteristics of IOSC devices fabricated using ZnO as the ETL under AM 1.5.

1.8 The layout of the thesis

This study highlights the history of PV devices, how they operate, the different materials used for PV devices fabrication, the theory of devices' materials of choice in Chapter 1. This study will focus on the effect of the ZnO nanoridge height on the performance of organic solar cells. Therefore, the theoretical background on the ZnO is discussed in chapter 1.

The general synthesis processes and characterisation techniques for the nanomaterials are illustrated in chapter 2. The synthesis techniques are the hydrothermal method and sol-gel spin-coating technique. The hydrothermal method is used to synthesise ZnO NPs, and the sol-gel spin-coating technique was used to synthesise ZnO NPs-seeded ZnO nanoridges. Characterisation

techniques used to analyse the ZnO NPs characteristics are Fourier transform infra-red spectroscopy, X-ray diffraction technique, high-resolution transmission electron microscopy, and ultraviolet-visible absorption spectroscopy. The characterisation techniques utilised to study the ZnO NPs-seeded ZnO nanoridges include high-resolution scanning electron microscopy, energy dispersive spectroscopy, thickness profilometry, and UV-Vis transmittance spectroscopy. The general designing and building of the OPV device(s), the testing of the OPV device (s), and measurements in dark and under AM 1.5 simulated illumination of 1000 W/m^2 that were done for current-voltage characterisation of solar cells is outlined in Chapter 2.

Chapter 3 outlines an experimental report on the synthesised ZnO NPs' structural, morphological, crystallographic, and optical properties of ZnO NPs.

Chapter 4 reports on the effect of synthesis conditions of the ZnO NPs on ZnO nanoridges and the chemical composition, morphological, topographical, and optical properties.

And lastly, the analysis of the performance of the fabricated PV devices and a summary of the findings, together with the future work, are reported in Chapters 5 and 6, respectively.

References

- [1.1] D.C. Lim, W.H. Shim, K.D. Kim, H.O. Seo, and J.H. Lim, "Spontaneous formation of nanoripples on the surface of ZnO thin films as hole-blocking layer of inverted organic solar cells," *Solar Energy Materials&Solar Cells*, vol. 95, p. 3036–3040, 2011.
- [1.2] I.M. Dharmadasa, "Science," in *Advances in Thin-Film Solar Cells*, Sheffield, CRC Press, 2018, p. 286.
- [1.3] Andlinger Center, "Article 3. From the Sun to the Solar Project," *For Energy + The Environment*, pp. 1-11, 2016.
- [1.4] M.J. Aschwanden, "Chapter 11 - The Sun," in *Encyclopedia of the Solar System (Third Edition)*, CA, Elsevier, 2014, pp. 235-259.
- [1.5] K.A. Mazzi and C.K. Luscombe, "The future of organic photovoltaics," *Chem Soc Rev*, pp. 1-13, 2014.

- [1.6] C.S. Psomopoulos, "Solar Energy: Harvesting the Sun's Energy for Sustainable Future," in *Handbook of Sustainable Engineering*, Agaleo, Springer Science+Business Media B.V., 2012, p. 117.
- [1.7] Z. Abdin, M.A. Alim, R. Saidur, M.R. Islam, W. Rashmi, S. Mekhilef, and A. Wadi, "Solar energy harvesting with the application of nanotechnology," *Renewable and Sustainable Energy Reviews*, vol. 26, p. 837–852, 2013.
- [1.8] K.A. Ibrahim, P.M. Gyuk, and S. Aliyu, "The effect of solar irradiance on solar cells," *Science World Journal*, vol. 14, no. 1, pp. 1-3, 2019.
- [1.9] D. Leitão, J.P.N. Torres, and J.F.P. Fernandes, "Spectral irradiance influence on solar cells efficiency," *Energies*, vol. 5017, no. 13, pp. 1-18, 2020.
- [1.10] V. Bellesiotis, S. Kalogirou, and E. Delyannis, "Chapter six- Indirect solar desalination (MSF, MED, MVC, TVC)," in *Thermal solar desalination*, 125 London Wall, London EC2Y 5AS, UK, Elsevier, 2016, pp. 283-326.
- [1.11] A. Augustyn, E. Gregersen, G. Lotha, and S. Singh, "Astronomical unit: Additional Information," *Astronomical unit*, 2018.

- [1.12] C.J. Rhodes, "Solar energy: principles and possibilities," *Science Progress*, vol. 93, no. 1, p. 37–112, 2010.
- [1.13] M. Günther, "Chapter 2: Solar Radiation," in *Advanced CSP Teaching Materials*, Enermena, pp. 1-19.
- [1.14] V. Walter, M. Saska, and A. Franchi, "Fast Mutual Relative Localization of UAVs using Ultraviolet LEDMarkers," *2018 International Conference on Unmanned Aircraft Systems (ICUAS)*, pp. 1-10, 2018.
- [1.15] S. Hermann, A. Miketa, N. Fichaux, "Estimating the Renewable Energy Potential in Africa," *IRENA-KTH working paper, International Renewable Energy Agency*, pp. 1-73, 2014.
- [1.16] J. Huang, Z. Yin, and Q. Zheng, "Applications of ZnO in organic and hybrid solar cells," *Applied Physics*, vol. 4, pp. 3861-3877, 2011.
- [1.17] Z.R. Tahir and M. Asim, "Surface measured solar radiation data and solar energy resource assessment of Pakistan: A review," *Renewable and Sustainable Energy Reviews*, pp. 1-23, 2017.

- [1.18] Y.N. Sudhakar and D. Krishna, "Biopolymer Electrolytes for Solar Cells and Electrochemical Cells," in *Biopolymer Electrolytes*, Elsevier, 2018, pp. i-ii.
- [1.19] K.E. Jasim, "Quantum dots solar cells," in *New approaches and reviews*, Kingdom of Bahrain, Intech, University of Bahrain, 2018, p. 305.
- [1.20] K.P. Musselman and K. Poorkazem, "Fundamental Understanding of Solar Cells," in *Advanced Micro- and Nanomaterials for Photovoltaics*, Waterloo, ON, Canada, Department of Mechanical and Mechatronics Engineering, University of Waterloo, 2019, pp. 1-17.
- [1.21] N. Guerra, M. Guevara, C. Palacios, and F. Crupi, "Operation and physics of photovoltaic solar cells: an overview," *Revista de I+D Tecnológico*, vol. 14, no. 2, pp. (84-95), 2018. , vol. 14, no. 2, pp. 84-95, 20 April 2018.
- [1.22] O.K. Simiya, P. Radhakrishnan, and A. Ashok, "Engineered nanomaterials for energy application," in *Nanomaterials for solar energy generation*, Tamil Nadu, Elsevier, 2018, p. 751.
- [1.23] B.V. Zeghbreek, "Chapter 4: p-n junctions," in *Principles of semiconductor devices*, Colorado, 2011.

- [1.24] I. Massiot, "Design and fabrication of nanostructures for light-trapping in ultra-thin solar cells," HAL Id, Paris, 2014.
- [1.25] K.C. Kao, "6 - Charge Carrier Injection from Electrical Contacts," in *Dielectric Phenomena in Solids*, Manitoba, Academic Press, 2004, pp. 327-380.
- [1.26] S.J. Fonash, "Chapter Three - Structures, Materials, and Scale," in *Solar Cell Device Physics (Second Edition)*, Academic Press, 2010, pp. 67-120.
- [1.27] A. Gusain, R.M. Faria, and P.B. Miranda, "Polymer solar cells- Interfacial processes related to performance issues," *Solar Energy Harvesting*, vol. 7, no. 61, pp. 1-25, 2019.
- [1.28] L.A. Dobrzański, M. Szczęsna, M. Szindler, and A. Drygała, "Electrical properties mono- and polycrystalline silicon solar cells," *Journal in Achievements in Materials, Manufacturing, and Engineering*, vol. 59, no. 2, pp. 67-71, 2013.
- [1.29] M.H. El-Ahmar, A-H.M. El-Sayed, and A.M. Hemeida, "Mathematical modeling of Photovoltaic module and evaluate the effect of various parameters on its performance," *Conference Precedings*, pp. 1-6, 2016.

- [1.30] L.H. Callejoa, S.G. Saavedraa, and V.A. Gómezb, "A review of photovoltaic systems: Design, operation and maintenance," *Solar Energy*, vol. 188, p. 426–440, 2019.
- [1.31] A. Le Donne, A. Scaccabarozzi, S. Tombolato, S. Marchionna, P. Garattini, B. Vodopivec, M. Acciarri, and S. Binetti, "State of the Art and Perspectives of Inorganic Photovoltaics," *Renewable Energy*, vol. 8, pp. 1-8, 2013.
- [1.32] M. Tao, "Inorganic Photovoltaic Solar Cells: Silicon and Beyond," *The Electrochemical Society*, vol. 8, pp. 30-25, 2008.
- [1.33] F.A. Roghabadi, N. Ahmadi, V. Ahmadi, A.D. Carlo, K. Oniy, A.S. Tehrani, F.S. Ghoreishi, M. Payandeh, and N.M.R. Fumani, "Bulk heterojunction polymer solar cell and perovskite solar cell: Concepts, materials, current status, and opto-electronic properties," *Solar Energy*, vol. 173, pp. 407-424, 2018.
- [1.34] M. Zendehtel, N.Y. Nia, and M. Yaghoubinia, "Emerging Thin Film Solar Panels," *Reliability and Ecological Aspects of Photovoltaic Modules*, pp. 1-27, 2019.
- [1.35] G. Yilan, M.A. Kadirgan, and G. A. Çiftçioglu, "Analysis of electricity generation options for sustainable energy decision making: the case of Turkey," *Renewable Energy*, vol. 146, pp. 519-529, 2020.

- [1.36] M. Kus and D.A. Kara, "Synthesis of Nanoparticles," in *Handbook of Nanomaterials for Industrial Applications*, New Jersey, Elsevier, 2018, pp. 392-429.
- [1.37] A.M. Bagawan and K.S. Ghiwari, "Perovskite Solar Cells," *International Journal of Advance Research in Science and Engineering*, vol. 06, no. 10, pp. 1347-1353, 2017.
- [1.38] A. Manikandan, Y. Slimani, A. Dinesh. A. Khan, K. Thanrasu, A. Baykal, S.K. Jaganathan, H. Dzudzevic-Cancar, and A.M. Asiri, "8-Perovskite's potential functionality in a composite structure," in *Hybrid Perovskite Composite Materials*, Kidlington, Woodhead Publishing Series in Composites Science and Engineering, 2021, pp. 181-202.
- [1.39] N-G. Park, "Perovskite solar cells: An emerging photovoltaic technology," *Materials Today*, vol. 00, no. 00, pp. 1-8, 2014.
- [1.40] T.D. Lee and A.U. Ebong, "A review of thin film solar cell technologies and challenges," *Renewable and Sustainable Energy Reviews*, vol. 70, no. C, pp. 1286-1297, 19 February 2017.
- [1.41] C. Zhang, C. Kang, H. Zong, S. Liang, C. Geng, and M. Li, "Roles of TiO₂ buffer layer for preparation of high performance VO₂ thin films with Monoclinic polymorph," *Results in Physics*, vol. 10, pp. 628-632, 2018.

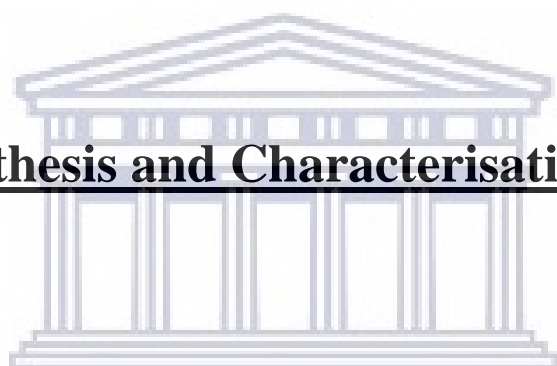
- [1.42] M.C. Scharber and N.S. Sariciftci, "Efficiency of bulk-heterojunction organic solar cells," *Progress in Polymer Science*, vol. 38, p. 1929–1940, 2013.
- [1.43] G. Yu, J. Gao, J.C. Hummelen, F. Wudl, and A.J. Heeger, "Polymer Photovoltaic Cells: Enhanced Efficiencies via a Network of Internal Donor-Acceptor Heterojunctions," *Science*, vol. 5243, no. 270, pp. 1789-1791, 1995.
- [1.44] I. Ullah, S.K. Shah, S. Wali, K. Hayat, S.A. Khattak, and A. Khan, "Enhanced efficiency of organic solar cells by using ZnO as electron transport layer," *Material Research Express*, vol. 4, p. 125505, 2017.
- [1.45] B. Parida, "A review of solar photovoltaic technologies," *Renewable and Sustainable Energy Reviews*, vol. 15, pp. 1625-1636, 2011.
- [1.46] M.A. Green, Y. Hishikawa, W. Warta, E.D. Dunlop, D.H. Levi, J. Hohl-Ebinger, and A.W.Y. Ho-Baillie, "Solar cell efficiency tables (version 50)," *Progress in Photovoltaics*, vol. 25, pp. 668-676, 2017.
- [1.47] NREL, "solar-cell-power-conversion-efficiencies-NREL-2018," NREL, 2018. [Online]. Available: <https://cdn.shopify.com/s/files/1/0823/0287/files/solar-cell-power-conversion-efficiencies-nrel-2018.PNG?11735421312187217475>. [Accessed 07 April 2021].

- [1.48] S. Lattante, "Electron and hole transport layers: Their use in inverted bulk heterojunction polymer solar cells," *Electronics*, vol. 3, pp. 134-164, 2014.
- [1.49] N. Nagayasamy, S. Gandhamathination, and V. Veersamy, "The effect of ZnO thin film and its structural and optical properties prepared by sol-gel spin coating method.," *Open journal of metal.*, vol. 3, pp. 8-11, 2013.
- [1.50] P.A. Rodnyi and I.V. Khodyuk, "Optical and luminescence properties of Zinc Oxide (Review)," *Condense matter spectroscopy*, vol. 111, pp. 814-824, 2011.
- [1.51] M.A. Borysiewicz, "ZnO as a Functional Material, a Review," *Preparation, Characterization, and Application of Zinc Oxide-Based Nanostructures*, vol. 9, pp. 1-29, 2019.
- [1.52] D. da Silva Birona, V. dos Santosb, and C.P. Bergmann, "Synthesis and Characterization of Zinc Oxide Obtained by Combining Zinc Nitrate with Sodium Hydroxide in Polyol Medium," *Scielo Brazil*, vol. 23, no. 2, pp. 1-6, 06 October 2020.
- [1.53] Ü. Özgür, Y.I. Alivov, C. Liu, A. Teke, M. A. Reshchikov, S. Doğan, Vitaliy Avrutin, S.-J. Cho, and H. Morkoç, "A comprehensive review of ZnO materials and devices," *Applied Physics Reviews*, vol. 98, pp. 041301-2- 041301-12, 2005.

- [1.54] F. Hoffmann, *Introduction to Crystallography*, Switzerland AG: Springer, Cham, 2020.
- [1.55] R. Kumar, O. Al-Dossary, G. Kumar, and A. Umar, "Zinc Oxide Nanostructures for Nitrogen Gas–Sensor Applications," *A Review. Nano-Micro Letter*, vol. 7, pp. 97-120, 2015.
- [1.56] E. Jang, J. Won, S. Hwang, and J. Choy, "Fine Tuning of the Face Orientation of ZnO Crystals to Optimize their Photocatalytic Activity," *Advance Material Science*, vol. 18, pp. 3308-3312, 2006.
- [1.57] V. Kumar, V. Kumar, S. Som, A. Yousif, N. Singh, O. M. Ntwaeaborwa, A. Kapoor, and H. C. Swart, "Effect of annealing on the structural, morphological and photoluminescence properties of ZnO thin films prepared by spin coating.," *Journal of colloid and interface science.*, vol. 428, pp. 8-15, 2014.
- [1.58] Z. Yang, T. Zhang, J. Li, W. Xue, C. Han, Y. Cheng, L. Qian, W. Cao, Y. Yang, and S. Chen, "Multiple electron transporting layers and their excellent properties based on organic solar cell," *Scientific Reports*, vol. 7, pp. 1-9, 2017.

- [1.59] B.L. Muhammad and F. Cummings, "Nitrogen plasma treatment of ZnO and TiO₂ nanowire arrays for polymer photovoltaic applications," *Surfaces and Interfaces*, vol. 7, p. 100382, 2019.
- [1.60] S.E. Jung, E.J. Lee, D.K. Moon, and J.R. Haw, "Surface modification of line-patterned electron transfer layer for enhancing the performance of organic solar cells.," *Journal of industrial and engineering chemistry*, vol. 52, pp. 147-152, 2017.
- [1.61] J.Y. Kim, E. Cho, J. Kim, H. Shin, J. Roh, M. Thambidurai, C-m. Kang, H-J. Song, S.M. Kim, H. Kim, and C. Lee, "Improved photovoltaic performance of inverted polymer solar cells through a sol-gel processed Al-doped ZnO electron extraction layer," *Optic Express*, vol. 23, no. 19, pp. A1336-A1341, 2015.
- [1.62] O. Wiranwetchayan, Z. Liang, Q. Zhang, G. Cao, and P. Singjai, "The Role of Oxide Thin Layer in Inverted Structure Polymer Solar Cells," *Materials Sciences and Applications*, vol. 2, pp. 1697-1701, 2011.
- [1.63] A. Ranjitha, M. Thambidurai, F. Shini, N. Muthukumarasamy, and D. Velauthapillaie, "Effect of doped TiO₂ film as electron transport layer for inverted organic solar cell," *Materials Science for Energy Technologies*, vol. 2, p. 385–388, 2019.

Chapter 2: Synthesis and Characterisation Techniques



UNIVERSITY *of the*
WESTERN CAPE

Chapter 2: Synthesis and Characterisation Techniques

Introduction

This chapter deals with the description of the methods and techniques used for synthesising and characterising samples. The first sections will describe the hydrothermal synthesis method of nanoparticles production, the procedure used to prepare the glass substrates, and the nanomaterial thin-film synthesis method, i.e. the sol-gel technique. The following section describes the methods used to characterise the nanoparticles' compositional, structural, and optical properties of the thin-film nanostructure. These techniques include: Fourier transform infrared spectroscopy (FTIR), X-ray diffraction (XRD), high-resolution transmission electron microscopy (HR-TEM), high-resolution scanning electron microscopy (HR-SEM), energy dispersive spectroscopy (EDS), thickness profilometry, ultraviolet-visible (UV-Vis) absorption and transmission spectroscopy, while the last section describes the J-V characterisation of the devices. Table 2.1 represents a summary of the synthesis methods and characterisation techniques for ZnO nanoparticles, ZnO NPs-seeded ZnO nanoridges, and inverted organic solar cells.

Table 2. 1: Analytical characterisation techniques.

<i>Synthesis Techniques</i>		
<i>Technique</i>	<i>Description</i>	<i>Final products</i>
Hydrothermal Synthesis	Crystal growth via hot chemical solution reaction under pressure in an autoclave in an oven.	ZnO Nanoparticles
Sol-gel Synthesis (spin-coating)	Nanoscale thin-film fabrication via spin-coating of gel solution at high speed onto a glass-coated substrate, followed by drying via thermal annealing.	ZnO NPs-seeded ZnO nanoridges
<i>Characterization Techniques</i>		
<i>ZnO Nanoparticles</i>		
Technique	Property	Information
FTIR	Structural	Functional Groups, Atomic Composition & Atomic Bonding
XRD	Atomic and Molecular Structural	Crystallographic Structure, Strain Value, Lattice Parameters, & Grain Size
HRTEM	Structural & Morphological	Particle Shape, Particle Size, & Lattice Parameters
UV-Vis Spec	Optical	Electronic Transitions
<i>ZnO NPs-seeded ZnO nanoridges</i>		
<i>Technique</i>	<i>Property</i>	<i>Information</i>
HRSEM	Morphological	Surface/Particle Shape(s)

EDS	Chemical Composition	Sample Purity & Atomic Composition
Thickness Profilometry	Topographic	Thickness/Height
UV-Vis	Optical	Transmittance Percentage, Electronic Transitions, & Band Gap

Solar Cell Devices

<i>Technique</i>	<i>Property</i>	<i>Information</i>
Current-Voltage Measurement	Electrical	Power Conversion Efficiency, Fill Factor, & V_{OC} , I_{SC}

2.1 Synthesis techniques

2.1.1 Hydrothermal synthesis

2.1.1.1 Background

Hydrothermal synthesis is a technique used to synthesise crystalline material via chemical reactions in a sealed, highly compressed stainless-steel autoclave at high temperature and high pressure [2.1]. Hydrothermal synthesis has been developed and named after a geological process. The Earth, owing to its ability to produce precious crystals such as crystal quartz sealed underground at high temperature and high pressure, thus inspired the development of hydrothermal synthesis [2.1, 2.2].

In hydrothermal synthesis, a hydrolysis reaction occurs whereby an aqueous mixture of reagents reacts to produce oxide ceramics [2.3]. This process is achieved by placing the reagents in a sealed container and heating the system to the desired reaction temperatures [2.3] ranging at $< 300^{\circ}\text{C}$ [2.1] and high pressure [2.3]. The reagents are usually a combination of water (H_2O), a metal hydroxide (e.g. NH_3OH) as a mineraliser, and a metal alkoxide as the source of the ceramic/metal ions [2.3]. During the hydrothermal synthesis process, particle growth produces powder crystals of distinct particle size distribution [2.3]. Factors affecting the reaction rate in hydrothermal synthesis are the concentration of precursors, the solvent, the stabilising agents, the temperature, and the reaction time [2.4].

Advantages of hydrothermal synthesis include operation of the synergistic effect whereby moderate reaction temperature and pressure provide a one-step process of synthesising highly crystalline materials without post-annealing [2.4]. Moreover, hydrothermal synthesis is environmentally friendly and inexpensive in infrastructure, engineering, and operation [2.1]. Figure 2.1 below illustrates a schematic diagram outlining the general process steps and further details on the hydrothermal reaction to synthesise nanoparticles.

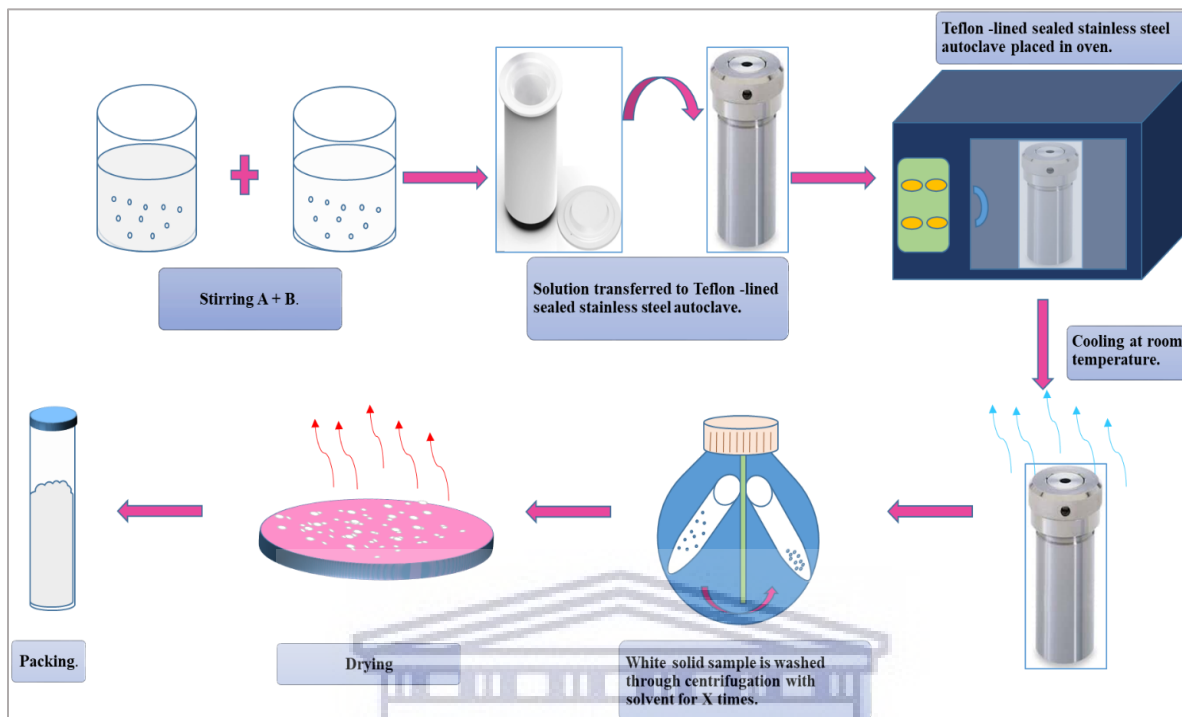


Figure 2. 1: General hydrothermal synthesis of NPs calibrated at $X^{\circ}\text{C}$ temperature for Y period.

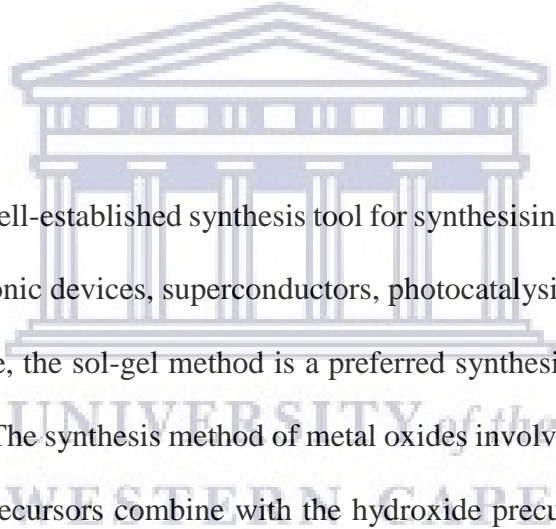
2.1.1.2 Experimental setup

This study used the hydrothermal synthesis technique to fabricate ZnO Nanoparticles prepared for 3 hrs and 6 hrs at 200°C , and 140°C and 180°C for 6 hrs. All reagents were analytically pure and used without further purification. To synthesise ZnO NPs, a stock solution of zinc acetate dihydrate (99.99% purity) was prepared in methanol whilst stirring. To the stirring stock solution, sodium hydroxide solution prepared in methanol separately, was added. The solution was left to stir till reaching a pH of $\sim 10-12$. As the solution reached the required pH, it was removed and transferred to a Teflon-lined sealed stainless steel autoclave and placed in an oven at 200°C for 3 hrs and 6 hrs, and at 140°C and 180°C for 6 hrs, respectively. Post reaction-completion the resultant

white solids were removed. The solids were washed with ethanol, and deionised water, by centrifugation at 12 000 rpm speed for 10 minutes. The washing steps were repeated ten times to remove impurities. The washed products were left to dry at 60⁰C overnight in the oven and packaged in vials. The ZnO NPs were synthesised to achieve the optimal nanoparticle size leading to effectively grown ZnO NPs-seeded ZnO nanoridges for OPV application. The synthesis of the ZnO NPs was undertaken in Bellville, at The University of the Western Cape, Department of Physics and Astronomy.

2.1.2 Sol-Gel Method

2.1.2.1 Background



The Sol-gel technique is a well-established synthesis tool for synthesising functional materials and devices such as ferro-electronic devices, superconductors, photocatalysis instruments, and optical devices [2.5, 2.6]. Therefore, the sol-gel method is a preferred synthesis method for metal oxide and rare earth oxides [2.6]. The synthesis method of metal oxides involves an array of consecutive steps. Initially, the metal precursors combine with the hydroxide precursors and form the metal oxide solution, forming three-dimensional gels [2.5] of discrete particles [2.7], followed by a gel-drying process. Depending on the drying process, the resultant final product can be converted to xerogel or aerogel [2.5]. Due to the nature of the solvent used in the sol-gel method, water is utilized as the reaction medium in aqueous sol-gel synthesis, and the organic solvent is utilized as a reaction medium in non-aqueous sol-gel synthesis [2.5]. Reaction processes that occur during sol-gel synthesis are influenced by several experimental factors such as pH, concentration, and the

temperature of reactants [2.7]. Advantages of the sol-gel method are low processing temperatures, casting coating into complex shapes, and the use of precursor material that leads to highly purified end products [2.7]. The sol-gel method is widely used to fabricate thin-films [2.7]. There are two main methods of coating metal-coated substrates surface with gel solutions, the dip-coating technique and spin-coating technique [2.7, 2.8, 2.9].

Substrate cleaning plays an essential role in the attainment of pure defect-free thin-film nanomaterial. In many laboratory settings, glass substrates are commonly used. Glass substrate cleaning process is a method used to remove any contaminants on the surface of the substrate, therefore leading to effective utilization of slides as though they are new for coating. Furthermore, an impurity-free and dust-free substrate environment allow uniform wetting to the sol-gel solutions [2.10].

Sol-gel synthesis involves the coating of hydroxyl-based molecules containing inorganic and organic segments. These molecules are designed, best fitted to cross-links, and polymerize when coated onto a substrate and dried. Furthermore, substrate cleaning exposes sites that the hydroxyl groups can attach to the substrate during the coating [2.10].

Substrate cleaning is categorized into two sections. The first category presents foreign particles removal and the second deals with exposing active hydroxyl sites on the surface of the substrate [2.10].

Foreign particles on the surface of the substrate are removed through the implementation of standard ultrasonic baths. Ultrasonic baths are systems of two transducers that generate ultrasonic

vibrations and frequencies of ~40 kHz to create white noise, which uniformly generates uniform cleaning effects throughout the system [2.10]. By generating standing wave patterns, ultrasonic baths give rise to vigorous substrate cleaning, leaving the hydroxyl sites of the substrate exposed for uniform wetting of the sol-gel solution. In ultrasonic baths, two solutions can be used. The first solution can be a surfactant solution, whereby the sample slide to be cleaned is placed. The second solution effectively creates standing waves of a low, medium, and high frequencies in the ultrasonic baths [2.10].

Effective substrate cleaning in ultrasonic baths requires control of essential parameters: the correct surfactant with the right concentration level, operation at the right temperature, and the degassing of the solution. The importance of the first parameter is to create the threshold for transient cavitation in the water. The cavitation threshold must be lower than the energy available in the bath. The temperature plays an important role, as it facilitates the surfactant to remove the foreign particles effortlessly. Finally, degassing the solution provides a uniform cleaning as gas bubbles may absorb cavitation energy and lead to failure in cleaning the substrate(s) [2.10].

In sol-gel synthesis, the attainment and maintenance of clean, dry substrates are vital. The presence of moisture can attract new foreign particles after washing, leading to improper wetting of the sol-gel solution on the substrate. Therefore, the effective way to eliminate the risk of foreign particle invasion is through the application of nitrogen gas. Nitrogen gas is an effective applicant as it is clean and is an inert gas [2.11]. Dry cleaning by nitrogen gas provides a significant advantage of less to minimal contact cleaning. Therefore a clean, dry substrate gets ready to receive coating

without tempering with the surface of the substrate [2.10]. When samples are initially prepared, they often contain dirt and production remnants. Therefore, it is required that after the sample substrates are washed, the substrates are dried immediately to prevent the accumulation of moisture and impurities [2.11].

In most experimental set-ups, nitrogen gas is chosen over compressed air due to reactions between the substrate and the air during drying by compressed air. Nitrogen gas provides the advantage of eliminating oxygen molecules at the surfaces of the substrate, leaving the sample substrate with dry nitrogen free from impurity attachment. Due to the dew point of nitrogen gas of -40°C to -73.3°C , nitrogen gas provides high dry quality, meaning that condensation can't occur at the surface of the substrate [2.11]. The only disadvantage that comes with the use of nitrogen gas is the handling, maintenance, and safety measures surrounding the high-pressure nitrogen gas cylinders [2.11]. The following subsection below describes the two popularly performed sol-gel synthesis techniques, i.e. 2.1.2.2 and 2.1.2.3.

2.1.2.2 Dip-coating

The desired metal-coated substrate is progressively dipped into the precursor solution mixture and rotated at a controlled rate in dip-coating. The coated substrate is extracted and left for drying as the solvent evaporates and a homogeneous film is produced [2.7, 2.9]. The removal rate of the coating, surface tension, viscosity, and density of the gel solution affect the thickness of the film [2.7, 2.9]. Moreover, the thickness resulting from dip-coating is usually larger than the thickness

obtained from the spin-coating technique [2.7, 2.9]. A general schematic diagram of the dip-coating technique is indicated in Figure 2.2.

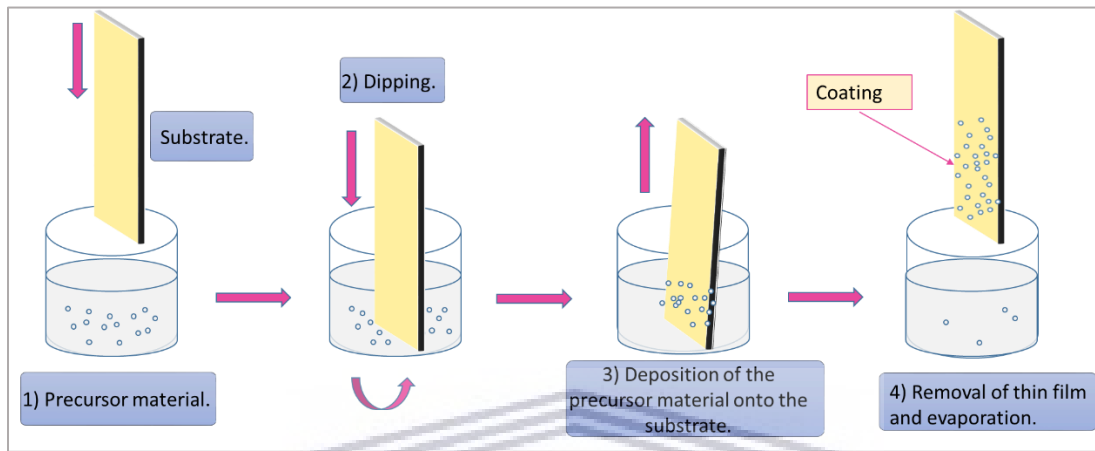


Figure 2.2: Schematic diagram of the general process steps involved in Sol-gel- Dip-coating techniques of nanomaterials synthesis.

2.1.2.3 Spin-coating

The spin-coating technique involves placing the desired amount of the mixed precursor solution onto the substrate and rotating it at high speed to obtain a homogeneous solution spread on the substrate surface area [2.7]. Moreover, reaction factors such as environmental temperature and time of reaction affect the thickness of the thin-film. However, higher spin rates and prolonged spinning times lead to relatively thinner films. Therefore, to achieve the desired thickness, a moderate spinning speed is recommended [2.7]. Furthermore, the uniform film is achieved by drying the coating at a slower drying rate [2.7]. Figure 2.3 illustrates the general process of the spin-coating technique.

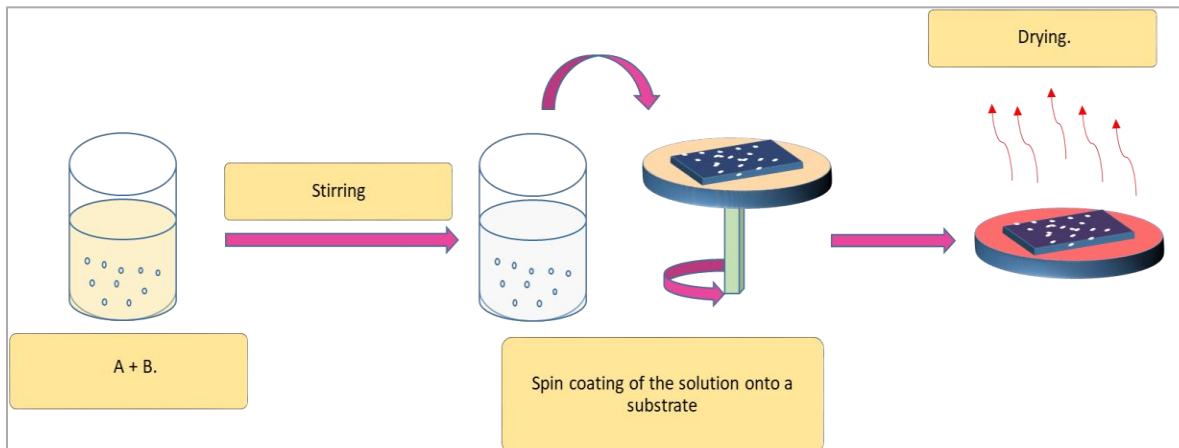


Figure 2.3: Sol-gel method- Spin-coating of unseeded ZnO NRs and seeded ZnO NPs-ZnO NRs calibrated at 140°C and 180°C for 6 hrs and calibrated at 200°C for 3 hrs and 6 hrs.

2.1.2.4 Experimental setup

All the materials and chemicals used for this project were used without further purification. To fabricate ZnO NPs-seeded ZnO nanoridge thin-films, 0.75M zinc acetate dihydrate was dissolved in 70 ml 2-methoxyethanol, and ethanolamine was added to stabilize the Zn (II) ions by facilitating Zn (II) chelation. The solution was left to stir at 60°C for 30 minutes. Afterwards, the solution was divided into batches of ZnO NPs. From each powder sample, 0.25 mg of ZnO NPs was drawn and dissolved in 21 ml of the zinc acetate solution. Five vials were prepared, containing a combination of zinc acetate solution and ZnO NPs prepared at 200°C for 3 hrs and 6 hrs and at 140°C and 180°C for 6 hrs. In preparation for the thin-film deposition, the ITO/clear quartz substrates were immersed and sonicated in isopropanol (IPA), acetone, ethanol, and de-ionized water at 60°C for 15 minutes each sequentially. Compressed nitrogen gas was used to dry the coated substrates after sonication.

The thin-films were prepared by spin coating the 0.40 μL of each solution at 200 revolutions per minute (rpm) for 40 s using an Ossila spin coater and ramp-annealed from room temperature to 275⁰C using a Chemat (Technology Inc) hotplate. The synthesis of the samples was undertaken in Bellville, at The University of the Western Cape, Department of Physics and Astronomy.

2.1.3 Inverted organic solar cells synthesis

The top electrode-ITO layer was commercially obtained. Detailed preparation and analysis of the electron transport layer (ETL) is illustrated in section 2.1.2.4 above. In preparation of the active layer, the hole transport layer (HTL) and the Ag electrode: 1:1 P3HT: PCBM was prepared by stirring 15 mg/ml P3HT and 15 mg/ml PCBM in 1, 2 dichlorobenzene at 60⁰C on a Lasec Hot plate stirrer; stirring at 400 rpm, overnight. 0.03 μL of the stirred solutions was spin-coated on top of ITO/ZnO-based ETLs at 900 rpm for 100 seconds using an Ossila spin coater and ramp-annealed at 150⁰C for 30 min using Chemat (Technology Inc) hot plate. Figure 2.4 illustrates a summary of the synthesis process of the IOSCs in this study. Figure 2.5 (a) demonstrates the band diagram of IOSCs composed of an active layer (P3HT: PCBM), a hole-transport layer (MoO_3), and electron-accepting layer (ZnO NPs-seeded ZnO nanoridges) and both electrodes (ITO and Ag). Figure 2.5 (b) demonstrates the model design of the inverted organic solar cell respectively.

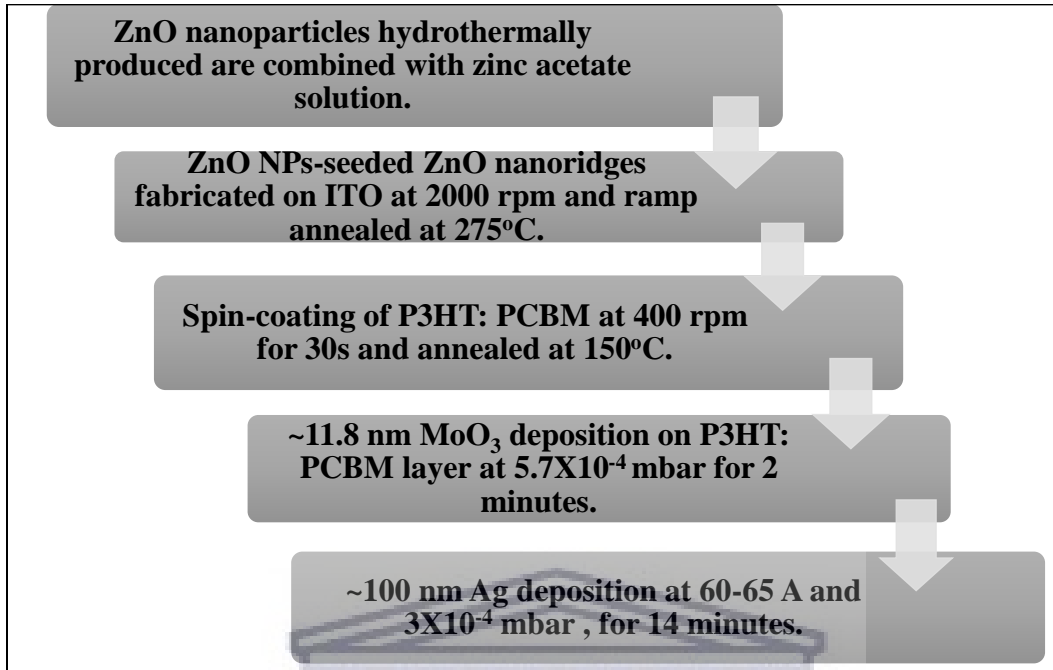


Figure 2. 4: The flow chart diagram illustrating the steps involved in fabricating IOSCs.

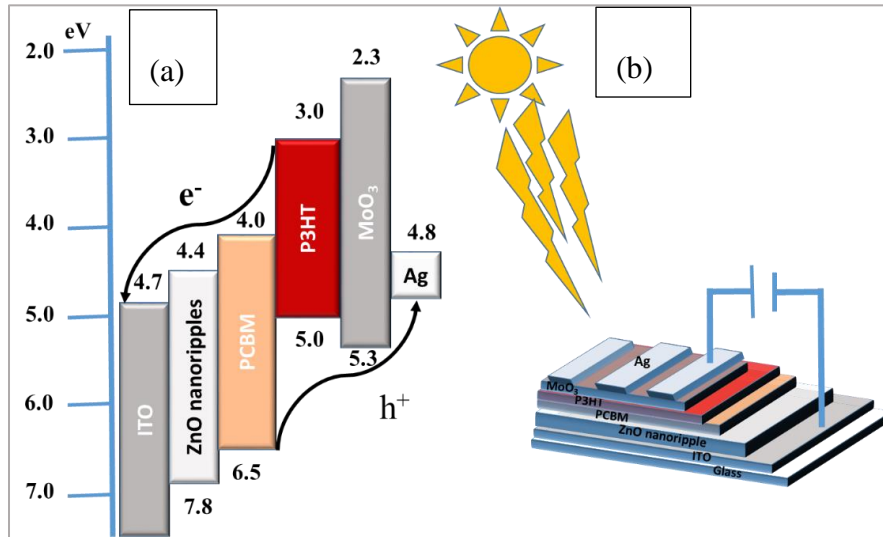


Figure 2. 5: (a) The band gap diagram of IOSCs made of 2 electrodes (indium-tin-oxide and silver (Ag)), ETL (ZnO), a hole-transport layer, (MoO_3), and an active layer (P3HT: PCBM) (b) Schematic diagram of the IOSC-based P3HT: PCBM layer with ZnO nanoridge layer as ETL.

2.2 Characterisation Techniques

2.2.1 Fourier Transform Infra-Red Spectroscopy

2.2.1.1 Background

Fourier Transform Infrared spectroscopy (FTIR) is utilized to identify the structural characteristics of materials [2.12]. FTIR instruments are cost-effective, easier, and faster to use than conventional spectrometers. In FTIR spectroscopy, infrared light can interact with a material causing atomic bonds within the material to either stretch or/and vibrate. Due to this interaction, IR radiation is

absorbed in a given wavelength [2.13]. The mass of the atoms and the type of bonding determines the IR radiation's absorption wavelength.

Furthermore, different materials absorb at different regions of the IR spectrum [2.14]. Therefore the IR absorption spectrum can identify the material investigated (at hand) [2.14]. In FTIR spectroscopy, as light is guided through an interferometer, the whole range of IR wavelengths is simultaneously measured. A Fourier transform is performed on the results, and mathematical adjustments are made to be identical to the conventional IR spectroscopy data. The FTIR instrument [2.15] and the working principle of FTIR spectroscopy are illustrated in Figure 2.6 (a) and (b). The FTIR technique has been utilized to study the vibrational frequencies of ZnO nanoparticles molecules and, as a result, to identify the functional groups present in the molecules.

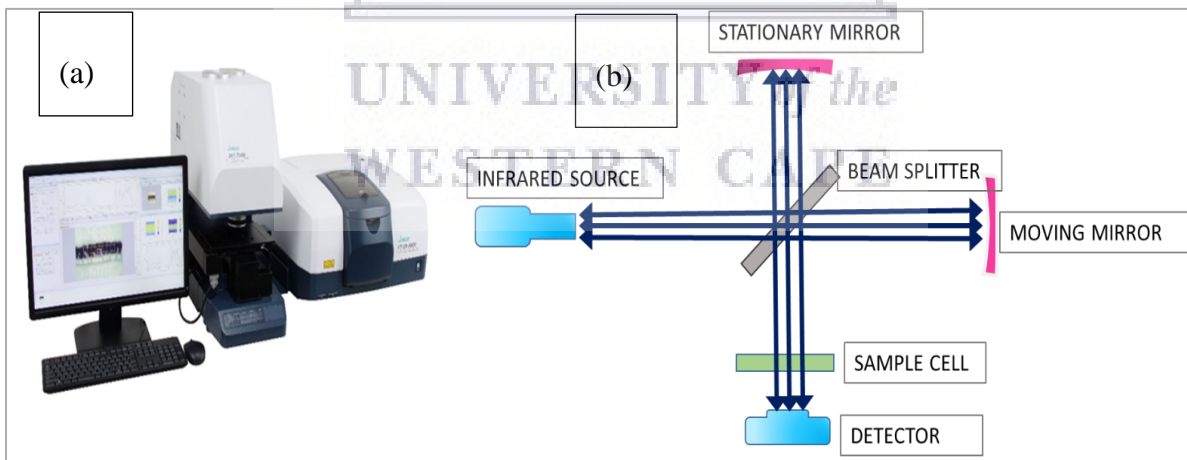


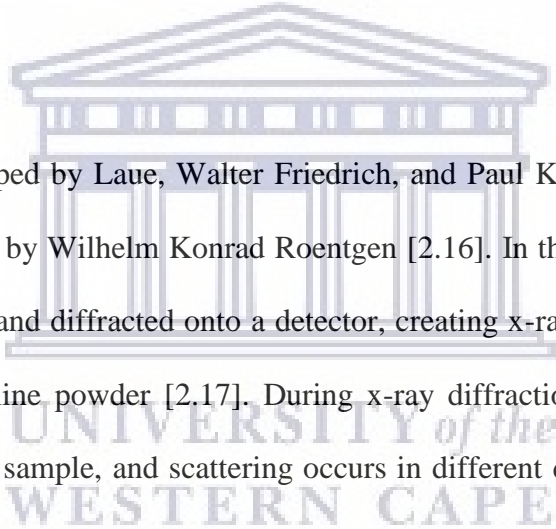
Figure 2. 6: (a) FTIR instrument [2.15] and (b) Working principle behind FTIR.

2.2.1.2 Experimental setup

FTIR was used to identify various functional groups present in ZnO nanoparticles. Products of hydrothermal synthesis were measured using a Perkin-Elmer Spectrum 100 FTIR spectrometer. The samples were subjected to KBr powder, and the combination was converted to a pellet. The compressed pellets were analysed in the IR range of 400-4000 cm^{-1} . The measurements were taken in Bellville, at The University of the Western Cape, Department of Chemical Sciences.

2.2.2 X-ray Diffraction Technique (XRD)

2.2.2.1 Background



XRD is a technique developed by Laue, Walter Friedrich, and Paul Knipping in 1912 after the discovery of x-rays in 1895 by Wilhelm Konrad Roentgen [2.16]. In the XRD technique, x-rays are scattered onto a crystal and diffracted onto a detector, creating x-rays signalled to determine the structure of the crystalline powder [2.17]. During x-ray diffraction, monochromatic x-ray photons are directed onto a sample, and scattering occurs in different directions. Intensities and angles are measured. From these measurements, unit cell, atomic ordering, crystal structure, and crystallite size information can be obtained from the theory of crystallography [2.17, 2.18]. In crystallography [2.17, 2.19], every single crystal rotation is ideally represented in real space. The average crystal rotation represents the three-dimensional reciprocal space onto a one-dimensional space. Bragg's law (equation 2.1) represents the relationship between the diffraction angle, θ , the wavelength of x-rays, λ , and the interplanar spacing of the lattice d_{hkl} .

$$2d_{hkl} \sin \theta = \lambda. \quad (2.1)$$

Every crystal has its unique diffraction pattern, called fingerprints. Therefore, from the XRD diffraction pattern, i.e. I_{hkl} as a function of 2θ , the broadness of the diffraction peaks (full-width-at-half-maximum) FWHM is extracted. The Debye-Scherrer equation can be used to calculate the crystal size, where d_{hkl} is the crystal size in Å, k is the shape factor for ideally spherical structures (0.9), λ is the x-ray wavelength, and β_{hkl} is the FWHM in radians. θ is half of the observed scattering angle [2.17], in equation 2.2.

$$d_{hkl} = \frac{k\lambda}{\beta_{hkl} \cos \theta}. \quad (2.2)$$

Furthermore, the FWHM may be used to estimate the lattice strain by:

$$\varepsilon = \frac{\beta_{hkl}}{4 \tan \theta}. \quad (2.3)$$

where ε is the lattice strain.

XRD analysis provides information about the deformations such as point defects and stacking faults present in crystal structures. These deformations are investigated using crystallite size, lattice strain, lattice parameters, and Uniform Deformation Model (UDM) analysis [2.20].

Analysis of material formation involves discussion on crystallography [2.21, 2.19], analysis of the formation, and the structure and properties of crystals. The crystal structure(s) is formed from a 3-D arrangement of atoms, molecules, or ions within the crystal structure. The internal arrangement of the atoms in crystals is referred to as the crystal structure. The physical appearance and the internal arrangement of the crystal structure are interdependent. Therefore, internal changes of the atoms throughout due to chemical and mechanical effects on the crystal may affect the physical appearance of the crystal. Furthermore, it is essential to understand the nomenclature of crystallography [2.19].

Due to different effects on materials, one element or molecule may exist in various structural forms containing different periodic atomic arrangements with respect to each other. This phenomenon whereby a material may exist in different crystallographic forms is called polymorphism [2.22]. An example of a polymorphic element or molecule is Carbon. It exists as Graphite and Diamond [2.23, 2.24]. Diamonds are formed under high temperature and pressure in the Earth's mantle; it is hard and used in jewellery and cutting tools [2.23]. Graphite is also made of Carbon, and however, in contrast to Diamond, it is a soft material formed in the Earth's crust under standard conditions and can be used in pencils and lubricants [2.24]. Diamond possesses a cubic crystal structure, while Graphite exists as a hexagonal crystal structure [2.23]. Therefore, from the phenomenon of polymorphism, it is essential to study the crystallographic properties of materials.

UDM is one of the Williamson-Hall Methods of crystal deformation analysis methods. In Williamson-Hall, both strain-induced and crystallite size-induced broadening of the diffraction

peak is considered [2.20]. The lattice strain and crystallite size have different contributions to the line broadening of the diffraction peak. Equations (2.2) and (2.3) above illustrate their respective contribution to the diffraction peak. Therefore, diffraction peak widening is related to the decrease in the lattice strain (ϵ) and vice versa.

In contrast, the crystallite size D decreases with peak widening [2.20, 2.25]. Therefore the relation between the broadening of the diffraction peak in size and the strain is vital for crystal deformation analysis. Usually, a standard material that has sharp and high crystallinity is utilised to subtract the instrumentation effects. The standard material used is often silicon. Therefore the diffraction crystallite size-induced width is given by $\beta_{crystallite}$, and strain-induced width is given by β_{strain} [2.25, 2.26]. The contribution of the lattice strain and the crystallite size to the crystal deformation is related by equation (2.4.1). Therefore, substituting equations (2.2), (2.3), and (2.4.2) yield equation (2.5) and equation (2.5) relate the relationship between the widening of the peak in size and the strain.

$$\beta_{hkl} = \beta_{crystallite} + \beta_{strain}, \quad (2.4.1)$$

$$\therefore \beta_{hkl} = k\lambda D \cos\theta + 4\epsilon \tan\theta; \quad (2.4.2)$$

multiplying by $\cos\theta$

$$\therefore \beta_{hkl} \cos\theta = k\lambda D + 4\epsilon \sin\theta. \quad (2.5)$$

The above equation (equation 2.5) is used to plot UDM Williamson-Hall data. The size and strain are extracted from the y-intercept and the slope. To extract the data for the parameters from the plot, the x-axis is set as $4\sin(\theta)$ and the y-axis as $\beta\cos(\theta)$ [2.25]. In UDM, strain is considered

uniform in all directions [2.26]. The XRD instrument and schematic images are shown in Figures 2.7 (a) and (b).

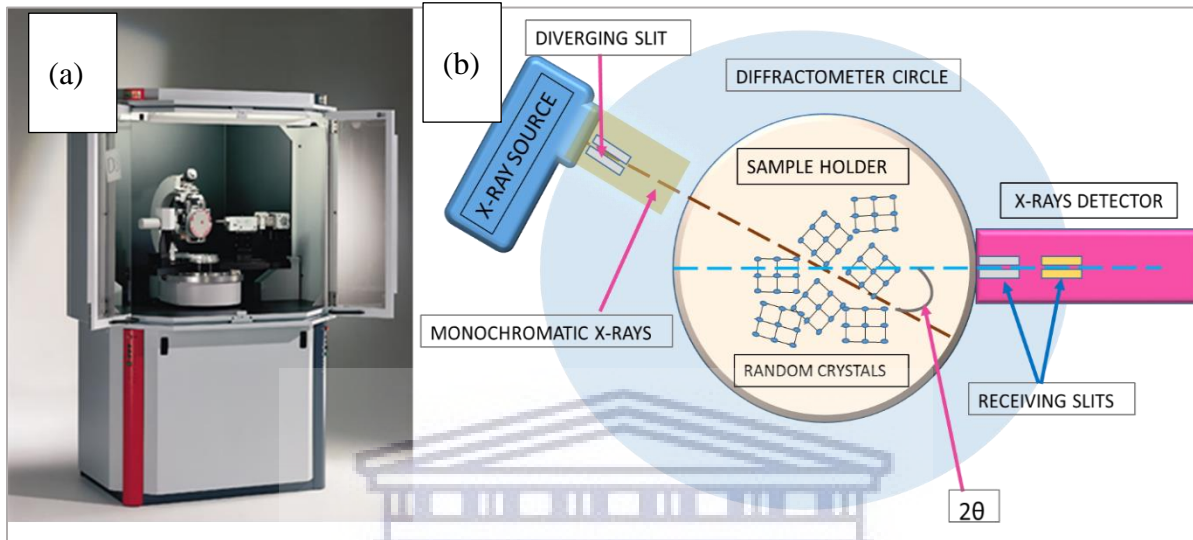


Figure 2. 7: (a) XRD instrument [2.27]. (b) Schematic diagram of working principle of XRD.

2.2.2.2 Experimental setup

In this study, XRD technique was used to analyse the structural formation of ZnO NPs due to the hydrothermal synthesis temperature and time allocated for the formation of ZnO NPs. A Bruker D8-advanced-8-X-ray powder diffractometer with Cu K_{α} radiation ($\lambda=1.54050 \text{ \AA}$) was employed to study the crystallinity and crystal phase of ZnO NPs. at iThemba labs, Faure, Cape Town. The accelerating voltage and applied current were set at 40 kV and 40 mA at room temperature. The Bragg angle ranges from 25° to 85° with a typical step size of 0.034° at 0.5 sec/step.

2.2.3 High-Resolution Transmission Electron Microscopy

2.2.3.1 Background

Transmission electron microscopy (TEM) is a technique developed to achieve a high magnification of the specimen information compared to the conventional optical microscope [2.28]. TEM instruments can examine fine detail at a small scale of ~ 1000 times smaller than the smallest resolvable object in the light microscope using a beam of electrons instead of light. In contrast to the conventional transmission electron microscope, a high-resolution transmission electron microscope (HRTEM) can examine fine details of specimens at a nano-scale resulting in atomic lattice images. The HRTEM technique is applied in significant fields of science that include biology [2.28], semiconducting research [2.28], nanotechnology [2.28], material sciences [2.28], and chemical sciences [2.28].

An HRTEM operates on the principle of quantum mechanical behaviour of electrons, the principle that electrons have both wave and particle nature. In a typical HRTEM, the electron gun is a cathode filament, the source of the electrons. It is usually a hairpin-shaped tungsten wire producing electrons of high energy levels of \sim hundreds keV. A stream of these produced electrons is accelerated and focused by the metal apertures and the magnetic lenses into a thin, focused monochromatic beam. The monochromatic beam strikes the ultra-thin specimen, and a portion of the beam is transmitted through it. As the electrons are transmitted through the specimen, they interact with the ultra-thin specimen. The electrons can scatter or backscatter inelastically or elastically or create many different interactions and give off different signals, such as x-rays or

Auger electrons [2.28]. The interaction of these signals and the sample yield the information that can electronically form and construct the resultant image of the electrons transmitted through the specimen using a set of objective lenses. The beam is further accelerated down the column and gets transmitted through the intermediate and projector lenses. These lenses, therefore, enlarge the image with a set of magnification settings. The resultant image in real space can be focused and magnified onto an imaging device or a sensor device. These devices include a fluorescent screen or CCD screen [2.28]. The instrument [2.29] and the schematic diagram of the working principle behind HRTEM are indicated in Figure 2.8 (a) and (b).

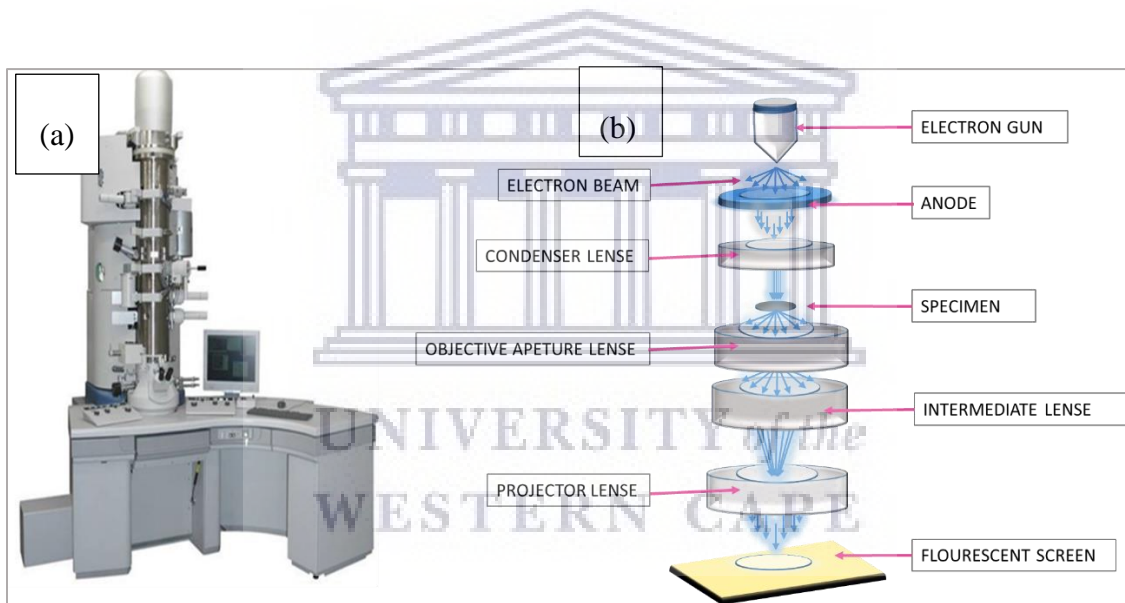


Figure 2. 8: (a) HRTEM instrument [2.29] and (b) schematic is depicting the working principle behind HRTEM.

There are different techniques in TEM that provide different information about samples. These techniques include selected-area electron diffraction (SAED) [2.30], bright-field (BF) TEM imaging, dark-field TEM imaging, HRTEM imaging, and diffraction patterns.

Quantitative SAED provides an observable diffraction pattern on the TEM viewing screen. The diffraction pattern is created from the random orientation of nanoscale fibres or particles. The discernible diffraction pattern indicates the crystallinity, atomic growth direction, crystal structure and can be used to set up dark-field imaging conditions [2.30, 2.31].

Bright-field images are constructed by transmitting the direct beam of electrons, whereby only a few scattered electrons are allowed to pass the aperture and create the bright-field image [2.31].

In dark-field (DF) imaging, only one diffraction beam can pass through the objective aperture. The image is dark with weak diffraction and bright where diffraction is strong [2.31].

HRTEM imaging uses a phase-contrast imaging mechanism whereby the interference of the transmitted beam and diffracted beams generate atomic-scale images. Projected atomic arrangement images are obtained from the HRTEM imaging technique. HRTEM is capable of resolving individual planes of atoms in a crystalline lattice. The lines achieved from the image are closely related to the planes of atoms in the crystalline lattice [2.32].

By adjusting the intermediate lenses in the rear focal plane of the objective lens with the electrons scattered on the sample and a combination of the electrons to form an image, diffraction patterns are generated [2.33, 2.32].

2.2.3.2 Experimental setup

In this study, an FEI Tecnai G2 20 field-emission gun (FEG) High-resolution transmission electron microscope (HRTEM) operating in bright field mode at an accelerating voltage of 20 kV was employed to study the crystallinity, size, and morphological properties of ZnO NPs. The TEM specimen measurements were done by depositing a drop of ZnO in ethanol solution on a 400 mesh copper grid coated by an amorphous carbon film. The solution on the 400 mesh copper grid was left to evaporate in the air at room temperature. The measurements were taken from the Electron Microscope Unit, University of the Western Cape.

2.2.4 High-Resolution Scanning Electron Microscopy

2.2.4.1 Background

High-resolution scanning electron microscopy (HRSEM) uses a focused electron beam with high-energy electrons to scan over a specimen to create a high-quality image with a high resolution ranging to a nanometre scale [2.34, 2.35]. HRSEM operates similarly to the light microscope. However, the HRSEM technique uses a set of electromagnetic lenses to direct and focus the electron beam onto a sample [2.36], coils to scan over a specimen in a raster motion. Electrons are reflected or knocked off at proximity with the surface area of the specimen to generate an image at a nanoscale [2.36]. The electron-specimen interaction resulting in SEM images provides valuable information concerning the topography, crystallography, and the specimen's chemical composition [2.34]. Furthermore, HRSEM was developed to overcome the limiting factors of a conventional SEM microscope by using shorter wavelengths to generate better resolution [2.35].

In HRSEM, an electron gun generates electrons of high energy at the top of the column. The electrons are accelerated down the column, passing through a series of electromagnetic lenses and apertures, generating a focused beam of electrons. The focused beam then hits the surface of the specimen [2.35]. HRSEM operates at low vacuums with impurities within the column and chamber removed [2.35, 2.37]. The electron-specimen interaction gives rise to a series of signals which are detected by suitable detectors. During specimen-electron interaction, secondary electrons, backscattered electrons, and characteristic x-rays are collected by respective detectors to generate images on the computer screen [2.35, 2.36]. When the accelerated electrons strike the surface of the sample, they penetrate the depth of the sample up to ~ micrometres, depending on the acceleration voltage and the density of the sample [2.35].

While a light microscope can provide a resolution of ~400-700 nanometre (nm) and the total maximum magnification of ~ 1,000 X [2.35], SEM can provide a maximum resolution of 50-100 nm [2.34]. SEM provides maximum resolution ranging from 20 X to ~ 30,000 X and spatial resolution of ~ 50-100 nm [2.36]. Furthermore, SEM is considered a non-destructive technique and can operate with a single detector [2.36]. Figure 2.9 (a) and (b) shows the basic SEM tool [2.36], the working principle, and the sample-electron interaction

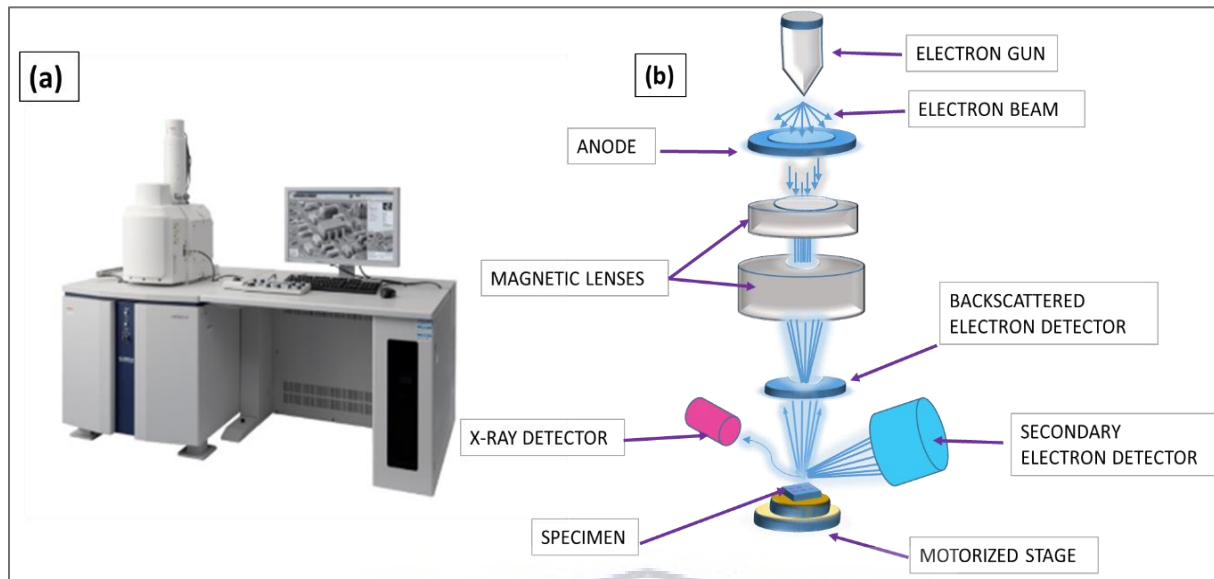


Figure 2. 9: (a) HR-SEM instrument [2.36] and (b) Working principle behind HR-SEM.

2.2.4.2 Energy Dispersive X-ray Spectroscopy (EDS)

Quantitative analysis of material making up the sample is critical as it provides elemental information by detecting elements present in the sample and the quantified amount [2.38]. This method of analysis was developed in the 1970s [2.39]. Energy dispersive energy x-ray spectroscopy is a technique for analysing qualitative and quantitative information from samples in the electron spectroscope [2.40]. During the compositional analysis, the energy dispersive x-ray detector works on the pulse-height analysis of the characteristic X-ray radiation obtained from electrons knocked off from the atom's core of the sample by an incident electron [2.41]. A plot of intensity as an energy function is generated (Figure 2.10 as an example). Theoretical tabulated energy values are compared to the elemental results of the sample. Moreover, EDS can generate

elemental distribution maps to give a background of elements spread/contained on the sample's surface (shown in Figure 2.11 as an example) [2.40]. Therefore, energy dispersive x-ray spectroscopy is a vital tool to investigate the chemical composition of an unknown sample [2.41].

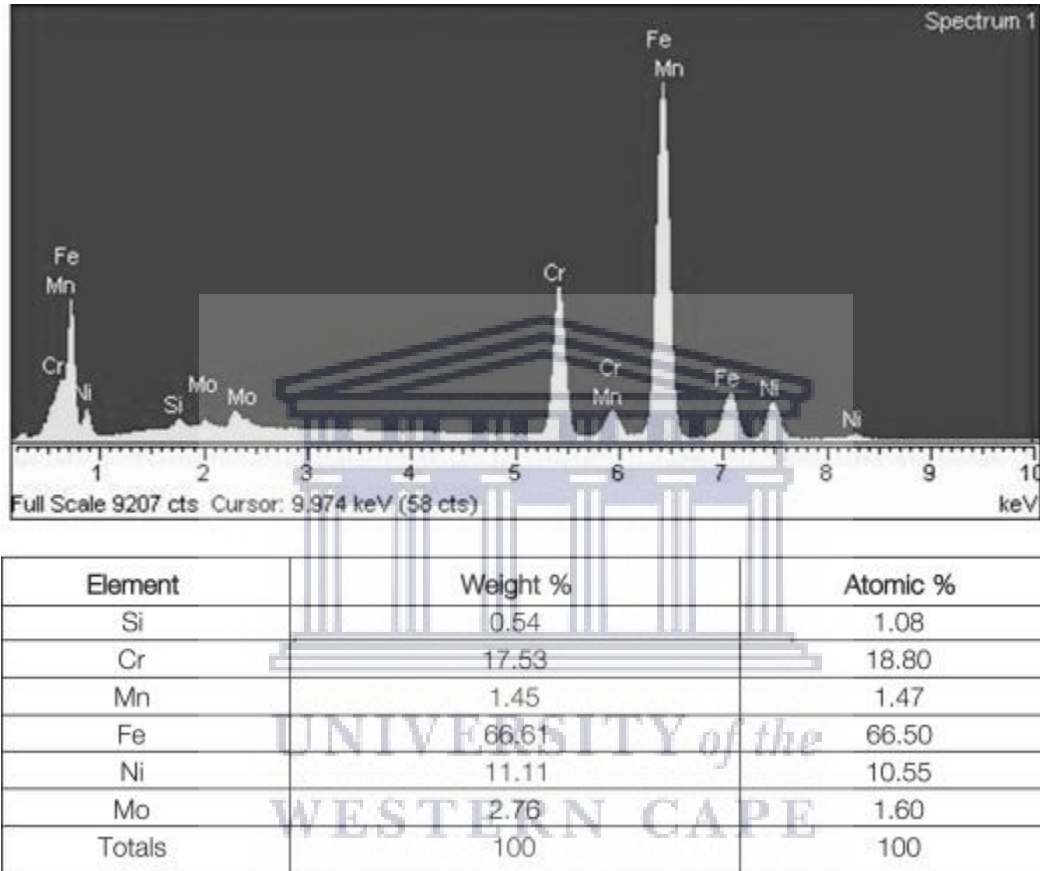


Figure 2. 10: EDS elemental distribution and quantification data [2.38].

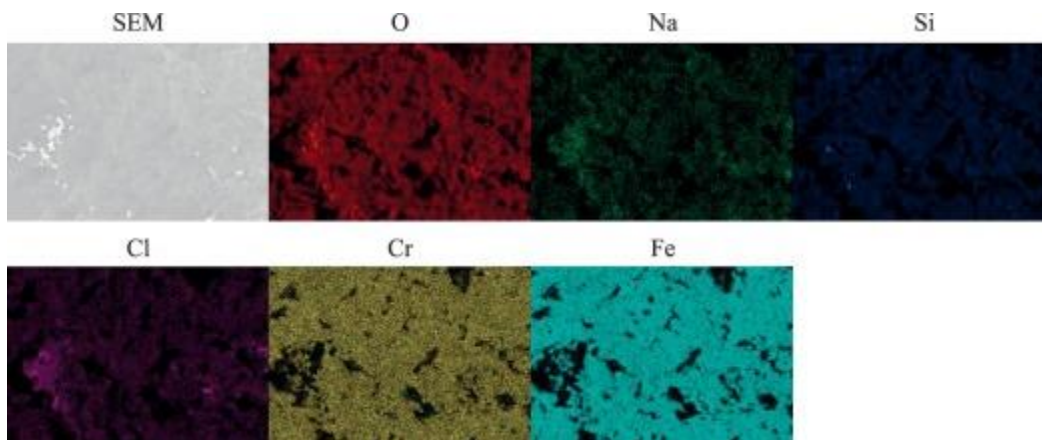


Figure 2.11: Elemental distribution map of NaCl [2.40].

2.2.4.3 Experimental setup

The High-Resolution Scanning Electron Microscopy (HR-SEM) technique was employed to study the morphological and chemical composition properties of the ZnO NPs-seeded ZnO nanoridges structures, coated on indium-tin oxide-coated glass and clear quartz substrates. A Zeiss Auriga emission gun SEM (FEG-SEM) was used to generate electrons for the analysis. The electrons' accelerating voltage was set to 5 kV during operation, and secondary electron images were collected with an in-lens detector. EDS spectra were collected at a high electron tension of 20 kV. All the spectra were collected for 30 seconds using Oxford X-Max solid-state drift detector. The electron images and EDS spectra were obtained in the Electron Microscope Unit at The University of the Western Cape.

2.2.5 Thickness Profilometry

2.2.5.1 Background

Profilometry is a method used to analyse the topographical features on the sample's surface [2.42]. The sample's surface can be scanned by line scan, 3-dimensional scan, or single point scan. The importance of the profilometry technique is to understand the nature of the sample's surface profile, step heights/thickness, and roughness. These results can be achieved by using a physical probe or light as a probe [2.42].

In operation, all profilometers are made up of two parts, i.e. the stage and the detector. During the measurements, the stage can either move with the sample or be fixed as the sample is being scanned. The detector moves in a grid pattern on the sample's surface to determine the topographical features [2.42].

There are two types of profilometry; stylus profilometry and optical profilometry. Stylus profilometry operates by using a probe to raster scan over along the sample's surface to analyse the height of the sample's surface. The feedback loop mechanically monitors the force as a sample function against the probe as the sample is measured [2.42]. The feedback system then uses the arm at a specific value of torque to reconstruct the topography as the Z position of the arm changes. By physically touching the sample and provision of the feedback loop, high Z-resolution is obtained. Stylus profiling is highly sensitive to soft, thin surfaces, and the probe can contaminate the samples. Moreover, samples can also be destroyed in the process through this technique [2.42].

In stylus profilometry, X, Y, and Z positions are considered as the probe is in contact with the sample during scanning. Therefore, in contrast to the non-contact technique, this technique is slower during scanning. Its determination of the lateral resolution can be influenced by the probe tip size and shape [2.42]. Figure 2.12 shows the setup of stylus profilometry.

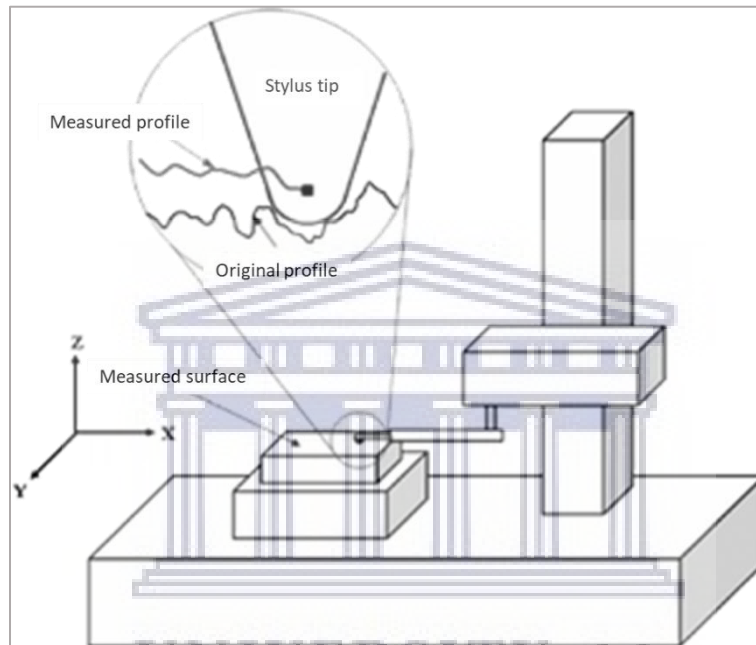


Figure 2. 12: Schematic diagram of a stylus profilometry setup [2.42].

In light profilometry, light is used to penetrate the sample to give off topographical information. Light passes through a beam splitter and is directed onto a sample, detected through a camera, and creates a 3-D image of the surfaces displayed on output. Optical profilometry includes optical interference, confocal aperture, focus, and detection [2.42]. Figure 2.13 shows the setup of the light profilometry- an interferometric profilometer.

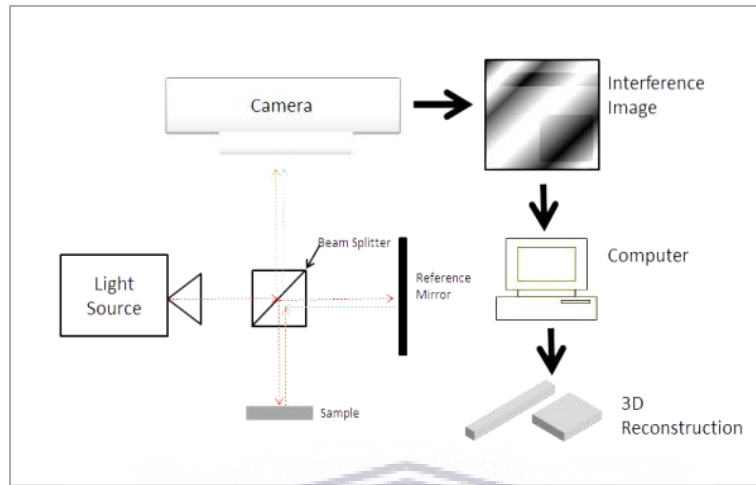


Figure 2. 13: Schematic diagram of an Interferometric profilometer [2.42].

2.2.5.2 Experimental setup

In this study, a 6M Dektak stylus profilometer was used to measure and estimate the surface morphology and thickness of the prepared thin-film samples. The profilometer makes use of a 12.5 μm diamond-tipped stylus, with programmed force ranging from 1-15 N; designated to measure soft to hard surfaces. The measurements were taken in Bellville, at The University of the Western Cape, at the Department of Physics and Astronomy.

2.2.6 Optical Spectroscopy

2.2.6.1 Background

Optical spectroscopy is a technique used to study the interaction between electromagnetic radiation and matter [2.43]. Atoms of molecules can react with incoming light, and they may either scatter or be absorbed [2.43]. Quantitative analysis of this process is usually acquired by recording spectroscopic functions. This technique is used to characterize the electronic structure of material systems that include electromagnetic quantities, electronic emission, absorption, transmission, reflection, and band-gap values due to a limited portion of the spectrum exposure [2.43]. Ultraviolet-visible spectroscopy (UV-Vis) makes use of the wavelength coverage from 200 nm-800 nm.

Optical spectroscopy is a light-based technique, and therefore, a steady monochromatic light source is used to emit light over a wide range of UV-Vis wavelengths. The nature of the instruments requires two different light sources for electromagnetic radiation switchover during measurements. Usually, halogen lamps and a tungsten filament emits visible light, while deuterium lamps are commonly used as the UV light source. During scanning, the electromagnetic wavelength switchover occurs between 300 and 350 nm due to the emission of light occurring similarly at that wavelength for both light sources, thus leading to a smooth transition. As the light is emitted, a specific wavelength of light suited for the sample's optical characterisation is selected from a broad range of emitted wavelengths by using different wavelength selectors. These wavelength selectors include monochromators, absorption filters, and interference filters [2.44].

Monochromators are usually based on diffracting gratings or prisms. They are optical devices that operate as narrow band wavelength filters that can be rotated to adjust the incoming and reflected wavelength. For a typical monochromator, the incoming beam passes through an incoming slit and is directed to the diffracting grating, and gets focused on the output slit [2.44]. Absorption filters commonly absorb a specific wavelength of the electromagnetic spectrum due to their coloured glass or plastic design. Interference filters are wavelength selectors made of several layers of dielectric materials. Interference usually occurs at the interfaces of these layers, and therefore interference filters act as wavelength selectors by causing destructive interference and eliminating unwanted wavelengths [2.44]. Light of the selected wavelength is then directed to the sample and passes through the sample. For all the measurements, a measuring reference sample is usually used as a blank to obtain the accurate measured optical values of the specimen at hand by omitting unwanted absorbed, transmitted, or any other electronic interaction of light and a “blank” [2.45]. As light passes through the sample, the light is directed to the detector. The data acquisition module converts the light into a digitised output for an operator to read on a computer. The mathematical relationship between the pixel position, linear CCD detector, and the wavelength yield an optical spectrum of the whole wavelength range at a single shot strategy [2.46]. Moreover, it is advantageous to utilize a multi-channel spectrophotometer as it yields the resultant optical spectrum at a faster time-scale of microseconds. However, the low measuring accuracy of ~5-8% is one of its drawbacks, leading to inaccuracy in the wave range, therefore, significantly limiting its application [2.46].

Optical spectroscopy is a powerful technique in science and technology, and geochemistry [2.46]. This tool does not only provide absorption spectra; however, it also provides transmittance spectra, diffuse reflectance spectra, etc. [2.46].

2.2.6.2 Absorbance Spectroscopy and Transmittance Spectroscopy

When light is absorbed, it may be redirected or altered in direction, and as light is absorbed, quantum excitation occurs, whereby atoms propagate to higher energy levels [2.47]. Absorption spectroscopy operates on the basis that radiation interacts with gas, solid, or liquid material. As radiation passes through the sample, the molecular excitation energy is recorded. The absorbance of atoms is given by [2.47]:


$$A = \alpha cl, \quad (2.6)$$

where α is the molar absorption coefficient, c is the sample solution's molar concentration, and l is the path length [2.47]. The absorption coefficient determines the amount of light absorbed [2.47]. The ratio of the incident light I to the intensity of the transmitted light (I/I_0) is known as transmittance (T) [2.47], and the absorbance is given by [2.47]:

$$A = -\log T = \log(1/T). \quad (2.7)$$

Furthermore, in semiconducting measurements, when the energy of the incident light is given by E and the energy of the semiconductor is given by E_g , Tauc's formula (equation 2.8) is used to determine the energy band gap from transmittance results given by:

$$\alpha h\nu = A(h\nu - E_g)^n, \quad (2.8)$$

where n is dependent on the nature of the electronic transition (direct or indirect transition), i.e. ½ (allowed) and 3/2 (forbidden) for direct transition and 2 (allowed) and 3 (forbidden) for indirect transition [2.48]. The UV-Vis instrument(s) [2.49] and the schematic diagram of the absorption spectroscopy technique are illustrated in Figure 2.14 (a) and (b), respectively. The transmittance instrumentation setup and the working principle behind transmittance spectroscopy are illustrated in Figure 2.15 (a) and (b), respectively. The effect of UV-Vis radiation absorption on ZnO NPs is studied using the UV-Vis spectroscopy technique, and the transmittance of the radiation on ZnO NPs-seeded ZnO nanoridges was studied using UV-Vis transmission spectroscopy.

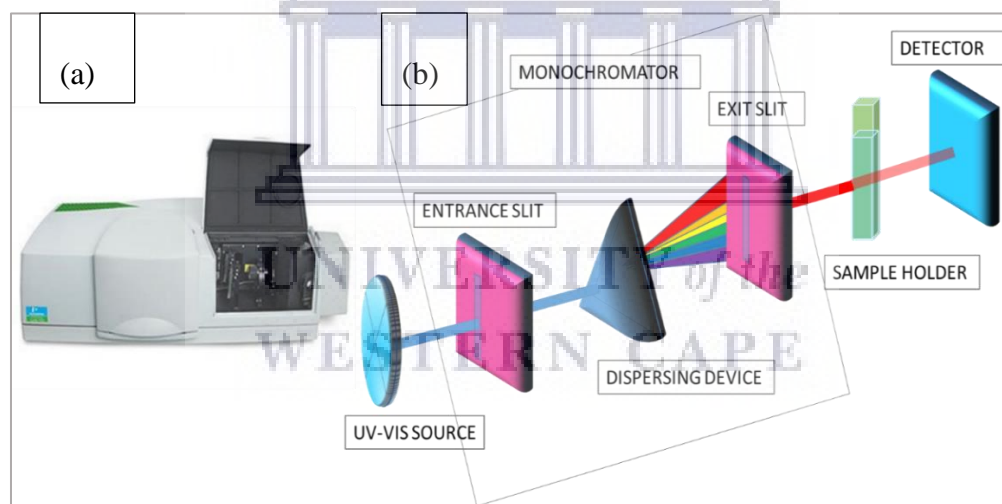


Figure 2. 14: (a) Spectrophotometer [2.49] and (b) Working principle behind UV-vis absorption spectroscopy.

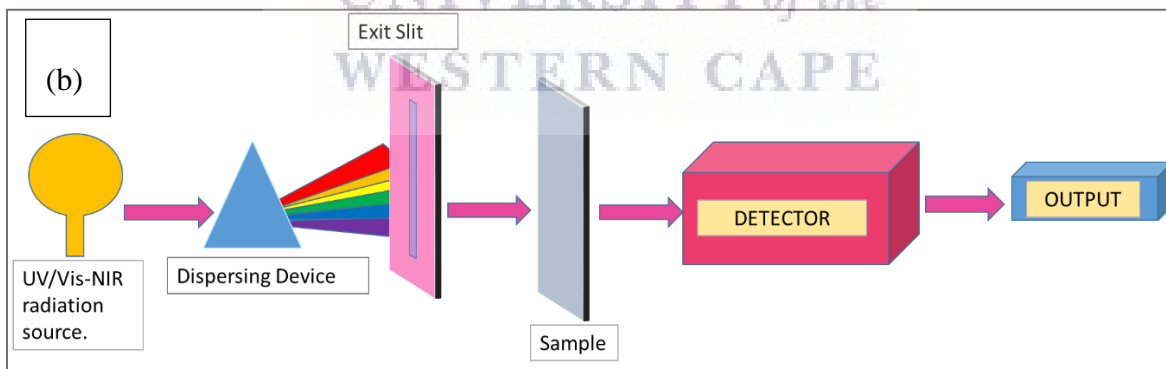
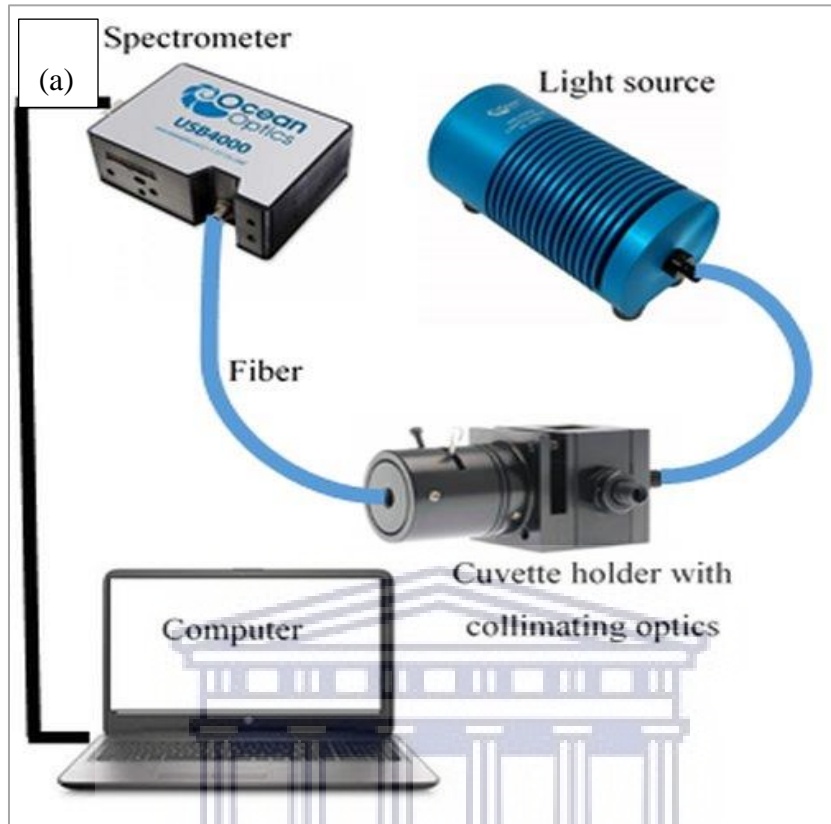


Figure 2. 15: (a) Experimental measurement setup for transmission spectroscopy [2.50] and (b) working principle behind UV-Vis transmittance spectroscopy.

2.2.6.3 Experimental setup

Ultraviolet-visible absorption spectroscopy was employed to study optical properties of ZnO NPs calibrated for 3hrs and 6 hrs at 200°C and at 140°C and 180°C for 6 hrs. ZnO NPs were subjected to ethanol, and their optical properties were measured using a Nicolet Evolution 100 UV-Visible spectrometer (Thermo-electron, UK) in the wavelength range of 250-500 nm. The spectra were collected at Bellville, The University of the Western Cape, Department of Chemical Sciences.

Ultraviolet-visible transmittance spectroscopy was utilized to study the optical properties of the ZnO NPs-ZnO nanoridges calibrated at 3hrs and 6 hrs at 200°C, and at 140°C and 180°C for 6 hrs. The samples were fabricated on clear quartz and ITO glass substrates. The UV-vis transmittance measurements were collected with a Semiconsoft UV-vis spectrometer over a spectral range of 200 nm to 800 nm in Bellville, at The University of the Western Cape, Department of Physics and Astronomy. The spectrometer operates with two independent radiation sources: a UV (deuterium lamp) and a visible (halogen lamp).

2.2.7 Current-Voltage characterization

2.2.7.1 Background

An I-V curve is a graphical representation of the characteristics of a solar cell. The I-V curve is attained as the voltage is applied across an electrical device and as current flows through it. I-V curve representation is a widely used method of determining how a PV device functions in a circuit. The shape and its characteristics give more critical information on the device's

performance under illumination [2.51]. The spectrum of the Sun is approximated to the spectrum of a black body at a temperature of ~ 5780 K. This spectrum shows high spectral irradiance in the visible region and long IR-rays spectral irradiance tail. Due to light-absorbing particles in the atmosphere, only a portion of the electromagnetic radiation passes through the Earth's atmosphere. Therefore, the outside environment may not be favourable for I-V measurements because discrepancies may occur. Therefore, an industrial standard AM 1.5 is used as the spectrum. This industrial standard is an average global solar spectrum as light has passed 1.5 atmospheres. The corresponding power density is 100 mW.cm^{-2} . Therefore, the light of 100 mW.cm^{-2} is simulated in the laboratory for PV I-V characterization purposes [2.52].

The voltage provided for PV I-V measurements may be between -1 V to 1 V. To achieve better characterization analysis, theory on the diode is used as reference. A diode is a semi-conducting device designed to allow current to flow in one direction. A characteristic I-V curve of a diode shows an exponential rise, illustrating a free flow of current through the device. Current remains zero as breakdown voltage is applied, causing the device to be conductive.

In the dark, a solar cell has a behaviour identical to that of an operating diode. However, when light is illuminated onto a PV device, the I-V curve is created and shifts concerning the current/ y-axis. Therefore, this sets the PV device apart as an active device that provides current from

harvesting solar energy to the circuit. Therefore, other properties such as FF and V_{oc} can be extracted from the representative I-V curve [2.52].

The essential characteristic of a PV device is the ability to convert energy to electricity [2.52], also known as power conversion efficiency (PCE). To attain PCE, I-V measurements are performed on PV devices. A domain of voltage is applied to a PV device during illumination. This process yields a characteristic J-V curve. In the current study, current density, J_{sc} is used instead of current (I) due to the area of the cell playing a role in the value of PCE by tuning the magnitude of the output current.

2.2.7.2 Experimental setup

In this study, the electrical properties of inverted organic solar cells were measured using the set-up of IOSCs' I-V testing system illustrated in Figure 2.16 (a) and (b) in Bellville, at The University of the Western Cape, Department of Physics and Astronomy. Dark measurements and measurements under AM 1.5 simulated illumination of 100 mW/m^2 were taken for the fabricated IOSCs. Solar cell area amounted to 0.0256 cm^2 of the individual solar cells of the prepared IOSCs in this study that were measured and analysed.

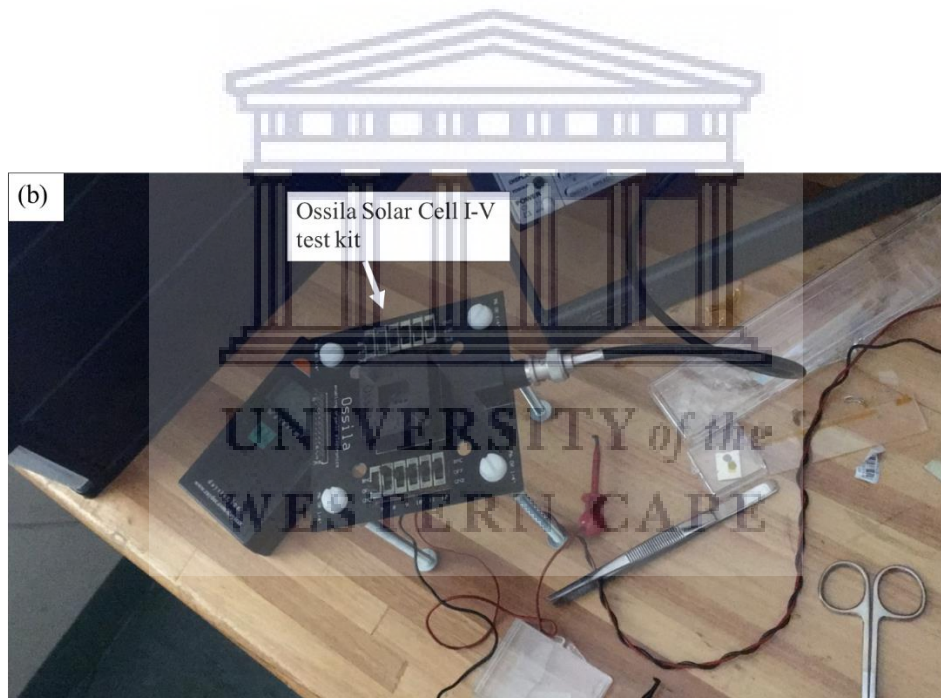
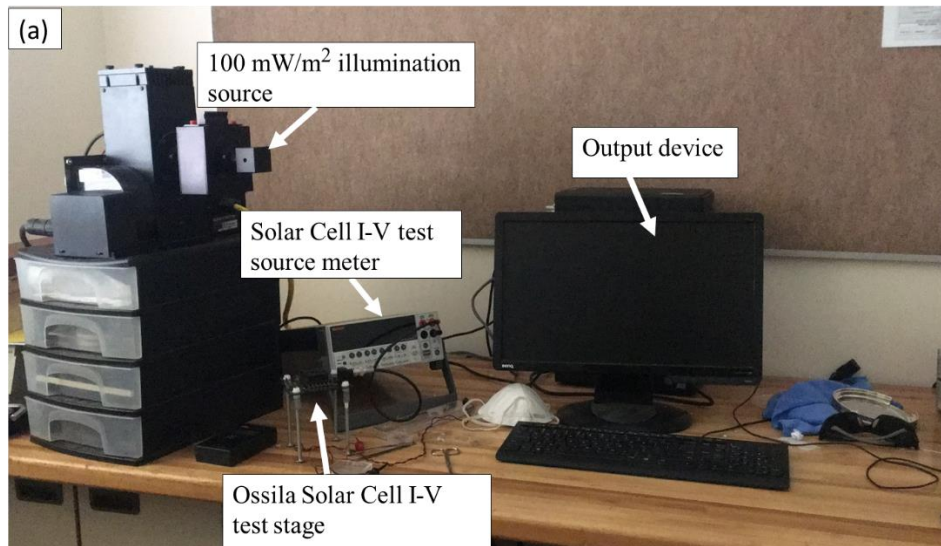


Figure 2. 16: (a) and (b): Solar modules measuring system in the Department of Physics (UWC).

References

- [2.1] A.D. Li and W.C. Liu, "4 - Optical properties of ferroelectric nanocrystal/polymer composites," in *Physical properties and applications of polymer nanocomposites*, Woodhead, 2010, pp. 108-158.
- [2.2] G. Yang and S-J. Park, "Conventional and microwave hydrothermal synthesis and application of functional Materials: A Review," *Materials*, vol. 12, pp. 2-18, 2019.
- [2.3] R. Dorey, "Chapter 2 - Routes to thick films: What is a thick film? How is it made," in *Ceramic thick films for MEMS and microdevices*, William Andrew, 2012, pp. 35-61.
- [2.4] G. Huang, C-H. Lu and H-H. Yang, "Novel nanomaterials for biomedical, environmental and energy applications," in *Chapter 3 - Magnetic nanomaterials for magnetic bioanalysis*, Elsevier, 2019, pp. 89-109.
- [2.5] B.G. Rao, D. Mukherjeer, and B.M. Reddy, "Chapter 1-Novel approaches for preparation of nanoparticles-Sol-Gel Method," in *Nanostructures for Novel Therapy*, Amsterdam, Elsevier, 2017, pp. 1-36.
- [2.6] S. Sakka, "Sol-gel process and application," in *Handbook of Advanced Ceramics (Second Edition)*, Tokyo, Academic Press, 2013, pp. 883-910.

- [2.7] L.M. Mureson, "Corrosion protective coatings for Ti and Ti alloys used for biomedical implants," in *Intelligent coatings for corrosion control*, Elsevier, 2015, pp. 585-602.
- [2.8] B.S Yilbas, A. Al-Sharafi, and H. Ali, "Chapter 3 - surfaces for Self-cleaning," in *Self-cleaning of surfaces and water droplet mobility*, 2019, pp. 45-98.
- [2.9] S.K. Sahoo, B. Monaharan, and N. Sivakumar, "Chapter 1 - Introduction: Why Perovskite and Perovskite Solar Cells?," in *Perovskite Photovoltaics*, 2018, pp. 1-24.
- [2.10] W.R. Birch, "Coatings: An introduction to the cleaning procedures," *The Sol-Gel Gateway*, Avon, 2000.
- [2.11] K. James Jr., "Substrate cleaning for methods for cleaning thin films," *General dynamics/Astronautics San Diego CA*, 1959.
- [2.12] D. Titus, E.J.J. Samuel and S.M. Roopan, "Chapter 12 - Nanoparticle characterization techniques," in *Green Synthesis, Characterization and Applications of Nanoparticles*, Elsevier, 2019, pp. 303-319.
- [2.13] K. Song, "4 - Interphase characterization in rubber nanocomposites," in *Progress in Rubber Nanocomposites*, Woodhead, 2017, pp. 115-152.

- [2.14] P.M. Shameer and P.M. Nishath, "Chapter 8 - Exploration and enhancement on fuel stability of biodiesel: A step forward in the track of global commercialization," in *Advanced Biofuels*, Woodhead, 2019, pp. 181-213.
- [2.15] JASCO Europe, "Measuring microscope IRT-5000/7000 Series," Direct industry by virtualexpogroup, [Online]. Available: <https://www.directindustry.com/prod/jasco-europe/product-30625-1561461.html>. [Accessed 21 September 2020].
- [2.16] N. Robotti, The discovery of X-ray diffraction, Springerlink, 2012.
- [2.17] K. Nygren, "Solar cells based on synthesized nanocrystalline ZnO thin films sensitized by chlorophyll a and photopigments isolated from spinach," *Materials Science*, no. 5, pp. 1-42, 2010.
- [2.18] N. Raval, R. Maheshwari, D. Kalyane, S.R. Yongren-Ortiz, M.B. Chougule, and R.K. Takade, "Importance of physicochemical characterization of nanoparticles in pharmaceutical product development," in *Basic fundamentals of drug delivery*, Academic Press, 2019, pp. 639-400.
- [2.19] F. Hoffmann, Introduction to Crystallography, Switzerland AG: Springer, Cham, 2020.

- [2.20] Heryanto, B. Abdullah, D. Tahir, and Mahdalia, "Quantitative analysis of X-Ray diffraction spectra for determine structural properties and deformation energy of Al, Cu and Si," *Journal of Physics: Conference Series*, vol. 1317, no. 1/012052, pp. 1742-6596, 2019.
- [2.21] P. Kathiresan, "CRYSTALLOGRAPHY AND MINERALOGY - Paper Code MTIGT0306," *6 Year Integrated M.Tech. Geological Technology and Geoinformatics being offered in CENTRE FOR REMOTE SENSING*, pp. 2-16, 2018.
- [2.22] R. Venugopalan and P. Purohit, "Polymorphism: An Overview," *RESONANCE*, vol. 14, no. 9, pp. 882-893, 2009.
- [2.23] T. Stachel and J.W. Harris, "Formation of diamond in the Earth's mantle," *Journal of Physics: Condensed Matter*, vol. 21, no. 36, p. 364206, 2009.
- [2.24] J. Keeling, "Graphite: properties, uses and South Australian resources," *Geological Survey of South Australia, Department of the Premier and Cabinet*, vol. 84, no. 3, pp. 28-33, 2017.
- [2.25] V.D. Mote, Y. Purushotham and B.N. Dole, "Williamson-Hall analysis in estimation of lattice strain in nanometer-sized ZnO particles," *Journal of theoretical and applied physics*, vol. 6, no. 6, pp. 1-8, 2012.

[2.26] M. Rabiei, A. Palevicius, A. Monshi, and S. Nasiri , "Comparing Methods for Calculating Nano Crystal Size of Natural Hydroxyapatite Using X-Ray Diffraction," *Nanomaterials*, vol. 10, pp. 1-21, 2020.

[2.27] B.L. Dutrow and C.M. Clark, "X-ray Powder Diffraction (XRD)," *Geochemical Instrumentation and Analysis*, [Online]. Available: https://serc.carleton.edu/research_education/geochemsheets/techniques/XRD.html. [Accessed 21 September 2020].

[2.28] M.S. Bobji, N. Kumar, U. Mukherjee, and D.S. Dewangan, "Transmission Electron Microscope," in *Material characterization technique*, pp. 3-13.

[2.29] Topic: Who inventes SOIC16? (Read 5245 times), "Who inventes SOIC16?," *EEVblog Electronics Community Forum*, 02 June 2018. [Online]. Available: <https://www.eevblog.com/forum/beginners/who-inventes-soic16/25/>. [Accessed 21 September 2020].

[2.30] R. Li, Z. Li, Z. Dong, and K.A. Khor, "A Review of Transmission Electron Microscopy of Quasicrystals—How Are Atoms Arranged?," *Crystals*, vol. 105, no. 6, pp. 1-6, 2016.

- [2.31] T. Sabu, T. Raju, K.Z. Ajesh, and K.K. Raghvendra, "A volume in Micro and Nano Technologies," in *Microscopy Methods in Nanomaterials Characterization*, Elsevier, 2017, pp. 109-112.
- [2.32] K.D. Vernon-Parry, "TEM: an introduction," *Review*, vol. 13, no. 6, pp. 36-40, 2000.
- [2.33] L. Reimer, "Electron Diffraction Methods," *Scanning*, vol. 2, no. 1, pp. 1-17, 1979.
- [2.34] S. Swapp, "Scanning electron microscope (SEM)," *Geochemical Instrumentation and Analysis*, 2004. [Online]. Available: https://serc.carleton.edu/research_education/geochemsheets/techniques/SEM.html. [Accessed 25 April 2020].
- [2.35] Nanoscience Instruments, "Scanning Electron Microscope," Nanoscience Instruments, Phoenix.
- [2.36] A. Mohammed, A. Abdullah, "Scanning Electron Microscopy (SEM): A Review," *Proceedings of 2018 International Conference on Hydraulics and Pneumatics - HERVEX*, vol. 7, no. 9, pp. 1-8, 15 11 2018.

- [2.37] L.K Herrera , S. Le Borgne and H.A Videla, "Scanning electron microscopy (SEM), environmental scanning electron microscope (ESEM), and energy dispersion x ray (EDX) analysis," in *Modern methods for materials characterization and surface analysis to study the effects of biodeterioration and weathering on buildings of cultural heritage*, Taylor & Francis Group, 2008, pp. 2-3.
- [2.38] W.J Wolfgong, "Chemical analysis techniques for failure analysis," in *Handbook of Materials Failure Analysis with Case Studies from the Aerospace and Automotive Industries*, Elsevier, 2016.
- [2.39] Y. Harada, Y. Ikuhara, "The latest analytical electron microscope and its application to ceramics," in *Handbook of Advanced Ceramics (Second Edition)*, Tokyo, Institute of Engineering Innovation, 2013.
- [2.40] S. Nasrazadani, S. Hassani, "Chapter 2-Modern analytical techniques in failure analysis of aerospace, chemical, and oil and gas industries," in *Handbook of Materials Failure Analysis with Case Studies from the Oil and Gas Industry*, Texas, Butterworth-Heinemann, 2016, pp. 39-54.

- [2.41] R.K.M. Sendi, "Influence of Zinc Oxide particle size and surface properties on the electrical, optical and cytotoxicity characteristics of zinc oxide discs," Universiti Sains Malaysia, 2015.
- [2.42] J.W. Haus, "6 - Nanocharacterization," in *Fundamentals and Applications of Nanophotonics*, Dayton, Woodhead Publishing, 2016, pp. 185-210.
- [2.43] W.S Choi, S.S.A. Seo, and H.N. Lee, "Optoelectronics: optical properties and electronic structures of complex metal oxides," in *Growth of complex metal oxides*, Seoul, Woodhead, 2015, pp. 331-363.
- [2.44] J. Rietdorf and E.H.K. Stelzer, "Special Optical Elements," in *Handbook of Biological Confocal Microscopy*, New York, Springer Science+Business Media, LLC, 2006, pp. 43-55.
- [2.45] S.P.S. Shabudeen, "6.1-Analytical Techniques," in *Basic Spectroscopy*, 2014, pp. 1-46.
- [2.46] S-H. Wang, S-J. Liu, W-W. Wang and Z-G. Zhang, "Fast and high-accuracy measuring technique for transmittance spectrum in UV-Vis-NIR," *Spectroscopy and spectral analysis*, pp. 1-14, 2018.

- [2.47] V. Sudarsan, "8 - Optical Materials: Fundamentals and Applications-Preparation, Processing and Applications," in *Functional Materials, Preparation, Processing and Applications*, Elsevier, 2012, pp. 285-322.
- [2.48] B.D. Vierzicke, S. Pate, E.B. Davis, and D.P. Birnie, "Evaluation of the Tauc Method for Optical Absorption Edge Determination: ZnO Thin Films as a Model System," *Physica Status Solidi*, vol. 252, pp. 1700-1710, 2015.
- [2.49] PerkinElmer, "LAMBDA 850+ UV/Vis Spectrophotometer," PerkinELmer, [Online]. Available: <https://www.perkinelmer.com/product/lambda-850-uv-vis-spectrophotometer-1850>. [Accessed 21 September 2020].
- [2.50] A. Shahin and W. Bachir, "Broadband spectroscopy for characterization of tissue-like phantom optical properties," *Polish Journal of Medical Physics and Engineering*, vol. 23, no. 4, pp. 121-126, 2017.
- [2.51] A. Devasia and S.K. Kurinec, "Teaching solar cell I-V characteristics using SPICE," *American Journal of Physics* 79(12):1232-1239, vol. 79, no. 12, pp. 1232-1239, 2011.

- [2.52] M.H. El-Ahmar, A-H.M. El-Sayed, and A.M. Hemeida, "Mathematical modeling of Photovoltaic module and evaluate the effect of various parameters on its performance," *Conference Precedings*, pp. 1-6, 2016.





Chapter 3: ZnO nanoparticles Synthesis and
Characterisation

UNIVERSITY *of the*
WESTERN CAPE

Chapter 3: ZnO nanoparticles Synthesis and Characterisation

Introduction

Low-temperature synthesis techniques for NPs have gained increased attention. They have become the primary synthesis technique for many nanopowders, delivering high yields at a low controllable temperature [3.1]. Hydrothermal synthesis is one of the commonly used techniques to fabricate nanomaterials [3.2]. It has been adopted by a vast majority of material science researchers because of various distinct advantages such as low cost and less complex preparation conditions [3.3]. The hydrothermal method is an environmentally friendly technique that provides the ability to tune the properties of the nanoparticles. Properties such as shape and size to suit various respective applications. Mainly, the morphology of nanoparticles depends on the synthesis temperature, reacting solution concentration, and synthesis period. Therefore, this may alter the chemical, optical and physical properties of the nanoparticles.

Particles are best suited for various applications based on their morphology. This study outlines the analysis of the effect of reaction conditions on the structural, optical, and morphological properties of ZnO NPs. The ZnO NPs were incorporated at a later stage of the study to facilitate the growth of the ZnO-based nanoridges (NRs). Finally, the effect of ZnO NPs' reaction conditions is further analysed upon utilisation of the ZnO NPs: ZnO nanoridges as ETLs in IOSCs for performance investigation [3.3].

In this work, the hydrothermal reaction period conditions were set to 200°C for 3 hrs and 6 hrs, and the temperature conditions were set at 140°C and 180°C for 6 hrs. The pH is set to ~10-12

because all the other conditions need to be set constant so as not to interfere with the experimental conditions of interest studied. In nanoscience, the change in the morphology of the nanoparticles due to different experimental conditions when synthesised affects the optical and structural properties immensely [3.4]. Therefore, it is imperative to consider tuning the reaction parameters for improved nanostructure to advance the IOSC performance.

3.1 Synthesis of ZnO Nanoparticles by Hydrothermal Method

In this study, all reagents were analytically pure and used without further purification. To synthesise ZnO NPs, a stock solution of 2M zinc acetate dihydrate (99.99% purity) was prepared in 50 ml methanol while stirring. To the stirring stock solution, 0.5M sodium hydroxide solution prepared in 15 ml methanol was added. The solution was left to stir for 30 minutes. As the solution reached a pH of ~10-12, it was removed and transferred to a Teflon-lined sealed stainless steel autoclave at 200°C for 3 hrs, and 6 hrs and at 140°C and 180°C for 6 hrs, respectively. These conditions represent two individual sets of experiments, series one: period variation and series 2: temperature variation. The reaction equations for the hydrothermal synthesis of ZnO NPs is illustrated in equations (3.1) and (3.2). The resultant white solids were removed post-reaction completion. The solids were washed with ethanol and deionised water through centrifugation at 12 000 rpm for 10 minutes. The washing steps were repeated ten times to remove impurities. The washed products were left to dry in the oven at 60°C overnight and packaged in vials. The ZnO NPs were synthesized to obtain the optimal nanoparticles that can improve the morphological,

topographical, chemical, and optical properties of ZnO nanoridges and also improve the performance of IOSCs.

Figure 3.1 is a schematic diagram that summarises the processing steps and shows further details on the hydrothermal reaction followed to synthesise the ZnO NPs in this study.

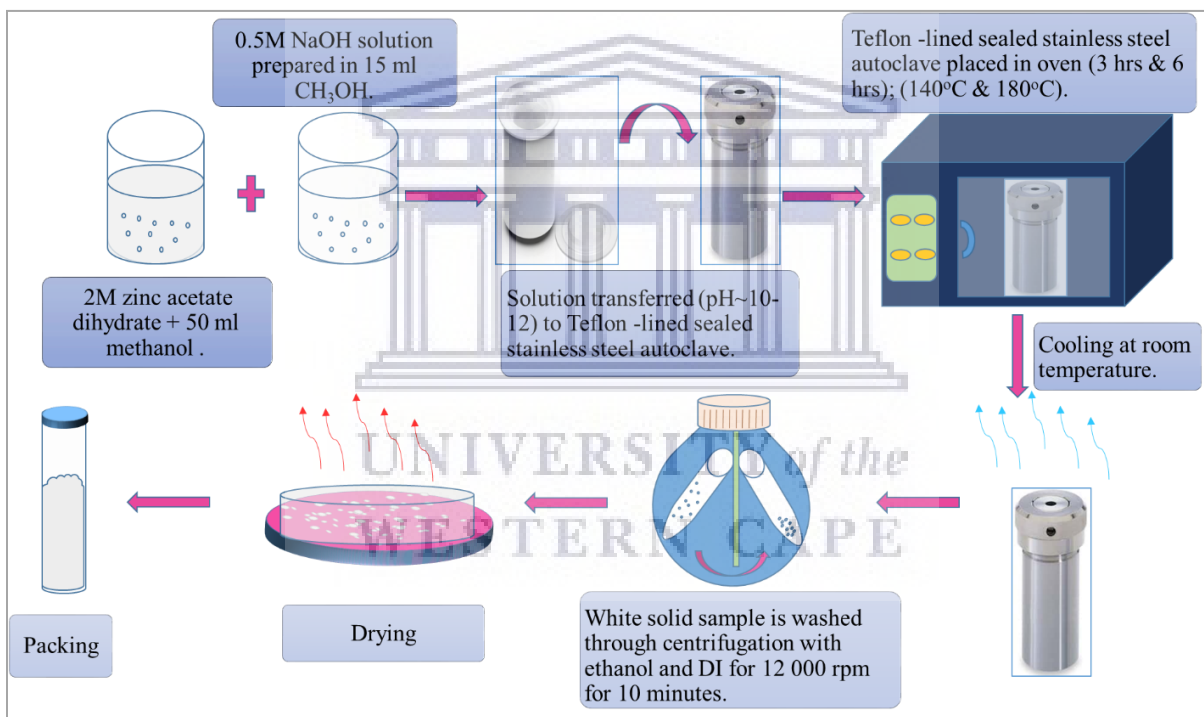
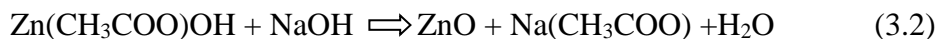


Figure 3. 1: Hydrothermal synthesis of ZnO NPs calibrated at 200°C for 3 hrs and 6 hrs and calibrated at 140°C and 180°C for 6 hrs.

The reaction period is the time required for reducing precursor elements as the formation of nanoparticles due to synthesis reaction completion occurs. It has been reported that nanoparticle production is attained within minutes of the synthesis period of the reaction of metal salt precursors [3.5]. As the reaction period was increased, the nanoparticles' yield increased, and the nanoparticles' size decreased [3.5]. Furthermore, it has been reported that the synthesis process of ZnO NPs bears nearly spherically shaped NPs [3.6]. Therefore it is essential to acquire ZnO NPs of high purity and various morphologies, and one kind of particle shape. Temperature variation on the synthesis of ZnO NPs has been reported to affect the morphology and purity of ZnO NPs [3.7]. In this present study, the effect of synthesis period and temperature on ZnO NPs to attain an optimal ZnO NPs sample is investigated to obtain highly undulated nanoridges of increased surface area that in turn may increase light absorption when integrated as an electron transport layer in inverted organic solar cells. For this study, to attain an understanding of the effects of period and temperature conditions on the chemical, physical and optical properties of the ZnO nanoridges that may increase the surface area and light absorption in ETL application.

3.2 ZnO Nanoparticles Characterization

FTIR was used to identify various functional groups present in ZnO NPs. The products of hydrothermal synthesis were measured using a Perkin-Elmer Spectrum 100 FTIR spectrometer. The samples were subjected to KBr powder, and the combination was converted to a pellet. The compressed pellets were analysed in the IR range of 400-4000 cm^{-1} . A Bruker D8-advanced-8-X-ray powder diffractometer with $\text{CuK}\alpha$ radiation ($\lambda=1.54050 \text{ \AA}$) was employed to study the

crystallinity and crystal phase of ZnO NPs. The accelerating voltage and applied current were set to 40 kV and 40 mA at room temperature, respectively. The Bragg angle ranges from 25° to 85° with a typical step size of 0.034°. An FEI Tecnai G2 20 field-emission gun (FEG) High-resolution transmission electron microscope (HRTEM) operating in bright field mode at an accelerating voltage of 20 kV was employed to study the crystallinity, size, and morphological properties of ZnO NPs. The TEM specimen measurements were done by depositing a drop of ZnO powder in ethanol solution on a 400 mesh copper grid coated by an amorphous carbon film. The solution on the 400 mesh copper grid was left to evaporate in the air at room temperature. Ultraviolet-visible spectroscopy was employed to study the optical properties of ZnO NPs calibrated for reaction time at 3 hrs and 6 hrs at 200°C and temperature of 140°C-180°C for 6 hrs. ZnO NPs were subjected to ethanol, and their optical properties were measured using a Nicolet Evolution 100 UV-Visible spectrometer (Thermo-electron, UK) in the wavelength range of 250-500 nm.

3.3 Results and discussion

3.3.1 Chemical analysis of ZnO Nanoparticles

FTIR has been an excellent technique for the chemical analysis of material in laboratories for the past seven decades. FTIR provides qualitative information about a material's identity, the amount of components in a mixture, and the quality of a sample [3.8]. An FTIR spectrum provides a sample fingerprint with transmittance bands corresponding to the frequencies of vibrations between bonds in a molecule or compound. Due to each material's unique combination of atoms, no two

molecules or compounds may produce the same FTIR spectrum [3.8]. Moreover, the amount of the material present in the mixture is measured by the size of the bands.

In this study, the FTIR spectra of ZnO NPs hydrothermally synthesised for 3 hrs and 6 hrs at 200°C and 140°C and 180°C for 6 hrs were recorded in the range ~400-4000 cm⁻¹. All the FTIR spectra in Figure 3.2 and Figure 3.3 show the characteristic vibrational modes of ZnO [3.7, 3.8]. Tables 3.1 and 3.2 summarise the functional groups present of particles in the samples.

3.3.1.1 FTIR analysis of ZnO Nanoparticles under period calibration

Figure 3.2 shows the FTIR spectra of ZnO NPs hydrothermally synthesised for 3 hrs and 6 hrs at 200°C. From the spectra, significant vibrational bands range from ~400 cm⁻¹-595 cm⁻¹, corresponding to Zn-O stretching modes [3.9, 3.10]. The intensity of the band decrease due to the variation in time series. The bands at ~1250-1650 cm⁻¹ are assigned to the Zn-OH vibration mode. The bands at ~3250-3550 cm⁻¹ are assigned to the O-H vibration mode [3.9, 3.10]. The Zn-OH and O-H modes indicate the presence of a hydroxide group due to the pH of the environment [3.11].

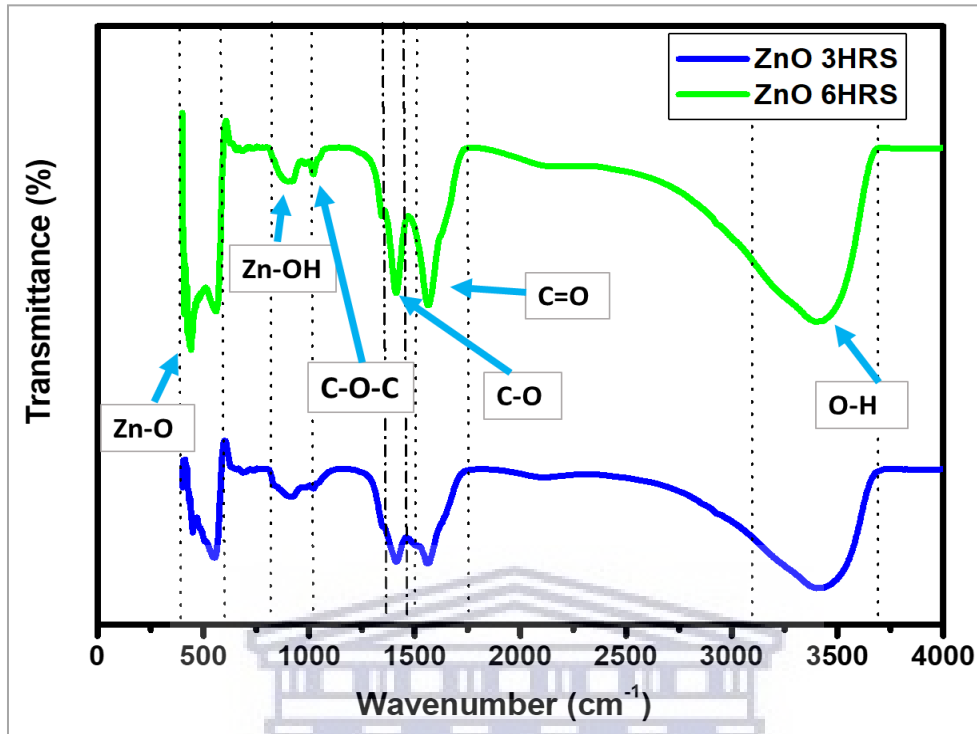


Figure 3. 2: FTIR spectra of ZnO NPs calibrated at 3 hrs and 6 hrs at 200°C, respectively.

The Zn-O band ranges from $401\text{-}575\text{ cm}^{-1}$ to $435\text{-}578\text{ cm}^{-1}$; this shift is attributed to the conversion of Zn(OH)_2 to ZnO shown in Table 3.1. Previously reported results by S.S. Alias et al., [3.4] have revealed a Zn-O band ranging from $453\text{ to }550\text{ cm}^{-1}$ [3.4]. In this study, the ZnO bands of ZnO NPs produced at 3 hrs and 6 hrs show an increase in the wavenumber with the increasing synthesis period. The shift indicates the completion of the NaOH reaction with the $\text{Zn(CH}_3\text{COO)}_2 \cdot 2\text{H}_2\text{O}$ [3.4]. The shift in the Zn-O FTIR wavenumber is attributed to the change in the particle size. Therefore the effect of the particle size change on the FTIR wavenumber is further analysed by XRD and TEM technique because they provide information about the particle size the particles possess and the possible defects that may attribute to the shift in FTIR.

Table 3. 1: FTIR of ZnO NPs at various synthesis time intervals.

Period	Wavenumber (cm ⁻¹)	Functional group
3 hrs	3191-3680	O-H
	1356-1456,1472-1733	C-O, C=O
	1024	C-O-C
	791-1016	Zn-OH
	410-592	Zn-O
6 hrs	3099-3697	O-H
	1356-1464,1500-1720	C-O, C=O
	1024	C-O-C

Period	Wavenumber (cm ⁻¹)	Functional group
	833-958	Zn-OH
	435-578	Zn-O

3.3.1.2 FTIR analysis of ZnO Nanoparticles under temperature calibration

Figure 3.3 shows the FTIR spectra of ZnO NPs synthesized at various temperature values, recorded in the range 400-4000 cm⁻¹. The bands at 3041-3697 cm⁻¹ correspond to the O-H mode of vibration [3.12]. The narrow O-H peaks become broader with an increase in the temperature value due to the additional O-H present from the NaOH and Zn(CH₃COO)₂·2H₂O at pH of ~12 and from 180°C synthesis temperature. The strong asymmetric stretching mode of vibration of C=O was observed, ranging from 1506-1720 cm⁻¹ [3.4]. The symmetric stretching observed between 1453 and 1333 cm⁻¹ is assigned to the C-O band.

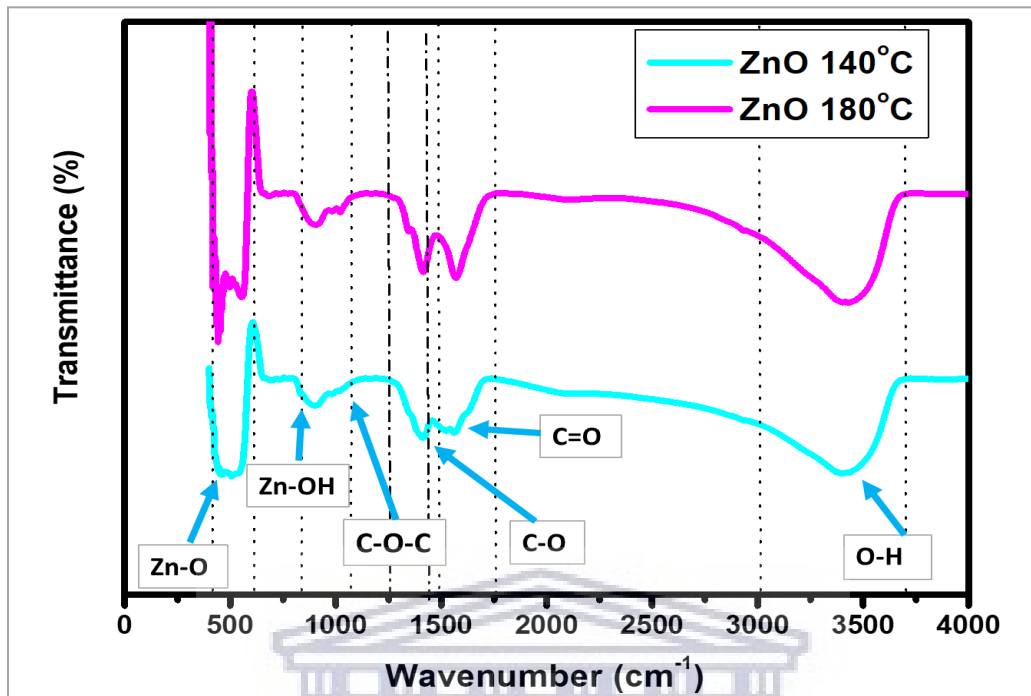


Figure 3. 3: FTIR spectra of ZnO calibrated at 140°C and 180°C for 6 hrs, respectively.

Table 3.2 illustrate the FTIR analysis of ZnO NPs at various temperature values. The diverging morphological properties in alkaline conditions cause the C-O bands to shift inconsistently with the change in the temperature [3.4]. The C–O–C band resonates at 1024 cm^{-1} and is absent at 140°C. This suggests that the chemical reaction of ZnO at 140°C had not been completed compared to ZnO at 180°C. The presence of other bands besides Zn-O and O–H; the C=O, C–O, and C–O–C bands are evident and are attributed to the presence of $\text{Zn}(\text{CH}_3\text{COO})_2 \cdot 2\text{H}_2\text{O}$ precursor. CH_3OH solvent effects on the synthesized ZnO powders are negligible because methanol mainly acts as a facilitating agent for the solvation of zinc and acetate ions [3.13]. The FTIR analysis results in Figure 3.3 above and Table 3.2 below proved this concept because there is an observed shift in

the wavenumber of the carbon-based bands; however, the change leaves the Zn-O bands unaffected. These three functional groups' wavenumbers slightly change with increasing temperature values confirming different ZnO precipitation rates that support the additional ZnO yield that different temperature values produced with stoichiometric composition. XRD and TEM techniques are further utilised to analyse the interaction of the observed FTIR bands in sections 3.3.2 and 3.3.3, respectively.

Table 3. 2: FTIR of ZnO NPs at various temperature values.

Temperature	Wavenumber (cm ⁻¹)	Functional group
140°C	3141-3680	O-H
	1323-1430, 1430-1721	C-O, C=O
	-	C-O-C
	808-983	Zn-OH
	418-582	Zn-O

Temperature	Wavenumber (cm ⁻¹)	Functional group
180°C	3133-3664	O-H
	1348-1456,1489-1713	C-O, C=O
	1024	C-O-C
	817-999	Zn-OH
	401-575	Zn-O



3.3.2 Structural analysis of ZnO Nanoparticles

The XRD patterns of hydrothermally synthesised ZnO nanoparticles at varying reaction times and temperature values are illustrated in Figures 3.4 and Figure 3.7 respectively.

The diffraction peaks have been indexed as the hexagonal wurtzite phase of ZnO [3.14] with theoretical values of lattice constants $a=b= 0.324$ nm and $c= 0.521$ nm (JPCDS card number: 36-1451) [3.14]. The crystallite size of the synthesized ZnO nanoparticles was calculated using the Debye-Scherrer formula (3.3) [3.14]:

$$D = \frac{k\lambda}{\beta \cos\theta} \quad (3.3)$$

where D is the crystallite size, k is the Scherrer's constant, equal to 0.89 for spherical particles, λ is the wavelength of the type of X-rays used, θ is the Bragg diffraction angle, and β is the full width at half-maximum (FWHM) of the diffraction peak corresponding to the planes.

Williamson-Hall analysis was used to evaluate the XRD pattern broadening. The lattice strain found in the nanoparticles causes peak broadening and is represented by equation (3.4). The lattice strain due to crystal defect and deformation is evaluated using equation (3.5):

$$\beta_{strain} = 4\epsilon \tan\theta. \quad (3.4)$$

$$\epsilon = \frac{\beta_{hkl}}{4 \tan\theta}. \quad (3.5)$$

Usually, a standard material that has sharp peaks and high crystallinity is utilised to subtract instrumental effects. The diffraction peak width β can be obtained as the crystallite size width and the lattice strain width summed up together, giving

$$\beta_{hkl} = \beta_{crystallite} + \beta_{strain}. \quad (3.6)$$

Therefore substituting (3.4) and (3.5) in (3.6), we obtain

$$\beta_{hkl} \cos\theta = \frac{k\lambda}{D} + 4\epsilon \sin\theta. \quad (3.7)$$

Equation 3.7 is the W-H equation representing uniform deformation model (UDM) analysis and a plot of $4\epsilon \sin\theta$ on the x-axis and $\beta \cos\theta$ along the y-axis representing a linear fit data. Therefore, the crystallite size may be measured/estimated from the y-intercept, and the strain may be estimated from the slope of the linear fit data [3.15].

3.3.2.1 XRD analysis of ZnO Nanoparticles produced under period variation

3.3.2.1.1 Structural analysis

Figure 3.4 represents the X-ray diffraction patterns of ZnO nanopowder produced for 3 hrs and 6 hrs at 200°C, respectively. From these XRD patterns analysis, position and width, full-width at half-maximum (FWHM) data of the peaks were determined. The diffraction peaks were located at 31.84°, 34.52°, 36.33°, 47.63°, 56.71°, 62.96°, 68.13°, and 69.18°. The peaks have been indexed as those of the hexagonal wurtzite phase of ZnO [3.14]. The corresponding diffraction peaks to the planes are <100>, <002>, <101>, <102>, <110>, <103>, <200>, <112>, <201>, <004>, <202>, and <104>. The average crystallite sizes by Scherrer and UDM methods of the samples were found to range at 21.6 nm and from 41.1-49.0 nm for ZnO NPs prepared at 3 hrs and 6 hrs, respectively. The average crystallite size was derived from the FWHM of more intense peaks corresponding to <101> planes located at ~ 36.38° using Scherrer's formula.

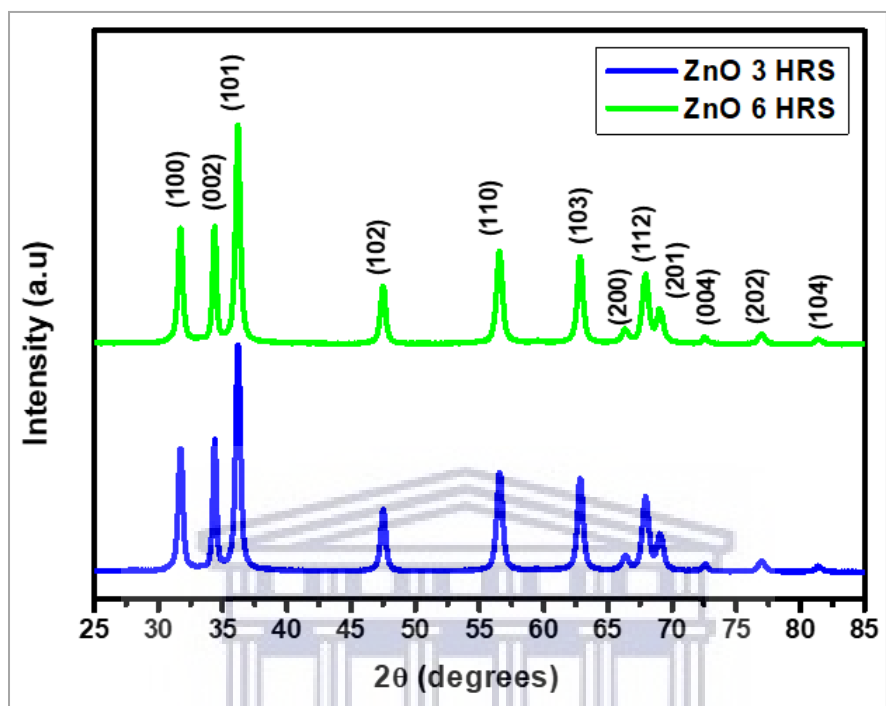


Figure 3. 4: XRD pattern of ZnO NPs synthesised for 3 hrs and 6 hrs at 200°C, respectively.

3.3.2.1.2 Williamson-Hall analysis

Figure 3.5 illustrates the $\langle 101 \rangle$ peaks utilised to analyse XRD pattern broadening. In the XRD pattern (Figure 3.5), the growth is along the $[101]$ axis with an increase and decrease in the lattice parameters c and a respectively [3.16]. Figure 3.5 confirms the presence of crystalline nanoparticles in the two samples as the $\langle 101 \rangle$ peak is very sharp. As the synthesis period change, the lattice parameters change, indicating the exchange of Zn and O atoms' positions at the (101) plane [3.16]. The change in the minor strain may have caused changes in the crystal structures of

ZnO at 6 hrs from 3 hrs. These changes are not visible from the XRD peaks of these samples. However, HRTEM will further translate the crystallographic properties that may have been invisible for analysis under XRD.

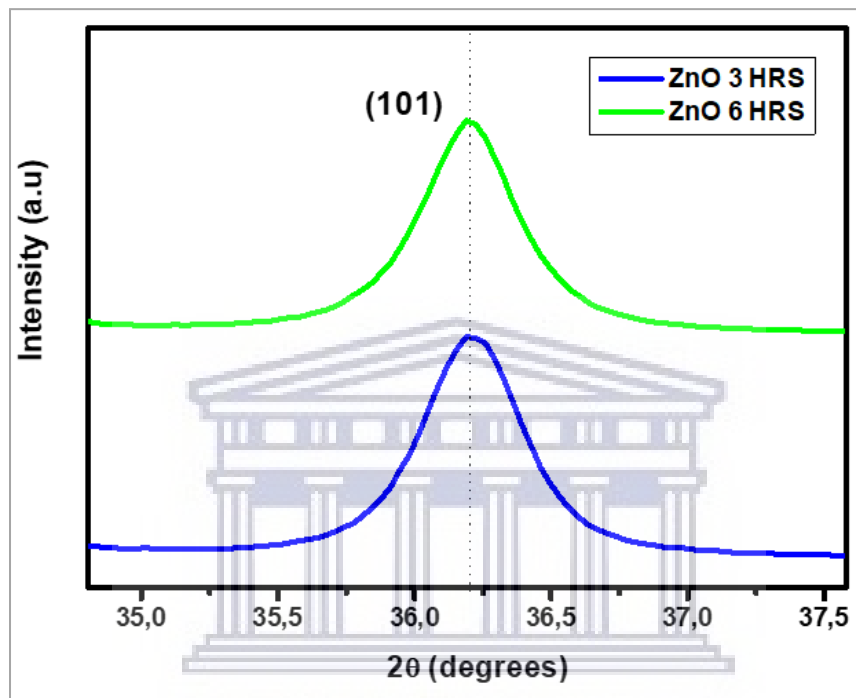


Figure 3. 5: Intensity versus 2θ around (101) peaks of ZnO NPs synthesised for 3 and 6 hrs at 200°C , respectively.

Figure 3.6 shows W-H models of ZnO prepared for 3 hrs and 6 hrs at 200°C , respectively. Table 3.3 illustrates the crystallite size and strain extracted from W-H models in Figure 3.6. Due to the subtraction of the instrumental effects, the crystallite size range has drastically changed from 21.6 nm by the Scherrer method to 41.1-49.0 nm by the UDM method [3.16]. The effects of the instrument account for the discrepancies in the crystallite size. Therefore, the crystallographic

features are further analysed and discussed in TEM analysis; to further assist in understanding the observable crystallographic properties of ZnO NPs in detail. The lattice strain and crystallite size values of ZnO NPs prepared for 3 hrs and 6 hrs at 200°C by UDM analysis is illustrated in Table 3.3. The strain values have a positive slope (Figure 3.6). The positive slope indicates that the synthesis period calibration of the sample leads to an expansion of the ZnO crystal structure during calcination. The change in strain affects the lattice parameters, and this change (illustrated in Table 3.3) may be due to the threading dislocations within the structure [3.16].

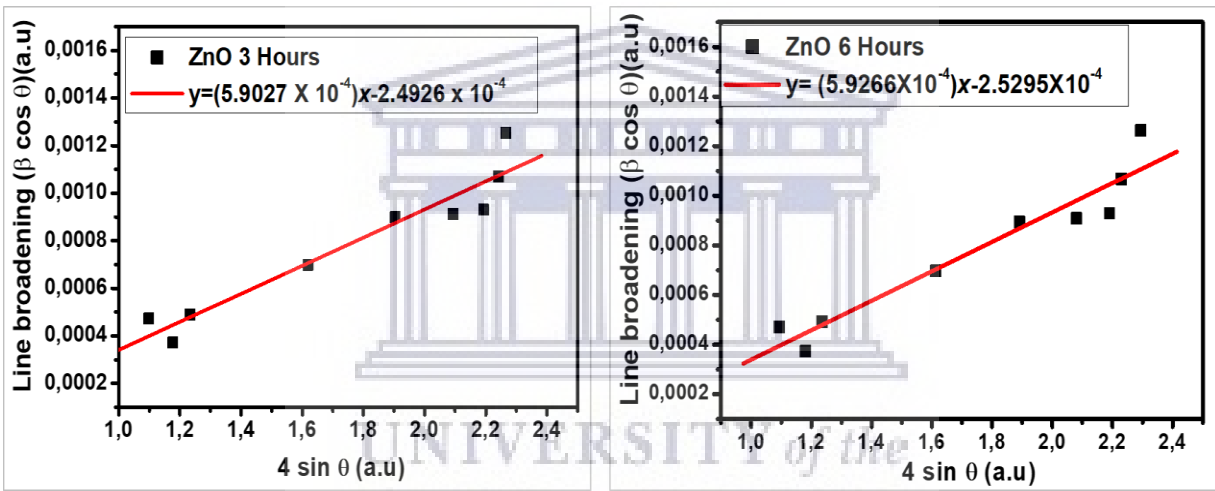


Figure 3. 6: W-H models of ZnO NPs prepared for 3 hrs and 6 hrs at 200°C, respectively.

Table 3. 3: Calculated crystallite size and microstrain for ZnO NPs prepared at 200°C 3 hrs and 6 hrs at 200°C, respectively.

Sample	Lattice parameters (Å)		D (nm)		Lattice Strain
	a	c	(Scherrer method)	(UDM)	
ZnO (3 hrs)	3.24	5.23	21.6	41.1	5.91 x10 ⁻⁴
ZnO (6 hrs)	3.25	5.22	21.6	49.0	5.93 x10 ⁻⁴

3.3.2.2 XRD analysis of ZnO NPs hydrothermally produced under temperature variation

3.3.2.2.1 Structural analysis

Figure 3.7 represents the X-ray diffraction patterns of ZnO nanopowder produced at 140°C and 180°C for 6 hrs, respectively. In Figure 3.7, all the samples of the prepared nanoparticles were indexed as ZnO hexagonal wurtzite structure with standard reference to data (JCPDS: 36-1451) [3.14]. The XRD patterns of the obtained nanoparticles did not display any foreign peaks except that of ZnO wurtzite structure, which indicates the high purity of the prepared ZnO nanoparticles. There is an observed sharpness of all the reflection peaks, showing good crystallinity. These results are consistent with the previously reported work [3.17].

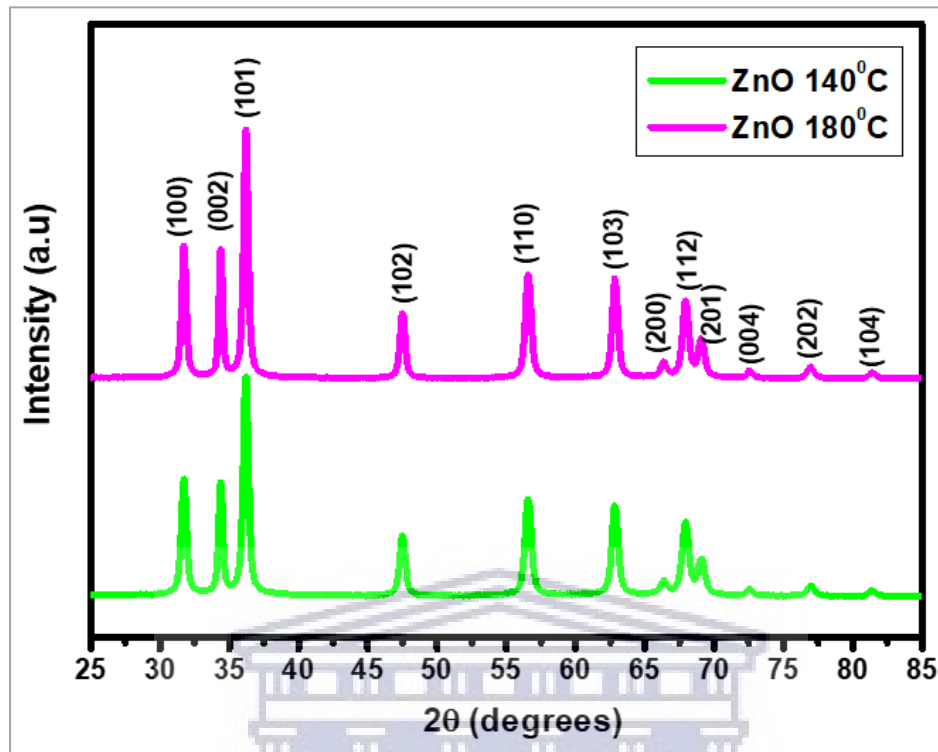


Figure 3. 7: XRD pattern of ZnO NPs synthesised at 140°C and 180°C for 6 hrs, respectively.

3.3.2.2 Williamson-Hall analysis

Figure 3.8 shows the $\langle 101 \rangle$ peaks of ZnO NPs prepared at 140°C and 180°C for 6 hrs, respectively. Figure 3.9 shows W-H models for crystallite sizes and strain values extraction of ZnO NPs prepared at 140°C and 180°C for 6 hrs, respectively. Table 3.4 summarises the calculated lattice parameters, crystallite size and strain extracted from the Scherrer method and W-H models (UDM method). The intensity of the (101) plane is found to be relatively intense for all the samples. Therefore, the preferred orientation is along the [101] axis [3.18]. In Figure 3.8, there is no shift of 2θ values observed, illustrating less to no lattice strain application on the ZnO nanoparticles.

This is supported by the values of the lattice strain in Table 3.4. The value of the lattice strain for 140°C is close to that of 180°C. Furthermore, the $\langle 101 \rangle$ peaks in Figure 3.8 show an increase in sharpness with an increase in the temperature, suggesting slight movements of atoms within the crystal structure. The movement of the particles may include the vibration of the atoms at their crystal positions [3.16].

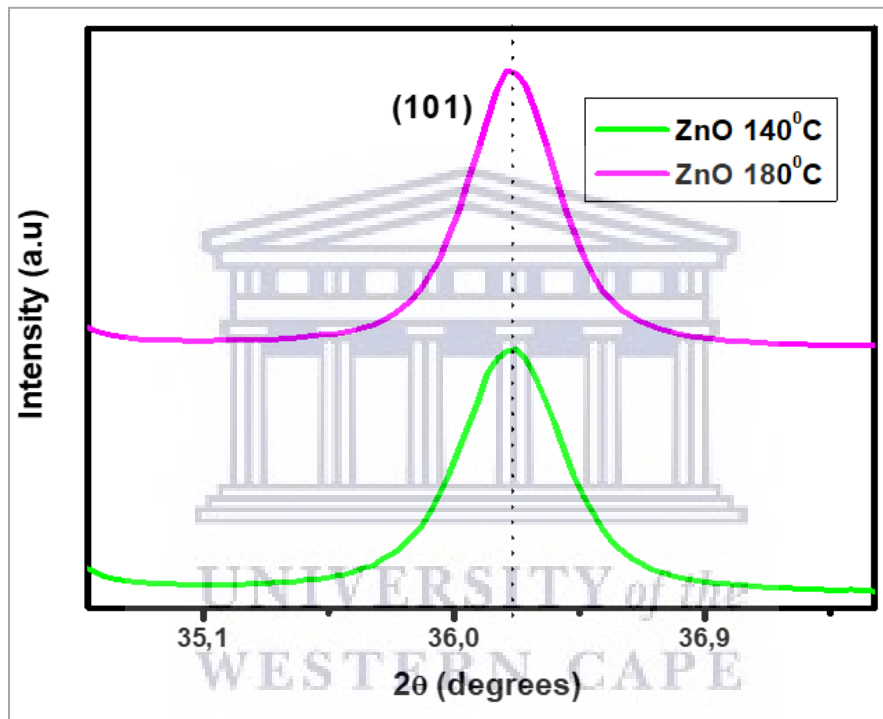


Figure 3. 8: Intensity versus 2θ around $\langle 101 \rangle$ peaks of ZnO NPs synthesised at 140°C and 180°C for 6 hrs, respectively.

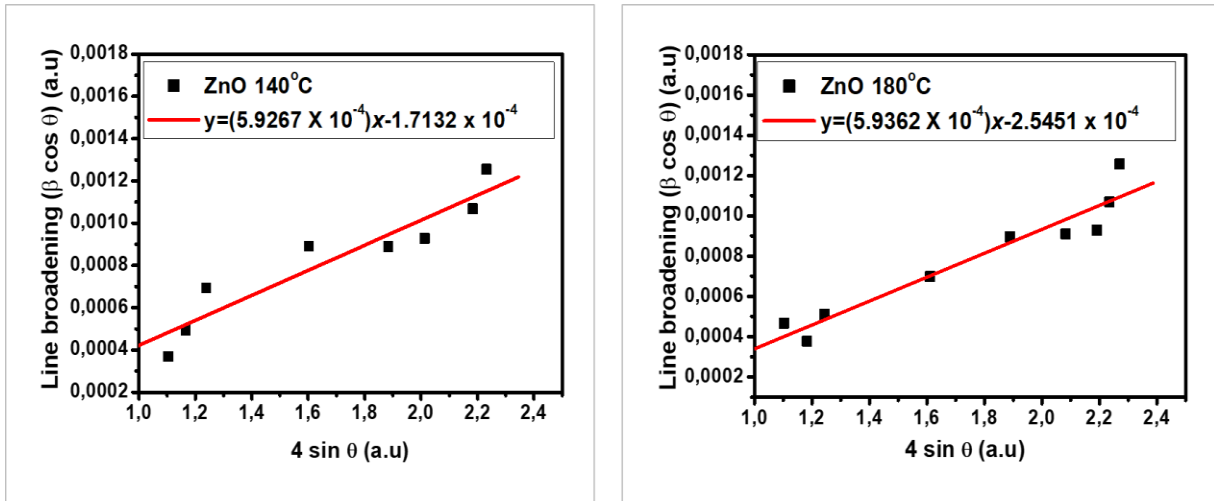


Figure 3. 9: W-H models of ZnO NPs prepared at 140°C and 180°C for 6 hrs.

The strain values were extracted from W-H plots in Figure 3.9, and the positive slope supports the lattice expansion. These results are in agreement with the work of V. Koutua et al., [3.19]. In reality, the ZnO crystal structure show deviation from the ideal ZnO crystal structure. The digression stems from the lattice stability, which affects the lattice parameters; a and c [3.16]. As illustrated in Table 3.4, the lattice parameters change with the change in the synthesis temperature. The change may be due to point defects that include Zn anti-sites, O vacancies, or misfit dislocation [3.19]. These defects and dislocations may cause either an increase or a decrease in the lattice parameters. The Scherrer method and W-H method illustrate the contribution of the change in crystallite sizes. From Table 3.4, it may be observed that there are considerable discrepancies in the resultant crystallite size. The discrepancies may further be analysed under high-resolution transmission electron microscopy to evaluate the crystal structures better in terms of the particle sizes and lattice fringes.

Table 3. 4: Calculated crystallite size and microstrain for ZnO NPs prepared at 140°C and 180°C for 6 hrs

Sample	Lattice parameters (Å)		(Scherrer method)	(UDM)	
	<i>a</i>	<i>c</i>	<i>D</i> (nm)	<i>D</i> (nm)	Lattice Strain
ZnO (140°C)	3.25	5.23	21.6	40.1	5.93 x10 ⁻⁴
ZnO (180°C)	3.23	5.21	21.6	40.0	5.94 x10 ⁻⁴

3.3.3 Structural & Morphological analysis of ZnO Nanoparticles

HR-TEM provides precise imaging of nanomaterial at an atomic level. TEM uses a high accelerating electron beam to interact with a nanostructured sample to provide an image. HRTEM is essential for providing higher resolved images that can provide quantitative and qualitative information of a sample. Information may include the crystallographic features, the particle size and the diffraction pattern of a material [3.20].

In this study, bright-field TEM, the HRTEM lattice images, average particle sizes by histogram and the SAED images of ZnO NPs prepared for 3 hrs and 6 hrs at 200°C are shown in Figure 3.10-3.13. Bright-field HRTEM, the HRTEM lattice images, average particle sizes by histogram

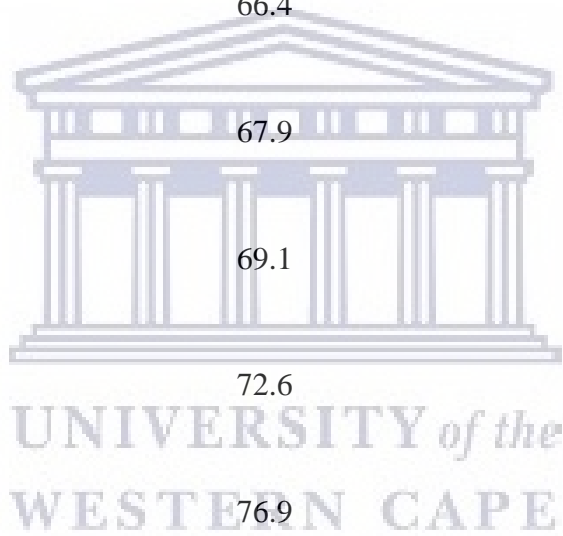
alongside the SAED images of ZnO NPs prepared for 6 hrs at 140°C and 180°C are presented in Figure 3.14-3.17. In selected area electron diffraction (SAED) analysis, the observed diffraction spots and ring patterns in SAED images were indexed with the assistance of bulk ZnO JCPDS card 00-036-1451 data [3.14] shown in Table 3.5. In this study, morphological and crystallographic properties of ZnO NPs produced for 3 hrs and 6 hrs at 200°C and ZnO NPs hydrothermally synthesised for 6 hrs at 140°C and 180°C are investigated. The properties are analysed by investigating the change in the average particle size. The lattice planes from the lattice fringes analysis due to the different synthesis conditions. The results were compared with the analysis obtained in XRD.

Table 3. 5: Bulk ZnO JCPDS card 00-036-1451 [3.14].

Hexagonal wurtzite ZnO (JCPDS No. 00-036-1451)		
d (Å)	2θ	(hkl)
2.81	31.7	100
2.60	34.4	002
2.48	36.3	101
1.91	47.6	102

Hexagonal wurtzite ZnO (JCPDS No. 00-036-1451)

d (Å)	2θ	(hkl)
1.62	56.6	110
1.48	62.9	103
1.41	66.4	200
1.38	67.9	112
1.36	69.1	201
1.30	72.6	004
1.24	76.9	202



3.3.3.1 HR-TEM analysis of ZnO Nanoparticles produced under period variation

3.3.3.1.1 Bright-field transmission electron microscopy (BF-TEM)

BF-TEM images for the hydrothermally synthesised ZnO nanopowders prepared for (a) 3 hrs and (b) 6 hrs at 200°C are illustrated in Figure 3.10. BF-TEM images in Figure 3.10 show plate-like shaped and rod-like shaped nanocrystals that correspond to a hexagonal crystal structure. The images confirm the presence of hexagonal wurtzite ZnO structures with some agglomeration observed in Figure 3.10 (a). The aggregation of particles observed in the BF-TEM images may be due to calcination that occurs during hydrothermal synthesis. Figure 3.10 (b) show that an increase in the hydrothermal synthesis period converts more spherical ZnO NPs to mainly nanorods. Moreover, the agglomeration decrease as a result of increasing synthesis duration.

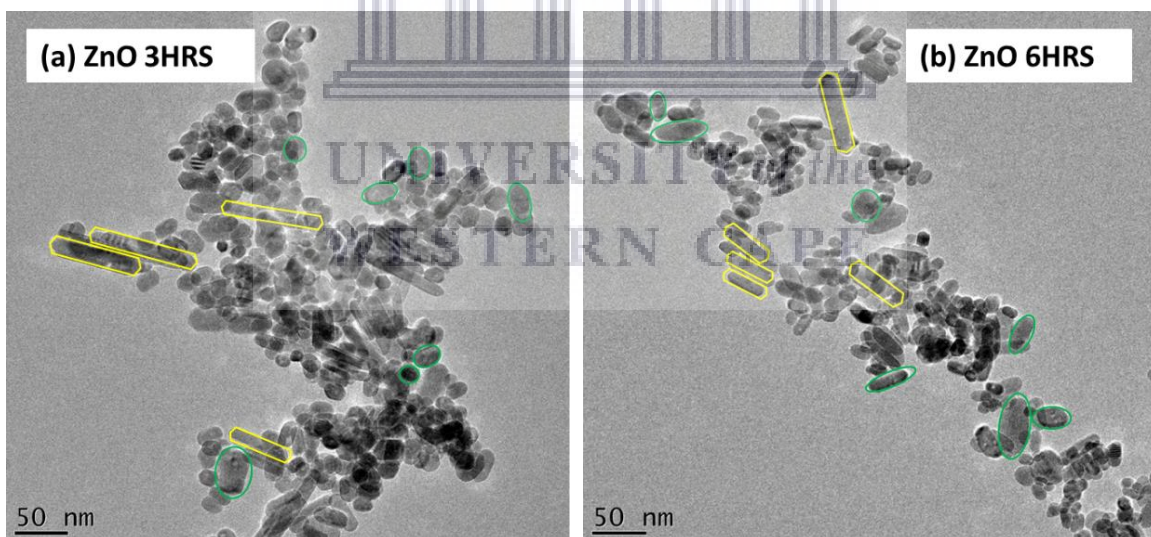


Figure 3. 10: The bright-field HR-TEM images of ZnO NPs prepared for (a) 3 hrs and (b) 6 hrs at 200°C.

3.3.3.1.2 Particle size distribution

Particle size distribution images of the ZnO prepared for 3 hrs, and 6 hrs at 200°C are illustrated in Figure 3.11 (a)-(b) respectively by histogram. The average particle sizes of the ZnO NPs prepared for (a) 3 hrs and (b) 6 hrs at 200°C are 18.3 ± 0.6 nm and 15.7 ± 0.9 nm, respectively. The decrease in the particle size as the synthesis period increases suggests that the sample at longer period may affect the optical properties. The quantum confinement effect may play a part in revealing information about the evolving electronic structure by detailing properties such as polarizable excited states and discretisation of a material's electron energy levels [3.21]. Therefore, it is imperative to investigate the optical properties of ZnO NPs produced for 3 hrs and 6 hrs to understand further the relationship between the evolving particle sizes found in TEM and the electronic structures.

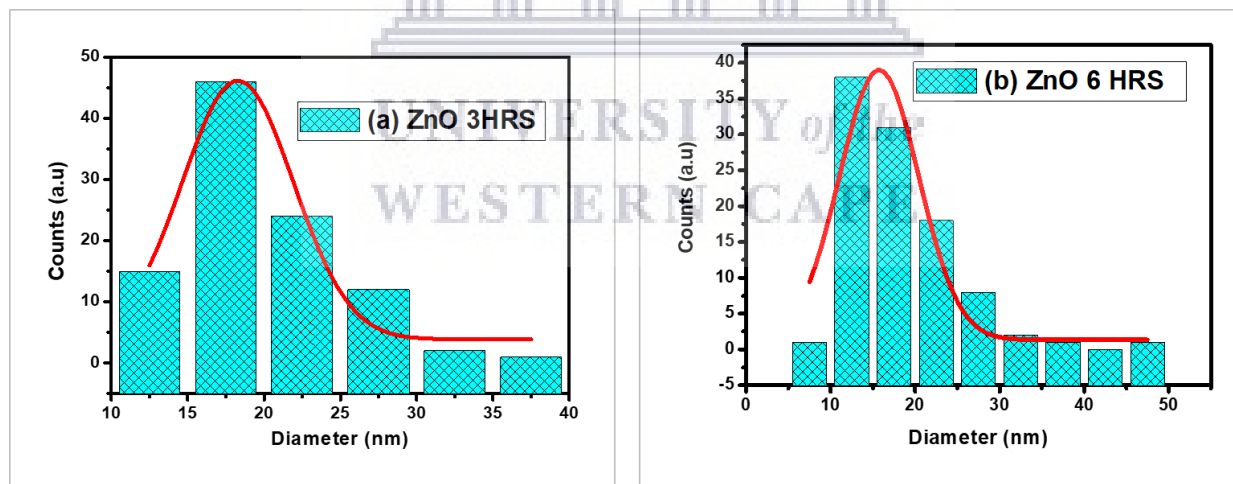


Figure 3. 11: Particle size distribution of ZnO NPs prepared for (a) 3 hrs and (b) 6 hrs at 200°C.

3.3.3.1.3 HR-TEM lattice images

HR-TEM images were recorded for ZnO NPs prepared at 200°C for 3 hrs, and 6 hrs and are illustrated in Figure 3.12 (a)-(b).

HR-TEM reveals that for all standards of ZnO synthesis, well-crystallised particles were obtained. Therefore the estimated interplanar spacing between two adjacent lattice fringes were found to be 0.28 nm for both ZnO NPs prepared for (a) 3 hrs and (b) 6 hrs at 200°C. These experimental d-spacing values agree with the reported d-spacing of 0.28 nm corresponding to the Miller indices (100) orientation. These results agree with the previously reported work by J. Qiu et al., [3.22] and the XRD results obtained in this study.

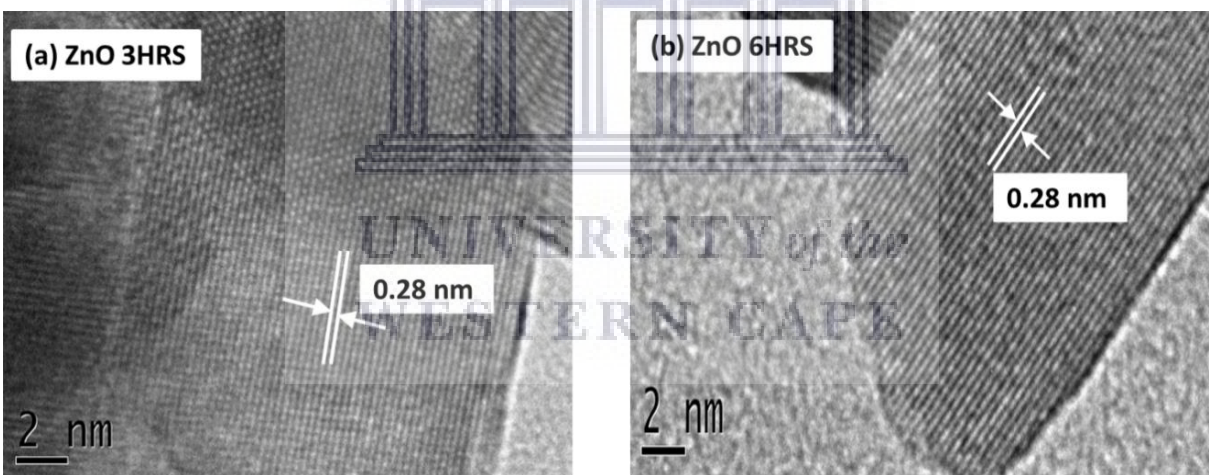


Figure 3. 12: (a) The HR-TEM lattice images of ZnO NPs prepared for (a) 3 hrs and (b) 6 hrs at 200°C.

3.3.3.1.4 The scattered area electron diffraction (SAED)

SAED images were recorded for ZnO NPs prepared at 200°C at 3 hrs, and 6 hrs are illustrated in Figure 3.13 (a)-(b). The SAED indicates randomly scattered diffraction spots and diffraction ring patterns, revealing the presence of single and polycrystalline ZnO NPs in the sample. The intensity of the SAED pattern of ZnO decreases with an increasing synthesis period. However under both period calibrations the intensity of the rings is very high indicating the resultant polycrystalline phase contribution. It may be noted that these patterns match very well with the Miller indices of wurtzite hexagonal ZnO along (100), (002), (101), (102), (110), (200), (112), and (201) planes of the XRD results obtained in this study. SAED pattern observed in Figure 3.13 (a) shows less intensity of the ring patterns. However, both the samples reveal that the powders present consist of polycrystalline crystals.

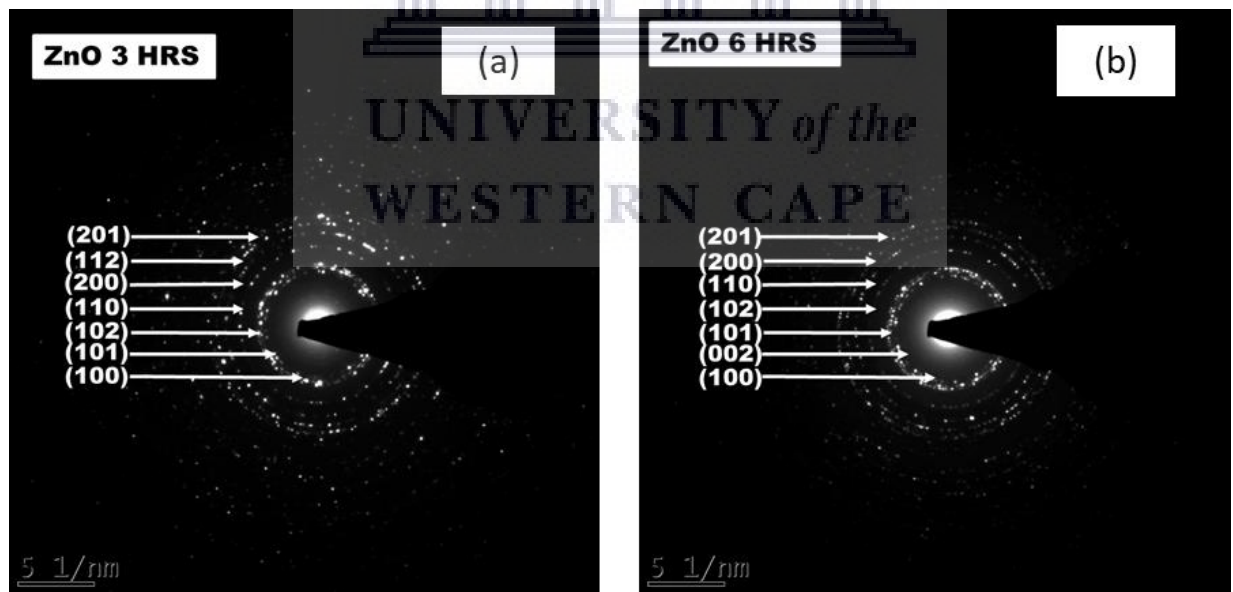


Figure 3. 13: SAED pattern of ZnO NPs prepared for (a) 3 hrs and (b) 6 hrs at 200°C.

3.3.3.2 HR-TEM analysis of ZnO NPs produced under temperature variation

3.3.3.2.1 Bright-field transmission electron microscopy (BF-TEM)

The BF-TEM images of ZnO prepared for 6 hrs at (a) 140°C and (b) 180°C are presented in Figure 3.14. It may be noted that the NPs show spherical structures in Figure 3.14 (a). A combination of primary spherical nanostructures and a small yield of nanorods is observed in Figure 3.14 (a). An increase in temperature to 180°C (Figure 3.14 (b)) resulted in the presence of primary nanorods and secondarily sphere-shaped ZnO NPs. The nanorods in Figure 3.14 (b) confirm the presence of hexagonal wurtzite structured ZnO as most of the particles have hexagonal shapes. On the basis of HRTEM micrographs, it was supposed that the growth mechanism for the formation of structures shown in Figure 3.14 (a) and (b) must have involved the following two stages as shown in equations (3.1) and (3.2.1 & 3.2.2). First stage evolved the formation of Zn(OH)₂ white precipitates on titrating aqueous zinc acetate with NaOH. Zn²⁺ and OH⁻ ion concentration strongly influence the growth of Zn(OH)₂ [3.23]. Upon the heat treatment of 140°C to Zn(OH)₂ in stage 2, ZnO spherical structures were formed (Eq. (3.2.1)) [3.23]. Furthermore, in the second stage, the crystals was allowed to grow under the controlled environment of autoclave at 180°C (Eq. (3.2.2)) resulting in the growth of hexagonal wurtzite structures of ZnO nanoparticles (Figure 3.14 (b)).

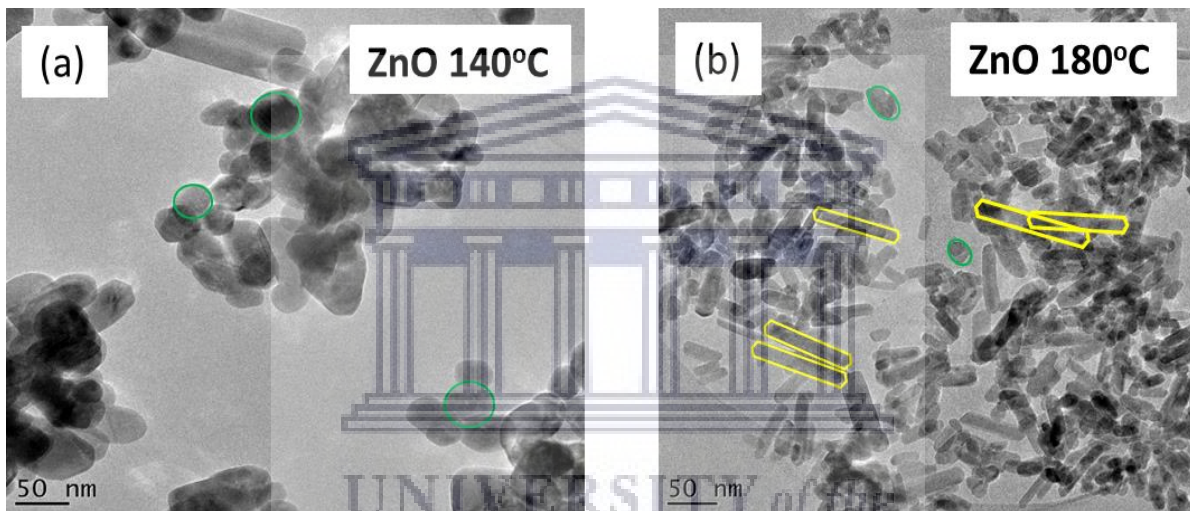
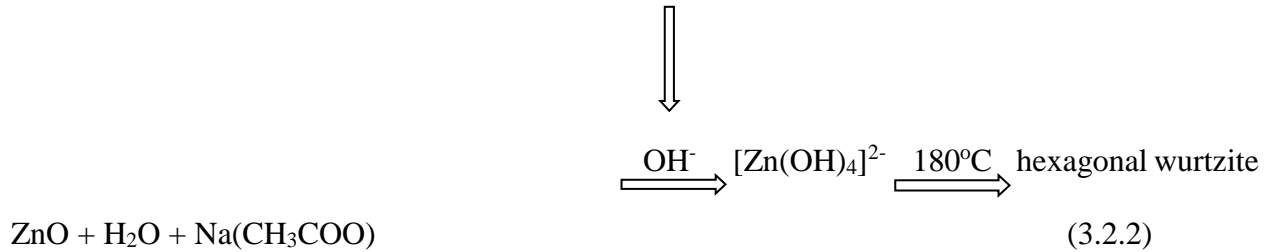
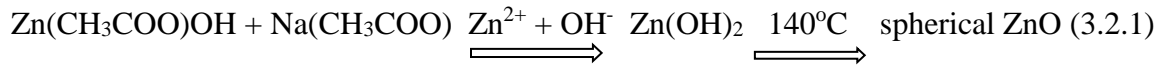
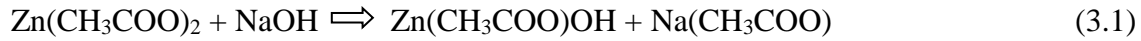


Figure 3. 14: The bright-field HR-TEM image of ZnO prepared for 6 hrs at (a) 140°C and (b) 180°C.

3.3.3.2.2 Particle size distribution

Particle size distribution images of ZnO prepared for 6 hrs at (a) 140°C and (b) 180°C are presented in Figure 3.15 by the histogram, respectively. The average particle sizes of ZnO NPs prepared at 140°C and 180°C are 36.9 ± 0.9 nm and 20.9 ± 0.9 nm, respectively. These results show that the

ZnO NPs depend on the synthesis temperature as the particle size decreases with increasing temperature. The histograms results presented in Figure 3.15 (a) and (b) and the dependence of the particle sizes on temperature are consistent with the reported structures of S. Mohan et al., [3.3].

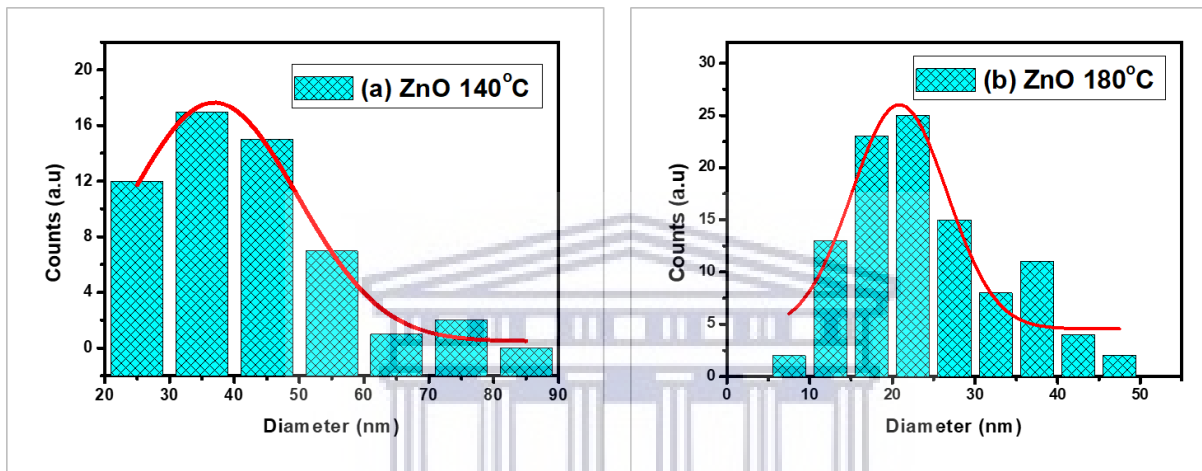


Figure 3. 15: The particle size distribution of ZnO prepared for 6 hrs at (a) 140°C and (b) 180°C.

3.3.3.2.3 HR-TEM lattice images

HR-TEM images of ZnO prepared for 6 hrs at (a) 140°C and (b) 180°C were recorded and are presented in Figure 3.16 (a)-(b), respectively. The estimated d-spacing values between two adjacent lattice fringes for ZnO NPs prepared for 6 hrs at ZnO prepared for 6 hrs at (a) 140°C and (b) 180°C are 0.28 nm and 0.26 nm, respectively. These estimated d-spacing values are in agreement with the previously reported 0.28 and 0.26 nm ZnO d-spacing corresponding to (100) [3.22] and (002) [3.24] planes of the hexagonal wurtzite ZnO structure, respectively.

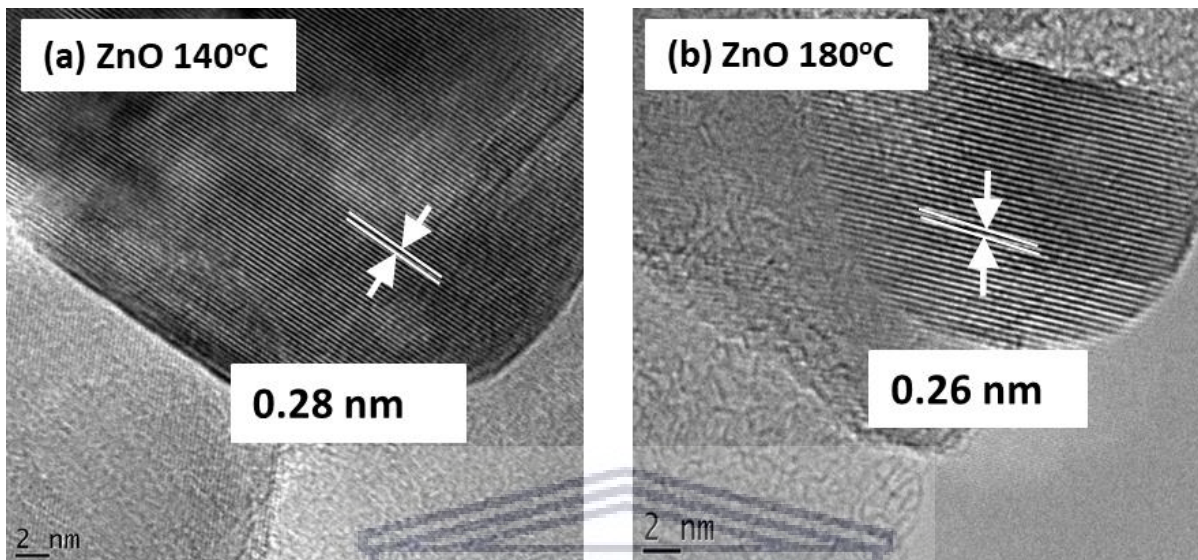


Figure 3. 16: The HR-TEM lattice image of ZnO prepared for 6 hrs at (a) 140°C and (b) 180°C.

3.3.3.2.4 The scattered area electron diffraction (SAED)

SAED images were recorded for ZnO NPs synthesized for 6 hrs at 140°C and 180°C are presented in Figure 3.17 (a) and (b) respectively. The SAED patterns illustrate that the samples are hexagonal wurtzite ZnO structures in crystallography, which agrees with XRD results. Their particle size determined from TEM analysis of ZnO NPs at 140°C is greater than the Scherrer method-extracted crystallite size in XRD analysis. Furthermore, the particle size of ZnO NPs at 180°C was less than the crystallite size. The intensity of the diffraction rings increases with the synthesis temperature of the ZnO NPs, which suggests an increase in the polycrystallinity of the nanomaterial [3.25].

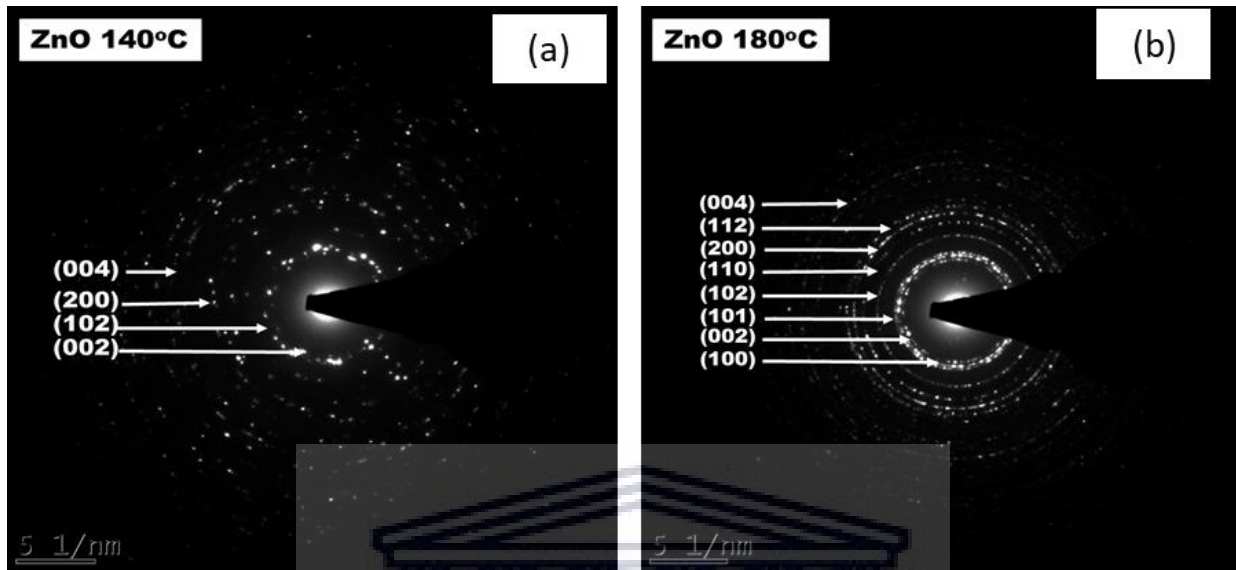


Figure 3. 17: The HR-TEM image SAED pattern of ZnO prepared for 6 hrs at (a) 140°C and (b) 180°C.

3.3.4 Optical properties of ZnO Nanoparticles

Usually, the electronic properties of semiconductors are evaluated from the extracted energy band diagram [3.26]. In an ideal UV-Vis spectrum of a perfect semiconductor with a direct band gap, absorption of photons occurs when the energy is equal to or greater than the band gap. Usually, spectra are recorded in units assigned to the wavelength of light instead of the energy. Therefore the conversion of the absorption spectra wavelength (nm) and the band gap (eV) is given by equations (3.8) and (3.9) [3.27]:

$$hv = \frac{hc}{\lambda} = \frac{1239.8 (eV \cdot nm)}{\lambda (nm)}, \quad (3.8)$$

$$\approx \frac{1240 (eV \cdot nm)}{\lambda (nm)}, \quad (3.9)$$

The speed of light is given by c , ν is the frequency of the wave, and λ is the absorption wavelength [3.28]. Where h is the Planck's constant of 1.504×10^{-34} Joules-second [3.29], this constant sets the scale of the quantum regime with dimensions of time and energy [3.29]. In the absorption spectrum, the band gap corresponds to the point at which absorption of photons occurs from the baseline. This case illustrates the absorption of photons with equal or greater energy than the band gap, energy that excites the electrons from the valence band to the conduction band. There is a non-linear increase in absorption in an ideal UV-Vis spectrum due to the density of states at the top valence and minimum conduction bands and the excitonic effects [3.27].

The technique is used to measure the electronic behaviour of materials containing inhomogeneous grains that may give rise to light-scattering and absorption within a material [3.30]. UV-Vis absorption spectroscopy has been reported to estimate the highly justified electronic transition of electrons from the different electron orbitals of ZnO nanoparticles. Therefore, diffuse reflectance may be employed as another optical spectroscopy technique to study the relationship between the absorption and scattered light in the structure of the prepared ZnO NPs.

3.3.4.1 UV-Vis absorption analysis of ZnO Nanoparticles synthesised hydrothermally under period variation

UV-Vis spectra of ZnO nanoparticles prepared at 200°C for 3 hrs and 6 hrs (Figure 3.18) over the range of 250-500 nm showed photo-absorption properties at wavelengths of no longer than 380 nm, which suggests that the NPs are photoactive under UV light irradiation. These absorption peaks indicate blue shifts than the bulk ZnO absorbance peak (368 nm) [3.31].

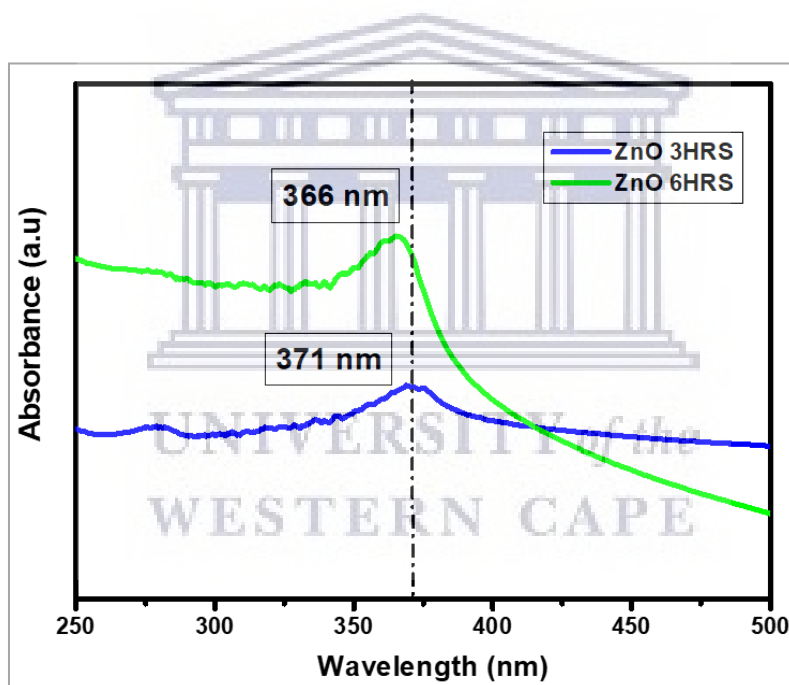


Figure 3.18: UV-Vis optical absorption spectra of ZnO NPs synthesised at 200°C for 3 hrs and 6 hrs.

Furthermore, one peak present for each spectrum in Figure 3.18 indicates the presence of homogeneous polydispersity of ZnO particles. Table 3.6 indicates the band gap's estimated values for ZnO NPs hydrothermally synthesised for 3 hrs and 6 hrs. The increase in the band gap values with decreasing particle size is due to the quantum confinement effect whereby there is electronic transition(s) from the valence band to the conduction band. The blue shifts in the band edges signify the presence of nano-sized particles. The blue shift is commonly attributed to excess carriers obtained from impurities [3.32], however, in this study, the excess carriers may be that of Zn carriers [3.16].

Table 3. 6: The estimated band gap values of the absorption peaks observed in Figure 3.18.

<i>ZnO preparation hrs</i>	<i>Approximated absorption peak centre (λ)</i>	<i>Estimated band gap from $E_g=1240/\lambda$</i>
3 hrs	371 nm	3.34 eV
6 hrs	366 nm	3.39 eV

3.3.4.2 UV-Vis absorption analysis of ZnO NPs prepared under temperature variation

Typical UV-Vis absorption spectra of the synthesised ZnO nanoparticles prepared at 140°C- 180°C for 6 hrs are shown in Figure 3.19. The measurements taken were between 250 to 500 nm. The ZnO NPs exhibit strong absorption at the approximated absorption peaks tabulated in Table 3.7.

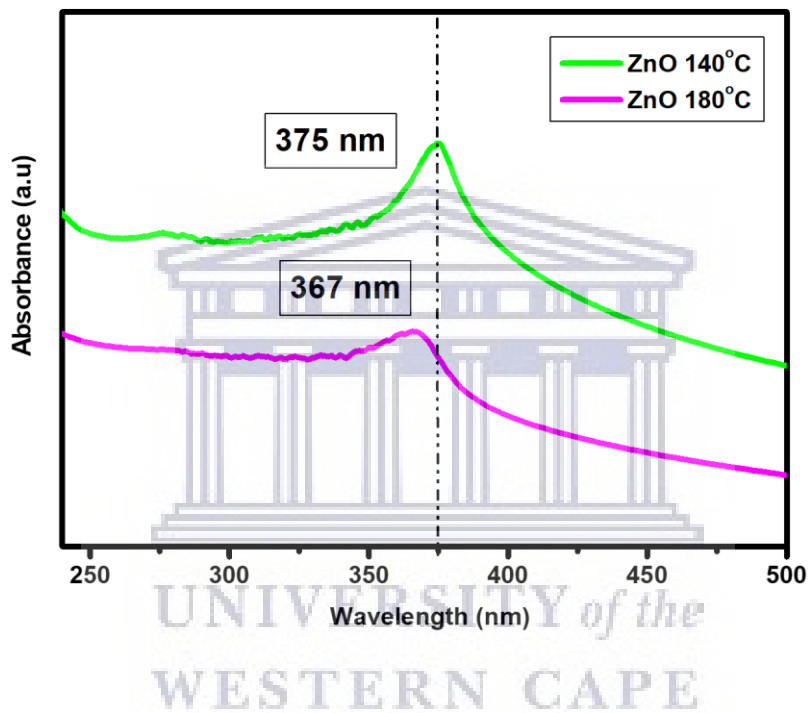


Figure 3. 19: UV-Vis optical absorption spectra of ZnO NPs synthesized at 140°C and 180°C for 6 hrs.

The prepared zinc oxide nanoparticles show transparency in the visible range of the electromagnetic spectrum and an average absorption in the UV range at ~367 nm, confirming the presence of ZnO NPs in the samples. The approximated optical band gap values illustrated in Table

3.7 are close to the intrinsic band gap value (3.37 eV). The band gap value of ZnO nanoparticles prepared at 140°C is the same as the ZnO intrinsic band gap value, which suggests the high purity of the ZnO NPs present in the sample.

Table 3. 7: The estimated band gap values of the absorption peaks observed in Figure 3.19.

ZnO preparation temperature	Approximated absorption peak centre (λ)	Estimated band gap from $E_g=1240/\lambda$
140°C	375 nm	3.31 eV
180°C	367 nm	3.38 eV

The band gap value of ZnO nanoparticles prepared at 180°C is close to the ZnO intrinsic band gap value; this suggests the high purity of ZnO NPs present in the sample. The band gap value for 180°C increased compared to the bulk ZnO band gap value (3.37 eV). This decrease suggests band gap enhancement due to the quantum confinement effect, which could be due to movements of either Zn or O atoms in the form of vibration that may have caused point or edge dislocations [3.16]. These results suggest that atoms within the unit cell rearrange such that electron-hole density becomes enhanced, promoting suitable UV-shielding properties [3.33], which may strengthen the ZnO-nanoridges for photovoltaic application.

3.4 Conclusion

A. Sangeetha et al., [3.34] stressed that carboxylate IR spectral signature disappears with increased ZnO calcination temperature. The disappearance is attributed to the conversion of zinc carboxylate to ZnO and the dissociation of zinc acetate [3.4]. Further studies by A. Sangeetha et al., [3.34] illustrated that the lattice strain might have caused a slight shift in the FTIR Zn-O band as the temperature was increased and particle size alteration. Therefore, the presence of the Zn-O shoulder at $\sim 400\text{-}595\text{ cm}^{-1}$ for the samples illustrated in Table 3.2 may be associated with oxygen vacancies (V_O), defects in the ZnO crystal structures. Thus, this discovery leads to the importance of analysing the samples under XRD and HRTEM. The techniques further provide advanced crystallographic properties information, such as the change in the lattice parameters. The increase or decrease in the lattice parameters with respect to the theoretical values give information on the position of the atoms in the crystal structure [3.35]. Highly performing ETLs for IOSC application are supported by utilising an n-type semiconductor to facilitate excess electrons to the respective electrode (ITO). Therefore, the presence of excess oxygen may enhance the n-type property of ZnO NPs, which improves the conductivity of the sample(s). Thus, the ETL can be enhanced with the addition of ZnO NPs as seeds.

X. Wang et al., [3.35] explored the interaction of oxygen with defective ZnO. The exploration was undertaken by studying the effects of time on the formation and interaction between Zn and O in the X. Wang et al., [3.35] study. It was highlighted that increasing synthesis time gradually results in a shift in the Zn-O band to the higher IR position, illustrating a strong absorption in the IR

position of the electromagnetic spectrum. Therefore, in this study, the shift of the Zn-O bands under both period and temperature experimental conditions attribute to the solid absorption of free charge carriers [3.35]. Furthermore, the change in the Zn-O band to the higher IR position with an increasing synthesis period promotes an increase in charge carriers, as illustrated by X. Wang et al., [3.35].

The XRD patterns are consistent with the previously reported work [3.1]. The UDM analysis illustrated minor strain discrepancies. The Williamson-Hall plots showed least-square lines through the points with a positive slope, and that strongly suggests that the diffracting domains are isotropic, and there is line broadening due to the microstrains contribution within the samples. Line broadening is the one factor that affects the microstrain within a crystal structure. Therefore the change in the microstrain alters the arrangements of atoms within unit cells [3.20].

The hydrothermally synthesised ZnO NPs were characterised under HRTEM. All the samples show good agreement with the XRD results. The samples show some dependence on the experimental conditions employed. The particle size of the ZnO NPs in the period series decreases with increasing synthesis period and also under temperature variation. The ZnO NPs' particle sizes decrease with the change in temperature from 140°C to 180°C. The results suggest that the samples may have good optical properties for IOSC application due to the quantum confinement effect. Therefore, the samples were further analysed to gather electronic information to understand the effect of the various conditions of hydrothermal synthesis on the ZnO NPs properties.

UV-Vis absorption spectra are analysed for all samples from 250 nm to 500 nm. The absorption peaks observed are due to the intrinsic defects levels, exciton effects, and the transition of electrons from the valence bands to the conduction bands [3.3]. S. Mohan et al., [3.3] have analysed the impact of experimental conditions on the growth and particle size alteration of ZnO nanoparticles by the hydrothermal method. The experimental conditions selected were temperature and period of ZnO nanoparticle synthesis. In the analysis, S. Mohan et al., [3.3] suggested that the characteristic peak ~360-380 nm observed under the synthesis period calibration is ascribed to ZnO's intrinsic band gap absorption. However, the wavelength is widening and shifting to lower values for the absorption peak of the highest temperature value. This can be attributed to the nanoparticle shape and size change to spherical and smaller, respectively. Therefore, in this study, the maximum blue shift in the wavelength is observed for the 6 hrs sample. The transition may have been attributed to the hexagonal-rod shape observed in the bright-field HRTEM image for 6 hrs sample. The change in the band gap values from the intrinsic value of 3.31 eV to 3.38 eV and 3.34 eV-3.39 eV for 140°C-180°C and 3 hrs-6 hrs respectively, may be ascribed to the absorption of visible light.

S. Mohan et al., [3.3] further analysed ZnO nanoparticles produced by hydrothermal method at different temperature values under UV-Vis absorption spectroscopy. The results obtained suggested that an increase in the synthesis temperature leads to the occurrence of an intense peak around 360 -380 nm, the intense peak attributed to the maximum absorption of the visible light, corresponding to the highest synthesis temperature. Similarly, in this study, the intense peak for these experimental conditions correspond to the maximum absorption of UV-Vis light for 6 hrs

and 180°C. These values are also the highest period and temperature values for these calibrations. In contrast to the study by S. Mohan et al., [3.3], in this work, NPs produced at 6 hrs illustrates the maximum blue-shift in the wavelength than the rest of the samples. This maximum blue shift for a sample produced for 6 hrs under this period series may be due to the predominant hexagonal-shaped ZnO NPs present in the sample, as illustrated in Figure 3.10 (a) of the bright-field HRTEM image. The blue shift of ZnO is usually due to the particle size decrease, leading to an increase in visible light [3.4]. This shift may be due to a rise in the number of oxygen vacancies (V_O). In this study, the absorption peaks have shifted inconsistently because of the change in the pH, ranging from ~10-12 [3.3].



References

- [3.1] P.M. Aneesh, K.A Vanaja, M.K. Jayraj., “Synthesis of ZnO nanoparticles by hydrothermal method,” *Optoelectronics Devices*, vol. 6639, pp. 1-9, 2007.
- [3.2] Y.X. Gan, A.H. Jayatissa, Z. Yu, X. Chen, and M. Li, “Hydrothermal Synthesis of Nanomaterials,” *Journal of Nanomaterials*, vol. 2020, pp. 1-3, 2020.
- [3.3] S. Mohan, M. Vellakkat, A. Aravind, and U. Reka, “Hydrothermal synthesis and characterization of Zinc Oxide nanoparticles of various shapes under different reaction conditions,” *Nano Express*, vol. 030028, pp. 1-15, 2020.
- [3.4] S.S. Alias, A.B. Ismail, and A.A. Mohamad, “Effect of pH on ZnO nanoparticle properties synthesized by sol–gel centrifugation,” *Journal of Alloys and Compounds*, vol. 499, no. 2, pp. 231-237, 2010.
- [3.5] U. Manzoor, F.T. Zahra, S. Rafique, M.T. Moin, and M. Mujahid, “Effect of Synthesis Temperature, Nucleation Time, and Postsynthesis Heat Treatment of ZnO Nanoparticles and Its Sensing Properties,” *Hindawi Publishing Corporation*, vol. 2015, pp. 1-6, 2015.
- [3.6] J. Polte, T.T. Ahner, F. Delissen, S. Sokolov, F. Emmerling, A.F. Thuenemann, and R. Kraehnert, “Mechanism of Gold Nanoparticle Formation in the Classical Citrate Synthesis

- Method Derived from Coupled In Situ XANES and SAXS Evaluation,” *Journal of American Chemical Society*, vol. 32, p. 1296–1301, 2010.
- [3.7] K. Kyoung-Ku, L. Byungjin, and L. Chang-Soo, “Recent progress in the synthesis of inorganic particulate materials using microfluidics,” *International chemical engineering*, vol. 98, pp. 2-19, 2019.
- [3.8] A.A. Ismail, F.R. van der Voort, and J. Sedman, “Chapter 4 Fourier transform infrared spectroscopy: Principles and applications,” in *Techniques and Instrumentation in Analytical Chemistry Volume*, Elsevier, 1997, pp. 93-139.
- [3.9] G. Nagarajua, Udayabhanu, Shivaraj, S.A. Prashanth, M. Shatri, K.V. Yatish, C. Anupama, and D. Rangapa, “Electrochemical heavy metal detection, photocatalytic, photoluminescence, biodiesel production and antibacterial activities of Ag–ZnO nanomaterial,” *Materials Research Bulletin*, vol. 94, pp. 54-63, 2017.
- [3.10] D. Manyasree, P. Kiranmayi, and R.K. Venkata, “Characterization and bacterial activity of ZnO nanoparticles synthesized by co-precipitation method,” *international journal of applied Pharmaceutics*, vol. 6, pp. 224-228, 2018.

- [3.11] R. Wahab, Y-S. Kim, and H-S. Shin, "Synthesis, Characterization and Effect of pH Variation on Zinc Oxide Nanostructures," *Material transactions*, vol. 50, no. 8, pp. 2092-2097, 2009.
- [3.12] D.M. Fernandes, R. Silva, A.A.W. Hechenleitner, E. Radovanovic, M.A.C. Melo, and E.A.G. Pineda, "Synthesis and characterization of ZnO, CuO and a mixed Zn and Cu oxide," *Materials Chemistry and Physics*, vol. 115, no. 1, pp. 110-115, 2009.
- [3.13] E. Hosono, S. Fujihara, T. Kimura, and H. Imai, "Growth of layered basic zinc acetate in methanolic solutions and its pyrolytic transformation into porous zinc oxide films," *Journal of Colloid and Interface Science*, vol. 272, no. 2, pp. 391-398, 2004.
- [3.14] F.H. Chung, "Journal of Applied Crystallography," vol. 7, p. 519, 1974.
- [3.15] M.S. Abd El-Sadek, H.S. Wasly, and K.M. Bato, "X-ray peak profile analysis and optical properties of CdS nanoparticles," *Applied Physics A*, vol. 125, p. 283, 2019.
- [3.16] S. Hussain, "Investigation of Structural and Optical Properties of Nanocrystalline ZnO," *Material Science*, pp. 15-24, 2008.

- [3.17] T.F.G. Muller, C.J. Arendse, A. Ramashia, D.E. Motaung, F.R. Cummings, G.F. and Malgas, "Influence of solvent casting and weight ratios on the morphology and optical properties of inorganic-organic hybrid structures," *Proceedings of SAIP2014*, pp. 1-6, 2014.
- [3.18] S. Mohan, M. Vellakkat, A. Aravind, U. Reka, "Hydrothermal synthesis and characterization of Zinc Oxide nanoparticles of various shapes under different reaction conditions," *Nano Express*, vol. 030028, pp. 1-15, 2020.
- [3.19] V. Koutua, P. Ojhab, L. Shastri, and M.M. Malik, "Study of the Effect of Temperature Gradient on the Thermal and Electrical Properties of ZnO Nanoparticles," *AIP Conference Proceedings*, vol. 953, pp. 030278-1-5, 2018.
- [3.20] T.A. Sonia, and C.P. Sharma, "4 - Experimental techniques involved in the development of oral insulin carriers," in *Oral Delivery of Insulin, 2014*, Woodhead publishing, 2014, pp. 169-217.
- [3.21] A.K.A Nurul and R.J Mohd, "Nanocrystals-Related Synthesis, Assembly, and Energy Applications 2012," *Quantum Size Effect in ZnO Nanoparticles via Mechanical Milling*, pp. 1-5, 2012.

- [3.22] J. Qiu, B. Weng, L. Zhao, C. Chang, Z. Shi, X. Li, H.K. Kim, and Y.H. Hwang, "Synthesis and Characterization of Flower-Like Bundles of ZnO Nanosheets by a Surfactant-Free Hydrothermal Process," *Journal of Nanomaterials*, vol. 2014, pp. 1-11, 2014.
- [3.23] R. Bhardwaj, A. Bharti, J.P. Singh, K.H. Chae, N. Goyal, and S. Gautam, Structural and electronic investigation of ZnO nanostructures synthesized under different environments, "Haliyon", vol. 4, no 4, pp 1-21, 2018.
- [3.24] V. Mohan, R. Mohan, B.U. Nair, and K.J. Sreeram, "Nanorod mediated collagen scaffolds as extracellular matrix mimics," *Biomed. Mater.*, vol. Biomed. Mater. 10 (2015), pp. 1-15, 2015.
- [3.25] B.H. Soni, M.P. Deshpande, S.V. Bhatt, N. Garg, S.H. Chaki, "Studies on ZnO Nanorods Synthesized by Hydrothermal Method and their Characterization," *Journal of nano and electronic physics*, vol. 5, no. 6, p. 04077 (6pp), 2013.
- [3.26] R. Lo'pez and R. Go'mez, "Band-gap energy estimation from diffuse reflectance measurements on sol-gel and commercial TiO₂: a comparative study," *Journal of Sol-Gel Science and Technology*, vol. 61, p. 1-7, 2012.

- [3.27] Z. Chen and T.F. Jaramillo, "Section 1: Introduction to UV-Vis spectroscopy," in *The Use of UV-visible Spectroscopy to Measure the Band Gap of a Semiconductor*, Stanford, 2017, pp. 1-18.
- [3.28] R. Hasan, S.B.A. Hamid, W.J. Basirun, Z.Z. Chowdhury, A.E. Kandjani, and S.K. Bhargava, "Ga doped RGO–TiO₂ composite on an ITO surface electrode for investigation of photo-electrocatalytic activity under visible light irradiation," *New Journal of Chemistry*, vol. 35, no. 1, pp. 369-376, 2015.
- [3.29] F.A. Bais and J.D. Farmer, "6.1 Quantum states and the definition of a qubit," in *The Physics of Information*, Elsevier, 2008, pp. 609-683.
- [3.30] W. Vargas, "Applicability conditions of the Kubelka-Munk theory," *Applied Optics*, pp. 1-7, 1997.
- [3.31] M. Kahouli, A. Barhoumi, A. Bouzid, A. Al-Hajry, and S. Guermazi, "Structural and optical properties of ZnO nanoparticles prepared by direct precipitation method," *Superlattices and Microstructures*, vol. 85, p. 7–23, 2015.

- [3.32] A. Ghosh and R. N. P. Choudhary, "Optical emission and absorption spectra of Zn-ZnO core-shell nanostructures," *Journal of Experimental Nanoscience*, vol. 5, no. 2, pp. 134-142, 2010.
- [3.33] M.R. Nath, A.N. Ahmed, M.A. Gafur, M.Y. Miah, and S. Bhattacharjee, "ZnO nanoparticles preparation from zinc-carbon dry batteries: studies on structural, morphological and optical properties," *Journal of Asian ceramic societies*, vol. 6, no. 3, pp. 262-270, 2018.
- [3.34] A. Sangeetha, S.J. Seeli, K.P. Bhuvana, M.A. Kader, and S.K. Nayak, "Correlation between calcination temperature and optical parameter of zinc oxide (ZnO) nanoparticles," *Journal of Sol-Gel Science and Technology*, vol. 91, p. 261-272, 2019.
- [3.35] X. Wang, B. Lu, L. Li, and H. Qiu, "Exploring the Interactions of Oxygen with Defective ZnO," *Chemistry Open*, vol. 7, no. 7, pp. 1-5, 2017.

Chapter 4: Synthesis and Characterisation of ZnO
nanoridges and ZnO NPs-seeded ZnO nanoridges



UNIVERSITY *of the*
WESTERN CAPE

Chapter 4: Synthesis and Characterisation of ZnO nanoridges and ZnO NPs-seeded ZnO nanoridges

Introduction

As mentioned in chapters 1 and 2 that there are various ways to synthesise ZnO nanostructures. These methods include pulsed laser deposition [4.1], sol-gel synthesis [4.2], CVD [4.1], hydrothermal synthesis [4.3], etc. The sol-gel spin coating technique is a method of synthesis that doesn't require complex and sophisticated apparatus to synthesise accurately aligned crystal nanostructures. This work used the sol-gel spin-coating technique to synthesise ZnO nanoridge thin films and seeded ZnO NPs-ZnO nanoridge thin films.

4.1 Synthesis of ZnO NPs-ZnO Nanoridges by sol-gel (spin-coating) technique

All the materials and chemicals used for this project were used without further purification. To fabricate ZnO NPs-ZnO nanoridges, 0.75M zinc acetate dihydrate was dissolved in 70 ml 2-methoxyethanol, and 3.1 ml ethanolamine were added to stabilise the Zn (II) ions by facilitating Zn (II) chelation. The solution was left to stir at 60°C for 30 minutes. Afterwards, the solution was divided and from the batches of ZnO NPs powder samples, 0.25 mg of ZnO NPs powder was drawn and dissolved in 21 ml of the zinc acetate solution. Five vials were prepared, containing bare zinc acetate solution, and a combination of ZnO NPs prepared at 140°C and 180°C for 6 hrs and calibrated at 200°C for 3 hrs and 6 hrs with zinc acetate solution, respectively. In preparation for the thin film deposition, the ITO/clear quartz substrates were immersed and sonicated in isopropanol (IPA), acetone, ethanol, and de-ionised water at 60°C for 15 minutes each,

sequentially. Compressed nitrogen gas was used to dry the substrates after sonication. The thin-films were prepared by spin coating the 0.40 μL of each solution at 200 revolutions per minute (rpm) for 40 s using an Ossila spin coater and ramp-annealed from room temperature to 275°C using a Chemat (Technology Inc) hotplate. Figure 4.1 illustrates a summarised process of the spin-coating procedure followed to synthesise ZnO NPs-ZnO nanoridge thin-films.

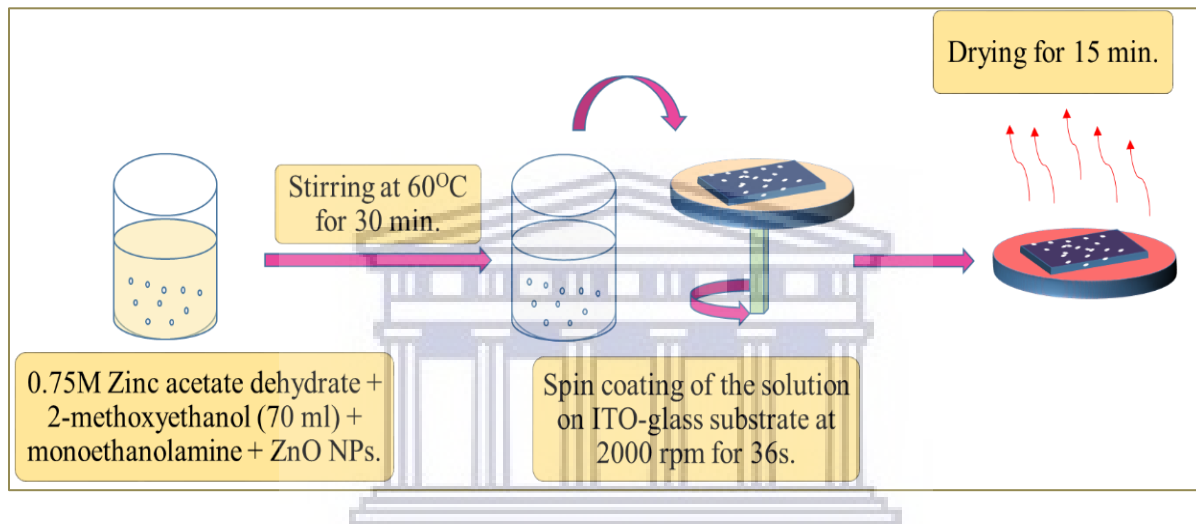


Figure 4. 1: Sol-gel-spin-coating synthesis of ZnO nanoridges and seeded ZnO NPs-ZnO NRs with ZnO NPs hydrothermally synthesised at 200°C for 3 hrs and 6 hrs and at 140°C and 180°C for 6 hrs.

4.2 ZnO NPs-ZnO Nanoridges Characterization

A 6M Dektak stylus profilometer was used to measure and estimate the surface morphology and height of the prepared nanoridge thin-film samples. The profilometer makes use of a 12.5 μm diamond-tipped stylus, with programmed force ranging from 1-15 N; designated to measure soft

to hard surfaces. The high-resolution scanning electron microscopy (HR-SEM) technique was employed to study the morphological properties of the ZnO NPs-ZnO nanoridges structures, coated on indium-tin oxide-coated and clear quartz substrates. EDX spectra were collected at a high electron tension of 20 kV. All the spectra were collected for 30 seconds using Oxford X-Max solid-state drift detector. Transmittance spectroscopy was utilised to study the optical properties of the ZnO nanoridges fabricated. The transmittance measurements were collected with a Semiconsoft UV-vis spectrometer over a spectral range of 200 nm to 800 nm. The spectrometer operates with two independent radiation sources: a UV (deuterium) and a visible (halogen) lamp.

4.3 Results and discussion

4.3.1 Topographic analysis of ZnO NPs-ZnO nanoridges

The stylus profilometer is the most used tool for thin-film height measurement. It can scan an area of tens of millimetres with a vertical range from a few nanometers up to hundreds of microns. In nanoscience, a typical contact profilometer measurement of the step between the substrate and the nanostructured layer [4.4]. In this study, the step height between the ITO substrate and the produced nanoridge structure from combining ZnO NPs synthesised at 140°C for 6 hrs is presented in Figure 4.2. The measurements were carried out at the maximal possible magnification after a precise sample levelling to extend the step over the full scale of the range. The range of height values of the prepared ZnO nanoridge thin-films measured are summarised in Table 4.1 and Table 4.2.

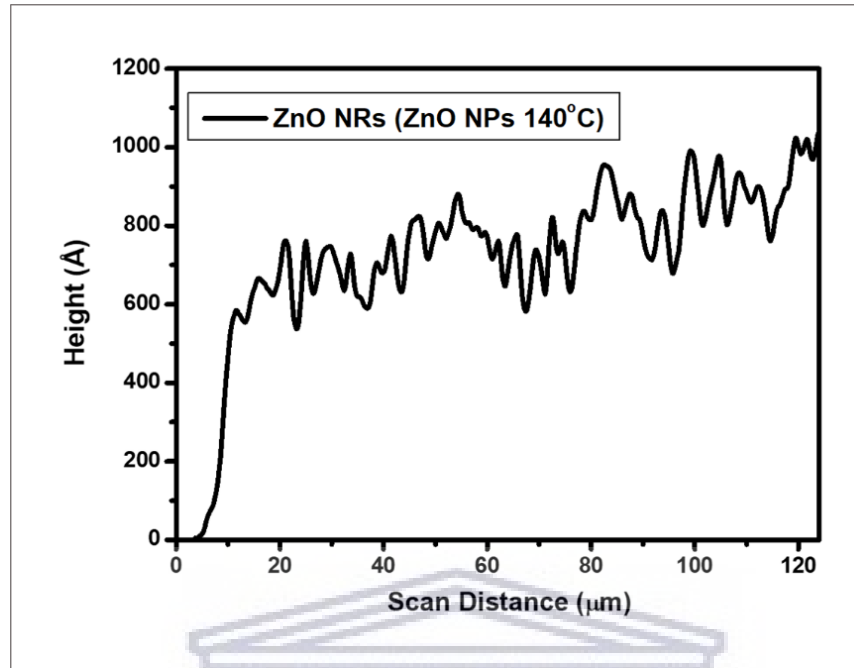


Figure 4. 2: The height profile of ZnO nanoridges synthesised from a zinc acetate solution and ZnO NPs seeds produced at 140°C for 6 hrs.

4.3.1.1 Analysis of ZnO NRs and ZnO NPs-ZnO nanoridges thin-film height under period calibration

Usually, the revolutions per minute (rpm) during spin-coating affect the height of the thin-film [4.5]. However, in this study, rpm was kept constant for all the samples. The height of the thin-films decreased with the initial incorporation of the ZnO NPs and further decreased with an increase in the hydrothermal synthesis period of the incorporated NPs (Table 4.1).

Table 4. 1: Average nanoridges height (nm) of seedless ZnO NRs and ZnO NPs-seeded ZnO NRs of NPs hydrothermally synthesised for 3 hrs and 6 hrs at 200°C.

<i>Sample</i>	<i>The height of the layer (nm)</i>
ZnO	188
ZnO 3 Hrs	112
ZnO 6 Hrs	111

Therefore, the size of the NPs may be one of the factors that affect the height of the nanoridge structures, as the NPs have been shown under HR-TEM analysis in Chapter 3, section 3.3.3.1 to possess various morphological properties and different sizes. Moreover, the height values obtained in Table 4.1 are in the range of 100-200 nm. Therefore, ZnO ETLs possessing up to 300 nm height are favourable in IOSCs applications because they are known to enhance the efficiency of IOSCs [4.6]. Moreover, optimised ETLs can transport electrons generated in the photo-active layer to the bottom electrode and simultaneously block holes from recombining with the electrons before they can travel to reach the bottom electrode.

4.3.1.2 Analysis of ZnO NRs and ZnO NPs-ZnO nanoridges thin-film height under temperature calibration

The height of the layers is affected by the incorporation of ZnO NPs. The uniformity of thin-films is usually affected by the change in the layer's height [4.7]. This change has a direct influence on the transparency of thin-films. Optical properties such as transmittance, absorbance, and reflection

depend on the thin-films' height [4.8]. Therefore, for IOSC application, ETLs height of optimal value is required to collect photogenerated charge carriers effectively to the cathode [4.7]. The height of the seedless ZnO NRs is larger than that of all the seeded ZnO NRs samples. As the hydrothermally synthesised ZnO NPs at various temperature values are incorporated, the height decreases with increased temperature (Table 4.2).

Table 4. 2: Average nanoridges height (nm) of seedless ZnO NRs and ZnO NPs seeded-ZnO NRs of NPs hydrothermally synthesised for 6 hrs at 140°C and 180°C.

<i>Sample</i>	<i>The height of the layer (nm)</i>
ZnO	188
ZnO 140°C	100
ZnO 180°C	96

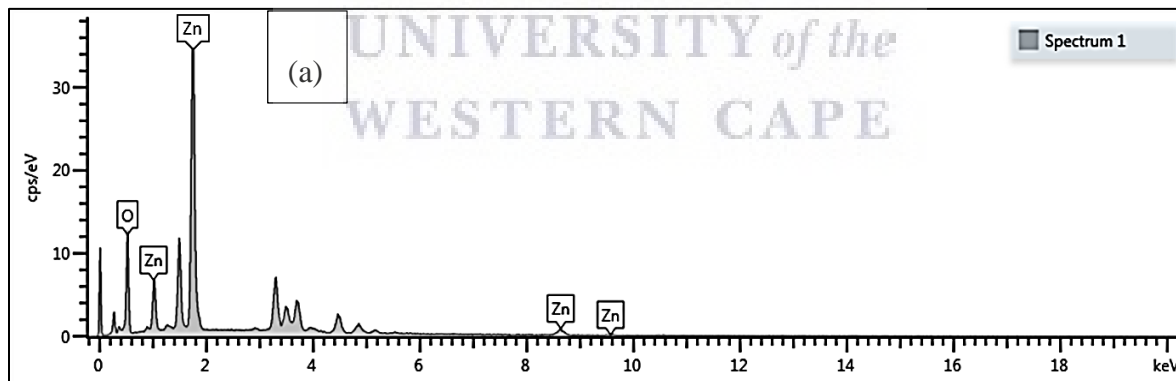
The height of the ETLs must be at an optimal level. Very low height < 50 nm may create pinholes in the layer. The formation of pinholes influences forward leakage current and creates a shunting path that causes a reduction in the V_{OC} [4.7]. Ultimately, the overall PCE will be negatively affected. Large height > 300 nm may cause defects states within the layers that cause recombination centres. The height values obtained in this study are between 50 and 300 nm, therefore, this suggests that the samples show good transparency that can influence working IOSCs with increasing efficiencies.

4.3.2 Morphological and chemical composition analysis of ZnO NPs-ZnO nanoridges

The HR-SEM technique was employed to study the morphological properties of ZnO nanoridges structures coated on indium-tin oxide-coated substrates. HR-SEM revealed the shape and the width size of the grains related to the materials. These ZnO nanoridge samples were utilised as ETLs in the fabricated IOSCs. SEM images of six kinds of ZnO nanoridges structures were fabricated for this study.

4.3.2.1 HR-SEM-EDS analysis

Figure 4.3 (a) and (b) illustrate the EDS spectrum and elemental composition table for ZnO, ZnO NPs-based ZnO nanoridges samples, respectively. The peaks related to Zn and O appeared in the spectrum. The atomic weight percentage and atomicity of the Zn and O elements present in the ZnO nanoridge samples are shown in the table: Elemental Composition in Figure 4.3 (b).



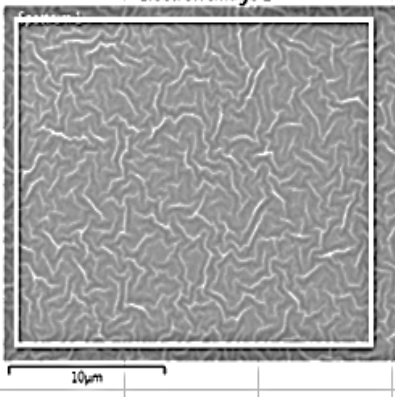
(b)	Elemental Composition			
	Element	Atomic %	Wt%	
	O	50	19.66	
	Zn	50	80.34	
	Total:	100	100	

Figure 4. 3 (a): HR-SEM-EDS spectrum analysis, (b): HR-SEM-EDS elemental composition of Zn and O for seedless ZnO NRs and ZnO NPs-seeded ZnO NRs with ZnO NPs that were hydrothermally synthesised at 140 °C and 180°C for 6 hrs, and 3 hrs and 6 hrs at 200°C, respectively.

From Figure 4.3 (a) and (b), Zn and O are the main components of the samples with weight percentage and atomicity of 50%, 50% and 80.34%, 19.66%, respectively. The atomic composition shows that the ZnO layer has uniformly covered the ITO substrate. The values of the weight percentage are close to the bulk ZnO atomic weight [4.9]. Furthermore, besides InSn due to the ITO substrate, no trace of any other impurities could be found within the detection limit of EDX as there were no other peaks detected in the spectrum. The presence of the InSn resonating around 3.00 keV to 4.40 keV accounts for the indium tin oxide substrate(s) and oxygen resonating around 0.50 keV.

Moreover, two strong peaks that correspond to the L shell of zinc and oxygen's K shell are present. These results confirm the purity of the ZnO nanostructures and the deep penetration of the electron beam into the inner layer to reach the zinc plate. The observed EDS results closely agree with the previously reported results by E. Kärber et al., [4.10]. The analysis under EDS illustrates the absorption of ZnO (100%), and it is attributed to the combination of ZnO nanoparticles and zinc acetate solution to produce ZnO nanoridges. Furthermore, annealing the zinc acetate solution is one of the processes that may have led to highly pure ZnO as the acetate particles precipitate.

4.3.2.2 HR-SEM analysis of ZnO NPs-ZnO nanoridges produced under period calibration

4.3.2.2.1 Bright-Field HR-scanning electron microscopy (BF-HR-SEM)

In Figure 4.4 (a), the seedless ZnO nanoridges show uniform formation with random orientation of the ripple structure on the ITO layer. The surface of the thin-film is rough with contracted dense undulated nanoridges.

Figure 4.4 (b) - 4.4 (c) represent HR-SEM images of the ZnO nanoridge structures seeded with hydrothermally prepared ZnO NPs by varying the synthesis period for 3 hrs and 6 hrs at 200°C, respectively. The ZnO nanoridge structures (Figure 4.4 (b) and (c)) show a decrease in density and increased undulation with an increasing synthesis period.

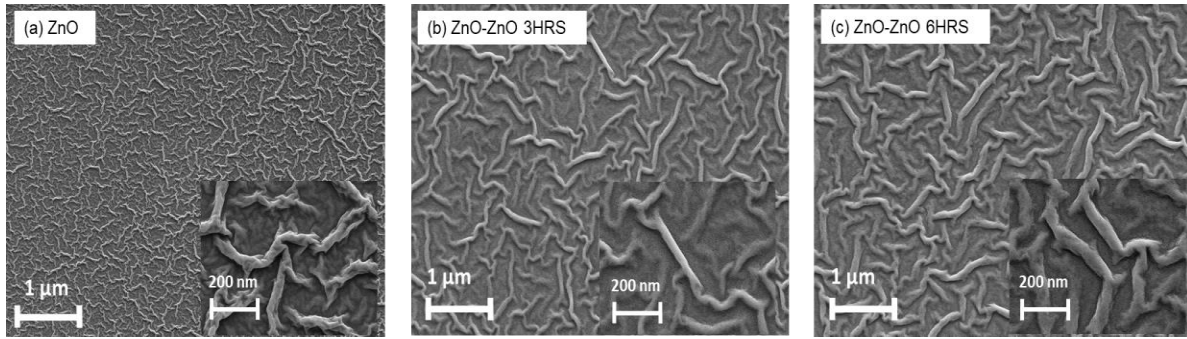


Figure 4.4: SEM images of unseeded ZnO and seeded ZnO NPs-ZnO nanoridges calibrated for 3 hrs and 6 hrs at 200°C.

4.3.2.2.2 Width size distribution

Figure 4.5 (a)- (c) show the width size distribution of the unseeded ZnO NRs and seeded ZnO NRs with hydrothermally synthesised ZnO NPs at 3 hrs and 6 hrs at 200°C. The density and width distribution size of the nanoridge ensembles that are further illustrated with the width distribution of the ripple shown in histogram analysis in Figure 4.5 (a) – (c). These ripple structures are shown to be affected by the addition of ZnO NPs to the zinc acetate solution.

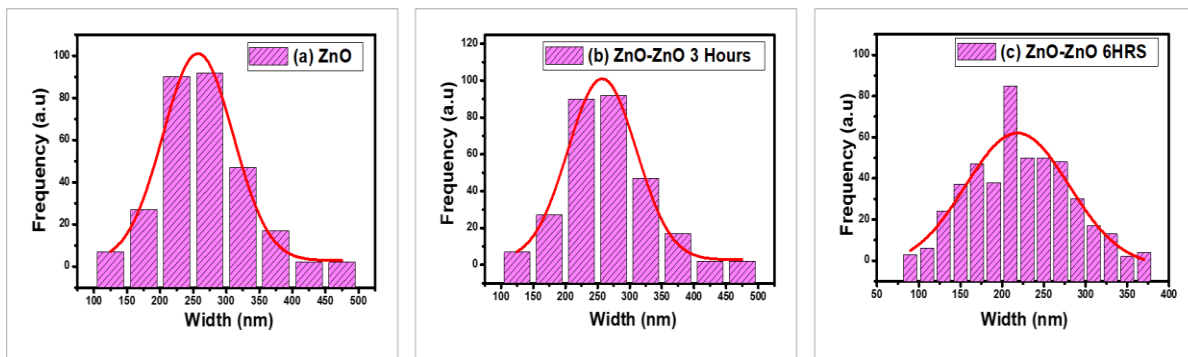
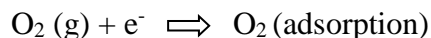
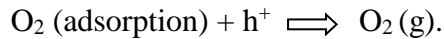


Figure 4. 5: Width size distribution of unseeded ZnO and seeded ZnO NPs-ZnO nanoridges calibrated for 3 hrs and 6 hrs at 200°C.

Experimental and theoretical analysis suggest that adsorption and desorption of oxygen plays a vital role in assisting the photo-response of ZnO crystal [4.11]. Therefore, these chemical processes change the width size of the nanoridges observed in Figure 4.4 (a) -4.4 (c). Therefore, photo-response dissolves into two processes whereby a ZnO material may undergo rapid chemical and mechanical processes and still retain nano-production in the process. The other process is a surface-related slow process. Moreover, the following chemical reaction may address the latter: an electron may be trapped by oxygen atoms and result in a state of chemically adsorbed surface as:



An electron-hole is generated when the photon energy is equal or greater than that of the bandgap directed to the ZnO crystal structure. Therefore, the chemisorbed/adsorbed oxygen is then neutralised by the positive charge:



In essence, the slow and rapid related reactions between ZnO nanoparticles and zinc acetate solution or the process of ramp-annealing may attribute to the decrease in the width size of the nanoridges with increasing hydrothermal synthesis period of the ZnO NPs incorporated observed in Figure 4.5 (a)-(c), and summarised in Table 4.3.

Table 4. 3: Average NPs sizes with error for ZnO NPs (period calibration), step-height (nm), and average nanoridges width sizes of unseeded ZnO and seeded ZnO NPs-ZnO nanoridges calibrated for 3 hrs and 6 hrs at 200°C.

<i>Sample</i>	<i>Average nanoridge width size with error (xc±σ) (nm)</i>	<i>The height of the layer (nm)</i>	<i>Average nanoparticle size (nm)</i>
ZnO	320.4±86.0	188	-
ZnO 3 Hrs	257.3±53.1	112	18.3 ± 0.6
ZnO 6 Hrs	218.3±61.9	111	15.7 ± 0.9

Furthermore, in uniformly formed ETLs [4.7], these processes may contribute to exciton generation as absorption of high-energy photons directed to the ZnO crystal structures occurs. Moreover, as photo-desorption occurs, free electrons result and increase the photoconductivity [4.11]. Other factors that may have affected the distribution of nanoridges width size per ITO area are further investigated and discussed in the optical spectroscopy section.

4.3.2.3 HR-SEM analysis of ZnO nanoridges produced under temperature calibration.

4.3.2.3.1 Bright-field HR-scanning electron microscopy (BF-HR-SEM)

Figure 4.6 (a)-(c) illustrates the unseeded ZnO NRs, seeded ZnO NPs-ZnO NRs with hydrothermally synthesised ZnO NPs at 140°C and 180°C, respectively. This section investigates the effect of ZnO NPs synthesis temperature on nanoridge ensembles' density and distribution size. The unseeded ZnO NRs sample in Figure 4.6 (a) shows the uniform formation of the nanoridges with random orientation and rugged ends of the ripple structure on the ITO structure. The surface morphology of the ZnO nanoridge structure in Figures 4.6 (b)-4.6 (c) shows highly undulated ripple structures with high density. These SEM images show that the surfaces of ITO substrates are fully covered with the ZnO NPs-ZnO NPs nanoridges. The diffusion rate of the zinc acetate precursor solution due to the addition of ZnO NPs prepared at 140°C and 180°C of ZnO nanoridges along the surface of the ITO was adequately high to sustain the formation of uniformity. Therefore, continuous lateral nanoridge structure formed simultaneously as the system underwent the nucleation process [4.12].

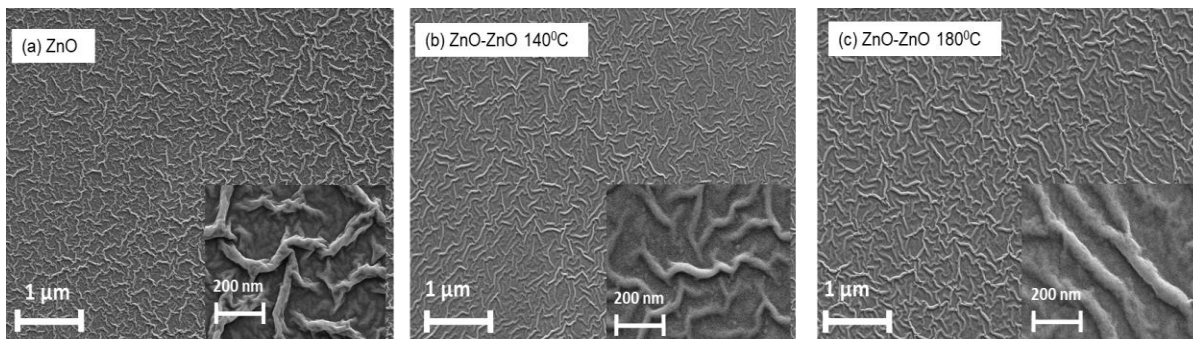


Figure 4. 6: SEM images of unseeded ZnO and seeded ZnO NPs-ZnO nanoridges calibrated at 140°C and 180°C for 6 hrs.

4.3.2.3.2 Width size distribution

Figure 4.7 shows the width size distribution histograms of the unseeded ZnO and seeded ZnO NPs-ZnO NRs as a temperature function.

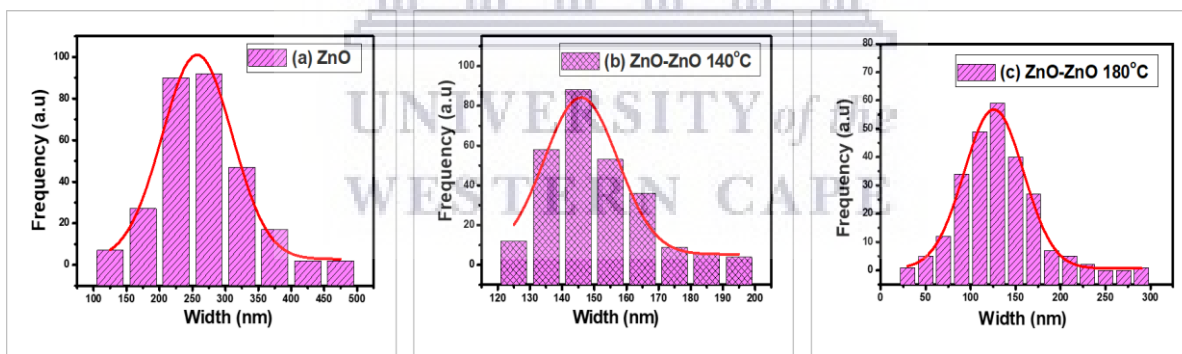


Figure 4. 7: Width size distribution of unseeded ZnO and seeded ZnO NPs-ZnO nanoridges calibrated at 140°C and 180°C for 6 hrs.

It must be noted that the discrepancies in the width size distribution, illustrated in Table 4.4, may be accounted for the error due to the non-uniformly aligned on the ITO. Furthermore, the decrease in the width size distribution of the ZnO-based nanoridges illustrated in Table 4.4 below may be due to the Van der Waals forces [4.13]. The forces may scatter the nanoridges' Zn²⁺ and O²⁻ ions at different valley-to-valley heights, widths and roughness. This scattering may support the transportation efficacy of dissociated electrons at the interface of the polymer absorber layer and the ETL from the absorbed charge carriers [4.7].

Table 4. 4: Average NPs sizes with error for ZnO NPs (temperature calibration), the Step-height, and the average nanoridges width size distribution of ZnO NPs-ZnO nanoridges calibrated at 140°C and 180°C for 6 hrs.

<i>Sample</i>	<i>Average nanoridge width size with error ($x \pm \sigma$)</i>	<i>The height of the layer (nm)</i>	<i>Average nanoparticle size</i>
ZnO	320.4±86.0	188	-
ZnO 140°C	246.4±74.7	100	36.9 ± 0.90
ZnO 180°C	125.8±33.0	96	20.9 ± 0.94

4.3.3 Optical properties of ZnO NPs-ZnO nanoridges

The use of various nanomaterials in different applications, including solar cells, has been witnessed in the past decades [4.14]. The applied nanomaterials usually possess physicochemical properties that best suit them for such applications. Hence their properties must be investigated prior to usage

in the designated application. For instance, thin-films of metal contacts and semiconductors have been widely utilised in solar cells, optimised to $<1 \mu\text{m}$ height. Usually, the properties such as the height, absorption coefficient, transmittance, and refractive index as a function of the wavelength are investigated to predict the behaviour of the thin-film to choose further the best suiting thin-film for the device's application [4.14]. Knowledge of these parameters helps determine the band gap.

Techniques such as the SEM, XRD, and stylus profilometry have been employed to study these properties of the nanostructures. Although all these sample analysis techniques may provide good precision and accuracy, the setback is that most of them are time-consuming, require large amounts of material for analysis and are very expensive [4.14].

Absorption and transmittance spectroscopies play a vital role in the characterization of materials. Unique optical properties of thin-films are a result of the collective electron vibrations in the conduction band, which get excited by the electromagnetic radiation from the valence band and become surface plasmon polariton resonances [4.14]. Therefore, these changes directly influence the refractive index in proximity to the nanomaterial surface, making it easier to analyse the optical properties of the nanomaterials using UV-Vis spectroscopy. Moreover, factors such as aggregation, variation in the particles size, and morphology affect the transition of electrons within the energy levels in material. Therefore the UV-Vis spectra can provide specific information on the absorption, transmission, and emission between 200 and 800 nm and is divided into the

ultraviolet (200–400 nm) and visible (400–800 nm) regions of the electromagnetic spectrum [4.14].

In this study, the optical properties of unseeded ZnO NRs and ZnO NPs-seeded ZnO NRs of hydrothermally synthesized ZnO NPs at 3 hrs and 6 hrs at 200°C, and 140°C and 180°C for 6 hrs through UV-Vis transmittance spectroscopy is investigated.

4.3.3.1 UV-Vis transmittance spectroscopy of ZnO nanoridges produced under period variation

Figure 4.8 illustrates the absorbance spectra of unseeded ZnO nanoridge thin-film and ZnO NPs-ZnO NRs that were hydrothermally prepared for 3 hrs and 6 hrs at 200°C. The absorbance spectra show a blue shift in the absorption of the fabricated ZnO-based NRs ranging from ~359-362 nm. The presence of a high level of defects leads to visible emission from the ZnO crystal structure observed at ~419-422 nm. The defects attributed to the visible emission may include zinc vacancies or any interstitial defects.

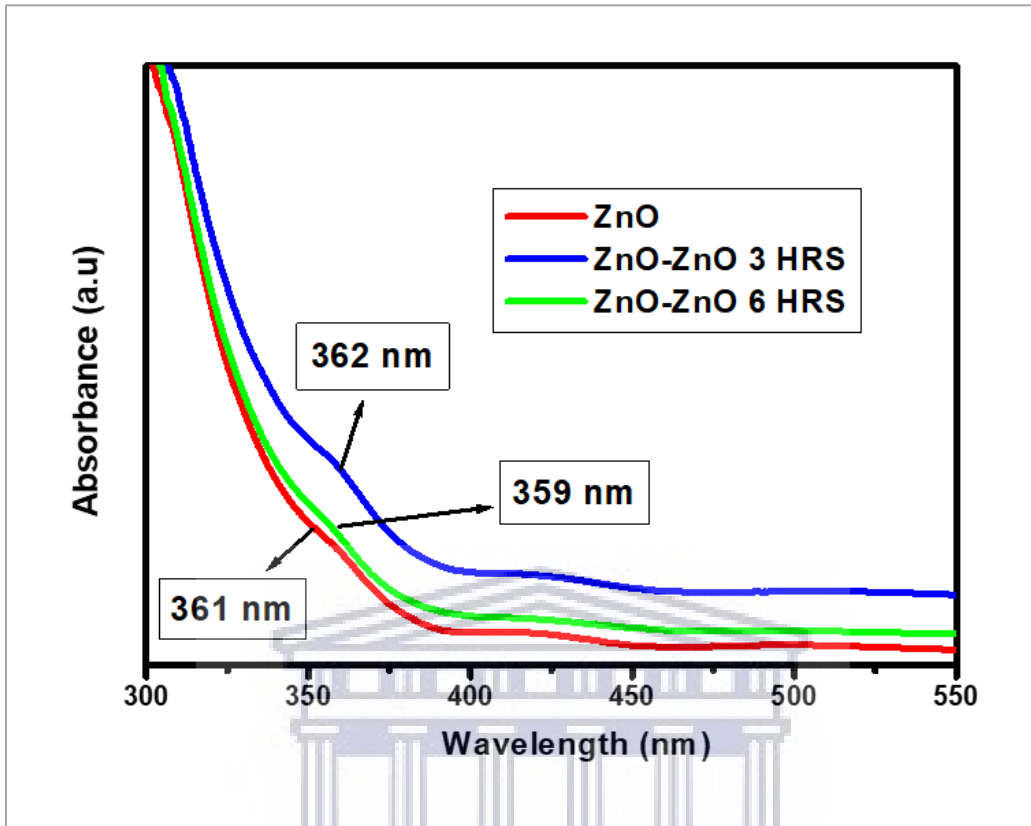


Figure 4. 8: Absorbance spectra of unseeded ZnO NRs and seeded ZnO NPs-ZnO NRs for 3 hrs and 6 hrs, at 200°C.

Figures 4.9 illustrates the spectra of transmittance as functions of wavelength for ZnO nanoridges prepared with bare zinc acetate solution and nanoridges prepared with the combination of ZnO NPs prepared hydrothermally for 3 hrs and 6 hrs at 200°C on clear quartz substrates, respectively.

All the samples fabricated on clear quartz substrates show high transparency $T > 75\%$ at the longer wavelength of $\lambda > 550$ nm in the visible region of the electromagnetic spectrum (Figure 4.9). From

transmittance results, the absorption edge at around ~359-360 nm corresponds to the intrinsic defects and from the electronic transitions between the VB to the CB.

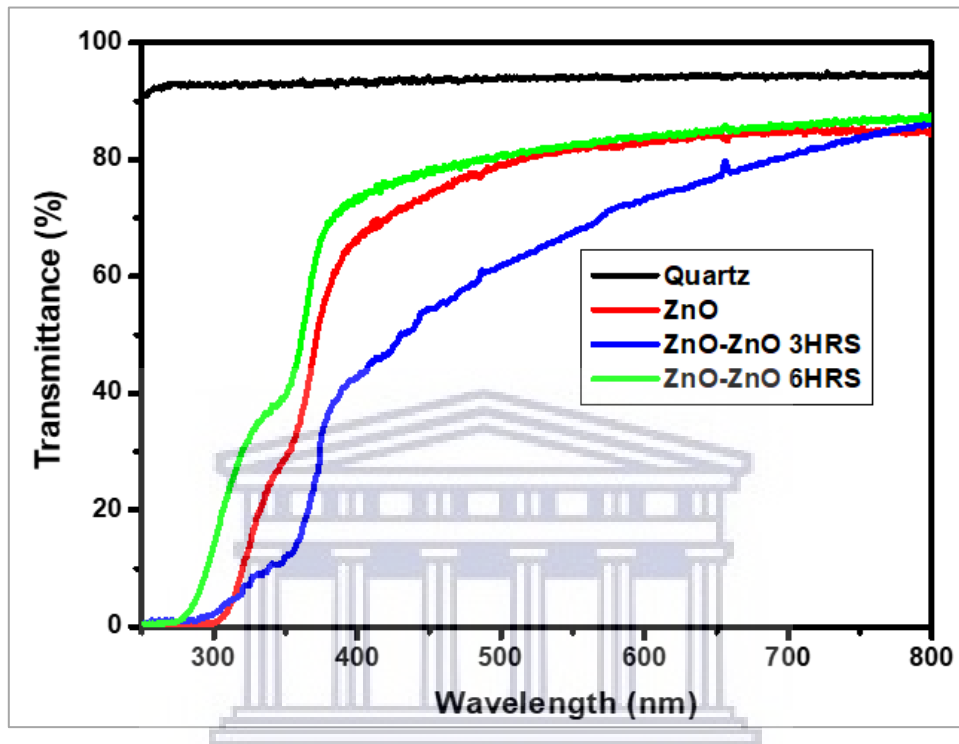


Figure 4. 9: Optical transmittance of unseeded ZnO NRs and seeded ZnO NPs-ZnO NRs for 3 hrs and 6 hrs, at 200°C.

Figure 4.10 shows the Tauc plots, representing the extrapolated band gap values for the unseeded ZnO NRs and the seeded ZnO NPs-ZnO NRs of ZnO NPs fabricated for 3 hrs and 6 hrs. The optical band gap values of ZnO nanoridge structures agree with the intrinsic band gap value of 3.37 eV, ranging from 3.19 to 3.32 eV [4.15]. The increase in the band gap as the width size distribution of the NRs at various synthesis period values decreases may have been attributed to

the overlapping of Zn and O atoms and the molecular orbitals, causing a decline in the gap between the VB to the CB [4.16].

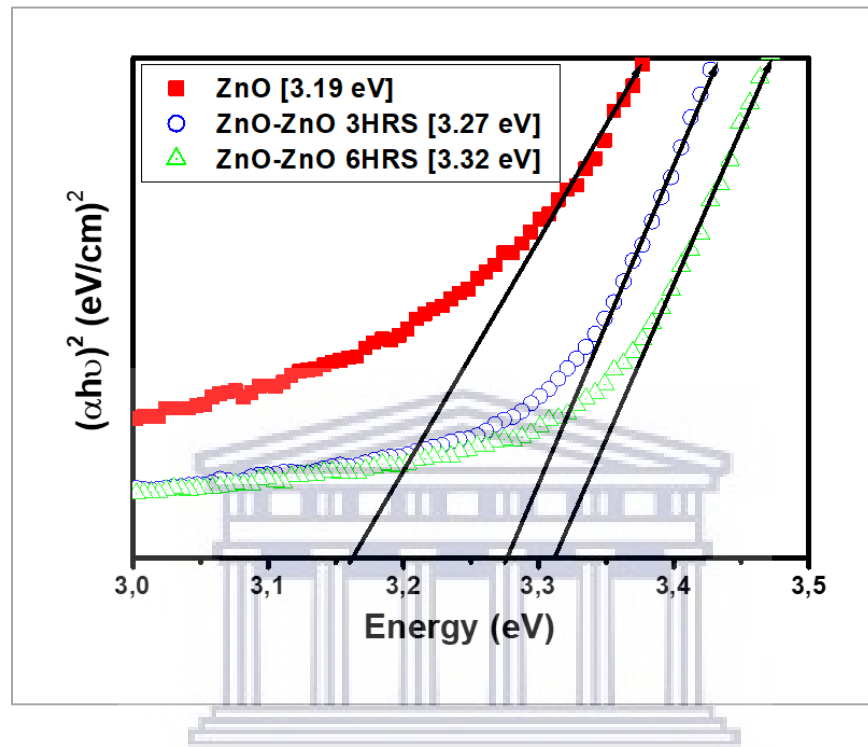


Figure 4. 10: Tauc plots with direct band gap values of unseeded ZnO NRs and seeded ZnO NPs-ZnO NRs for 3 hrs and 6 hrs, at 200°C.

Table 4.5 summarises the extrapolated band gap values, width size distribution and corresponding height values of the unseeded ZnO NRs and seeded ZnO NPs-ZnO NRs synthesised for 3 hrs and 6 hrs. The energy band gap is dependent on the period at which the incorporated ZnO NPs were produced with other fixed experimental conditions (Table 4.5). The incorporation of the ZnO NPs causes a decrease in the height of the thin-films. The width size distribution of the nanoridges decreases as the period of the hydrothermal synthesis of ZnO NPs increases. This may be

influenced by the decrease in the agglomeration of ZnO NPs structure with decreasing particle size of 18.3 ± 0.6 nm and 15.7 ± 0.9 nm for 3 hrs and 6 hrs respectively, observed in Figures 3.10 (a) and (b) in chapter 3. This result suggests that the transitioning electronic levels decreased as the width size of the nanoridges increased. The change in the particle size of the NPs influences the decrease in the width size of the nanoridges. The decrease is due to electron-hole pairs positioned at closer distances from each other. Therefore, the Coulombic interaction between them is considered, resulting in less significant energy required to excite an electron from the VB to the CB [4.17].

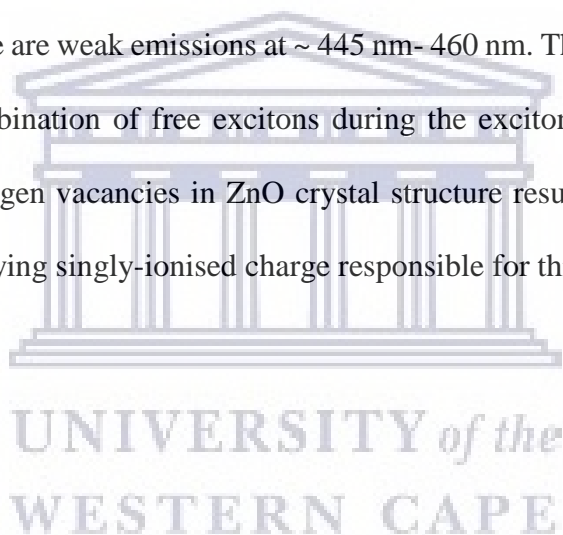
Table 4. 5: Band gap values (eV) and width distribution of the nanoridges (nm) and height values of the films (nm) of unseeded ZnO nanoridges ZnO NPs-ZnO NRs with ZnO NPs that were synthesised at 200°C for 3 hrs and 6 hrs.

<i>Sample</i>	<i>Band gap value (eV)</i>	<i>Average nanoridge width size with error ($\bar{x} \pm \sigma$) (nm)</i>	<i>The height of the layer (nm)</i>
ZnO	3.19	320.4±86.0	188
ZnO-ZnO 3 Hrs	3.27	257.3±53.1	112
ZnO-ZnO 6 Hrs	3.32	218.3±61.9	111

4.3.3.2 UV-Vis transmittance spectroscopy of ZnO nanoridges produced under temperature variation

The absorption spectra (Fig 4.11) show an exciton band at ~364, 360 and 357 nm for ZnO NRs and a blue-shift compared to the bulk value (~375 nm).

These bands corresponds to ZnO NPs-based ZnO nanoridges that were prepared from bare zinc acetate solution, and zinc acetate solution combined with ZnO NPs prepared at 140°C and 180°C for 6 hrs are illustrated in Figure 4.11. Therefore these samples show a blue-shift compared to the bulk value (~375 nm). There are weak emissions at ~ 445 nm- 460 nm. These long UV band values are attributed to the recombination of free excitons during the exciton-exciton collision event. Usually, singly-ionised oxygen vacancies in ZnO crystal structure result from recombination of photo-generated holes, carrying singly-ionised charge responsible for this defect [4.11].



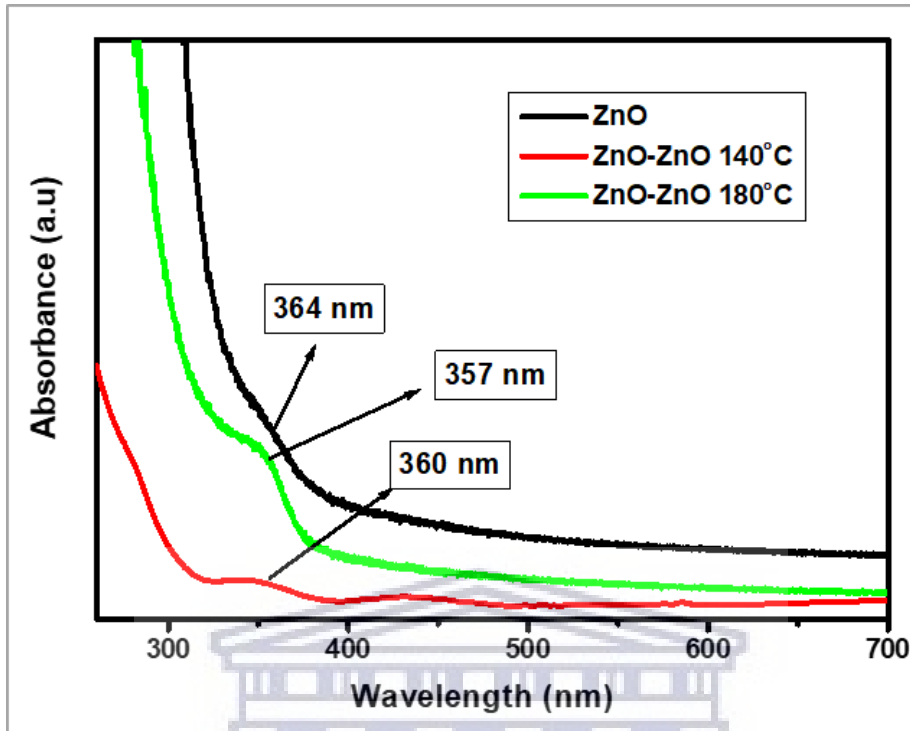


Figure 4. 11: Absorbance spectra of unseeded ZnO and seeded ZnO NPs-ZnO NRs with ZnO NPs hydrothermally fabricated at 140°C and 180°C for 6 hrs.

Figure 4.12 shows transmittance as a function of wavelength spectra for unseeded ZnO nanoridges and ZnO NPs-ZnO NRs with ZnO NPs seeds prepared hydrothermally at 140°C and 180°C for 6 hrs on a clear quartz substrate, respectively.

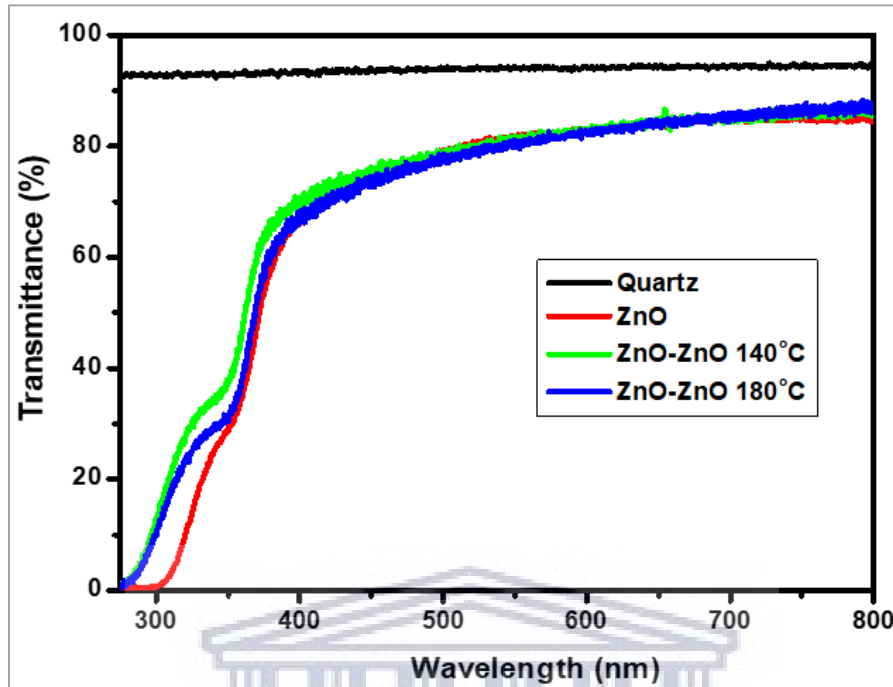


Figure 4. 12: Optical transmittance of ZnO nanoridge structured thin-films deposited with the combination of bare zinc acetate solution and ZnO nanoparticles synthesised at 140°C and 180°C for 6 hrs

All the samples fabricated on clear quartz substrates show $T > 75\%$ transparency at the longer wavelength of $\lambda > 410$ nm in the visible region of the electromagnetic spectrum (Figure 4.12). The absorption edge at around ~ 356 - 360 nm corresponds to the intrinsic defects from the transmittance results. The absorption edge results from the electronic transitions between the VB to the CB. These results are also reported by F. Bouaichia [4.15].

Figure 4.13 illustrates the Tauc plots, representing the extrapolated band gap values at $\alpha = 0$ for the above set of experimental conditions, respectively.

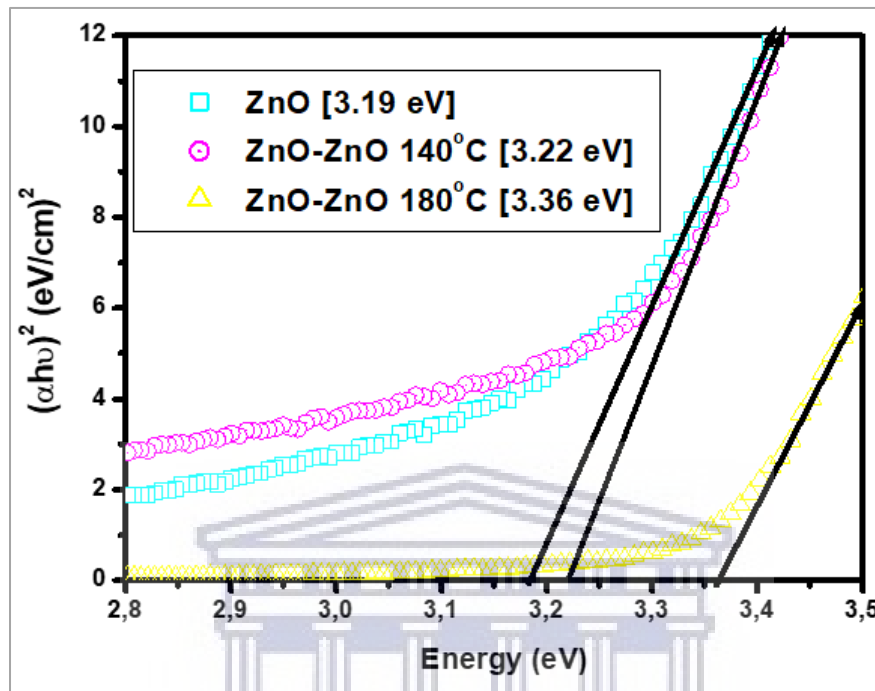


Figure 4. 13: Tauc plots with direct band gap values of ZnO NPs-ZnO nanoridges calibrated at 140°C and 180° for 6 hrs.

The transparency of these samples is directly related to the morphology and the height of the thin-film layers. The decreased thin-film height may provide enhancement of the optical properties of the ZnO-nanoridges for photovoltaic application. The ZnO nanoridge structures' optical band gap values (Figure 14.13) agree with the intrinsic band gap value of 3.37 eV as they range from 3.19-3.36 eV [4.15]. Due to the atoms and the molecular orbitals overlapping, a decrease in the gap between the VB and CB causes a reduction in the band gap [4.15]. The presence of green band emissions observed ~ 445 nm- 460 nm for the samples is mainly attributed to excess Zn ions in

the sample, as was reported by S. Hussain [4.18]. However, other green band emission mechanisms observed in the absorption spectra (Figure 4.11) contribute to the lattice defects.

Observed in Table 4.6 is the step height of the ZnO layer affects the band gap value.

Table 4. 6: Band gap values (eV) and average width distribution of the nanoridges (nm) and height values of the films (nm) of ZnO NPs-ZnO nanoridges calibrated at 140°C and 180°C for 6 hrs.

<i>Sample</i>	<i>Band gap value (eV)</i>	<i>Average nanoridge width size with error ($x\pm\sigma$) (nm)</i>	<i>The height of the layer (nm)</i>
ZnO	3.19	320.4±86.0	188
ZnO-ZnO 140°C	3.22	246.4±74.7	100
ZnO-ZnO 180°C	3.36	125.9±33.0	96

There is a decrease in the height of the seedless ZnO NRs, ZnO NPs-seeded ZnO NRs at 140°C and 180°C and a decrease in the average nanoridge width size with an increase in the respective band gap values. The shift in the band gap values may be due to an increase in the oxygen vacancies at higher temperatures. These oxygen vacancies are responsible for the efficient photocatalysis process [4.19]. Therefore, these samples' properties, such as high transparency, 50 nm < optimal height < 300 nm, may enhance the working of IOSCs.

4.4 Conclusion

ZnO's morphological and optical properties were investigated using stylus profilometry, high-resolution scanning electron microscopy (HR-SEM), and ultraviolet-visible (UV-vis) transmittance spectroscopy.

The SEM results have shown that the nanoridge structures depend on the synthesised period and temperature of the incorporated ZnO NPs. The morphology of the thin-films prepared using a sol-gel method can be easily controlled by adjusting the temperature and period conditions of the hydrothermal synthesis ZnO NPs incorporated as seeds in the formation of the ZnO-based NRs.

UV-vis absorption spectra showed that the absorption band of the seeded ZnO NRs is around 355 - 360 nm, which is blue-shifted relative to the bulk exciton absorption (373 nm). This blue-shift is due to NPs strain as the synthesis period and temperature are altered. The optical properties of ZnO thin-films make it suitable to serve as ETL in an inverted OSC device. Furthermore, electrical properties are outlined in chapter 5. The study will explore the effect of nanoridge step height due to incorporating ZnO NPs that were hydrothermally synthesised at various synthesis temperatures and period conditions on the performances of inverted solar cells.

References

- [4.1] P.M. Aneesh, K.A Vanaja, M.K. Jayraj., "Synthesis of ZnO nanoparticles by hydrothermal method," *Optoelectronics Devices*, vol. 6639, pp. 1-9, 2007.
- [4.2] B.G. Rao, D. Mukherjeer and B.M. Reddy, "Chapter 1-Novel approaches for preparation of nanoparticles-Sol-Gel Method," in *Nanostructures for Novel Therapy*, Amsterdam, Elsevier, 2017, pp. 1-36.
- [4.3] R. Wahab, Y-S. Kim and H-S. Shin, "Synthesis, Characterization and Effect of pH Variation on Zinc Oxide Nanostructures," *Material Transactions*, vol. 50, no. 8, pp. 2092-2097, 2009.
- [4.4] V. Siderov, D. Mladenova, R. Yordanov, V. Milenkov, M. Ohlidal, O. Salyk, I. Zhivkov, and M. Weiter, "Film thickness measurement by optical profilometer MicroProf® FRT," *Bulgarian Chemical Communications*, vol. 45, no. B, pp. 194-197, 2013.
- [4.5] N.A.A. Shaari, S.M.M. Kasim, N.S.M. Sauki, and S.H. Herman, "The effect of the sol-gel spin-coating deposition technique on the memristive behaviour of ZnO-based memristive device," *Materials Science and Engineering*, vol. 99, pp. 1-8, 2015.

- [4.6] P.S. Mbule, T.H. Kim, B. S. Kim, H.C. Swart, O.M. Ntwaeaborwa, "Thickness optimization of ZnO/CdS/CdTe solar cell by numerical simulation," *Solar Energy Materials & Solar Cells*, vol. 111, pp. 6-12, 2013.
- [4.7] D. Parashar, V.S.G. Krishna, S.N. Moger, R. Keshav, and M.G. Mahesha, "Thickness Optimization of ZnO/CdS/CdTe Solar Cell by Numerical Simulation," *Transactions on Electrical and Electronic Materials*, vol. 21, p. 587–593, 2020.
- [4.8] M.F.A. Alias, R.M. Aljarrah, H.KH. Al-Lamy, and K.A.W. Adem, "Investigation the Effect of Thickness on the Structural and Optical Properties of Nano ZnO Films Prepared by d.c Magnetron Sputtering," *International Journal of Application or Innovation in Engineering & Management (IJAIEM)*, vol. 7, no. 2, pp. 198-203, 2013.
- [4.9] S.N. Shaha, S.I. Alib, S.R. Alia, M. Naema, Y. Bibic, S.R. Alia, S.M. Razaa, Y. Khand, and S.K. Sherwani, "Synthesis and Characterization of Zinc Oxide Nanoparticles for Antibacterial Applications," *Journal of Basic & Applied Sciences*, vol. 12, pp. 205-210, 2016.
- [4.10] E. Kärber, T. Raadik, T. Dedova, T. Krustok, A. Mere, V. Mikli, and M. Krunks, "Photoluminescence of spray pyrolysis deposited ZnO nanorods," *Nanoscale Research Letters*, vol. 6, p. 359, 2011.

- [4.11] M. Kashif, U. Hashim, M.E. Ali, K.L. Foo, M. Syed, and U. Ali, "Morphological, Structural, and Electrical Characterization of Sol-Gel-Synthesized ZnO Nanorods," *Journal of Nanomaterials*, pp. 1-8, 2013.
- [4.12] S.I. Park, Y.T. Choe, H. Baek, J. Heo, J.K. Hyun, J. Jo, M. Kim, N-J. Kim, and G-C. Y, "Growth and optical characteristics of high-quality ZnO thin films on graphene layers," *APL Materials*, vol. 3, pp. 1-7, 2015.
- [4.13] T. Amakali, L.S. Daniel, V. Uahengo, N.Y. Dzade, and N.H. de Leeuw, "Structural and Optical Properties of ZnO Thin Films Prepared by Molecular Precursor and Sol-Gel Methods," *Crystals*, vol. 10, no. 2, pp. 1-11, 2020.
- [4.14] B.P. Kafle, "Introduction to nanomaterials and application of UV–Visible spectroscopy for their characterization," in *Chemical Analysis and Material Characterization by Spectrophotometry*, Elsevier, 2020, pp. 147-198.
- [4.15] F. Bouaichia, H. Saidia, A. Attafa, M. Othmanea, and N. Lehrakia, "The synthesis and characterization of sprayed ZnO thin films: As a function of solution molarity," *Main Group Chemistry*, vol. 15, no. 1, pp. 57-66, 2016.

- [4.16] B.M. John, S.W. Mugo, and J.M. Ngaruiya, "Dependence of optical band gap on the crystallite size of TiO₂ thin film prepared using Sol-Gel Process," *European Journal of Material Science*, vol. 8, no. 1, pp. 1-12, 2017 August 2017.
- [4.17] E. Tan, "What Makes Nanoparticles Different," in *An Introduction to Nanoparticles*, 2002, pp. 1-6.
- [4.18] S. Hussain, "Investigation of Structural and Optical Properties of Nanocrystalline ZnO," *Material Science*, pp. 15-24, 2008.
- [4.19] N. Verma, S. Bhatia, R.K. Bedi, "Effect of Annealing Temperature on Nanoparticles ZnO and its Applications for Photocatalytic Degradation of DR-31 dye," *International Journal of Pure and Applied Physics*, vol. 13, no. 1, pp. 118-12, 2017.



UNIVERSITY of the
WESTERN CAPE

Chapter 5: Synthesis and Characterisation of

Inverted Organic Solar Cells



UNIVERSITY *of the*
WESTERN CAPE

Chapter 5: Synthesis and Characterisation of Inverted Organic Solar Cells

Introduction

This section describes the fabrication of the inverted organic solar cells for this study. The ITO operates as the hole-collecting electrode (anode) in OSCs, and the metal-based thin-film works as an electron-collecting electrode (cathode). In principle, the ITO in inverted OSCs can collect electrons and holes depending on the HOMO and LUMO electronic transition between the adjacent layers within the IOSCs. Moreover, the working function of ITO lies between the frontier orbitals of the common IOSCs [5.1]. However, ITO is a conductive oxide that requires adjustment when incorporated in IOSCs to achieve a working IOSC. The polarity of ITO is required to be optimised by depositing an ETL with a low work function on ITO to adjust the ITO interface and attain efficient electron collection. A ZnO layer is commonly used as ETL material to ensure a working IOSC.

Different methods have been studied for ZnO production. Generally, there are two solution-based ways of fabricating ZnO thin-films. The solution can be deposited as water-based or as an organic solvent-based solution [5.1]. To obtain a working solar cell, the active layer, in this case, the P3HT:PCBM active layer, must be optimised. Molar ratios, the type of solvent used, film thickness, period of synthesis, temperature, and concentration are the parameters that influence the performance of IOSCs. Therefore it is essential to pay attention to every parameter, also looking out for any possible threat to the purity and thickness precision and accuracy of IOSCs' layers

during deposition. Potential threats may include improper substrate cleaning, dust, high pitch noise, etc. The solution-based synthesis of P3HT: PCBM is supported as it is an affordable method, however inaccurate as the system is not programmed to provide the desired results, such as full surface area coverage, thickness value, etc. [5.1]. These possible threats hinder the separation and transportation of electrons and holes to designated electrodes before recombination. Due to the high contact angle and hydrophobic nature of the P3HT: PCBM, it is continuously tricky to spin-coat MoO₃ [5.1]. Therefore, although expensive as operating a metal vapour deposition system, as explained in Chapter 1, section 1.4.3.3.2, MoO₃ is deposited onto the active layer as HTL through metal vapour deposition. In metal vapour deposition, the thermalised metal atoms are directed onto the active layer, post adsorption onto the film; the atoms then diffuse onto the surface of the film until the formation of the nucleus on the surface of the film [5.2]. These results can be achieved at any point of the given period, as the adsorption and diffusion depend only on the desorption rate [5.1]. The metal-based thin film is also deposited through thermal vapour deposition.

5.1 Experimental setup

5.1.1 Fabrication of IOSC layers

The IOSCs comprise a stack of indium tin oxide-coated substrates, ZnO NRs thin-films/ZnO NPs-ZnO NRs, RR-P3HT: PCBM thin-films, molybdenum oxide layers and top electrodes as silver (Ag).

The top electrode-ITO layer was commercially obtained. Preparation of the electron transport layer (ETL) is illustrated in section 4.1 in Chapter 4. In preparation of the active layer, the hole transport

layer (HTL) and the Ag electrode: 1:1 P3HT: PCBM was prepared by stirring 15 mg/ml P3HT and 15 mg/ml PCBM in 1, 2 dichlorobenzene at 60°C on a Lasec Hot plate stirrer; stirring at 400 rpm, overnight. 0.03 µL of the stirred solutions was spin-coated on top of ITO/ZnO-based ETLs at 900 rpm for 100 seconds using Ossila spin coater and annealed at 150°C for 30 minutes using Chemat (Technology Inc) hot plate. Due to P3HT/PCBM's rapid degradation, the samples were immediately taken for the deposition of MoO₃ under thermal deposition. 100 mg of MoO₃ was thermally evaporated on ITO/ZnO-based ETL/P3HT: PCBM at 5.7×10^{-4} mbar for 2 minutes, yielding films of ~11.8 nm thickness. Ultimately, 100 mg Ag was thermally evaporated at 60-65 °C and 3×10^{-4} mbar for 14 minutes on top of ITO/ETL/P3HT: PCBM/MoO₃, yielding an Ag thin-film of ~100 nm Ag thickness. All thermal evaporation experiments were done using the Vacutec vacuum system in the Cluster Apparatus for Device Application Research (CADAR).

The schematic diagram of the band gap diagram of IOSCs design and 3D cross-sectional diagram of on PCBM: P3HT-based IOSCs, with ZnO nanoridge-based layer, MoO₃, Ag, and ITO as the active layer, ETL, HTL, anode, and cathode, respectively, are illustrated in Figure 5.1 (a) and (b). The flow diagram in Figure 5.2 summarises the steps involved in fabricating IOSCs in this study.

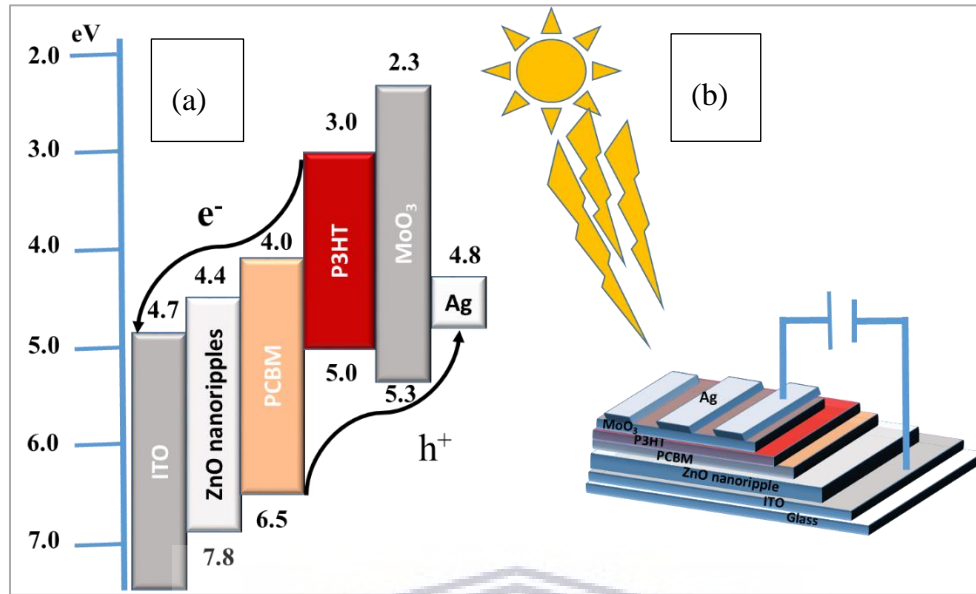
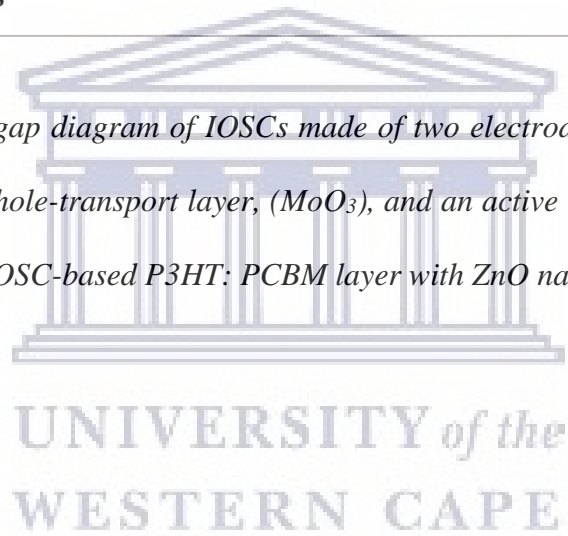


Figure 5. 1: (a) The band gap diagram of IOSCs made of two electrodes (indium-tin-oxide and silver (Ag)), ETL (ZnO), a hole-transport layer, (MoO_3), and an active layer (P3HT: PCBM) (b) Schematic diagram of the IOSC-based P3HT: PCBM layer with ZnO nanoridge layer as ETL.



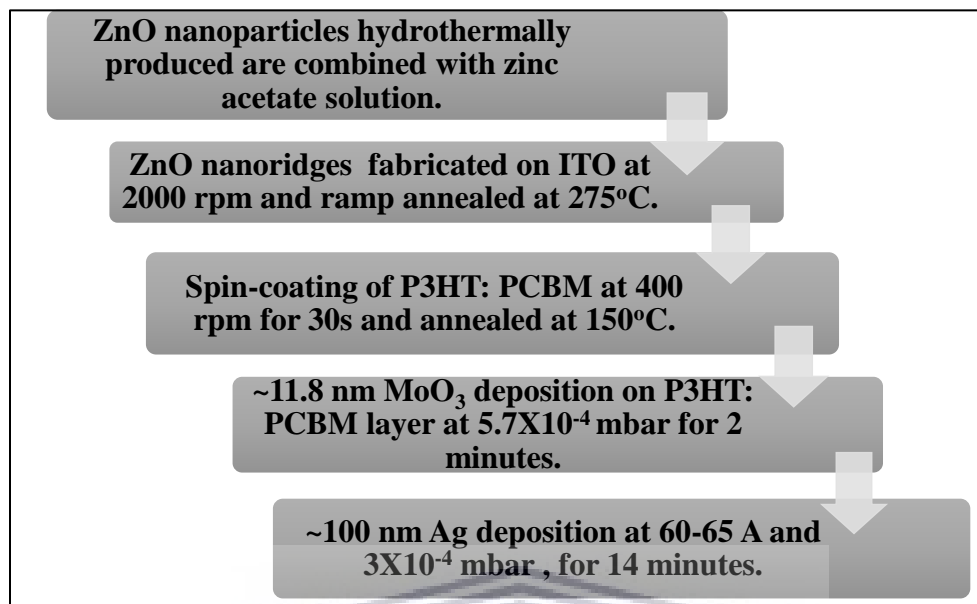


Figure 5. 2: The flow chart diagram illustrating the steps involved in fabricating IOSCs.

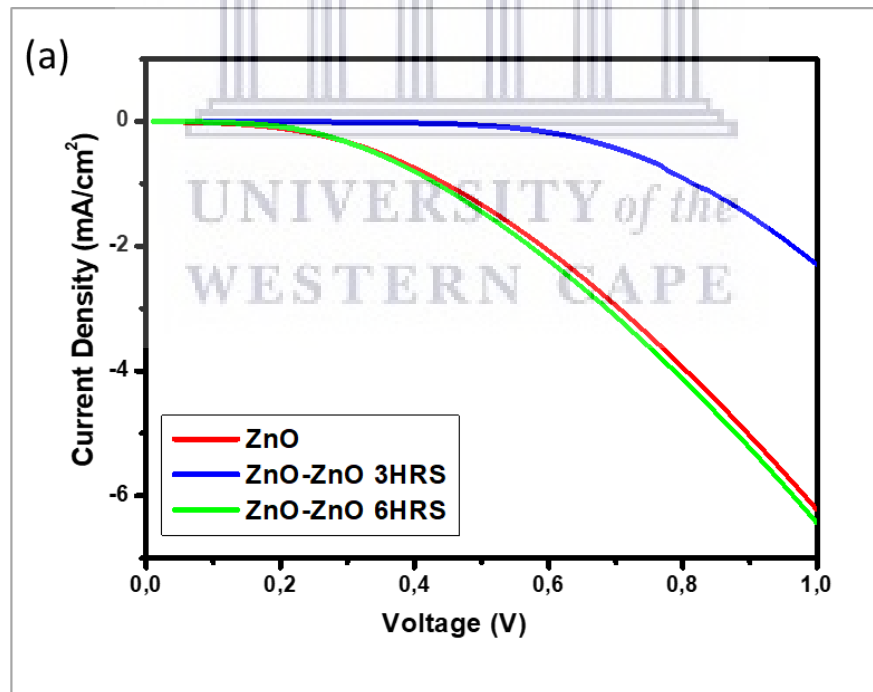
5.2 Inverted Organic Solar Cells I-V Testing set-up

Dark measurements and measurements under AM 1.5 simulated illumination of 100 mW/m^2 were taken for the fabricated IOSCs. Characteristic J-V curves were generated from the dark and simulated illumination measurements, and graphs are illustrated in Figure 5.3 (a) and (b) and Figure 5.4 (a) and (b) in section 5.3 below. Solar cell area amounted to 0.0256 cm^2 of the individual solar cells of the prepared IOSCs in this study that were measured and analysed.

5.3 IOSCs' J-V Curves results and discussion

5.3.1 Analysis of J-V curves of IOSC fabricated with ZnO NPs-ZnO nanoridges ETLs (ZnO NPs under synthesis period control)

ETLs assist in transporting dissociated charge carriers from the polymer layer to the ITO. The change in the morphological, structural and optical properties of ETLs can affect the performance of IOSC. Therefore to investigate the effect of seeded ZnO NRs by hydrothermally synthesised ZnO NPs as seeds at various ETL synthesis period on the performance of IOSCs, J-V curves were obtained and are presented in Figure 5.3 (a) and (b).



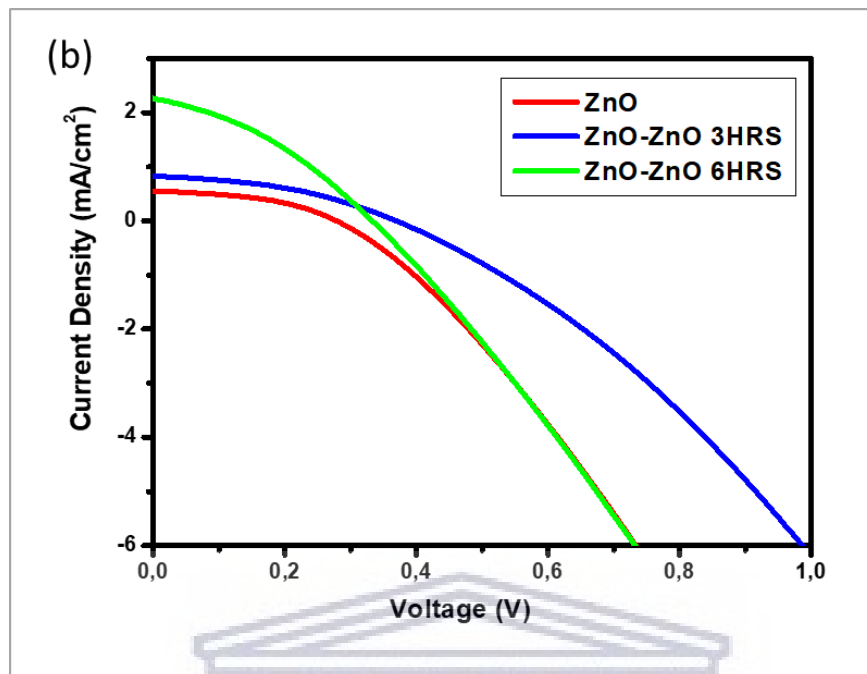


Figure 5. 3: (a) Dark JV-curve measurements and (b) JV-curves of IOISC containing unseeded ZnO NRs ETL and seeded ZnO NPs-ZnO NRs ETLs of ZnO NPs synthesised for 3 hrs and 6 hrs at 200°C.

The PCE, fill factor, open-circuit voltage, and short-circuit current density are vital in clarifying the efficacy of charge carrier dissociation and transportation of the respective electrodes in IOSCs. Therefore, IOSCs show respective PCEs, fill factor values, open-circuit voltages, short-circuit current densities, and the step height and width of the nanoridges are presented in Table 5.1.

As the addition of ZnO NPs as seeds in ZnO NRs-ETLs affects the height and width of the NRs, it also affects the performance of the IOSCs. The IOISC made with unseeded ZnO NRs as ETL showed PCE of 0.40%, and as seeded ZnO NRs as ETL were utilised in the IOISC, the PCE

increased to 0.63%. Moreover, seeding the ZnO NR-ETL with ZnO NPs prepared at an increased synthesis period of 6 hrs, the IOSC showed improvement in the PCE value of 1.66%. The short-circuit current density increases with high PCE, while the V_{OC} shows some discrepancies that may be attributed to the fluctuating photon absorption at the donor-acceptor interface within the IOSC. The ETLs showed band gap values (3.19-3.32 eV) less than the intrinsic value of 3.37 eV. However, the improvement of short-circuit current density suggests enhancement of the carrier mobility and conductivity induced by ZnO NPs-ZnO NRs [5.3]. The data in Table 5.1 show that the efficiency of the IOSCs is affected by step-height and the width size of the nanoridges. The IOSC containing unseeded ZnO NRs hold the highest step-height and contain nanoridges with large width sizes. The addition of the hydrothermally synthesised ZnO NPs led to the PCEs increasing with decreasing step-height of the ZnO NPs-ZnO NRs thin films. This result suggests that the high transparency of $T > 75\%$ observed in the transmittance spectra of these samples allow efficient generation and carrier mobility at the donor-acceptor interface, thus improving the PCEs of the IOSCs.



UNIVERSITY of the
WESTERN CAPE

Table 5. 1: Power conversion efficiency (PCE), fill factor (FF), open-circuit voltage (V_{oc}), and short-circuit J_{sc} of IOSC containing unseeded ZnO NRs ETL and seeded ZnO NPs-ZnO NRs ETLs of ZnO NPs synthesised for 3 hrs and 6 hrs at 200°C.

<i>Device</i>	<i>PCE (%)</i>	<i>FF</i>	<i>J_{sc} (mA/cm²)</i>	<i>V_{oc} (V)</i>	<i>Height of the layer (nm)</i>	<i>Average nanoridge width size with error ($x \pm \sigma$) (nm)</i>
ZnO	0.40	0.44	0.54	0.28	188	320.4±86
ZnO-ZnO 3 hrs	0.63	0.42	0.83	0.98	112	257.3±53
ZnO-ZnO 6 hrs	1.66	0.38	2.27	0.33	111	218.3±62

5.3.2 Analysis of J-V curves of IOSC fabricated with ZnO NPs-ZnO nanoridges ETLs (ZnO NPs under synthesis temperature control)

Figure 5.4 (a) J-V curves: measurements in the dark and (b) illustrate the J-V curves generated from IOSC with ETLs fabricated from ZnO prepared with bare zinc acetate solution and zinc acetate solution combined with ZnO NPs prepared for 140°C and 180°C for 6 hrs. Table 5.2 is the summary of power conversion efficiency (PCE), fill factor (FF), open-circuit voltage (V_{oc}), and short-circuit current density (J_{sc}) of the IOSCs fabricated, the height of the layers (nm) and average

nanoridge width size at various temperature conditions. Here, the effect of incorporating hydrothermally synthesised ZnO NPs at various temperature values to the ZnO NRs on the IOSC performance is illustrated.



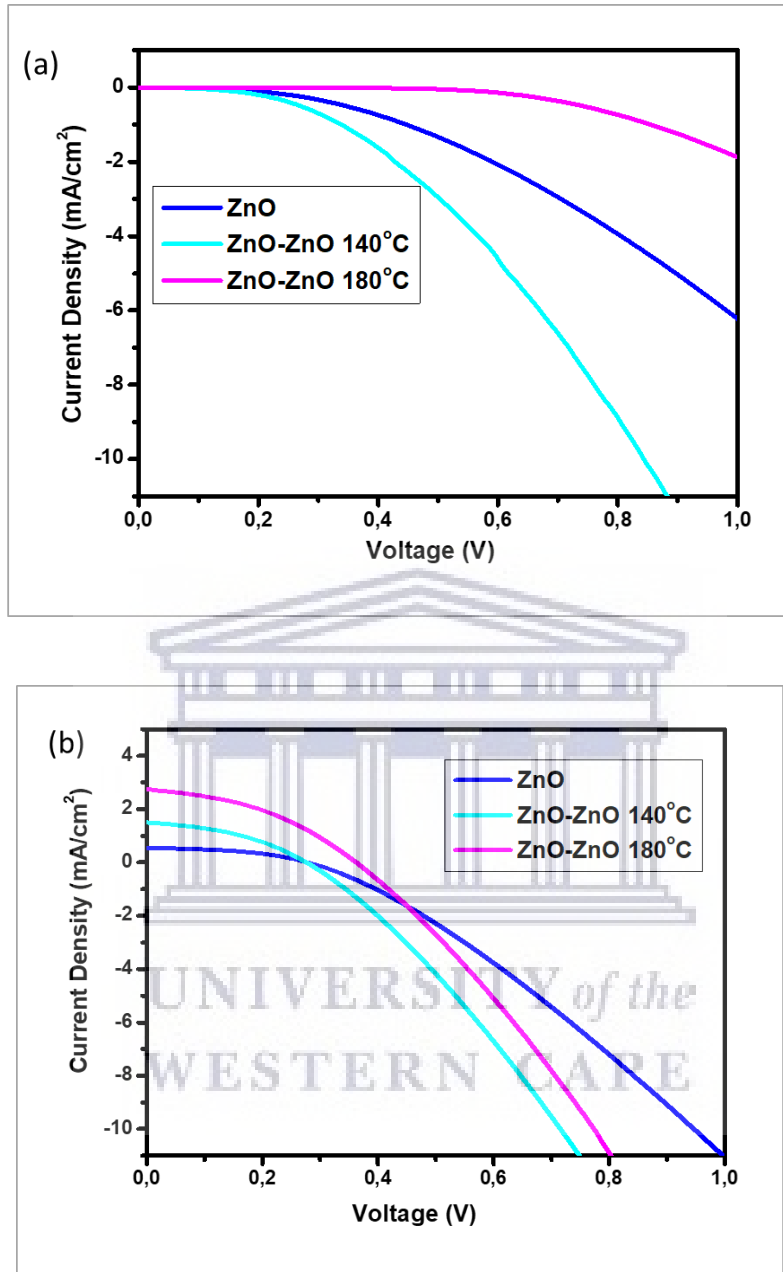


Figure 5. 4: (a) Dark JV-curve measurements and (b) JV-curves of IOSCs containing unseeded ZnO NRs ETL and seeded ZnO NPs-ZnO NRs ETLs of ZnO NPs synthesised at 140°C and 180°C for 6 hrs.

The performance of the IOSCs is dependent on the incorporation of hydrothermally synthesised ZnO NPs as seeds in the ZnO NRs ETLs. The efficiencies increase as the temperature increases while the width sizes and step-height decrease. These changes in the properties of the NRs causes the short-circuit current density to increase with the temperature, as shown in Figure 5.4 (b) and Table 5.2.

Table 5. 2: Power conversion efficiency (PCE), fill factor (FF), open-circuit voltage (V_{oc}), and short-circuit J_{sc}) of IOSC containing unseeded ZnO NRs ETL and seeded ZnO NPs-ZnO NRs ETLs of ZnO NPs synthesised at 140°C and 180°C for 6 hrs, respectively.

<i>Device</i>	<i>PCE (%)</i>	<i>FF</i>	<i>J_{sc} (mA/cm²)</i>	<i>V_{oc} (V)</i>	<i>Height of the layer (nm)</i>	<i>Average nanoridge width size with error ($x\pm\sigma$) (nm)</i>
ZnO	0.40	0.440	0.54	0.280	188	320.4±86.0
ZnO-ZnO 140°C	0.97	0.399	1.49	0.807	100	246.4±75.0
ZnO-ZnO 180°C	2.30	0.397	2.73	0.673	96	125.9±33.0

The stability of the IOSC is an imperative factor that significantly contributes to the device's electrical characteristics [5.4]. Stability is greatly influenced by the morphology of the thin-films [5.5]. Increasing PCEs from 0.40% to 2.30% (Table 5.2) suggests increasing the IOSCs layers' interface stability. Therefore the increasing PCE indicates that the morphology of the thin-films, seeded ZnO NPs-ZnO NRs positively influence the performance of the IOSCs. The formation of thinner films containing lower width sizes of the nanoridges decreases the phase separation

between the donor-acceptor interfaces such that the charge generation may increase, thus increasing percolation pathways for charge carrier generation [5.6].

5.4 Conclusion

In general, surface morphology, thickness, area coverage, etc., of interfacial charge-transporting layers can critically affect IOSCs' parameters. These parameters include the fill factor and the open-circuit voltage (V_{OC}), whereby an increase in series resistance favours an increase in the current generated by the solar cell and vice versa [5.7].

In this study, the incorporation of ZnO NPs directly affects the performance of IOSCs as they exhibit lattice parameters values that deviate from the theoretical parameter values of a and c of ZnO at a small scale. Lattice parameters play an essential role in the development of semiconductor devices [5.8]. These crystallographic properties are affected by the free-electron concentration of foreign elements, external strain and temperature. Furthermore, the potential at the bottom of the conduction band occupied with electrons is affected. Due to these factors, some changes in the ionic radii may exist between the defects and foreign elements as the matrix ions are substituted [5.8]. Therefore the slight deviation from an ideal hexagonal wurtzite structure observed in UDM analysis in Table 3.3 and 3.4 in sections 3.3.2.1 and 3.3.2.2 of Chapter 3 is attributed to ionicity and lattice stability. Furthermore, point defects that include V_{O}^{+} and Zn anti-site and extended defects which causes the slight deviation in the lattice constant(s) of the hexagonal wurtzite structure and thus affect the IOSCs [5.8].

The change in optical properties of ETLs is facilitated by careful filling of optical bands by particles. Semiconductors have an unprecedented tunability in the optical features [5.9]. Tuning of optical properties of semiconductors is often associated with intrinsic and extrinsic defects. Intrinsic defects are often mainly due to excitonic effects, whereby an overlap of the band-edge absorption steps occurs due to the excitonic resonance facilitated by Coulomb interaction [5.9, 5.8]. Excitons may be free and bound; therefore, they can exhibit excited states given that the sample is of high quality with less to no impurities [5.8]. Extrinsic effects are associated with the presence of dopants or defects in the crystal structure. The extrinsic effects usually cause discrete electronic states in the band gap (valence band and conduction band). Therefore, extrinsic effects “in turn” influence or affect the absorption edge and the emission processes [5.8]. Moreover, the change in the IOSC performances illustrated in Tables 5.1 and 5.2 are mainly due to the intrinsic and extrinsic defects. These defects lie at/within the surface of the ETLs, as shown in Tables 4.5 and 4.6 in Chapter 4. ZnO is a TCO that has a direct band gap. The change in the carrier concentration leads to a shift in the absorption edge. This change is called the Burstein-Moss shift [5.10]. Therefore, an absorption edge shifts of ZnO NPs-based NRs observed in Chapter 4-section 4.3.3 may have been due to the Burstein-Moss effect. Furthermore, the unprecedented Burstein-Moss shift may have led to the observed efficiencies in Tables 5.1, and 5.2 of J-V curves illustrated in Figures 5.3 and 5.4, respectively. Moreover, it should be noted that the intrinsic effects are due to emissions such as the green emission, near UV-emission band and occasionally a yellow emission band in some instances [5.8].

The increase in step-height may have led to an improvement in the performance of the IOSC, as it should be noted that the buffer layer fabricated from ZnO NPs at 180°C combined with zinc acetate solution has shown an efficiency value of 2.30%. The value of efficiency has increased with decreasing height. These PCEs values suggest efficient photon absorption, dissociation of charge carriers and transfer of dissociated electrons by the ETL to the ITO, as reported previously by D.C. Lim et al., [5.11] and N. Sekine et al., [5.12]. These results suggest an increase in the charge carriers produced at the surface of the active layer and an increase in charge carrier transportation to the respective electrodes for the 180°C sample compared to the rest of the models, both under period calibration and temperature calibration. There is an illustration that the devices are functional, as they behave like a diode under dark measurements and show a change in J_{sc} as they were placed under AM 1.5 100 mW/m² illumination.

Analysing the IOSC fabricated under period variation, the highest PCE obtained is 1.66%, corresponding to IOSC synthesised with the incorporation of ETL synthesised with ZnO bare acetate solution and ZnO NPs prepared 6 hrs. The highest efficiency obtained is 2.30%, corresponding to ZnO nanoridge ETL-based IOSC prepared by adding ZnO NPs prepared at 180°C for 6 hrs to zinc acetate solution. The height of the ETL layer may have influenced the value of the efficiency and the decrease in width of the nanoridges formed, leading to an increase in the number of electrons injected from the active layer into the ETL and transported to the respective electrode effectively. Furthermore, the voltages show an increase compared to their adjacent dark J-V curves, indicating an increase in the squareness of the J-V curves. The increase in voltage

shows that the maximum power the solar cells produced increased under standard testing conditions.

Considering the recent technological standpoint and developments: the continual increase of PCEs and advancement of long-term stability of IOSCs emerge as an essential issue to accelerate the achievement of low-cost solar cells. As it has been continuously emphasised in the above chapters, in terms of PCE and stability improvement, inverted organic solar cells containing highly transparent ZnO NPs-seeded ZnO NR-based ETLs are considered a good design. A study on the effect of ZnO NPs in ZnO NRs for PCE improvement and stability of IOSCs has been done. The devices illustrate an improvement compared to the reference device whereby the ZnO ETL was fabricated in the absence of ZnO NPs. The reference device showed a PCE value of 0.40%, and an improvement in PCE was obtained as the highest PCE value is 2.30% due to the incorporation of ZnO NPs produced at 180°C for 6 hrs. Furthermore, IOSCs calibrated under temperature series show improved efficiency compared to the devices fabricated under period calibration. In conclusion, future work on ZnO nanoridges based-IOSC may include further calibrations under different temperature conditions to achieve the optimum temperature condition, further improving IOSC to a commercial PCE value.

References

- [5.1] V. Kumar, "Fabrication and characterisation of high efficiency inverted P3HT: PCBM polymer solar cells," *Materials Science*, pp. 13-233, 2014.
- [5.2] F. Hubenthal, "Nanomaterials," in *Comprehensive Nanoscience and Technology*, Kassel, Academic Press, 2011, pp. 375-435.
- [5.3] D.C. Olson, S.E. Shaheen, R.T. Collins, and D.S. Ginley, "The Effect of Atmosphere and ZnO Morphology on the Performance of Hybrid Poly(3-hexylthiophene)/ZnO Nanofiber Photovoltaic Devices," *Journal of Physical Chemistry*, vol. 111, no. 44, p. 16670–16678, 2007.
- [5.4] D. Han and S. Yoo, "The stability of normal vs inverted organic solar cells under highly damp conditions: Comparison with the same interfacial layers," *Solar Energy Materials and Solar Cells* 128:41–47, vol. 128, p. 41–47, 2014.
- [5.5] D.C. Tiwari, S.K. Dwivedi, P. Dipak, and T.C.R. Sharma, "Sol-gel derived ZnO as an electron transport layer (ETL) for inverted organic solar cells," *AIP Conference Proceedings*, vol. 1832, pp. 060024-1-060024-3, 2017.

- [5.6] T.F.G. Muller, C.J. Arendse, A. Ramashia, D.E. Motaung, F.R. Cummings, G.F. and Malgas, "Influence of solvent casting and weight ratios on the morphology and optical properties of inorganic-organic hybrid structures," *Proceedings of SAIP2014*, pp. 1-6, 2014.
- [5.7] M. Chegaar, A. Hamzaoui, A. Namoda, P. Petit, M. Miller, and A. Herguth, "Effect of Illumination Intensity on Solar Cells Parameters," *Energy Procedia*, vol. 36, p. 722 – 729, 2013.
- [5.8] S. Hussain, "Investigation of Structural and Optical Properties of Nanocrystalline ZnO," *Material Science*, pp. 15-24, 2008.
- [5.9] Z. Qiu, M. Trushin, H. Fang, I. Verzhbitskiy, S. Gao, E. Laksono, M. Yang, P. Lyu, J. Li, J. Su, M. Telychko, K. Watanabe, T. Taniguchi, J. Wu, A.H.C Neto, L. Yang, and G. Eda, "Giant gate-tunable bandgap renormalization and excitonic effects in a 2D semiconductor," *Science Advances*, vol. 5, pp. 1-7, 2019.
- [5.10] S. Gahlawat, J. Singh, A.K. Yadav, and P.P. Ingole, "Exploring Burstein–Moss type effects in nickel doped hematite dendrite nanostructures for enhanced photo-electrochemical water splitting," *Physical Chemistry Chemical Physics*, no. 36, 2019.

- [5.11] D.C. Lim, W.H. Shim, K.D. Kim, H.O. Seo and J.H. Lim, "Spontaneous formation of nanoripples on the surface of ZnO thin films as hole-blocking layer of inverted organic solar cells," *Solar Energy Materials & Solar Cells*, vol. 95, p. 3036–3040, 2011.
- [5.12] N. Sekine, C. H. Chou, W. L. Kwan, and Y. Yang, "ZnO nano-ridge structure and its application in inverted polymer solar cell.," *Organic Electronics*, vol. Vol 10, p. 1473–1477, 2009.



The logo of the University of the Western Cape, featuring a classical building with a pediment and six columns.

Summary and Future Work

UNIVERSITY *of the*
WESTERN CAPE

6.1 Summary

The study on OPV devices is tremendous. It provides room for promising devices to be fabricated at low-cost, devices that are compatible with roll-to-roll commercial production. OPVs, however, suffer instability under ambient conditions and thus, rapid deterioration of the device occurs. These issues were addressed by introducing an inverted organic solar cell (IOSC) structure. IOSC has low-work function metal oxide cathode and high-work function metal as the top electrode. This method of orientation eliminates the risk of the device undergoing fast oxidation and deterioration. Moreover, the polymeric layer was used as the active layer and a metal oxide as an HTL. Therefore, optimization of the respective IOSC layers is an essential requirement for working IOSC devices.

This work reported on a simple approach to improving the optoelectronic properties of ZnO nanoridges by means of incorporating hydrothermally synthesised wurtzite ZnO nanoparticles under a controlled synthesis period and temperature. ZnO nanoparticles were initially investigated and subsequently utilised as seeds to induce ripple growth in sol-gel spin-coated ZnO thin-films incorporated into IOSCs as ETLs. The chemical, structural, morphological and optical properties of ZnO NPs were analysed in detail with FTIR, XRD, HR-TEM, and UV-Vis absorption spectroscopic techniques. FTIR results revealed the presence of the Zn-O shoulders at $\sim 400\text{-}595\text{ cm}^{-1}$. X-ray diffraction and HR-TEM analyses demonstrated that the samples have a wurtzite structure and are polycrystalline in nature. XRD analysis revealed that ZnO NPs are stoichiometric with a c/a crystal lattice ratio close to ZnO single crystal. The HR-TEM results revealed that all the samples are in good agreement with the XRD results. UV-vis absorption spectra illustrated that

the absorption peaks of the ZnO are decreasing from 371 to 366 nm and 375-367 for hydrothermal synthesis period and temperature conditions, respectively, which is blue-shifted relative to the bulk exciton absorption (373 nm) due to the quantum confinement effect.

The effect of incorporating ZnO NPs on the morphological, topographical and optical properties of ZnO nanoridges thin-films was investigated. The EDS confirmed the presence of Zn and O atoms on the surface of the ITO. The incorporated nanoparticles lead to the decreasing nanoridge width sizes in SEM analysis. The thin-films showed a decrease in the step-height with the increase in the hydrothermal synthesis period and temperature, attributed to the decreasing particle sizes. Furthermore, the SEM analysis revealed uniform orientation of the nanoridges on the surface of the ITO. These uniformly oriented NRs lead to high transparency in the UV-Vis transmittance measurements greater than 75%. UV-Vis absorption spectra of the unseeded ZnO NRs and ZnO NPs-seeded ZnO NRs of hydrothermally synthesised NPs under period and temperature control showed a decrease in the wavelength, ranging from ~359-362 nm and ~357-360 nm, respectively. The transparency in the ETLs attributed to the seeding of ZnO NPs in ZnO NRs played a significant role in the performance of the IOSCs. Both the experimental conditions confirm the dependence of IOSCs' performance on the change in the synthesis temperature and period of the ZnO NPs. The IOSCs under period control showed the highest PCE of 1.66%, and under temperature control, the highest obtained PCE is 2.30%, corresponding to 6 hrs and 180°C hydrothermally synthesised NPs, respectively. These PCEs confirm the improvement of the IOSCs compared to the IOSC with unseeded ETL. The enhanced band gaps attribute to the improvements. Therefore the improved band gaps of ZnO NPs-ZnO NRs ETLs introduced a heterojunction

electric field created at the ZnO and polymer active layer interface that supports increasing the electron-hole pairs dissociation, efficiently transporting the charge carriers to their respective electrodes and thus increasing the photovoltaic property of the IOSC layers.

6.2 Future work

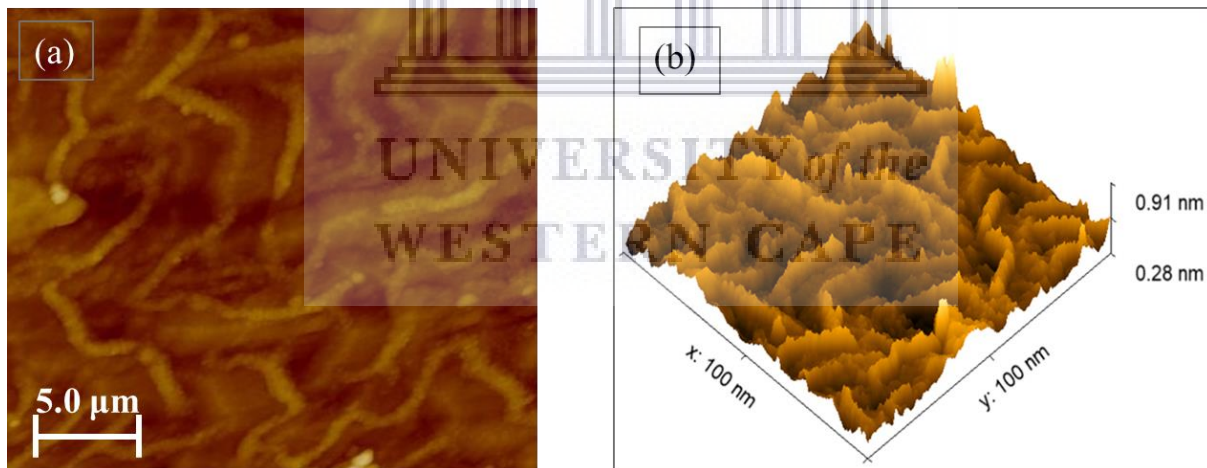
A manuscript emanating from this work for participation at the Conference of the South African Advanced Materials Initiative (CoSAAMI-2021) was submitted for publication. Another manuscript for a journal article is being prepared. Further studies on the effect of stability between the interfaces of layers on the performance of the photovoltaic devices are planned.



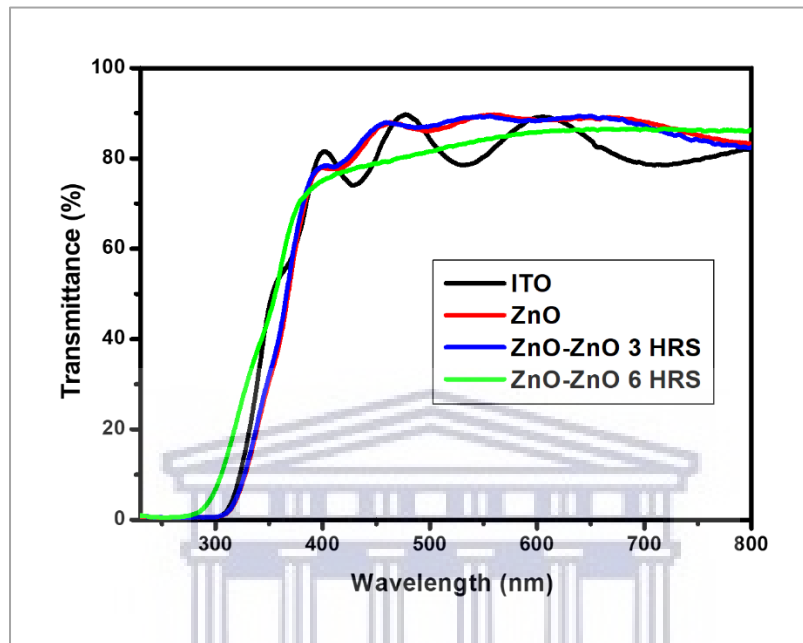
APPENDIX

Appendix A 1: Sample surface characterisation

Atomic force microscopy (AFM) or scanning force microscopy (SFM) is a highly-resolution kind of scanning probe microscopy (SPM), demonstrating a resolution on the order of fractions of a nanometre. In AFM, a cantilever tip is integrated at the end of the spring cantilever. The tip is brought into close proximity with the interatomic layer of the sample. The topographic features of the surface are mapped down as the deflection of the cantilever is measured. AFM images (a) and (b) show the plain and 3D imaging of ZnO NPs- ZnO nanoridges of hydrothermally synthesised ZnO NPs seeds at 180°C. The optical analysis (transmittance spectroscopy) of this sample is illustrated in appendix A 3.

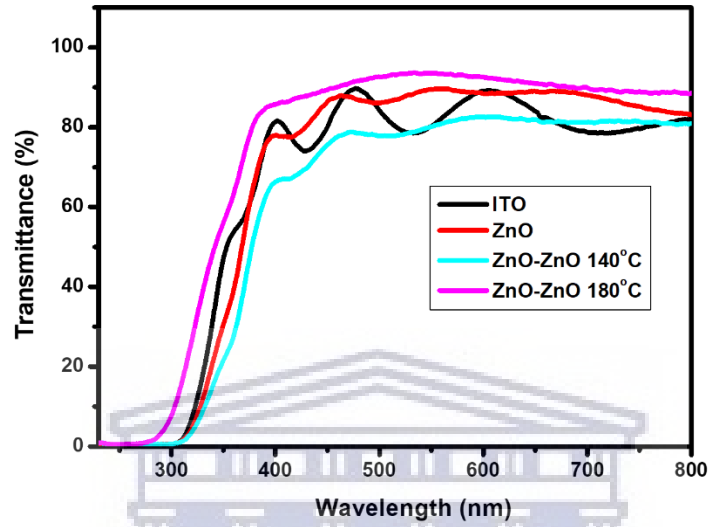


Appendix A 2: Optical transmittance spectra of unseeded ZnO NRs and seeded ZnO NPs-ZnO NRs for 3 hrs and 6 hrs, at 200°C on ITO substrate.



UNIVERSITY of the
WESTERN CAPE

Appendix A 3: Optical transmittance spectra of unseeded ZnO NRs and seeded ZnO NPs-ZnO NRs at 140°C and 180°C for 6 hrs.



UNIVERSITY of the
WESTERN CAPE